

Smart attitude control system for small satellites

ZIHAO WANG

M.Eng



THE UNIVERSITY OF
SYDNEY

Supervisor: Xiaofeng Wu
Associate Supervisor: Gregory Chamitoff

A thesis submitted in fulfilment of
the requirements for the degree of
Doctor of Philosophy

School of Aerospace, Mechanical and Mechatronic Engineering
Faculty of Engineering
The University of Sydney
Australia

8 December 2022

Statement of originality

This is to certify that to the best of my knowledge, the content of this thesis is my own work. This thesis has not been submitted for any degree or other purposes.

I certify that the intellectual content of this thesis is the product of my own work and that all the assistance received in preparing this thesis and sources have been acknowledged.

Name: Zihao Wang

Signature:

Authorship attribution statement

Chapter 3 of this thesis has been submitted to the journal "IEEE transactions on aerospace and electronic systems". I designed the study, conducted the experiments, analysed the data, and wrote the drafts of the MS.

Chapter 4 of this thesis is published as [134]. I designed the study, conducted the experiments, analysed the data, and wrote the drafts of the MS.

Section 3.2.4 of this thesis is published as [37]. I co-designed the study with the co-authors, prepared the experiments, collected and visualized the data.

In addition to the statements above, in cases where I am not the corresponding author of a published item, permission to include the published material has been granted by the corresponding author.

Student Name: Zihao Wang

Signature:

Date: 26 August 2022

As supervisor for the candidature upon which this thesis is based, I can confirm that the authorship attribution statements above are correct.

Supervisor Name: Xiaofeng Wu

Signature:

Date:

Abstract

The attitude control system is one of the most important systems for satellites, which is essential for the satellite's detumbling, pointing, and orbital maneuver. The conventional attitude control system consists of magnetorquers, reaction wheels, and thrusters. Among these actuators, magnetorquers are widely used for satellite detumbling and attitude control, especially for small satellites and CubeSats. It consumes zero propellant compared with thrusters and has a high chance of survival compared with the reaction wheel as it does not contain any moving parts, which makes them last longer in harsh environments.

Conventional magnetorquers utilize air or soft magnetic materials, e.g., iron and alloys, as core, and the magnetic field is generated by feeding the electric current to the wrapped solenoid. Due to the power limit of the small satellites, the magnetic field strength is strictly limited, and the continuous current supply results in massive energy consumption for detumbling and other attitude adjustment missions. The long copper wire of the solenoid will also result in high resistance and generate significant heat. To improve the current design and overcome the proposed drawbacks, a novel electro-permanent magnetorquer has been designed and developed in this thesis as one actuator of the attitude control system. Unlike conventional magnetorquers, the electro-permanent magnetorquer utilizes hard magnetic materials as the core, which can maintain the magnetization when the external magnetic field is removed, to generate the required magnetic field. A special driving circuit is designed to generate the desired dipole moment for the magnetorquer, and the components used for the circuit are carefully selected. The experiments show that the electro-permanent magnetorquer can generate 1.287 A m^2 dipole moment in either direction. The magnetorquer works in pulse mode to adjust the dipole moment, and it requires around 0.75 J energy maximum per pulse. A single-axis detumbling experiment has been conducted using only one torque rod on the air-bearing table inside an in-house manufactured Helmholtz cage. The experiment results show that the magnetorquer can detumble the air bearing table with 0.0612 kg m^2 moment of

inertia from an initial speed of around $27^\circ/\text{s}$ to zero within 800 s, and total energy of 82.92 J was consumed for the detumbling experiment. A single torque rod single-axis pointing experiment has been conducted with a sliding mode controller on the same platform. The results show that a single torque rod can achieve the target angle and maintain the error discrepancy within the $\pm 0.4^\circ$ boundary under a specific system configuration.

A micro air-fed magnetoplasmdynamic thruster has been designed and tested as another attitude control system actuator. The thruster is a miniaturized electric propulsion system based on the conventional full-scale magnetoplasmdynamic thruster that operates at hundreds of kilowatts. The thruster is designed and tested using normal air as the propellant under the pulse operation mode on a calibrated micro-force measurement thruster stand. The experiments revealed that the thruster could generate a $34.534 \mu\text{Ns}$ impulse bit with an average power input of $1.857 \pm 0.0679 \text{ W}$ and thrust to power ratio of $8.266 \mu\text{N/W}$. The specific impulse is calculated to be 2319 s with a thruster efficiency of 9.402%, which is quite competitive compared with other solid-state and liquid-fed pulse-mode thrusters. This paper presents the design and test results for the thruster under a low power level, as well as an analysis of its problems and limitations with corresponding future research and optimization directions noted at the end.

The electro-permanent magnetorquer as a payload of the CUAVA-2 satellite mission has been introduced in this thesis. The design considerations and adjustment based on the requirement of the CUAVA-2 has been introduced in detail. A simple sliding mode controller has been developed to achieve three-axis attitude control using both electro-permanent magnetorquer and the micro air-fed magnetoplasmdynamic thruster. The controller's performance has been tested using MATLAB-based simulation with the experimentally obtained performance parameters and some assumptions. The results show that the smart attitude control system can achieve $\pm 0.005^\circ$ pointing error discrepancy with the help of both actuators.

Acknowledgements

I would like to express my deepest appreciation to my supervisor Dr. Xiaofeng Wu, for his invaluable advice, continuous support, and patience during my PhD study. I am also grateful to my colleague and friends, Mr. Zhicheng Xie, Mr. Xianliang Chen, and Mr. Yijun Huang for their technical support and inspiration. I would like to thank all the members in the CUAVA. Their help and support made my study and life in the University of Sydney a wonderful journey. Finally, I would like to express my gratitude to my parents. It would be impossible for me to complete my study without their support and encouragement.

Contents

Statement of originality	ii
Authorship attribution statement	iii
Abstract	iv
Acknowledgements	vi
Contents	vii
List of Figures	xi
List of Tables	xvi
Chapter 1 Introduction	1
1.1 Thesis aim and structure	4
Chapter 2 Literature review	6
2.1 Magnetorquer	7
2.1.1 Air core magnetorquer	7
Delfi-PQ mission	10
FORESAIL-1	10
Commercial off-the-shelf product	11
2.1.2 Torque rod magnetorquer	12
2.1.3 Embedded coil magnetorquer	16
2.1.4 Low power magnetic torquer	21
2.2 Micro air-fed magnetoplasmadynamic thruster	25
Chapter 3 Electro-Permanant Magnetorquer	30
3.1 Introduction	30

3.1.1	Magnetic basics	31
3.1.1.1	Magnetic field strength and magnetic flux density	31
3.1.1.2	Magnetization	32
3.1.1.3	Dipole moment	33
3.1.1.4	Hysteresis loop	34
3.1.1.5	Soft magnetic material and hard magnetic material	36
3.2	EPM design and functional test	38
3.2.1	Material selection	38
3.2.2	Driving circuit	42
3.2.2.1	Operation logic	43
3.2.2.2	Main capacitor and discharge voltage	44
3.2.2.3	Charging module	51
3.2.2.4	H-Bridge	54
3.2.2.5	Feedback control method	57
3.2.3	Torque rod design and parametric study	59
3.2.3.1	Torque rod solenoid	59
3.2.3.2	Torque rod performance vs. shape parametric study	66
3.2.4	EPM test result	74
3.2.4.1	Experimental setup	75
3.2.4.2	Basic working principle	75
3.2.4.3	Measured flux density vs. capacitor voltage	77
3.2.4.4	Demagnetize and residual B field	78
3.2.4.5	Discharge profile	83
3.2.5	Conclusion	88
3.3	Performance measurement	89
3.3.1	Helmholtz cage	89
3.3.1.1	Basic theory	90
3.3.1.2	Cage design and development	90
3.3.1.3	Calibration and verification	95
3.3.2	Air bearing table	102

3.3.2.1	Basic theory	103
3.3.2.2	Table design and development	104
3.3.3	Magnetic dipole moment measurement	106
3.3.4	EPM for satellite detumble	111
3.3.4.1	B-dot controller	112
3.3.4.2	Setup	114
3.3.4.3	Result	115
3.3.5	EPM for single axis control	117
3.3.5.1	Equation of motion	117
3.3.5.2	Controller design	118
3.3.5.3	Experiment setup	119
3.3.5.4	Result	119
3.3.5.5	Discussion	121
3.3.6	Conclusion	122
Chapter 4	Micro Air-fed Magnetoplasmdynamic Thruster	124
4.1	Methodologies	124
4.1.1	Thruster design	124
4.1.2	Performance calculation	125
4.1.2.1	Mass bit determination	127
4.1.2.2	Pulse energy determination	129
4.1.2.3	Impulse measurement	130
4.1.3	Calibration	133
4.1.3.1	Thruster stand calibration	133
4.1.3.2	Solenoid calibration	133
4.1.4	Experiment environment	134
4.2	Results	135
4.2.1	Calibration results	135
4.2.2	Thruster test results	137
4.3	Discussion	139
4.4	Conclusions	143

Chapter 5	EPM for CUAVA-2 Payload Design	145
5.1	Electronic design	145
5.1.1	Main controller	146
5.1.2	Power system	147
5.1.3	System status monitoring	149
5.1.4	Interface	150
5.1.5	PCB layout	150
5.2	Hardware design	152
5.2.1	Shielding shell	153
5.2.2	Torque rod stand	155
5.2.3	Integration and vibration test results	157
5.3	Conclusion	159
Chapter 6	Three axis control algorithm for Smart Attitude Control System	160
6.1	Controller design	160
	Theorm 1	162
	Proof	163
6.2	Simulation	165
6.3	Analysis	166
6.4	Conclusion	169
Chapter 7	Conclusion and future work	170
Bibliography		174
1	Appendix A: MATLAB Code for detumbling experiment	187
2	Appendix B: Design and validation of the sliding mode controller for single axis attitude control using EPM	192
3	Appendix C: MATLAB Code for the single torque single axis pointing experiment	195
4	Appendix D: EPM for CUAVA-2 vibration test results	198

List of Figures

1.1	Magnetorquer working principle.	2
2.1	iMTQ Magnetorquer air core magnetorquer [53]	8
2.2	EXA MT01 Compact Magnetorquer [38]	8
2.3	Air core magnetorquer prototype for Delfi-PQ mission [21].	10
2.4	Air core magnetorquer for FORESAIL-1 mission [59].	11
2.5	iMTQ magnetorquer board sold by ISISPACE [53]	13
2.6	NCTR-M002 Magnetorquer Rod sold by NewSpace Systems [97]	13
2.7	Demagnetization curve	14
2.8	Incomplete demagnetization curve	15
2.9	(a) Dipole moment and (b) power consumption vs. different length radius ratio and current for a fixed radius cylindrical core magnetorquer [18].	15
2.10	Cross sectional view of PCB embedded magnetorquer and layer arrangement [8]	18
2.11	The NanoPower P110 (P110) solar panels with embedded magnetorquer [1]	18
2.12	Parameters for general PCB magnetorquers.	19
2.13	Comparison of dipole moment and power efficiency for a single layer PCB magnetorquer with controlled parameters operating in (a)(c) Constant voltage mode and (b)(d) constant current mode in terms of different trace width, number of traces and power. The isometric contours indicate power input with units of W. [124]	19
2.14	PCB magnetorquer with different and non-uniform trace width [64]	20
2.15	PCBSat in (a) flat unfold state and (b) orthogonal fold state [46].	21
2.16	Control circuit of the magnetorquer with "changeable magnet" as core [39]	22
2.17	Theory of quantizing the dipole moment.	24
2.18	Cross-sectional view of the general MPD thruster.	28
3.1	Ideal solenoid.	31
3.2	Hysteresis loop (BH Curve).	35

3.3	Minor hysteresis loop.	37
3.4	Hysteresis loop for the hard and soft magnetic material.	37
3.5	Property distribution for common magnetic materials.[132]	39
3.6	Demagnetization curve for common permanent magnetic material [3, 4]	39
3.7	Demagnetization curve comparison between AlNiCo 5 and other alloys [54]	41
3.8	Demagnetization curve of the LNG40 used in this thesis [5]	42
3.9	Block diagram of the control circuit used for the EPM in this thesis.	43
3.10	Simplified discharge circuit consists of the main capacitor array, equivalent series inductance, and equivalent series resistance.	45
3.11	Inductance estimation for different torque rod length and radius.	47
3.12	Coefficient Ψ and the time when maximum current occurs T_{max} as a function of capacitance with fixed inductance L and resistance R .	48
3.13	Major and minor hysteresis curve for the AlNiCo magnet under measurement [27].	49
3.14	Hysteresis curve for the AlNiCo magnet with reducing applied field intensity [58]	50
3.15	Schematic of the charge module.	54
3.16	Schematic of one of the H-Bridge.	57
3.17	Coefficient Ψ as a function of inductance L with fixed capacitance and resistance.	60
3.18	Coefficient Ψ as a function of resistance R with fixed capacitance and inductance.	61
3.19	Maximum field intensity H_{max} and maximum discharge current i_{max} as a function of turns of wire with 60 mm torque rod and AWG 28 enameled copper wire.	63
3.20	Time of maximum current t_{max} as a function of turns of wire with 60 mm torque rod and AWG 28 enameled copper wire.	63
3.21	Maximum field intensity H_{max} as a function of turns of wire and wire with different AWG for 60 mm length torque rod.	65
3.22	Time when maximum current occurs t_{max} as a function of turns of wire and wire with different AWG for 60 mm length torque rod.	65
3.23	Indication of the torque rod configuration and parameters under control for the parametric performance study.	67
3.24	Magnetic field intensity inside a 60 mm long 6 mm diameter cylindrical solenoid carrying 100 A current.	68

3.25	Magnetic field intensity inside a 60 mm long cylindrical solenoid carrying 100 A current with various diameter.	69
3.26	Magnetic field intensity inside a 6 mm diameter long cylindrical solenoid carrying 100 A current with various length.	70
3.27	Measured dipole moment and corresponding magnetization for magnet bars with different diameters and lengths.	73
3.28	Prototype board of the EPM (left) top view, (right) bottom view.	76
3.29	Waveform of capacitor voltage and corresponding hall sensor reading.	76
3.30	Torque rod magnetic flux density measurement for 120 charging pulses at 100 V.	78
3.31	Torque rod flux density versus incremental and alternating capacitor voltage in two directions.	80
3.32	Magnet flux density in response to different capacitor discharge at the alternating direction.	81
3.33	Saturated magnetic density versus the capacitor voltage.	82
3.34	Two capacitor voltage profile for the demagnetization process.	82
3.35	Charging response after different demagnetization profiles.	84
3.36	Alternating discharge direction at 100 V capacitor voltage after linearly decreasing capacitor voltage demagnetization with different pre-demagnetize torque rod status.	85
3.37	Measured discharge voltage trace and the fitted discharge current for a pulse at 400 V capacitor voltage.	86
3.38	Maximum current i_{max} for continuous 10 pulses at 400 V capacitor voltage to charge the torque rod in one direction and the reversed direction.	86
3.39	Square shaped Helmholtz coil configuration.	91
3.40	Magnetic flux density along the center axis of the two square Helmholtz coil.	92
3.41	Magnetic flux density along the center axis of the two square Helmholtz coil with adjusted separation coefficient.	93
3.42	Photo of the completed Helmholtz cage.	94
3.43	Schematic of the H-bridge used for Helmholtz Cage direction control.	95
3.44	Configuration of calibration device for the Helmholtz cage.	96
3.45	2-D magnetic field measurement results under different types of distortion.	97

3.46	Calibration results for different planes and overall sphere plot.	98
3.47	Natural magnetic field measurement in the middle plane of the Helmholtz cage.	99
3.48	Magnetic field measurement in the middle plane after the cancellation of the Earth's magnetic field.	99
3.49	3-Axis magnetic flux density measurement with an increasing current in different axis.	102
3.50	Working principle of the air bearing.	103
3.51	SolidWorks model of the designed ABT.	105
3.52	Complete setup of the ABT and EPM inside the Helmholtz Cage with OptiTrack camera.	107
3.53	Detumble test result of the ABT with negative initial velocity.	115
3.54	Torque generated by a magnet inside a uniform ambient magnetic field with flux density B .	118
3.55	System angular position history for a 60 DoctorofPhilosophy turning control input.	120
3.56	System angular speed (top figure), EPM command (middle figure), and control error (bottom figure) for the 60 DoctorofPhilosophy turning control input.	120
3.57	System angular position history for multi-target turning control input.	121
4.1	Cross-sectional view of the proposed μ AF-MPDT.	125
4.2	Photo of μ AF-MPDT with power cable and propellant feed pipe connected.	126
4.3	Layout of the experimental devices.	127
4.4	Schematic of the thruster stand.	130
4.5	Thruster testing device in a vacuum chamber.	135
4.6	Relationship between force, current and gap size (error bar too short for plot). (a) Force with increasing current. (b) Force with increasing gap size	136
4.7	Thrust stand reaction to the current sweep from 10 to 60 mA.	138
4.8	Plasma plume during one pulse.	138
4.9	Typical waveform for one pulse (a) Comparison of position history for one pulse for Cold Gas and Hot Pulse configuration. (b) Raw and filtered current trace for one pulse.	139

4.10	Simplified circuit diagram for μ AF-MPDT system.	142
5.1	Block diagram of the power system with current monitoring.	148
5.2	PCB Specifications of Pumpkin CubeSat [100]	151
5.3	PCB layout of EPM payload.	152
5.4	Photo of the top and bottom of the final EPM payload board.	153
5.5	Photo of the top and bottom of the aluminium box.	154
5.6	Photos of the assembly of the aluminium box with EPM board.	154
5.7	Assembly of the EPM payload board with copper shielding.	155
5.8	X and Y axis torque rod stand.	156
5.9	Z axis torque rod stand.	157
5.10	Assembled CUAVA-2 payloads for vibration test.	158
6.1	The system attitude history for the simulation using only EPM as the actuator. System angles are represented in roll, pitch, and yaw angle in degree.	167
6.2	The total amount of dipole moment generated by each axis torque rod of the simulation using only EPM as the actuator.	167
6.3	The system attitude history for the simulation using both EPM and μ AF-MPDT as the actuator. System angles are represented in roll, pitch, and yaw angle in degree.	168
6.4	The three axis torque force generated by the thrusters of the simulation using both EPM and μ AF-MPDT as the actuator.	168
.1	Sliding manifold illustrated on the phase plane.	193
.2	Load response to vibration in X axis from 20 to 2000Hz before and after 14.501 g RMV.	199
.3	Load response to vibration in Y axis from 20 to 2000Hz before and after 14.501 g RMV.	199
.4	Load response to vibration in Z axis from 20 to 2000Hz before and after 14.501 g RMV	200

List of Tables

2.1 Performance of the air core magnetorquer designed for Delfi-PQ mission [21].	10
2.2 Performance of the air core magnetorquer designed for FORESAIL-1 mission[59]	11
2.3 Summary of the performance of COTS air core magnetorquer	12
2.4 Summary of the performance of COTS torque rod magnetorquer	17
2.5 Summary of the performance of PCB magnetorquers	21
2.6 Characteristics of electric propulsion systems for small satellites	27
3.1 Two groups of magnet bars under test.	72
3.2 Dipole moment and the magnetization measurement result of two groups of magnet bars.	72
3.3 Curve fitting results and fitted amplification coefficient Φ for each axis.	100
3.4 Angular momentum measurement of the test platform along the vertical axis.	109
3.5 Mass and moment of inertia of two groups of magnet bars.	110
3.6 Fitted frequency for different magnetization directions, Helmholtz cage Y axis current, and the final calculated dipole moment.	111
4.1 Mathematical model for the quadratic curve fitting	136
4.2 Position measurement results	137
4.3 Torsional pendulum calibration results	137
4.4 Electrical parameters measurement results	137
4.5 Thruster test results	139
4.6 Comparison between the μ AF-MPDT and other PPTs/VATs	141

CHAPTER 1

Introduction

The attitude determination and control system (ADCS) is essential for satellites. One of the most common attitude control methods utilizes a reaction/momentum wheel and the law of conservation of angular momentum. A motor connects to the wheel and accurately controls the wheel's angular speed and acceleration. Due to the conservation of angular momentum, the satellites gain angular momentum. The other prevalent attitude control method is thrusters, relying on Newton's Third law of motion. The satellites accelerate and eject mass in the opposite direction to gain linear momentum in the desired direction. Instead of using the conservation of momentum, another commonly used attitude control method, magnetorquer, utilize the electromagnetism interactions with Earth's magnetic field to obtain torque, which is one of the subjects of this thesis.

Magnetorquer relies on the interaction between an artificially generated magnetic field and Earth's magnetic field. The basic working principle of the magnetorquer is shown in Fig. 1.1. The current passing through a solenoid with air or ferromagnetic material as the core generates its own magnetic field line. This magnetic field will try to align with Earth's magnetic field B , generating torque described by this equation:

$$\vec{T} = \vec{m} \times \vec{B} \quad (1.1)$$

Once the magnet is aligned with the external magnetic field direction ($\theta = 0$), it cannot generate any torque. Therefore a magnetorquer system typically consists of 2 or 3 perpendicularly placed solenoids together with a driving and control circuit to ensure that there are always at

least two solenoids fully functional. The direction and strength of the generated magnetic field can be fully controlled by controlling the current passing through the solenoid.

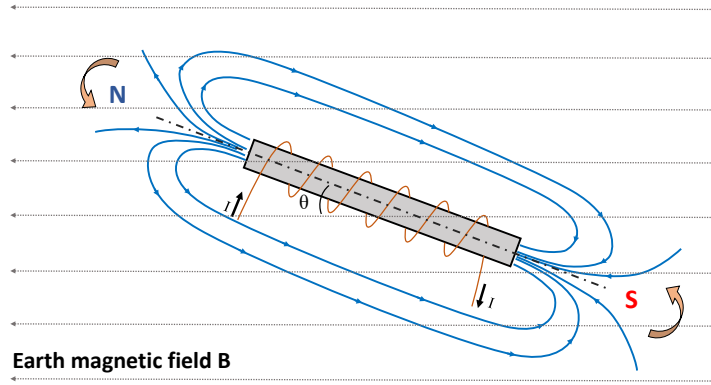


FIGURE 1.1. Magnetorquer working principle.

One significant advantage of magnetorquer is that it sources the momentum from the Earth and does not consume either propellant or momentum margin from the reaction wheel. It is crucially important as these are limited satellite resources and are usually designed for other dedicated missions. For example, when the reaction wheel reaches its maximum angular speed, it becomes saturated and cannot compensate for any more extra momentum. Furthermore, suppose the satellites obtained too high initial angular momentum after being deployed, beyond the momentum margin of the reaction/momentum wheel. In that case, they rely on magnetorquers or thrusters to dissipate the momentum and desaturate. Another advantage is that the magnetorquer has no moving parts and can operate as long as the solar panel is functional. This gives the magnetorquer higher reliability and durability than thrusters and reaction wheels.

However, for small satellites, such as CubeSats, the performance of the magnetorquers, if any, is strongly limited due to the power, size, and weight restrictions. Identical to a solenoid electromagnet, the power limits the maximum electric field it can generate, and the size and weight restrict the thickness and turns of the copper coil can be used. In addition, due to the nature of the electromagnets, it requires a continuous power supply to generate the magnetic field, which exerts a non-negligible pressure on the satellites' power system. Besides, the

solenoid will generate heat while operating, and a thermal control consideration is also required when designing the magnetorquer, which brings more complexity.

As one of the most famous actuators for space projects and applications, sometimes propulsion systems are directly linked to the space mission when discussing space-related topics. For example, launching rockets is the only way humans send satellites to space to date, and the most crucial component for them is the thruster. Satellites decrease their altitude due to atmospheric drag force from the collision between satellite bodies and air molecules. They rely on thrusters to overcome this force to maintain the orbit.

Propulsion systems for satellites are different from those for rockets. Since the total forces applied to satellites reaches equilibrium while the satellites are orbiting, a tiny force will break the equilibrium and change the satellites' attitude. Therefore most of the propulsion systems for satellites are designed to be working on providing small but accurate thrust force. Since the thrusters generate thrust force by ejecting material, the propellant that satellites can carry is strictly limited. Usually, thrusters for satellites have higher efficiency than rockets. Common types of thrusters for satellites include chemical thrusters, cold gas thrusters, resistor jets, electrospray thrusters, and plasma thrusters.

Thrusters for satellites can be categorized into two main types: chemical thrusters and electric thrusters. Chemical thrusters utilize chemical energy to accelerate the propellants, and electric thrusters utilize electrical energy to accelerate and propel propellants to gain kinetic energy. Among the two thruster types, the electric thruster has become increasingly popular thanks to its controllable power consumption and high propellant efficiency. Due to the power and size limit, most high-power electric thrusters are not applicable for small satellites. Pulsed plasma thrusters (PPTs), however, become a competitive candidate as the propulsion system for small satellites thanks to their shallow power requirement, relatively high thrust force, and efficiency. Considering the low power requirement, relatively easier driving circuit design, and control methods, a type of pulsed plasma thruster is chosen to be part of the actuator for small satellite attitude control in this thesis.

1.1 Thesis aim and structure

Low Earth Orbit (LEO) based small satellites have significant advantages in communication, remote sensing, earth observation, and constellation-based applications. [128, 70, 115, 24] Their relatively low cost and short development and test cycle compared with large satellites make them a cost-effective and powerful tool for today's space missions. LEO is generally defined as orbits lower than 1000 km above sea level. [85] The relatively low altitude makes the communication latency between the ground station and satellites remarkably shorter than those operating in geosynchronous equatorial orbit (GEO). However, despite the advantages of LEO-based satellites, such low altitude brings new problems and challenges. For example, as the orbit is too close to the Earth, the air molecule density increases, introducing a higher atmospheric drag force. The relatively faster orbiting speed makes this problem worse.

However, every coin has two sides. The higher air molecule density makes it possible to collect them as the propellant for the PPTs for orbital maneuver and attitude control. The Earth's magnetic field strength is stronger at a lower altitude, giving more room for magnetorquers to perform attitude control. Considering the problems and shortages of the current magnetorquer technology and the great potential and advantages of the LEO-based small satellites missions, this thesis aims to develop and test a novel smart attitude control system consisting of an Electro-Permanent Magnetorquer (EPM) and a micro Air-fed Magnetoplasma dynamic Thruster (μ Af-MPDT). Unlike the conventional magnetorquer made with solenoid with different material as the core, the EPM utilized a novel programmable permanent magnet as the magnetic field source to interact with Earth's magnetic field. The new EPM features higher torque performance, lower power consumption, low thermal stress, and faster response than conventional magnetorquer. The μ Af-MPDT is an ultra miniaturized plasma thruster that combines the merits of PPTs' low average power requirement and magnetoplasma dynamic thrusters' high efficiency and thrust force. The thruster nozzle is designed to be a tiny cylinder with a nine mm diameter and eight mm length that can be embedded into CubeSat's frame for ultra-accurate attitude control and orbit maneuver. Air is chosen as the propellant for the thruster for the direct compatibility with the potential air-breathing propulsion system.

The thesis is structured as follows. In Chapter 2, the background, history, the latest technologies, and satellite missions will be introduced and reviewed for both magnetorquer and thruster technologies. The performance of each actuator will be compared, and the innovative design will be analyzed and discussed.

Chapter 3 will describe the design, development, and test of the EPM in great detail, followed by a simple controller design and experimental verification to prove the ability to use the EPM for de-tumbling and pointing mission objectives.

Chapter 4 will detail the design, development, and performance evaluation of the μ Af-MPDT. A comparison between μ Af-MPDT and other similar thrusters will be concluded at the end of the chapter, followed by the suggested future research direction.

Chapter 5 will describe the design and considerations of the EPM as payload for the CUAVA-2 satellite mission. The mission requirement, objective, platform restrictions, and design adapted for the CUAVA-2 satellite will be detailed.

Chapter 6 will demonstrate the simulation results of using the smart attitude control system as part of the ADCS for the CUAVA-2 mission. A simple controller that utilizes both the EPM and μ Af-MPDT will be designed, and simulation results, including de-tumbling and pointing mission objectives, will be demonstrated using this controller.

Chapter 7 will conclude the work that has been done in this thesis. Future research direction and potential improvements will be highlighted at the end of this chapter.

CHAPTER 2

Literature review

Thanks to the rapid development of miniaturization technology, including integrated circuit (IC), microelectromechanical systems (MEMS), and additive manufacturing, the development, and evolution of small satellites, including microsattellites (total mass from 10 to 200 kg) and nanosatellites (total mass from 1 to 10 kg), has been accelerated. More than 552 NanoSats, including 500 CubeSats, less than 10kg in weight, have been launched successfully in only three years, from 2013 to the end of 2016 [137]. Most of the small satellites launched are placed in LEO, specifically the Sun-Synchronous and Non-Polar Inclined orbits, as they provide consistent light conditions over the Earth's surface, and also because the price per kg (\$/kg) is lowest compared to other orbits [69].

Due to the nature of the LEO, the communication signal delay is significantly shorter than in other higher orbits. Since it is exceptionally close to the Earth's surface, the image taken in the LEO provides higher resolution and richer details with an even cheaper camera and imaging sensor. Therefore LEO satellites are primarily used for providing low latency communication services and Earth observation. However, these mission objectives require high pointing accuracy and an assertive attitude control system as the period for one complete orbit for LEO is within the range of around 90 - 128 minutes, according to Kepler's third law. Some nanosatellite mission deployed by companies and organizations even requires ultra-high pointing and stabilization, which exert intense pressure on the ADCS.

To achieve high pointing and stabilization, not only the attitude determination system shall provide accurate, reliable, and stable position data, but a robust actuator is also mandatory to overcome the disturbance act on the satellites. Standard microsattellite actuators include magnetorquer, gravity gradient boom, wheel-based actuator, and thruster. The working

principle for magnetorquer and wheel-based actuator are introduced in the previous chapter. The gravity gradient boom is a passive stabilization system utilizing the gravity field around the Earth and the tidal force to align the satellite-deployable boom system towards the Earth, which is not attractive to this thesis. The following two sections will introduce and summarize the history, categories, and latest development status of the magnetorquer and thruster technologies.

2.1 Magnetorquer

As introduced in the previous chapter, magnetorquer is a type of electromagnet that can be controlled to interact with Earth's magnetic field to generate torque. The concept of the magnetorquer was firstly proposed by Kamm, LJ back in 1961 [61]. Kamm proposed an attitude control motor consisting of three orthogonal coils to generate the magnetic field, a three-axis magnetometer to measure the Earth's magnetic field, and a computer to handle the sensor data and calculate the required current to each coil. The topology is identical to today's magnetorquer system, and Kamm concluded that the system is simple, lightweight, and does not consume propellant [61].

Magnetorquer is exceptionally useful in LEO because of the negligible decay of the Earth's magnetic field at that altitude. There are three major types of magnetorquers being widely studied and used: air core magnetorquer, torque rod magnetorquer, and embedded coil magnetorquer. Each of them has its advantages, drawbacks, and design considerations.

2.1.1 Air core magnetorquer

Air core magnetorquer is a type of simplest magnetorquer consisting of copper wire winding and frame structure without any core in the middle. Fig. 2.1 shows a commercially available air core magnetorquer made by ISISPACE as part of its product "iMTQ Magnetorquer Board" [53]. In some specific cases where the size and weight budget for magnetorquer are extremely tight, the copper wire winding can be used as a "frame" after being treated with epoxy or adhesives, and the physical frame structure is not mandatory in this case. Fig. 2.2 shows

the commercial product of a compact air core magnetorquer with only 7.5 g and 3.2 mm thickness.



FIGURE 2.1. iMTQ Magnetorquer air core magnetorquer [53]



FIGURE 2.2. EXA MT01 Compact Magnetorquer [38]

The air core magnetorquers are usually used in combination with torque rod magnetorquers as they are generally thin on the vertical axis, which makes it possible to be mounted on the back of the solar panel board or magnetorquer controller board. The air core magnetorquer has zero residual induction after removing the power supply. In contrast, residual induction is a non-negligible problem for torque rod magnetorquer, especially for those using iron or

ferromagnetic material as the core. This will be introduced later in Chapter 3. The model of the air core magnetorquer is relatively simple as the air core magnetorquer can be treated as a solenoid with variable core diameter, wire diameter, and turns of wire, whose dipole moment can be written as:

$$m = nIS \quad (2.1)$$

where m is the dipole moment of the magnetorquer, n is the turns of the loop of the wire, I is the electric current supplied, and S is the area of the coil. However, when designing the air core magnetorquer, there are several things to consider. Firstly the copper wire diameter shall be considered as thicker wire allows more current to pass through and provides lower resistance per unit length. However, using thicker wire increases the total mass of the magnetorquer when the turns of wire increase. Secondly, the turns of wire, which is the n in Eq. (2.1), shall be determined. As for an air core magnetorquer with fixed wire thickness, area, and fixed supply voltage, the power consumption decreases when the number of turns increases as the increasing wire length increases the total resistance, reducing the power consumption. Lastly, the effective area of the magnetorquer S may differ from the designed area as the effective area must be a number bigger than the inner coil area and smaller than the outer coil area [18]. Specific correction factors shall be applied to the design parameters to avoid errors in the final performance. In addition, as most of the air core magnetorquers are made in-house, the unevenly distributed coil winding will cause overlapping of the copper coil, affecting the final magnetorquer performance.

Customized air core magnetorquers are widely used in 1U CubeSats missions, such as AAU CubeSat [11], CANX-1 [127], Cute-1.7+APD [14], and COMPASS-1 [117]. For some missions that require higher power and size for more complex payloads, well-designed magnetorquers are required.

Delfi-PQ mission

Fig. 2.3 shows the prototype of the miniaturized air core magnetorquer developed by van den Bos, M.F. [21]. The blue and green coils are the solenoids for either X or Y axis, and the red coil is for the Z axis. The measured performance data for this air core magnetorquer design for the Delfi-PQ mission is summarized in Table 2.1.

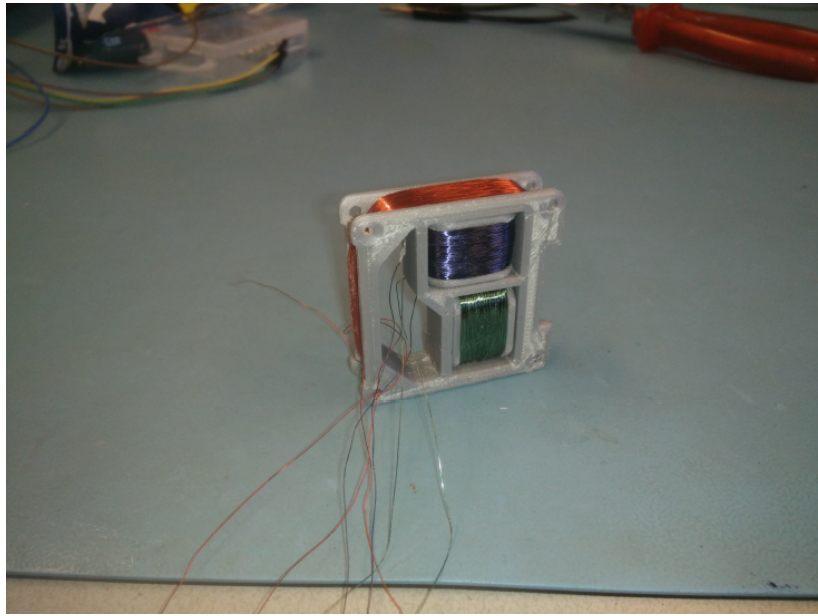


FIGURE 2.3. Air core magnetorquer prototype for Delfi-PQ mission [21].

TABLE 2.1. Performance of the air core magnetorquer designed for Delfi-PQ mission [21].

Coil color	Dipole moment [A m^2]	Voltage [V]	Power [mW]	efficiency [A m^2]/[mW]
Red	0.0165	1.43	91.43	0.000278
Green	0.0044	1.62	120.06	0.000056
Blue	0.0045	1.59	129.47	0.000053

FORESAIL-1

Another 3U CubeSat mission, FORESAIL-1, developed by the Finnish Centre of Excellence for Sustainable Space, relies solely on the magnetorquer to meet the attitude and mission requirement [98]. After the detumbling, the satellite shall maintain a spin rate of 24 $^\circ/\text{s}$ and eventually accelerate to 130 $^\circ/\text{s}$ for the plasma brake payload [59]. Jovanovic, N *et al.*

designed two sets of air core magnetorquer with each set consisting of two long and one short copper wire loop without the supporting structure as shown in Fig. 2.4 [59]. The driving circuit for the magnetorquer is chosen to be the combination of LC filtering circuit, and H-bridge as the system is similar to an electric motor with Earth's magnetic field as stator and satellite itself as rotor, which requires AC power to operate. Table 2.2 summarizes the key performance data for the two types of magnetorquers made by Jovanovic, N *et al.*.

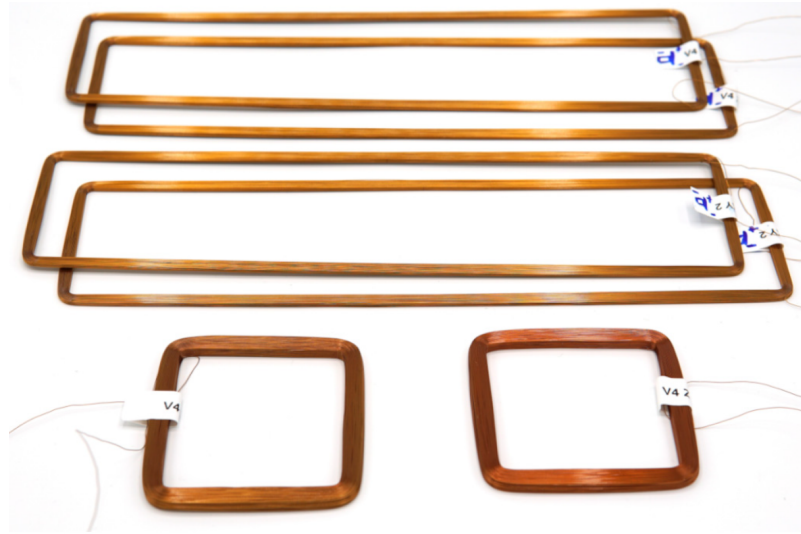


FIGURE 2.4. Air core magnetorquer for FORESAIL-1 mission [59].

TABLE 2.2. Performance of the air core magnetorquer designed for FORESAIL-1 mission[59]

Size	Dipole moment [A m ²]	Voltage [V]	Power @ 0.15 A m ² [mW]	Power @ 0.15 A m ² [mW]	efficiency [%]	Mass [g]
long	0.304	3.6	149.64	423.26	~ 82	17.71
short	0.188	3.6	208.75	334.08	~ 85	29.55

Commercial off-the-shelf product

As a mature and well-studied technology, numerous commercial off-the-shelf (COTS) products have detailed datasheets, comprehensive test results, and a strong flight heritage. Some of them are complete products with driver board and communication interfaces, and some are sold as a single part. Table 2.3 summarizes some of the COTS air core magnetorquers with their performance characteristics.

TABLE 2.3. Summary of the performance of COTS air core magnetorquer

Manufacture	Dipole moment [A m ²]	Residual moment [A m ²]	Voltage [V]	Power [mW]	Thickness [mm]	Mass [g]	Reference
Ecuadorian Space Agency	<0.39	<0.0045	1.25-7.5	250-1750	3.2	7.5	[38]
Cubespace	0.13 / 0.27	N/A	5	75	5.8	46 / 74	[31]
NanoAvionics	0.34	0.001	3.3-5	400 ^a	17	205 ^a	[88]
ISISPACE	0.2	N/A	5	<1200 ^a	17	196 ^a	[53]

^a This value is for a complete magnetorquer module containing both X, Y torque rod, and Z coil.

2.1.2 Torque rod magnetorquer

The torque rod magnetorquer is similar to the air core magnetorquer but has two significant differences. The first difference is the shape of the magnetorquer. Unlike the wounded wire with a usually square shape and rounded corner, the torque rod magnetorquer is in the form of a solenoid with a bigger length to radius ratio, making it more suitable to be placed horizontally on a controller board. Another difference is that a ferromagnetic material is inserted into the solenoid as a core to amplify the magnetic dipole. The performance, residual induction, and electric property change with different materials used as the core. In general, the torque rod magnetorquer generates a higher dipole moment than the air core magnetorquer under the same power level. Fig 2.5 shows the COTS complete magnetorquer board with two torque rod magnetorquer installed perpendicularly, and Fig. 2.6 is the individual torque rod developed and sold by Newspace System [97].

When designing the torque rod magnetorquer, two types of material can be used as core: paramagnetic and ferromagnetic. It is proven that paramagnetic material has a strong limitation as the contribution from the increase of dipole moment is far too less to compensate for the performance degradation from the increase of the weight [18]. However, demagnetization is the biggest issue when designing the ferromagnetic core magnetorquer. As the ferromagnetic material follows the hysteresis loop, once it has been magnetized due to the externally applied field, after removing the external field, the material will have a residual induction B . Therefore when designing the controller for ferromagnetic core magnetorquers, cutting the power to

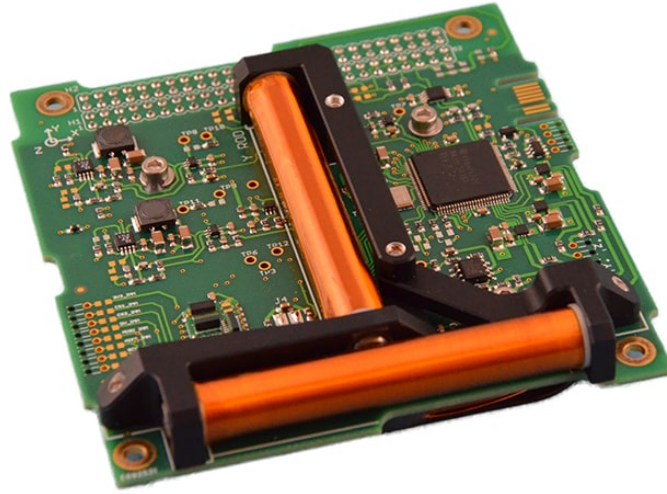


FIGURE 2.5. iMTQ magnetorquer board sold by ISISPACE [53]



FIGURE 2.6. NCTR-M002 Magnetorquer Rod sold by NewSpace Systems [97]

the torque rod does not turn off the magnetorquer. The proper demagnetizing process of the ferromagnetic core is shown in Fig. 2.7, as introduced by Bellini in [18]. An external magnetic field with alternating direction and decreasing magnitude following the numeric order shown in Fig. 2.7 shall be applied to achieve $B = 0$ and $H = 0$ in the hysteresis loop. This process is not power efficient and hard to achieve as the precisely controlled electric current must be supplied in an alternating direction to the coil. Another method is to utilize the minor

hysteresis loop defined in [136] by applying an external magnetic field to a well determined point H_m as labeled in Fig. 2.8. Then the magnetic field will follow the path "Hm-O" in the minor loop, ends at point O, where $B = 0$ when $H = 0$. However, executing the control command from point O will lead to point A following the minor hysteresis loop instead of point B for a complete demagnetized torque rod. Therefore utilizing soft magnetic material in the saturation region is preferred to avoid the demagnetization issue as the saturation will "reset" the magnet disregarding its previous status [18].

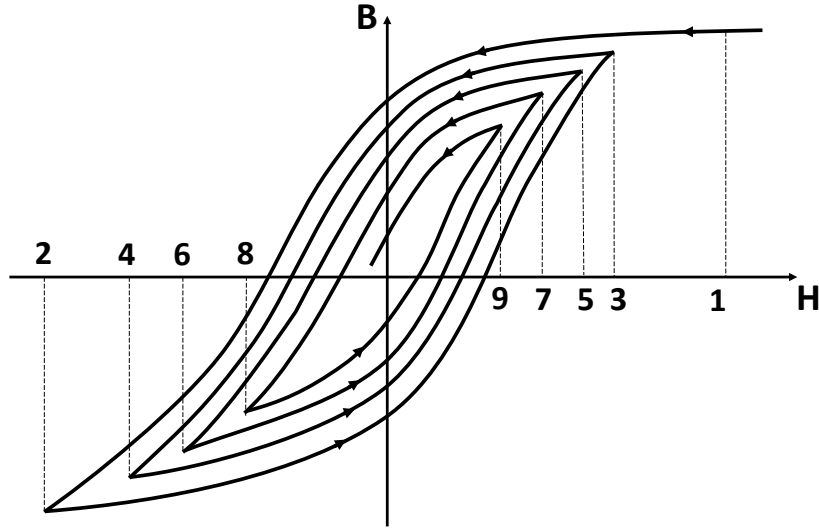


FIGURE 2.7. Demagnetization curve

After determining the core material, the geometry and shape of the core shall be determined. The dipole moment generated by the solenoid with core rod is expressed as [18]:

$$m = NI\pi r^2 + \frac{\pi r^2 NI(\mu_r - 1)}{(1 - N_d + \mu_r N_d)} \quad (2.2)$$

where the N_d is the demagnetizing factor, μ_r is the core material's relative permeability, N , r , and I are the number of coil turns, core radius, and electric current. From the equation, the dipole moment is contributed by two parts: the first comes from the core's volume, and the second affects the core's magnetization for a certain electric current. The relationship between the current, core shape described by the ratio of length and radius of the core, and

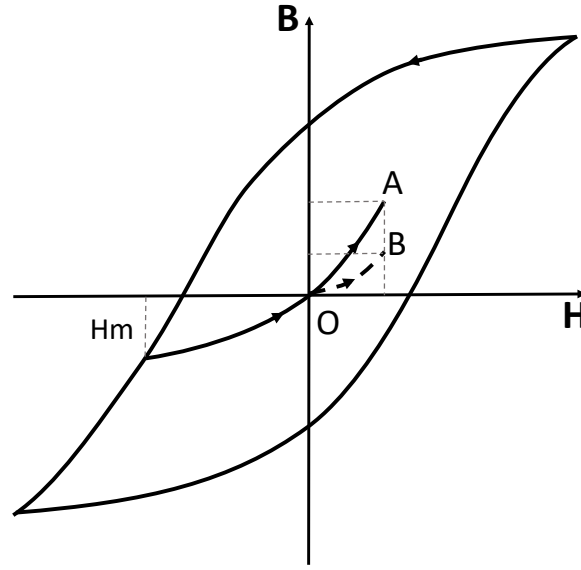
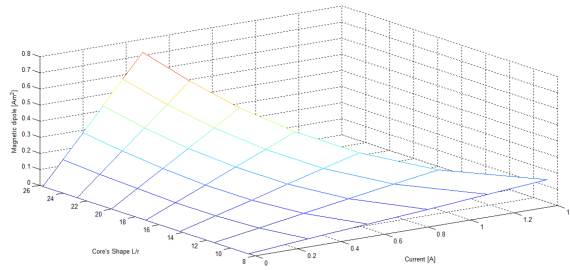


FIGURE 2.8. Incomplete demagnetization curve

dipole moment for a fixed radius cylindrical core and the corresponding power consumption is shown in Fig. 2.9 (a) and (b), respectively.

(a)



(b)

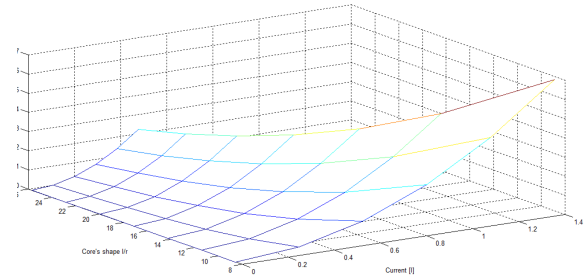


FIGURE 2.9. (a) Dipole moment and (b) power consumption vs. different length radius ratio and current for a fixed radius cylindrical core magnetorquer [18].

From Fig. 2.9, it can be concluded that the length to radius ratio shall be kept as big as possible to maximize the dipole moment and minimize the power consumption, which indicates that the core shall be designed to be thin and long within the size limit of the satellite.

Another aspect to consider when using a ferromagnetic core is the hysteresis losses. Most magnetorquers are controlled by using a controlled current source in combination with the pulse width modulation (PWM) method and H-bridge formed by metal–oxide–semiconductor

field-effect transistors (MOSFETs). Increasing the PWM frequency will increase the hysteresis losses, similar to the electric transformers. The problem can be relieved by using soft magnetic material with a thinner hysteresis loop to reduce the hysteresis loss due to the high-frequency control input.

For torque rod magnetorquer, a few CubeSat missions use their customized device. The QSAT small satellite developed at Kyushu University has customized its own magnetorquer with PB (Ni-Fe) Permalloy as core material wrapped by 1200 turns of copper coil. It can generate maximum dipole moment of 1 Am^2 [93]. However, the power, size, voltage, and residual moment data are not indicated. The HuskySat-1 3U CubeSat developed by the University of Washington equipped with in-house fabricated magnetorquers with a seven mm diameter cylindrical Hiperc 50A, a type of iron-cobalt vanadium soft magnetic alloy, as core material wrapped by around 1580 turns of 30 gauge copper wire [76]. The magnetorquer was driven with at 4 V from on Allegro A3903 H-bridge, consuming 200 mW and can generate a dipole moment of 0.15 Am^2 [76].

Due to sophisticated design processes and relatively high manufacture and calibration requirements, many CubeSat missions use COTS products instead of customizing their magnetorquer. The similar form factor and relatively rigid and compact design make it easier to be commercialized as a product. The CubeSat mission led by WPI, NASA Goddard Space Flight Center, and the Space Research Centre in Poland to test the Sphinx-NG utilized the ZARM Technik AG MTO.2-1 magnetorquer that can generate $\pm 0.2 \text{ Am}^2$ dipole moment with 5 V and 140 mW power supply [133]. The CUAVA-1 mission led by the University of Sydney utilized the CubeTorquer manufactured by CubeSpace as magnetorquer [16]. The torquer can generate $\pm 0.24 \text{ Am}^2$ dipole moment at 2.5V consuming 375mA power [31].

The performance of the COTS torque rod magnetorquers is summarized in Table 2.4 below.

2.1.3 Embedded coil magnetorquer

Embedded coil magnetorquer is another type of magnetorquer similar to the air core magnetorquer, but with the copper coil embedded into the frame or other structure. Since most of

TABLE 2.4. Summary of the performance of COTS torque rod magnetorquer

Manufacture	Dipole moment [A m ²]	Residual moment [A m ²]	Voltage [V]	Power [mW]	Dimension [L x W x H mm]	Mass [g]	Reference
CubeSpace	±0.24	N/A	2.5	375	18x14x62	28	[31]
CubeSpace	±0.66	N/A	5	750	18x14x77	36	[31]
NanoAvionics	0.3	0.005	3.3	400 ^a	96x94x17	205 ^a	[88]
ISISPACE	0.2	N/A	5	1200 ^a	95.9x90.1x17	196 ^a	[53]
NewSpace	>0.2	<0.001	5	200	D9x70	14	[97]
ZARM Technik AG	±0.2	0.001	5	140	D6x85	9	[133]

^a This value is for a complete magnetorquer module containing both X, Y torque rod, and Z coil.

the CubeSats and small satellites have solar panels, which commonly consist of solar cells soldered onto a printed circuit board (PCB), it is an ideal place to embed the magnetorquer. PCB for solar cells usually contains an elementary power conditioning circuit, which can also provide structural stiffness. By integrating the copper coils into the already-exist PCBs, magnetic control can be achieved with little extra weight and space. Thanks to the PCB manufacturing technology improvements, a certain thickness PCB can contain more and more layers of copper traces, giving more possibility and flexibility when designing PCB embedded magnetorquer. As shown in Fig. 2.10 [8], the copper wire traces are printed on each layer of the PCB similar to typical PCB traces but with controlled trace width and separation. Each layer of traces is connected through "vias" in PCB. Changing layer quantity and trace parameters will change the characteristics of the magnetorquer. Fig. 2.11 shows the commercial product of a solar panel with embedded magnetorquer manufactured and sold by GomSpace [1].

Like air core magnetorquer, the dipole moment of the PCB magnetorquer is governed by the eq. (2.1). However, as each layer of the PCB magnetorquer is constructed in 2D dimension, the area of each turn of the copper wire reduces quickly as the number of turns increases. Then considering the simplified trace dimension shown in Fig. 2.12, according to Hassan, A. *et al.*, the dipole moment of the PCB magnetorquer can be shown as:

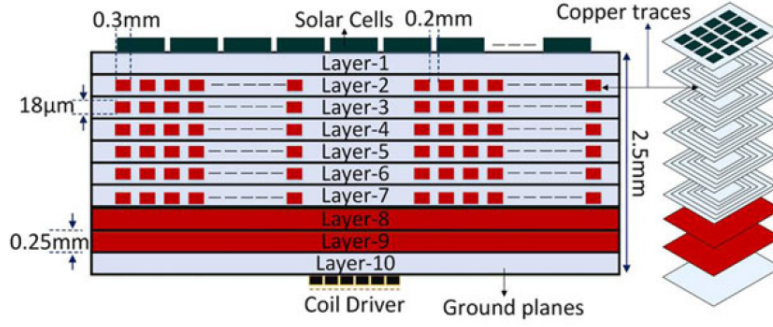


FIGURE 2.10. Cross sectional view of PCB embedded magnetorquer and layer arrangement [8]

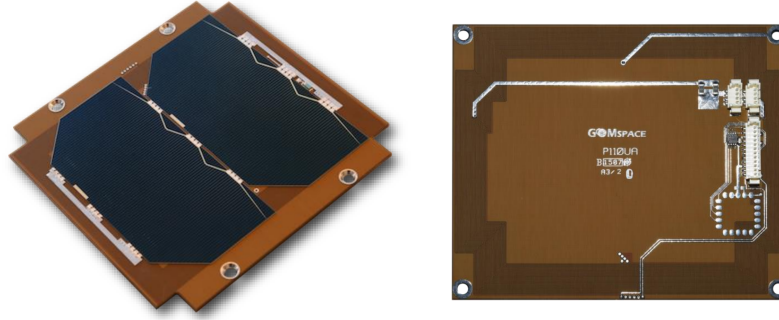


FIGURE 2.11. The NanoPower P110 (P110) solar panels with embedded magnetorquer [1]

$$m = \frac{(L_E \cdot W_E + \sum_{n=1}^{N-1} (L_E - 2n\Delta \cdot W_E - 2n\Delta) \cdot V \cdot A_{cross}}{[\delta \cdot 2(L_E + W_E) + \sum_{n=1}^{N-1} (L_E - 2n\Delta + W_E - 2n\Delta)]} \quad (2.3)$$

where L_E is the outer length of the coil, W_E is the outer width of the coil, Δ is the sum of trace width T_W and trace separation T_{dis} , V is the supplied voltage, δ is the resistivity of the trace, N is the number of turns, and A_{cross} is the cross-sectional area of each trace.

Since the PCB design has many degrees of freedom, such as trace width, copper thickness, trace shape, layer insulation material, base material, and via size, there are too many design considerations and optimization for different system requirements. NICHOLAS, J.S. analyzed the optimization design of the single layer PCB magnetorquers in terms of the dipole moment and power efficiency for constant voltage and constant current control mode with changing trace width and the number of traces [124]. The results are shown in Fig. 2.13 below.

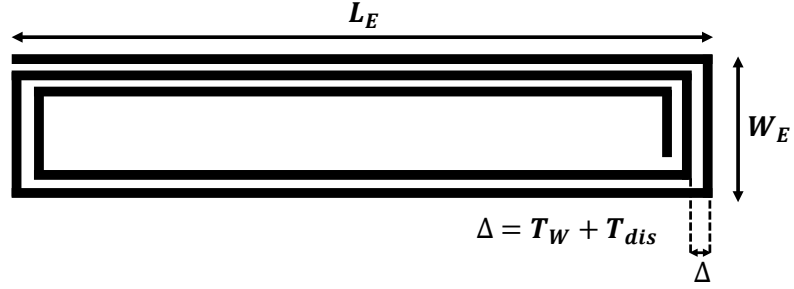


FIGURE 2.12. Parameters for general PCB magnetorquers.

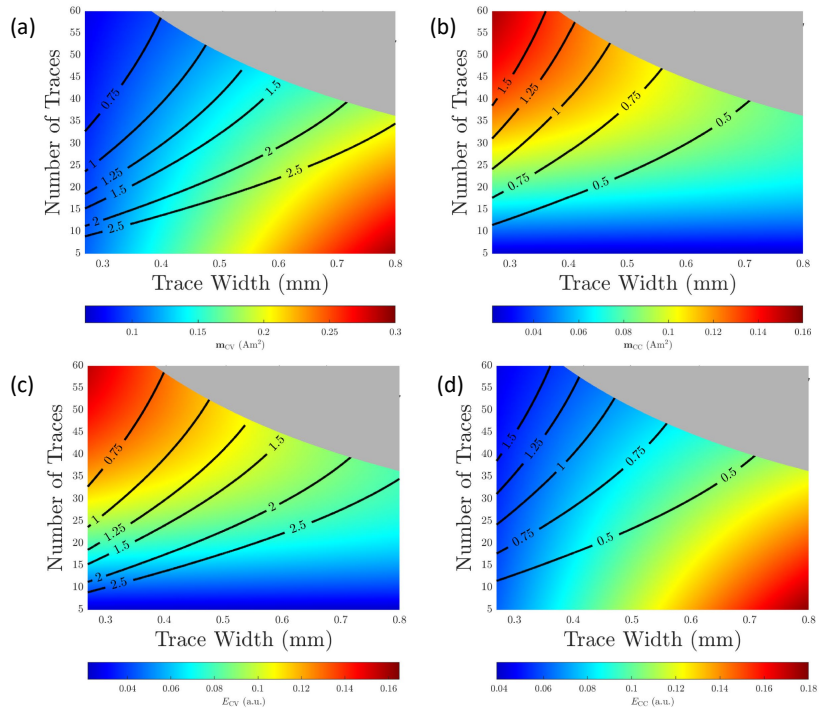


FIGURE 2.13. Comparison of dipole moment and power efficiency for a single layer PCB magnetorquer with controlled parameters operating in (a)(c) Constant voltage mode and (b)(d) constant current mode in terms of different trace width, number of traces and power. The isometric contours indicate power input with units of W. [124]

He claimed that under given geometric bounds and power consumption, the optimization algorithms developed could accurately calculate the optimized parameters for the PCB embedded magnetorquer. He concluded that the PCB magnetorquer systems are a good alternative to other forms of magnetorquers [124]. Muhammad, R.M. *et al* proposed an optimization design method for a re-configurable magnetorquers for CubeSats [96]. The

re-configurable design is achieved by connecting multiple PCBs that contain only trace coil in either series, parallel, or a series-parallel network to the main controller module. Therefore, different dipole moments and efficiency can be achieved by rearranging the connection methods. The thermal performance for different coils configurations has also been analyzed. Shoaib, A.K. *et al.* has analyzed similar design optimization utilizing the re-configurable PCB magnetorquer for a 3U CubeSat. The power circuit, various coil configurations, and thermal performance are analyzed in detail, and Shoaib, A.K. *et al.* concluded that a higher torque-to-power ratio compared with commercial options can be achieved using specific arrangements of the designed magnetorquers [7]. Utilizing the re-configurable PCB magnetorquer for multi-cube small satellites has also been analyzed in [9] with power and configuration optimization and thermal performance analysis. Another interesting research analyzed the performance difference of PCB magnetorquer with non-uniform asymmetrical trace width configuration, as shown in Fig. 2.14 [64]. The results indicate that it takes more current for a non-uniform trace width configuration to generate the same torque compared with the uniform trace width configuration. No significant variation can be observed with a non-uniform trace width configuration compared to the one with uniform trace width in terms of temperature, power, dipole moment, and torque with a constant voltage power supply.

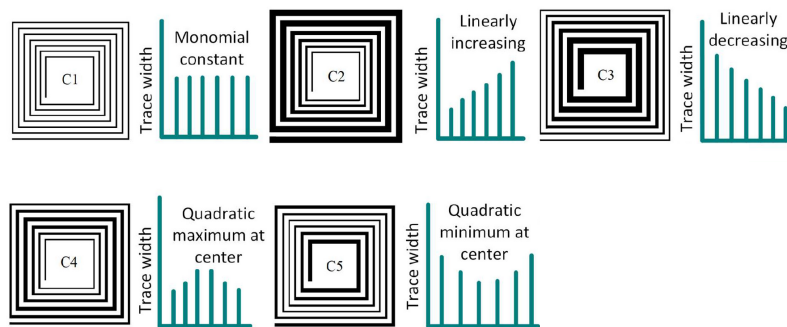


FIGURE 2.14. PCB magnetorquer with different and non-uniform trace width [64]

Another new type of foldable PCBs developed by Haoran, G., and Shengping, G. consists of three palm-sized PCBs connected by two strips of flexible boards and a folding mechanism, as

shown in Fig. 2.15. The PCB magnetorquer is embedded into the three PCBs and is claimed to be able to generate 0.0024 Am^2 dipole moment with around 0.8 W power [46].

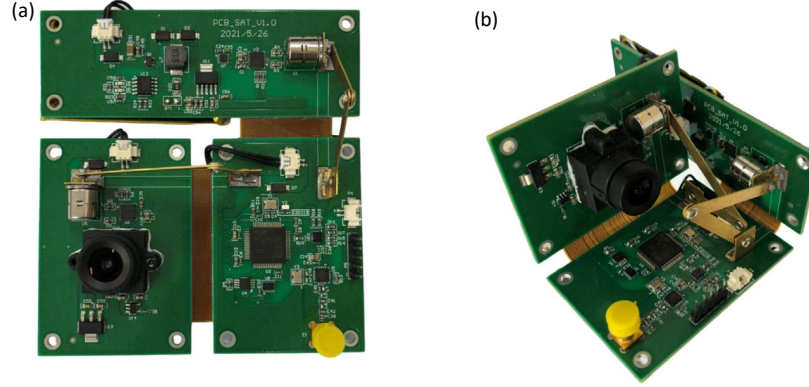


FIGURE 2.15. PCBSat in (a) flat unfold state and (b) orthogonal fold state [46].

The performance and characteristics of different PCB magnetorquers are summarized in Table. 2.5 below.

TABLE 2.5. Summary of the performance of PCB magnetorquers

Manufacture	Dipole moment [A m ²]	Voltage [V]	Power [mW]	Dimension [m ²]	Mass [g]	Efficiency [A m ²]/[mW]	Reference
GomSpace	0.043	3.3	3.3	1.55	57 ^a	-	[1]
Delfi-PQ	0.004	1.632	185.8	0.06	24	0.000033	[31]
PNSS	0.4281	3.3	1026	0.3441	-	-	[10]
Shoaib, A.K <i>et al</i>	0.31	0.21	37	-	-	438.3 ^b	[7]
Haoran, G <i>et al</i>	0.0025	-	800	-	0.47	-	[46]

^a include the solar cells electronic components.

^b torque to power ratio τ/P .

2.1.4 Low power magnetic torquer

All the previous types of magnetorquer use either air core, which has negligible residual induction, or soft ferromagnetic material, which has small residual induction, to avoid the continuous magnetic torque after turning off the magnetorquer. Hard magnetic material is well

known for its high residual induction and high coercive force, making it a good candidate for a permanent magnet. Using hard magnetic material for magnetorquer with the conventional control method will consume much energy to magnetize and demagnetize. As described in the previous section, it will cause enormous hysteresis losses if working in AC mode.

However, the disadvantages of using hard magnetic material for magnetorquers can become advantages with a proper control method. Once the hard magnetic material has been magnetized, it becomes a permanent magnet, which can continuously interact with the Earth's magnetic field to generate torque without consuming energy. The first concept of using hard magnetic material as the core of a magnetorquer for satellite attitude control was proposed by Robert, E.F back in 1966 [39]. The most frequently used attitude control method in the 1960s was to spin the satellites about their axis of maximum moment of inertia. Robert proposed and designed a magnetorquer based on the so-called "chargeable magnet" to maintain and control the rotational speed of the satellites. The control system consists of a capacitor to store energy, a relay to change the direction of pulse current, and a solenoid with a "chargeable magnet" as the core, as shown in Fig. 2.16.

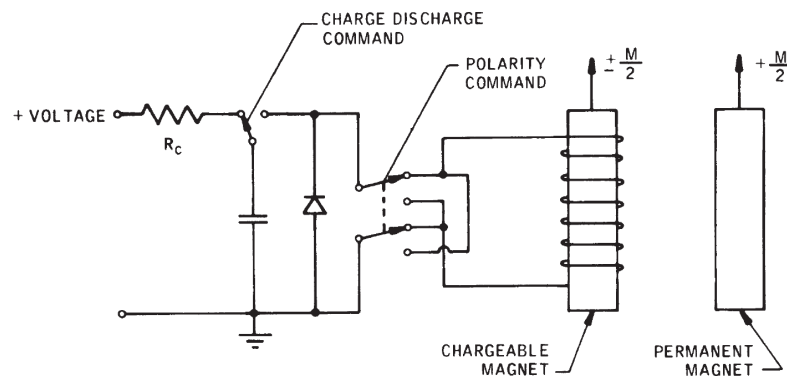


FIGURE 2.16. Control circuit of the magnetorquer with "chargeable magnet" as core [39]

Michael, E.P, and Charles, A.G developed a mathematical model and design formulas for this type of magnetorquer, named low-power magnetic torquer (LPMT), back in 1971, and a performance simulation was conducted based on assumed parameters. Base on their calculation, by using two capacitors of 1 mF charged to 200 V, it requires 40J to change

the magnetic dipole moment of a 36.5 mm diameter 1.82 m cylinder from -2000 Am^2 to $+2000 \text{ Am}^2$, while it requires about 4 W for a typical magnetorquer with soft magnetic material core to generate same level of dipole moment [104]. The performance data were obtained by simulation, and a cylindrical magnetorquer with 36.5 cm in diameter and 1.82 m in length made with Remendur 38 is used for simulation. The discharge capacitor had a capacitance of 1 mF and was designed to be charged to 200 V before discharge. From the simulation results, the dipole moment of this magnetic rod reaches its maxima after about 20 ms and the time interval between the switch of polarity is about 20 ms. Although the magnetorquer rod used in the simulation is too big for a small satellite, and no experimental data was provided, this paper provides a good validation of this type of magnetorquer on a theoretical level. However, since the magnetorquer was designed for satellites using spin stabilization and pointing, the demagnetization method of the magnetorquer was not mentioned in either paper. In addition, the mechanical relay was selected as a discharge actuator, which includes moving parts. Since the mechanical relay relies on the solenoid, this will introduce other magnetic elements on the satellites, which shall be avoided. Therefore improvements and modifications are required to adopt the magnetorquer system for small satellites.

After the proposal and mathematical verification and simulation of the LPMT, a satellite attitude stabilization system was proposed by Polites, M. 33 years later, utilizing the LPMT [103]. Polites quantized the dipole moment generated by the LPMT in 5 steps: $+2M, +M, 0M, -M, -2M$, where M is the dipole moment element generated by a single LPMT bar, and developed a controller to detumble a satellite from various initial angular velocity. The simulated results show that an average setting time of 5.8 and 7.4 orbits can be achieved with two different control methods with a maximum power consumption of 274 and 246 mW, and average power consumption of 57 and 55 mW, respectively. The simulation was performed based on a circular orbit at 600 km altitude with a period of 5793 s, and the dipole moment generated by two magnetorquers with different diameter were claimed to be obtained experimentally that are $\pm 13 \text{ Am}^2$ and $\pm 13 \text{ Am}^2$, respectively [103]. However, the cited paper cannot be found in the proposed journal, and thus the detailed experiment setup is unclear. Furthermore, the details of quantization of the dipole moment are unclear

due to the disappeared citation. Therefore the credibility of the performance data of the proposed magnetorquer is to be questioned. Then a PWM-based controller for LPMT was proposed by Polites, M. for more precise spacecraft attitude stabilization [102], where the same magnetorquer performance was cited.

Mentch, D.B developed another attitude control system based on LPMT and a magnetometer for CubeSat in 2011 [91]. As described in the previous paragraph, Mentch utilized the exact "dipole moment quantization" method as Polites proposed. The quantization was achieved by placing a pair of bar magnets with the same property in parallel, as shown in Fig. 2.17. Suppose the two magnets are magnetized in the same direction. In that case, the macroscopic dipole moment will equal the sum of the two moments. The magnetization in a different direction will cancel each other, resulting in zero macroscopic dipole moment.

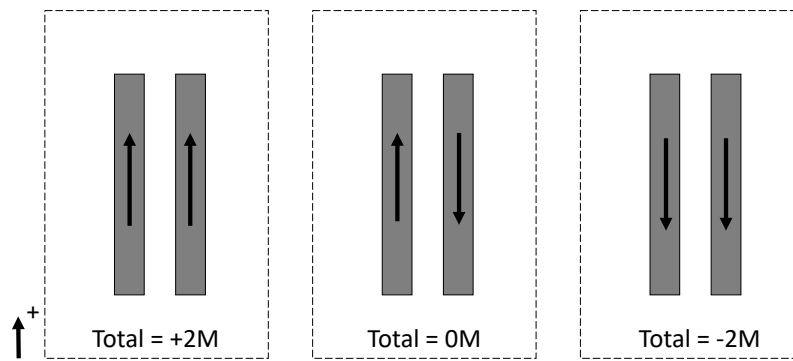


FIGURE 2.17. Theory of quantizing the dipole moment.

The magnetorquer bar element designed in [91] is a cylinder-shaped bar made with ALNICO1 with 1/16 inch (1.59 mm) diameter and 1 inch (25.4 mm) length, and a dipole moment of 0.023 Am^2 was measured using the Helmholtz cage. The attitude stabilization was simulated, and a $\pm 2^\circ$ pointing accuracy can be achieved. The complete ADCS board was constructed using the same magnetorquer system but with an extra pair of magnets for the Alaska Research CubeSat by Frey, J. in 2014 [40]. The extra pair of magnets adds another two steps to the dipole moment quantization, enabling the system to achieve $\pm 4M$, $\pm 2M$, and $0M$ dipole moment output. The compensation to the magnetometer due to the presence of a permanent magnet was explained in detail [40, 41]. However, no experimental attitude control or detumble data were provided.

In conclusion, the air core, iron core, and PCB embedded magnetorquers are well studied. The system model, control algorithm, optimization, and mission design analysis have been accurately modeled and deeply researched. However, not much work focuses on the magnetorquer using hard magnetic material as core (i.e., the magnetization efficiency and demagnetization method have not been studied), and the proposed control and stabilization data have not been verified experimentally. The complete ADCS system based on the hard magnetic material core-based magnetorquer has already been made. However, the zero induction state achieved by pair-magnet design highly relies on the symmetry of the two magnets, which is hard to measure and control. Adding more magnets makes it more challenging to achieve a macroscopic zero induction state, and the system weight increases. In addition, the maximum dipole moment available for ARC for each axis is four times the dipole moment generated by a single torquer ($4 \times 0.023 \text{ Am}^2 = 0.092 \text{ Am}^2$), which is slightly higher than the PCB embedded magnetorquer. The extra component, weight, and size make it not the prior choice when designing the magnetorquer for a small satellite.

Therefore, with all of the unsolved problems and defects, a new type of hard magnetic material-based magnetorquer, named Electro-permanent magnetorquer (EPM), is proposed, designed, and analyzed as part of the smart attitude control system in this thesis.

2.2 Micro air-fed magnetoplasma dynamic thruster

Small satellites, well known for their small size, short development period and low cost, have demonstrated their utility for scientific research and astronomy related missions [92]. Besides their contribution to the research area, small satellites are now being developed to democratized space and extend its application for everyone on earth, including internet of things (IoT), low latency internet access and constellation for geodetic applications [75]. Moreover, it brought huge benefit to astronomy as it allows astronomical instruments that exceed the size of the earth to be built through constellation, which is impossible through ground-based systems [79]. As all these tasks require constellation, the attitude and orbit control system is vitally important for small satellites. However, shrinking the size of the

satellites is not an easy job as it is tremendously more difficult to miniaturize the propulsion system than the micro controller [78]. This difficulty makes the low-power electric propulsion systems eagerly needed for ultra-small satellites, for instance 1U CubeSats, to perform orbit keeping and de-orbiting maneuver as their power, size and weight limit is even more strict than small satellites.

There is no doubt that miniaturization of the propulsion systems will lead and drive the future of spacecraft development [80]. Several miniaturized propulsion systems have been developed over several decades, including cold gas thruster [90, 99, 57, 65, 52], solid-state pulsed plasma thruster (PPT) [45, 20, 71, 106, 25, 109, 122, 77], electrospray thruster [77, 140, 95, 123], and miniaturized hall thruster [90, 131, 135, 50]. Several electric propulsion systems have been developed and currently used in satellite missions. The most common ones include the resistojet [90, 77], ion thruster [114, 72], and hall thruster [47].

The power requirements for thrusters vary from hundreds of watts to several kilowatts, which normally also requires kilograms of propellant and is impractical for small satellites [99]. To satisfy the power, size, and propellant requirements, some electric propulsion systems have been proposed and developed specifically for small satellites. Table 2.6 summarizes these propulsion methods.

PPTs operate at pulse mode with peak current reaching up to 30 kA in $\sim 5\text{-}10\ \mu\text{s}$ [25], resulting in several hundreds of kilowatts peak power during the pulse, whereas the average total power keeps minimum. Normal PPTs using solid propellant can produce 280-2800s specific impulse while some of those using liquid propellant generate up to 11860s specific impulse depends on the pulse energy, mass bit and propellant [110]. These PPTs require spark plug that delivers a voltage of several kilo-volts to initialize the plasma discharge [109], which complicates the entire structure and increases its size. Vacuum arc thruster (VAT), as one type of PPTs, use a cathode metal as the propellant, which requires a conductive layer on the insulation material to initialize the plasma discharge [101] and constrains the lifetime of the thruster.

The magnetoplasmadynamic thruster (MPDT) is another type of electrical propulsion system, which ionizes the propellant and accelerates them to generate thrust. However, unlike normal

TABLE 2.6. Characteristics of electric propulsion systems for small satellites

Method	Propellant	I_{sp} (s)	I_{bit} (μ Ns)	Thrust	Power	Ref.
Cold Gas	N_2 , ammonia, R-134a, R-236fa, SO_2 , Teflon, metal	~ 50	-	0.1–100 N	~ 50 W	[90, 99, 57, 65, 52]
Solid-state PPT		~ 300 –3200	10–800	~ 1.5 mN	0.5–50 W	[45, 20, 71, 106, 25, 109, 122, 77]
Resistojet	N_2 , hydrazine, Xe	100–300	-	5.4 mN – 0.5 N	0.1–1 kW	[90, 77]
Hall Thruster	Iodine, Xe, Bismuth, Krypton	1200–8000	-	10^{-2} – 2.5 N	0.2–100 kW	[47, 113, 130, 129, 90, 131, 135, 50]
Helicon Thruster	Xe, Ar, Nitrogen	280–4000	-	1–40 mN	0.2–3 kW	[105, 73, 26, 17, 119]
Electrospray Thruster	Indium, Cesium	EMI-DCA, 360 – 12000	-	0.001–1.4 mN	0.5–93 W	[77, 140, 95, 123]

ion and hall thrusters that use electric field to accelerate ions, MPDT ejects plasma beams using the magnetic field induced by its own plasma current [28]. Therefore MPDT requires high electric current to generate sufficient magnetic field strength to increase the performance. Fig. 2.18 shows the structure and working principle for general MPDTs.

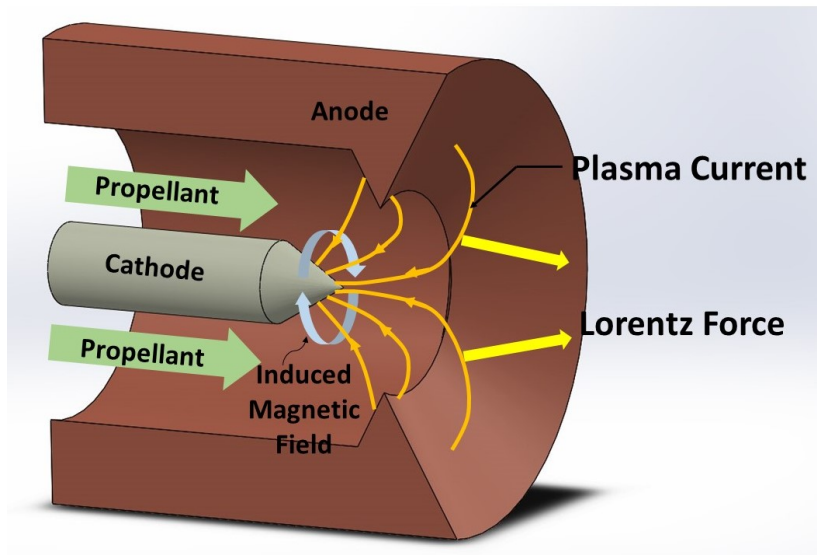


FIGURE 2.18. Cross-sectional view of the general MPD thruster.

Typical full size MPDT uses Argon, Hydrogen, Xenon and liquid Lithium as propellant and can generate 0.5–50 N thrust force with specific impulse ranging from 1000–10000s while most of them require power input ranging from as low as 30 kilowatts to up to 20 megawatts [90, 125, 28, 89]. Although the MPDT, especially those using gaseous propellant, is well-known for its high specific impulse, high efficiency, and high thrust, the power requirements, especially the discharge current, for this type of thruster to operate optimally limits its miniaturization and implementation for small satellites.

In this thesis we developed a miniaturized MPDT for small satellites, which is based on the structure and working mechanism of the full scale MPDT but operates in the pulse mode. The new MPDT can generate high thrust force and specific impulse taking advantage of the traditional MPDT while keep the thruster design as simple as the VAT. In addition, the new MPDT uses air as fuel and becomes a micro air-fed thruster (μ AF-MPDT), which can be used to offset the atmospheric drag force for small spacecraft that operates at very Low Earth Orbit (VLEO, about 200km altitude) with an air-collection device on-board [82]. With this

feature, the thruster has the potential to be used by small satellites to use atmospheric gases for orbit keeping and de-orbiting while operate in the VLEO, which adds more flexibility to those satellites that have very low orbit altitude and enormously extends their lifetime and durability.

The remainder of this thesis is organized as follows. Section 2 describes the details of the thruster design. The details of calibration of the thruster stand is also introduced; Section 3 presents the testing results; Section 4 discusses the performance of the μ AF-MPDT. The possibility of using the proposed thruster as a way to maintain the small spacecraft at VLEO is also discussed briefly; Section 5 concludes.

CHAPTER 3

Electro-Permanent Magnetorquer

In this chapter, the magnetic basics and details of the EPM, including the detailed board design considerations and test results, and magnetorquer performance measurement methodology and equipment, will be introduced, described, and analyzed in great detail. The performance comparison with state-of-the-art magnetorquers will be presented at the end of this chapter, along with a simple controller design and experimental results to validate the EPM.

3.1 Introduction

The magnetorquer has long been used for satellites to stabilize and adjust their attitude in space. Conventional magnetorquers consist of loops of copper wires and different materials as core, as described in the previous chapters. However, the weak dipole moment and continuous power consumption make it not ideal and efficient for small satellites, especially CubeSats, whose power, size, and weight are strictly restricted. A new type of magnetorquer utilized the changeable permanent magnet, a type of hard magnetic material as the core for satellites' attitude control [91, 40]. However, they are too heavy to fit into the CubeSats and can only generate a dipole moment at similar orders of magnitude to the PCB magnetorquer. In addition, all the previous work [91, 40, 102, 103] has either zero or sub-optimized solutions for demagnetizing the magnet, which is a big problem for small satellites, as the residual induction of the magnets will generate a continuous torque to the satellites at the presence of the Earth's magnetic field and will gradually affect the attitude of the satellites. Here a new type of magnetorquer, named Electro-Permanent Magnetorquer (EPM), is proposed for small

satellites, especially CubeSats, aiming to provide a new type of actuator that can achieve high power efficiency and high torque performance at the same time.

3.1.1 Magnetic basics

The basics of magnetism will be introduced and explained in this section to understand the parameters of magnetorquer better.

3.1.1.1 Magnetic field strength and magnetic flux density

It is well known that a wire that carries an electric current will induce a magnetic field around it. However, when describing the physical property of the magnetic field, the two parameters, magnetic field strength, and magnetic flux density, always confuse people who are not very familiar with magnetism. To better describe these two properties, consider a solenoid with air or vacuum as the core, as shown in Fig. 3.1.

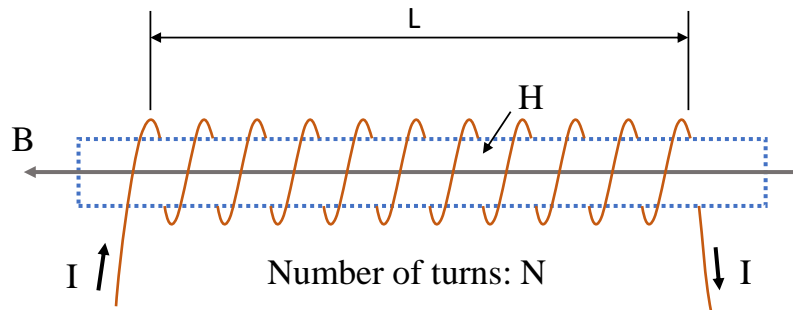


FIGURE 3.1. Ideal solenoid.

If a current I flows into the solenoid, a magnetic field will be generated inside the solenoid in the direction following the right-hand rule. If the solenoid has a total length of L with a total number of turns of wire N , the magnetic flux density generated by the solenoid can be described as [63]

$$B = \mu_0 \frac{N}{L} I \quad (3.1)$$

or

$$B = \mu_o n I$$

If we define n as the number of solenoid turns per unit length. The μ_o is the permeability of vacuum and has a value of 1.256637×10^{-6} and a unit of H/m . The magnetic flux density B has a unit of Tesla (T) in the SI unit system. The magnetic field strength, H , has a relationship with the magnetic flux density B as follows in vacuum [42]:

$$H = \frac{B}{\mu_o} \quad (3.2)$$

Comparing these two equations, it can be found that by substituting eq. (3.1) into eq. (3.2), the magnetic field intensity can also be written as:

$$H = n I \quad (3.3)$$

which has a unit of A/m . The magnetic flux density, by its name, can be imagined as the number of magnetic field lines passing through a unit area. The magnetic field strength, from its equation, is only related to the solenoid winding density and the current. Therefore this parameter can be imagined as the intensity of the magnetic field as at the constant current, the higher the winding density induces a higher field strength. In a vacuum, the magnetic field strength is directly proportional to the magnetic flux density. However, for different materials or media, the permeability does not equal μ_o . Therefore the quantity of the magnetic field line passing through the unit space inside the material may be less or more than it is in the vacuum under the same external magnetic field excitation.

3.1.1.2 Magnetization

Magnetization is a property of material, normally used to describe how strong the material is being magnetized or the density of magnetic dipole moment per unit volume of the material.

The vacuum cannot be magnetized. However, when there is material, for example, some iron bar inside the solenoid shown in Fig. 3.1, the eq. (3.1) have to be written as [42]:

$$B = \mu_o(H + M) \quad (3.4)$$

If the magnetization of a material M is parallel to an external magnetic field H , the following equation stands [42]:

$$M = \chi H \quad (3.5)$$

where χ is the magnetic susceptibility of the material. Then by substituting the equation eq. (3.5) into eq. (3.4), it becomes:

$$\begin{aligned} B &= \mu_o(1 + \chi)H \\ &= \mu_o\mu_r H \end{aligned} \quad (3.6)$$

Here $\mu_r = 1 + \chi$ is the relative permeability, which describes how the material is magnetized relative to vacuum. In vacuum $\mu_r = 1$ as defined. In some strong ferromagnetic material, μ_r can be as big as around 200,000 [2]. It is interesting to note that in the superconductor, the $\mu_r = 0$.

3.1.1.3 Dipole moment

Dipole moment is the most important performance parameter for magnetorquers as it connects directly to the torque it can generate. Consider the solenoid shown in Fig. 1.1, considering the 2D scenario, the torque generated can be calculated by [62]:

$$\tau = mB \sin \theta \quad (3.7)$$

where m is the dipole moment described as:

$$m = NIA \quad (3.8)$$

where N is the number of windings of the solenoid, and A is the cross-sectional area of the solenoid. The unit of dipole moment in the SI unit system is Am^2 , which is intuitive as it can be interpreted as a loop of wire carrying current times the loop area. Dipole moment also has another unit, Nm/T , which makes it easier to understand as a magnetorquer as it directly provides the maximum torque that can generate under the perpendicularly applied magnetic field. The dipole moment for the electromagnet is easier to understand and calculate.

For a permanent magnet, the dipole moment is represented as the production of magnetization and volume:

$$m = M \cdot V \quad (3.9)$$

From this equation, the magnetization of the permanent magnet can also be interpreted as the amount of dipole moment per unit volume of the magnet. However, a magnet's magnetization is usually not uniform and hard to obtain. Therefore the dipole moment is generally obtained through measurement using other non-direct methods, which will be introduced later. The dipole moment is the primary parameter of interest in this thesis.

3.1.1.4 Hysteresis loop

Before introducing the hysteresis loop, the susceptibility mentioned in section 3.1.1.2 shall be discussed further. Based on the range of the χ , materials can be roughly classified as three types: (1) diamagnetism ($\chi = \text{const.} < 0$), (2) paramagnetism ($\chi > 0$), and (3) collective magnetism ($\chi = \chi(T, H, \text{"history"})$) [42]. Ferromagnetism, which is of interest to be used in magnetorquers, is classified as one of collective magnetism. This material's susceptibility depends on the temperature, external magnetic field excitation, and historical susceptibility. One interesting thing to note is that for ferromagnetic material, there is a specific temperature

named Curie temperature (T_c), or Curie point, above which the ferromagnetic material loses its ferromagnetic properties and becomes a paramagnetic material. To further understand the property of the ferromagnetic material, a type of figure that describes the relationship between the external applied magnetic field and the magnetic field induced by the material itself is introduced, as shown in Fig.3.2, named hysteresis loop, or sometimes BH curve.

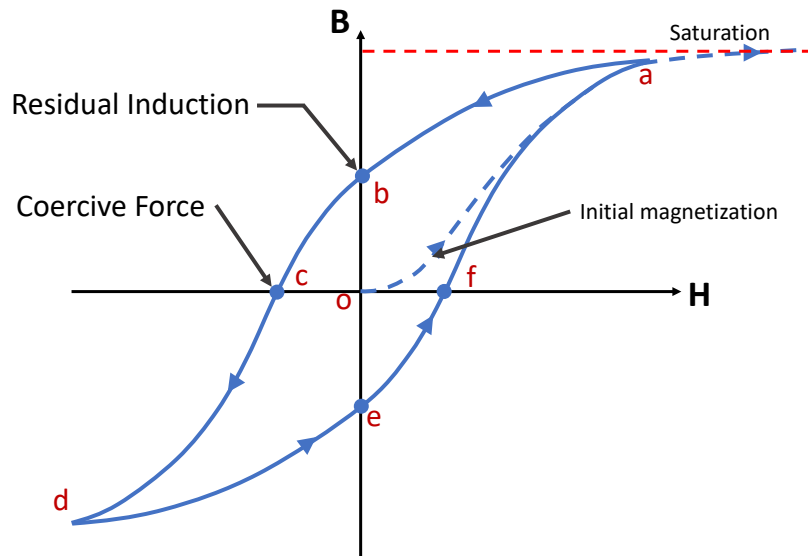


FIGURE 3.2. Hysteresis loop (BH Curve).

The horizontal axis named H in Fig. 3.2, is the externally applied magnetic field, and the vertical axis B represents the induced magnetic flux density of the material. Starting from point o , where the material is fully demagnetized. When applying a positive excitation magnetic field, the induced flux density will follow the "initial magnetization" curve until point "a," which is the saturation point. At this point, the magnetic flux density induced by material reaches the maximum, and further increasing the external magnetic field will result in leakage of the flux density. After reaching point "a," slowly reduce the applied field until zero. The induced magnetic field will drop to point "b" following the curve "ab" instead of going back to point "o." At this point, the material becomes a "permanent magnet" as no external magnetic field is applied to the material, and the magnetization remains. The magnetic flux density generated by the material at this point is named "residual induction," or sometimes "remanence," denoted by B_r , which is usually used to describe the strength of a permanent magnet. Now increasing the external field in the negative direction until point "c,"

the induced field decreases and reaches zero at point "c." This point represents the amount of external magnetic field strength required to reduce the macroscopic magnetization of material to zero. At this point, the material shows zero magnetic flux density and can be treated as demagnetized. The external magnetic field strength at this point is called "coercive force" or "coercivity" for a specific material, denoted by " H_c ." It is used to describe the ability of a magnet to withstand a demagnetizing magnetic field. Further increasing the external field in the negative direction will start to magnetize the material in the negative direction until saturation follows the "cd" curve. Increasing the field in the positive direction is symmetrical to the reducing field process, and the induced flux density will increase following the "defa" curve, where point "e" and "f" indicates the residual induction and coercive force in the negative direction.

The "history" dependency of the susceptibility is another important property of the ferromagnetic material. Even when the magnetic demonstrates a macroscopic zero magnetization, the future behavior of the material in reaction to the external field is not constant. Consider the hysteresis loop shown in Fig. 3.2, the magnetization is zero for both point "c" and point "f". However, the material will show a different magnetic flux density if the external field is removed. As shown in Fig. 3.3, the flux density of the material after removal of the external field will reach point "c'" from "c" and "f'" from "f," respectively. If the external field is further increased, the behavior of the magnet will follow the historical magnetization and end up at a new point (i.e., point "a'" for the "cc'" curve). The small hysteresis loop inside the major hysteresis loop is named the "minor hysteresis loop" and is an important property to consider when designing magnetorquer.

3.1.1.5 Soft magnetic material and hard magnetic material

Based on the coercive force, ferromagnetic material can be categorized into two groups: hard magnetic material and soft magnetic material, where hard and soft describe how easy the material can be demagnetized. As shown in Fig. 3.4, soft magnetic material is easier to demagnetize and thus has lower coercive force, resulting in a "thinner" hysteresis loop. On the

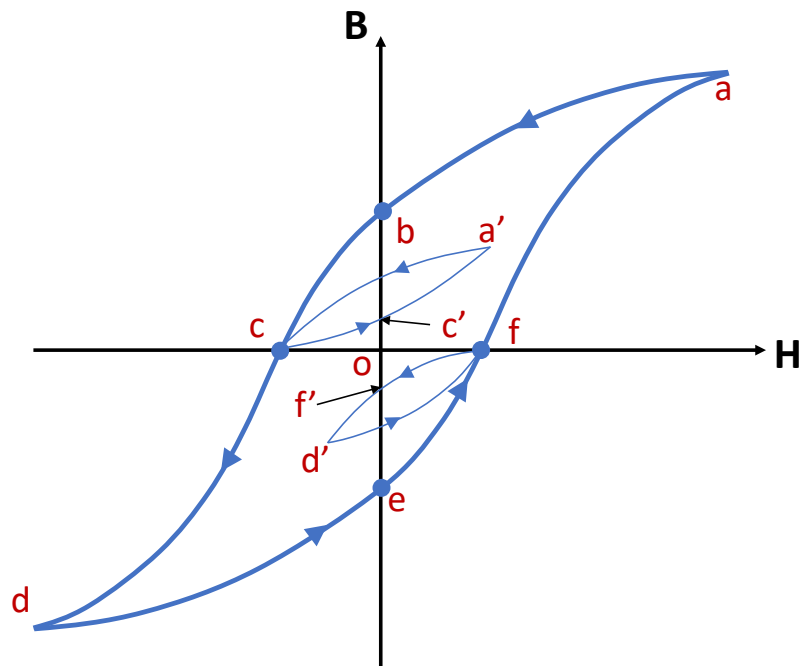


FIGURE 3.3. Minor hysteresis loop.

contrary, the hard magnetic material has a higher coercive force and is hard to demagnetized, therefore having a "fatter" hysteresis loop.

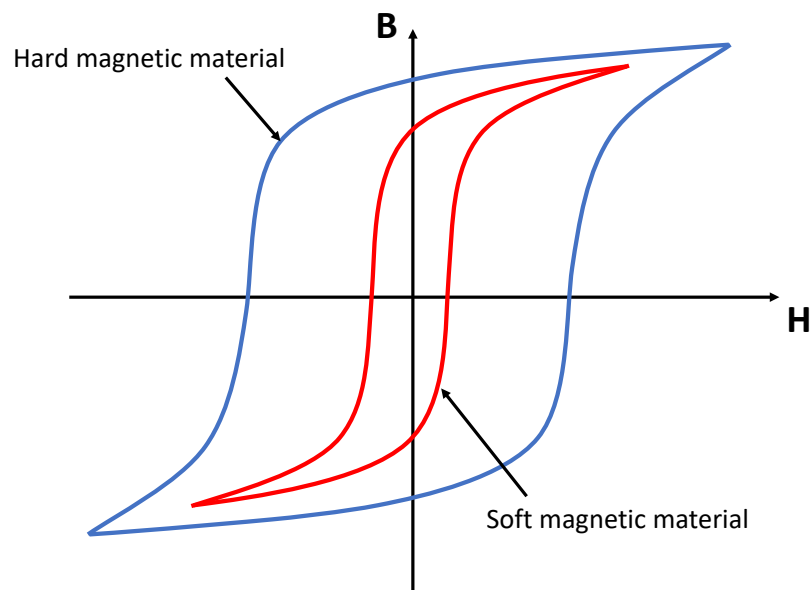


FIGURE 3.4. Hysteresis loop for the hard and soft magnetic material.

The soft magnetic material is usually used when the magnetic polarity is reversed frequently (i.e., transformers, inductors). The low coercive force makes it easier to demagnetize, thus reducing the energy loss during the polarity switching. Due to the higher coercive force, the hard magnetic material is generally used in environments where the material shall keep the magnetization under specific external magnetic field strength (i.e., DC motor, speaker). Therefore, most permanent magnets are made with hard magnetic material.

3.2 EPM design and functional test

This section will introduce and discuss the details of EPM design and test, including material selection, driving circuit design, torque rod design, and functionality test results.

3.2.1 Material selection

As the core of the EPM, the material shall be determined at the first design stage. Most magnetorquers use soft magnetic material as the core due to the low residual induction and low hysteresis loss when operating using PWM or other AC methods. However, hard magnetic material shall be used for EPM, as the core shall maintain magnetization after removing the external magnetic field. The material selection should aim for high residual induction B_r as this parameter directly connect to the dipole moment, which in turn connects to the maximum torque it can generate. The coercive force, H_c , however, shall be small to make the core easier to be demagnetized and switch the polarity. Fig. 3.5 shows the property distribution for some common permanent magnet materials.

The residual induction B_r and coercive force H_c are generally the most important properties for ferromagnetic materials and can be found in various magnetic material manufacturers. Commonly to accurately describe the relationship between B_r and H_c , and for a more intuitive demonstration and comparison, the material's second quadrant of the hysteresis loop is used to demonstrate the relationship between magnetization and applied field strength, named "demagnetization curve." The demagnetization curve can demonstrate most of the properties of the magnet, and one can easily compare and determine the material that meets

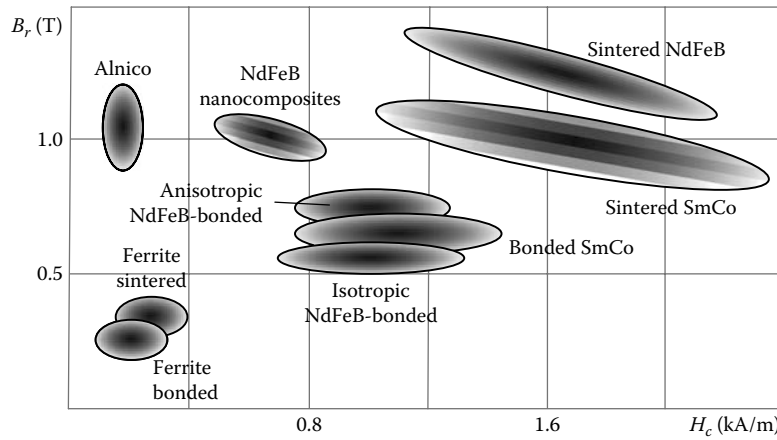


FIGURE 3.5. Property distribution for common magnetic materials.[132]

their requirements. The demagnetization curve for some of the common permanent magnet materials is shown in Fig. 3.6

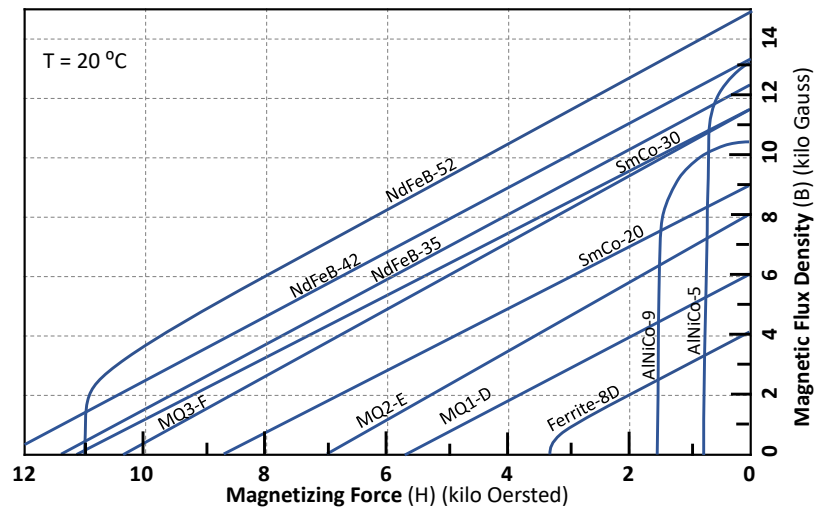


FIGURE 3.6. Demagnetization curve for common permanent magnetic material [3, 4]

The intersection with the vertical axis is the maximum residual induction, and that with the horizontal axis is the required external magnetic field to demagnetize the material. The maximum production of the magnetic flux density and the external magnetic intensity, reflected as the most significant area of the rectangle created by the data point on the curve, is defined as Maximum Energy Product, denoted as BH_{max} . This parameter defines the magnet's strength and is usually used to denote the grade of the magnet (i.e., grade N52 for NdFeB

magnet). It can be seen from the figure that the traditional magnetic (i.e., ferrite magnet, also called ceramic magnet) has relatively low residual induction and low coercive force, therefore making it a weak magnet. The strongest commonly available magnet on the market is the NdFeB grade N52 magnet, which has the highest residual induction (15 kGauss) and relatively high coercive force.

For the magnet used in the EPM, the material shall have as high as possible the residual induction to produce higher torque after being magnetized. At the same time, the coercive force shall be as low as possible to make the wiping or charging easier. Since the external magnetic intensity highly depends on the energy input to the magnetization coil, a magnet with high coercive force requires high energy to change the magnetization, which may be too stressful for small satellites. The high-intensity magnetic field might also cause interference to other satellite systems, which should be avoided.

The best choice is obvious from Fig. 3.6. AlNiCo 5 magnet has a high residual induction, which is even higher than the NdFeB grade N35 magnet, at around the same level as the grade N42 magnet, while the coercive force is around one-twelfth of the N42 magnet. However, some material has even higher residual induction and lower coercive force than AlNiCo 5 magnet. As shown in Fig. 3.7, the permanent magnet "Remendur 38", which is used for calculation in [104], has more than 16 kGauss residual induction, which is higher than that for the NdFeB N52 magnet ($\sim 14.8\text{ kGauss}$), and remarkably low coercive force ($\sim 48\text{ Oe}$). Note that the unit for the horizontal axis changed from "kilo Oersted" to "Oersted," and the demagnetization curve for AlNiCo 5 magnet is plotted in the same figure for comparison. Another permanent magnet, named "P6-Alloy", is mentioned in [54] and has similar residual induction with the coercive force around one-eleventh of that for the AlNiCo 5 magnet.

Although the "Remendur 38" and "P6-Alloy" seem more suitable for the EPM, they are hard to source on the market. There is minimal data that can be found online about these two materials, and there is not any retailer that can be found to supply these materials. However, on the contrary, the AlNiCo 5 magnets are easy to obtain and are available in various shapes and sizes. In addition, the AlNiCo 5 is extremely stable at high temperatures. The typical Curie temperature for AlNiCo 5 material is approximately 840°C , and for comparison, the

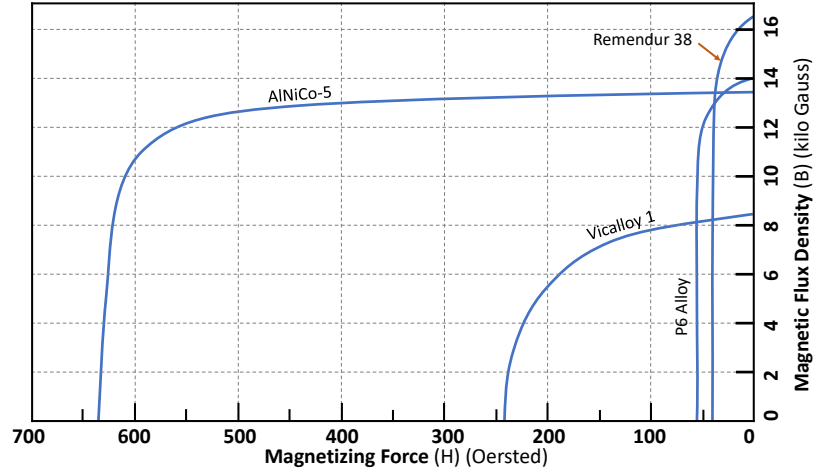


FIGURE 3.7. Demagnetization curve comparison between AlNiCo 5 and other alloys [54]

NdFeB magnets has typical Curie temperature of $310 - 365^{\circ}\text{C}$ [51]. This property makes AlNiCo 5 an ideal material for space applications due to extreme thermal environments in orbits.

In addition, AlNiCo material has been used for passive magnetic attitude control and has flight heritage. The Delft-C³ satellite designed by the Delft University of Technology utilized the AlNiCo 5 as the permanent magnet for passive attitude control [107]. The QuakeSat developed by Stanford University and QuakeFinder LLC utilized AlNiCo 8 HE magnets as passive stabilization actuator [84]. Donald, B.M. and Jesse, F. used AlNiCo 1 and AlNiCo 5 material as core when designing the LPMT for the ARC mission [91, 40]. All these heritages prove the feasibility and durability of using AlNiCo for space purposes.

In conclusion, the AlNiCo 5 bar magnet is selected as the core to be used for the EPM with the performance and demagnetization curve shown in Fig. 3.8. The magnet has a residual induction $B_r = 1.2037\text{ T}$ and the coercive force $H_c = 48\text{ kA/m}$. Note that the grade number LNG40 is equivalent to AlNiCo 5.

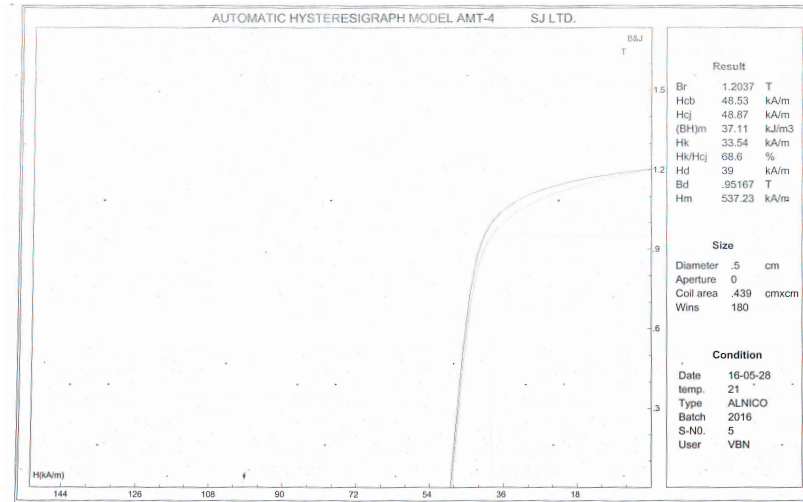


FIGURE 3.8. Demagnetization curve of the LNG40 used in this thesis [5]

3.2.2 Driving circuit

After determining the material, the driving circuit shall be designed and discussed before the torque rod as the configurations of the torque rod, including the dimension, size, and copper coil winding, highly depend on the driving method. There are several design objectives and requirements for the driving circuit. Firstly the driving circuit shall be able to change the magnetization and polarity of the torque rod as this is the basic functionality of the magnetorquer. Secondly, the circuit shall be able to demagnetize the torque rod when the magnetorquer is commanded to be turned off. It is the most challenging part due to the high non-linearity of the ferromagnetic hysteresis loop. The complete demagnetization shall follow the specific rule, which will be introduced and discussed later. Thirdly the magnetization, demagnetization, and switching polarity process shall be as fast as possible. The reason is that for small satellites operating in LEO, the orbital time is around 90 mins. Since the torque generated by the magnetorquers is generally low, if the control frequency is too low, it may not be able to stabilize or control the attitude of the satellites. Lastly, the power consumption shall be minimized to ensure its suitability for implementation on small and nanosatellites, especially CubeSats.

To meet all these design objectives, the detailed operation logic, components selection and considerations, and the feedback control method will be introduced and discussed in detail in this section.

3.2.2.1 Operation logic

Among all the designs mentioned in earlier objectives, the first aspect to consider is the operation logic. The basic operation logic is briefly mentioned in [39, 104, 91, 40, 103, 102]. A capacitor array shall be charged to a certain voltage level to store energy, and then discharge the energy into a solenoid in the form of a current pulse. The magnetization inside the solenoid can then be changed due to the induced high-intensity magnetic field. Fig. 3.9 shows the block diagram of the control circuit for the EPM.

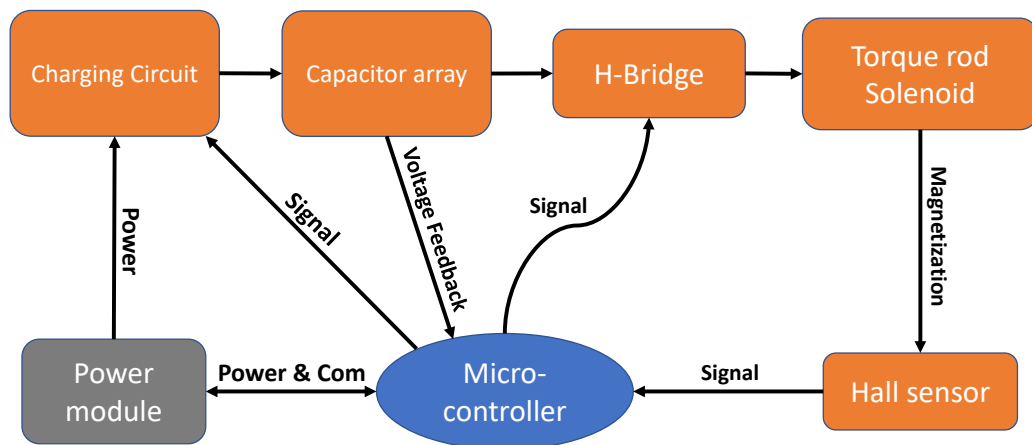


FIGURE 3.9. Block diagram of the control circuit used for the EPM in this thesis.

Since the system works in pulse mode, the operation sequence for each pulse is summarized in the following steps:

- (1) When receiving the command to alter the magnetization of the torque rod, the micro-controller will send the signal to the charging circuit to start charging the capacitor array. The microcontroller monitors the capacitor voltage through a feedback voltage divider;

- (2) Once the voltage reaches the defined threshold, the microcontroller will shut off the charging circuit and send the signal to the H-bridge to open the gates according to the desired dipole direction;
- (3) Then H-bridge opens, and the capacitor array discharges the energy into the torque rod solenoid in the form of the current pulse;
- (4) After each pulse, the magnetization of the solenoid is measured by hall sensors and monitored by the microcontroller;
- (5) Repeat step (1)(2)(3)(4) until the desired magnetization or the discharge times has been achieved.

The details of design considerations and analysis of each module in each step will be introduced and discussed in the following sections.

3.2.2.2 Main capacitor and discharge voltage

The main parameter for the driving circuit is the capacitance of the capacitor array and the operation voltage. According to the hysteresis loop, the higher residual induction of the magnet B_r requires a higher external applied magnetic excitation H_m . Therefore the excitation field H_m shall be as high as possible to achieve higher torque performance. Due to the system's configuration, the excitation field is provided by the torque rod solenoid, whose center magnetic field intensity is related to electric current and wire density, as described by equation (3.3). Therefore the high discharge current is desired to achieve higher magnetization of the magnet for a determined solenoid configuration.

The system model shall be determined first to achieve a high discharge current. The main discharge circuit consists of a capacitor array, H-Bridge, and Torque rod solenoid, which can be modeled as a passive "RLC" circuit, as shown in Fig. 3.10. Once the capacitor voltage reaches the desired level, the capacitor voltage and the inductor current strictly follow the passive "RLC" circuit law after opening the H-Bridge.

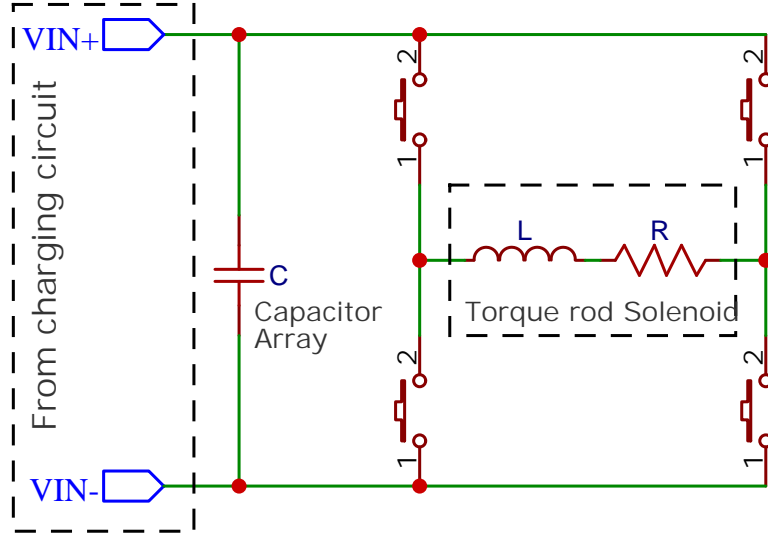


FIGURE 3.10. Simplified discharge circuit consists of the main capacitor array, equivalent series inductance, and equivalent series resistance.

Assuming the discharge circuit has the total equivalent resistance, R , total equivalent inductance, L , and the capacitance for the capacitor array is C , the following parameters can be defined:

$$\alpha = \frac{R}{2L} \quad (3.10)$$

$$\omega_o = \frac{1}{\sqrt{LC}} \quad (3.11)$$

$$\omega_d = \sqrt{\omega_o^2 - \alpha^2} \quad (3.12)$$

According to [87], the discharge current can be categorized into three scenario: (1) $\alpha < \omega_o$: underdamped; (2) $\alpha > \omega_o$: overdamped; (3) $\alpha = \omega_o$: critically damped. Assuming the underdamped scenario, the circuit shall meet the following requirements:

$$\begin{aligned}
\alpha &< \omega_o \\
\Rightarrow \alpha^2 &< \omega_o^2 \\
\Rightarrow \frac{R^2}{4L^2} &< \frac{1}{LC} \\
\Rightarrow R^2 C &< 4L
\end{aligned} \tag{3.13}$$

The inductance for a coil with ferromagnetic material as the core is described by:

$$L = \mu_r \mu_o \frac{N^2 \cdot A}{l} \tag{3.14}$$

where the N is the number of wire turns, A is the core cross-sectional area, l is the length of the coil, and μ_r and μ_o are the relative permeability and the permeability of free space, respectively. Assuming using the American wire gauge (AWG) 28 enameled copper wire is used for the magnetorquer, the relative permeability of AlNiCo 5 $\mu_{AlNiCo5} = 3$ [6], and there is only one layer of copper wire wrapped the full length of the torque rod, the calculated inductance of the torque rod solenoid is shown in Fig. 3.11. To maximize the dipole moment, according to eq. (3.9), the volume of the magnet shall be large. Due to the size and weight constraints of the CubeSats, the torque rod with $r > 0.003\text{m}$ and $l > 0.06\text{m}$ is considered to be used in arbitrary, which results in $L > 7.1 \times 10^{-5}\text{H}$. The details of the torque rod radius and length selection will be introduced later.

Assuming the total equivalent resistance $R = 2\Omega$ including the resistance of solenoid wire windings, PCB copper trace, H-Bridge On-Resistance, solder joint, and capacitor array series resistance, the capacitance of the capacitor array shall meet the requirement of $C < 71 \mu\text{F}$, to make the underdamped assumption valid.

According to [87], for underdamped passive RLC circuit, the current i is expressed as:

$$i = \frac{V_0}{\omega_d L} e^{-\alpha t} \sin \omega_d t \tag{3.15}$$

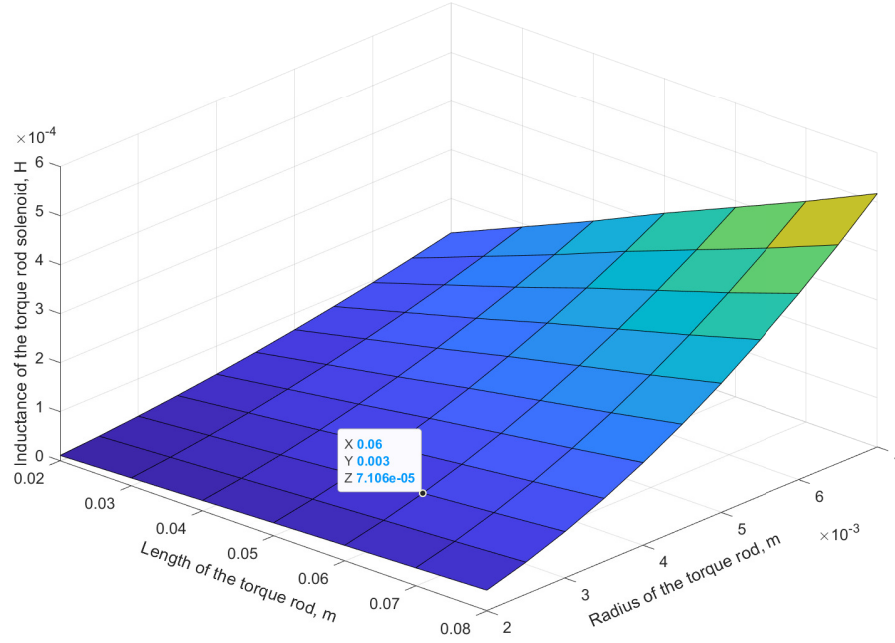


FIGURE 3.11. Inductance estimation for different torque rod length and radius.

where the V_0 is the initial capacitor voltage. Since the residual induction is related to the maximum external field intensity, the maximum current, in this case, will be used to analyze the magnetization performance. The peak current occurs when the derivative of current i equals zero:

$$\begin{aligned}
 \frac{di}{dt} &= 0 \\
 \Rightarrow \frac{V_0}{\omega_d L} \cdot [-\alpha e^{-\alpha t} \sin \omega_d t + e^{-\alpha t} \omega_d \cos \omega_d t] &= 0 \\
 \Rightarrow \tan \omega_d t &= \frac{\omega_d}{\alpha} \\
 \Rightarrow t_{max} &= \frac{1}{\omega_d} \arctan \frac{\omega_d}{\alpha}
 \end{aligned} \tag{3.16}$$

Therefore the peak current i_{max} can be expressed as:

$$\begin{aligned}
 i_{max} &= \frac{V_0}{\omega_d L} e^{-\alpha \frac{1}{\omega_d} \arctan \frac{\omega_d}{\alpha}} \sin \left(\arctan \frac{\omega_d}{\alpha} \right) \\
 &= V_0 \cdot \Psi(R, L, C)
 \end{aligned} \tag{3.17}$$

From equation (3.17), the maximum current is linearly proportional to the initial capacitor voltage at a rate of Ψ , where the coefficient Ψ is a function of R , L , and C . Firstly, the relationship between Ψ and capacitance C is analyzed. Assuming the unity voltage, $L = 7.1 \times 10^{-5} \text{H}$, and $R = 2 \Omega$ according to the previous assumption, the relationship between the maximum current and capacitance is shown in Fig. 3.12.

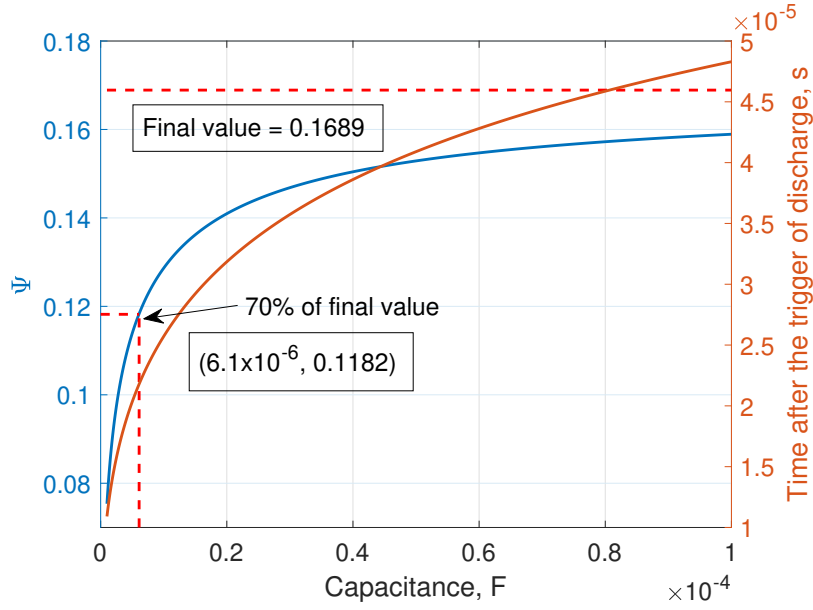


FIGURE 3.12. Coefficient Ψ and the time when maximum current occurs T_{max} as a function of capacitance with fixed inductance L and resistance R .

The Ψ will approach its final value $\Psi = 0.1689$ when increasing the capacitance, which is not shown in the curve and is indicated as the horizontal dashed line instead. It indicates that for a fixed inductance, series resistance, and initial voltage, the maximum current does not increase indefinitely with increasing capacitance. Further increasing the capacitance after reaching the theoretical maximum i_{max} will instead delay the time where the maximum current happens. Secondly, as pointed out in the figure, it only requires around $6.1 \times 10^{-6} \text{ F}$, which is around $6.1 \mu\text{F}$, to achieve 70% of the theoretical maximum current. This benefits when selecting components as the capacitors' voltage tolerance decreases as the capacitance increases for a fixed capacitor size. Since the parameter of interest for this driving circuit is the maximum current, smaller capacitance is enough to achieve 70% – 80% of the theoretical maximum i_{max} , which leaves a relatively wider margin for the voltage selection.

After analyzing the relationship between Ψ and capacitance C , the required i_{max} shall be determined to solve the required initial capacitor voltage. According to the hysteresis curve, the residual induction of the magnet is generated by the external applied magnetic field excitation, which is generated by the solenoid wrapped on the torque rod. The accurate magnetic field inside the solenoid depends on the location, turns of wires, and geometry of the solenoid, which is complicated and will be analyzed later. Here the simplified magnetic field inside the solenoid will be used for the analysis. Assuming a long solenoid that is evenly wrapped with the copper coil at a density n (Turns/m), the magnetic field intensity at the center of the solenoid with a current I is described by eq. (3.3), which is

$$H = nI$$

as a recap. Therefore, to determine the required i_{max} , the H_{max} shall be determined.

According to Fig. 3.8, the coercive force $H_c \approx 48$ kA/s, meaning an external magnetic field with intensity of 48 kA/s is required to drop the macroscopic residual induction to zero. However, the required external field intensity could be several times higher than its coercive force to bring the magnet to its saturated magnetization. Fig. 3.13 shows the hysteresis loop of the AlNiCo magnet tested by Chen, J. *et al* [27].

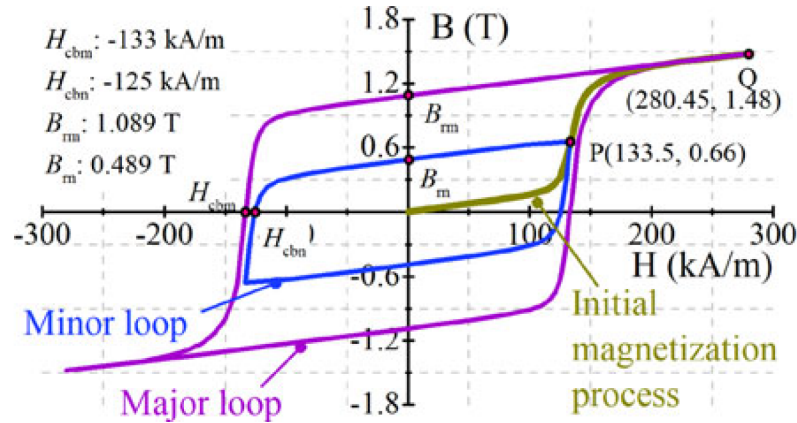


FIGURE 3.13. Major and minor hysteresis curve for the AlNiCo magnet under measurement [27].

Although the grade of the magnet is not indicated, the coercive force of the magnet can be read from the figure and is $H_c = -133$ kA/m. However, applying a magnetic field with the

same intensity in the positive direction will only leave a residual induction of 0.489 T, which is less than half of that generated by a more than doubled magnetic intensity.

The residual induction of the magnet is also susceptible to the applied field intensity. As shown in Fig. 3.14, the slight reduction in applied field intensity will result in a significant drop in magnet residual induction, as shown in path "O-N-M." A far stronger applied field intensity shall be applied to reach the saturated induction, as denoted by point K in the figure.

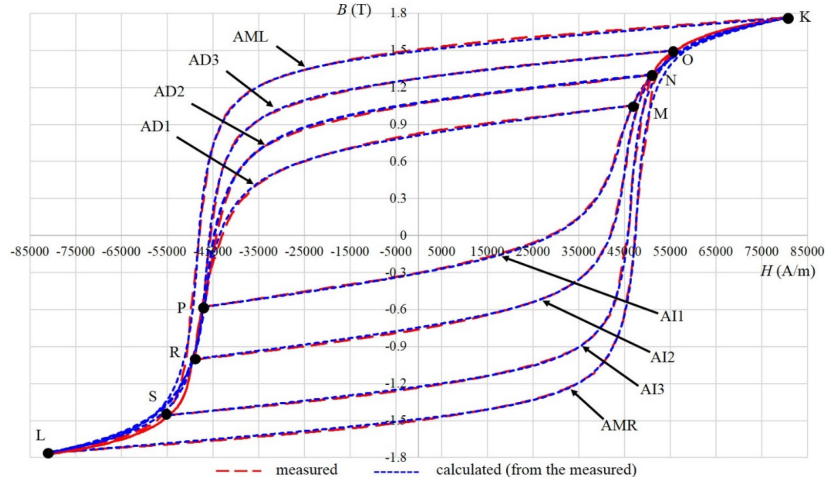


FIGURE 3.14. Hysteresis curve for the AlNiCo magnet with reducing applied field intensity [58]

Although the complete hysteresis loop is not available for the AlNiCo 5 magnet used in this thesis, the loop is expected to be more "slim" and "tall" after fitting the H_c and B_r into Fig. 3.13 indicates a higher field intensity to reach saturation. Due to the sensitivity of the residual induction to the applied field, in reference to Fig. 3.13, the desired H_{max} is determined to be 300 kA/m to ensure a high residual induction. Therefore the desired i_{max} according to eq. (3.3) can be calculated as $i_{max} = 90A$ assuming the use of AWG 28 copper wire.

After determining the i_{max} , the capacitance and initial capacitor voltage can be determined easily. In reference to Fig. 3.12, assuming a capacitance of 10 μF is used, which gives a value of $\Psi = 0.1287$ under the proposed inductance and resistance assumption, the required initial capacitor voltage can then be calculated as:

$$\begin{aligned}
V_0 &= \frac{i_{max}}{\Psi} \\
&= \frac{90}{0.1287} \\
&= 699.3V
\end{aligned} \tag{3.18}$$

Due to the restrictions on the types of capacitors allowed for space vehicles, ceramic and tantalum capacitors are commonly used for space-related electronic devices. However, there are not any ceramic or tantalum capacitors that can meet both capacitance and voltage requirements at the same time. Therefore the capacitor "C5750X6S2W225K250KA" made by TDK in a standard 2220 SMD passive component package is selected as the main discharge capacitor. Each capacitor is a small block with 5.7 mm in length and 5.5 mm in width. Due to the size limit, four of these capacitors are connected in parallel. Each capacitor has a capacitance of 2.2 μF and a voltage tolerance of 450 V, forming a capacitor array with a total capacitance of $C_{tot} = 8.8 \mu\text{F}$ that can be charged to a maximum of 450 V. This value is close enough to the calculated value and can be achieved in the real world. With this components selection, the i_{max} can achieve 56.74 A, and can achieve approximately 189.13 kA excitation magnetic field under the current assumption. This field intensity does not meet the design requirement. However, the inductance and resistance value may vary with the assumed ones, which may change the actual i_{max} . The actual discharge current profile will be measured experimentally in the later section.

3.2.2.3 Charging module

After determining the main discharge capacitor, the charging module shall be determined. The charging power, maximum charging voltage, charging speed, charging circuit form factor, and safety shall be considered for the charging module.

According to the previous section, the capacitor array has a total capacitance of 8.8 μF and maximum voltage tolerance of 450 V. For safety and components lifetime, the maximum charging voltage is limited to 400 V, leaving 50 V as a safety margin to avoid overvoltage

breakdown of the capacitor. Therefore the maximum energy stored in the capacitor array can be calculated using the capacitor energy equation:

$$W = \frac{1}{2}CV^2 \quad (3.19)$$

Substituting values, the maximum energy stored in the capacitor is calculated to be $W_{max} = 0.7$ J. Since the driving circuit works in pulse mode, this energy can be defined as energy per pulse, or energy bit W_{bit} . Note that the capacitor array does not need to be fully charged for every pulse. For different target capacitor voltage, various W_{bit} can be delivered to the torque rod, resulting in adjustable i_{max} . With a fine-tuned profile, this feature can be used as micro adjustment for the fine-tuning of the dipole moment of the magnetorquer.

After knowing the maximum W_{bit} , the charging power and charging time can be determined simultaneously. Since the power is defined as energy per second, defining the desired charging time directly yields the required charging power. Considering the nominal orbital time, 90 mins, and the long setting time for the general magnetorquer, the charging time shall be as short as possible to maximize the system's control frequency and overall stability. Assuming a charging time of 1 ms for a 0 to 400 volt charging process, the required power can be calculated as $P_{charge} = 0.7 \text{ J} / 0.001 \text{ s} = 700 \text{ W}$. This power requirement is too high for a small satellite, especially CubeSat. Although the duration for this power requirement is only one millisecond, such high power drawn will cause a significant voltage drop on the satellites' power bus, which may damage or reboot other payloads and even the main on-board-computer (OBC). Therefore the charging time is extended by a factor of 10, resulting in a 10 ms charging time. The required power is then dropped by a factor of 10, yielding a $P_{charge} = 70 \text{ W}$. This power consumption is within the capability of small satellites' power bus considering the 10 ms charging time. The actual power consumption should be higher than the calculated value due to the charging module conversion efficiency, capacitance variation, and charging voltage fluctuation.

Based on the analysis and calculation, the capacitor charging controller integrated chip (IC), LT3750, made by Linear Technology (Analog Devices), is selected as the main charging

module controller [86]. This tiny chip is packaged in 10-LEAD MSOP, which has only 3×3 mm center size and 3×4.9 mm overall size, including leads, which makes it easier to be integrated into the PCB. This controller IC features "single-pin-control," which allows the chip to be fully controllable by a simple general purpose I/O (GPIO). This makes the module relatively safer to use as the whole charging module can be shut off by the OBC or payload computer if any unexpected issue happens. Drag this pin low through a drop-down resistor makes it even safer as the module will shut off itself if the control signal is lost. The peripheral requirements are not complicated. The chip works in switch mode with an NMOS-FET and a transformer. The sense of the capacitor status, voltage feedback, and charging current constraint is achieved through several passive components. The transformer, the most important peripheral required by this IC, causes problems when designing the module. The IC requires a transformer with a 1 : 10 turns ratio and a dedicated primary-side induction. Therefore customized transformer is not considered to be used as the parameters are hard to control. However, most of the recommended commercial transformers are either unavailable from the market or obsolete. The transformers made by Coilcraft are the only options. However, the most miniature transformer on the recommendation list has a size of $17.2 \times 22 \times 8.9$ mm, which is still the biggest electric component on the final magnetorquer board. Therefore the location of the transformer shall be carefully designed to balance the final board mass distribution and minimize the interference with other components. The target voltage can be simply adjusted by changing one resistor. The final target voltage is selected to be 400 V as mentioned before, and the smallest transformer with part number DA2032-AL is selected, together with the NMOS-FET IRF7493 made by International Rectifier. With these components selection, the module can achieve an overall efficiency of around 90 % when works in "3A charging mode" with higher than 12 V input voltage. The final circuit schematic of the charging module is shown in Fig. 3.15. The module charging waveform and test results will be discussed in the test result section.

For a CubeSat mission, the power requirement is more strict, and 70 W instantaneous power consumption is still beyond the capability of the CubeSats' power bus. Therefore other charging modules will be selected to adapt to the extreme power requirement for the CubeSats and will be introduced in chapter 5.

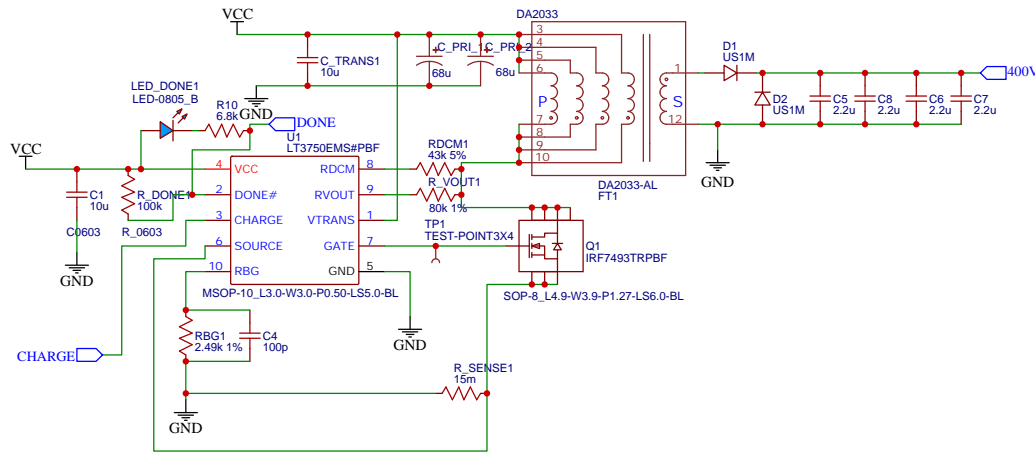


FIGURE 3.15. Schematic of the charge module.

3.2.2.4 H-Bridge

H-Bridge is another vitally important module for the magnetorquer as it determines the direction of the discharge current and the magnetization direction of the torque rod.

There are some requirements when designing the H-Bridge.

- (1) Firstly, the components shall be durable and robust. Since the H-Bridge consists of four independently controlled gates, the normal operation requires all of them to be fully functional. Therefore any failure of the gate will result in the malfunction of the whole magnetorquer. It is not a severe problem for normal magnetorquers as the satellites only lose one type of actuator and control input, which can be compensated by other actuators, such as thrusters and reaction wheels. However, for the EPM, if the H-Bridge brakes when the torque rod is at its full magnetization, there will be a constant torque applied on the satellite trying to align with the local Earth's magnetic field line, which is extremely hard to rectify using other actuators, and may cause the mission failure due to the loss of orientation and controllability. Therefore the reliability and robustness of the H-Bridge are crucially important.
- (2) Second requirement is that each gate of the H-Bridge should be easy to control and require as few peripherals as possible. The more peripherals it requires, the high possibility that it may fail. In addition, if the gates require multiple voltage levels to

operate, more voltage regulators will be used, which adds design complexity and reduces overall efficiency.

- (3) Lastly, the H-Bridge should be explicitly designed to handle high voltage and high current pulse in a small form factor. Since the average power the circuit should handle is relatively small, the component selection shall be as small as possible as most of the components' sizes are determined by the average power it can handle. However, the H-Bridge shall be able to handle a very high surge current as it is how the system is designed to be working. Moreover, the physical size of the H-Bridge shall be as small as possible since each axis of the magnetorquer shall be controlled independently, meaning that there will be three H-Bridges to handle all three axes, resulting in a total of 12 gates to be installed on a single board. If the components are too big, they may not be able to fit into a small board, which adds a considerable design difficulty as the component size, average power rating, and maximum surge power capability are generally tied together.

Three types of On-Off components commonly used for H-Bridges are compared to meet the requirements. The most common is metal–oxide–semiconductor field-effect transistor, or MOS-FET. This component is widely used in H-Bridge for motor driving, switching mode power supply, and other applications that require high-frequency switching operation. However, due to its voltage-driven feature, usually, MOS-FETs require a dedicated H-Bridge driver to operate. Before turning on, there is a high impedance between the drain and source pins of the MOS-FETs. Once a voltage is applied to the gate pin in reference to the source pin, the impedance between the drain and source pin will decrease. The impedance, or resistance, between the drain and source pin, is called On-Resistance, denoted by $R_{DS(on)}$. This value is highly dependent on the voltage on the gate pin. If there is not enough voltage applied to the gate, the high $R_{DS(on)}$ will cause a significant voltage drop, and there will be a large amount of power wasted in the form of heat built up within MOS-FETs, which further reduce the performance. Normal MOS-FETs require about 12 V to be fully turned on, which may not be easily available on small satellites' power bus. Furthermore, most MOS-FETs are used for low voltage, high frequency, and moderate current switching purposes. The required voltage tolerance for the EPM is more than 400 V, and the maximum pulse current could exceed

100 A, which makes MOS-FETs not the ideal choice to be used for H-Bridge. Another type of MOS-based transistor, insulated-gate bipolar transistor (IGBT), is commonly used for high voltage and high power switching. However, similar to MOS-FETs, these devices require high gate voltage to operate, and the pulse current handling capability highly relies on the package size. The common IGBTs that can withstand more than 600V gate-emitter voltage are in TO-247 or TO-220 packages and for very high power switching. These components are too big for the EPM circuit board, and the complex control circuit requires multiple voltage supplies and peripherals. Instead of a transistor, the last candidate component is thyristor, a type of silicon-controlled rectifier (SCR). The working principle is similar to the MOS-FETs and IGBTs. The gate pin controls the conductivity between anode and cathode. However, instead of being controlled by voltage, the thyristor is triggered by the current signal, and once opened, the anode and cathode will remain conductive until the current drops below a threshold and cannot be turned back off through the gate pin. This is not ideal for switching circuits as the conductivity is not fully controllable and depends on the circuit configuration, which makes the switching frequency relatively low and requires complex circuit design. However, the advantage of using thyristors is the low triggering conditions. With only several mA and around 1 V pulse signal, the thyristor can be fully opened with minimal power loss, and it does not require the presence of the signal to maintain the "open" state. In addition, the thyristor can handle the high instantaneous voltage and current pulse in a small package, which makes it the ideal choice for the H-Bridge of the magnetorquer.

Considering all these features, the thyristor is selected to be the gate of the H-Bridge for the magnetorquer. Specifically, the model "BT151S-650L" made by WeEn Semiconductors is chosen to be used to form the H-Bridge for the magnetorquer. This thyristor features 650 V maximum repetitive peak reverse voltage and 132 A non-repetitive peak on-state current for a 8.3 ms pulse time in a SOT428 package ($6.5 \times 10 \times 0.5$ mm) [23]. It can be easily triggered with 2 mA current at 0.4 – 0.6 V, which any microcontrollers can supply. Therefore the H-bridge can be connected and controlled by the microcontroller directly with some protection on the high side of the bridge, which meets the easy-to-control design requirement. The peak voltage and surge current capability also meet the design requirements directly. The

package is small enough to be embedded in a standard CubeSat circuit board, considering that twelve thyristors must be installed, with four each axis.

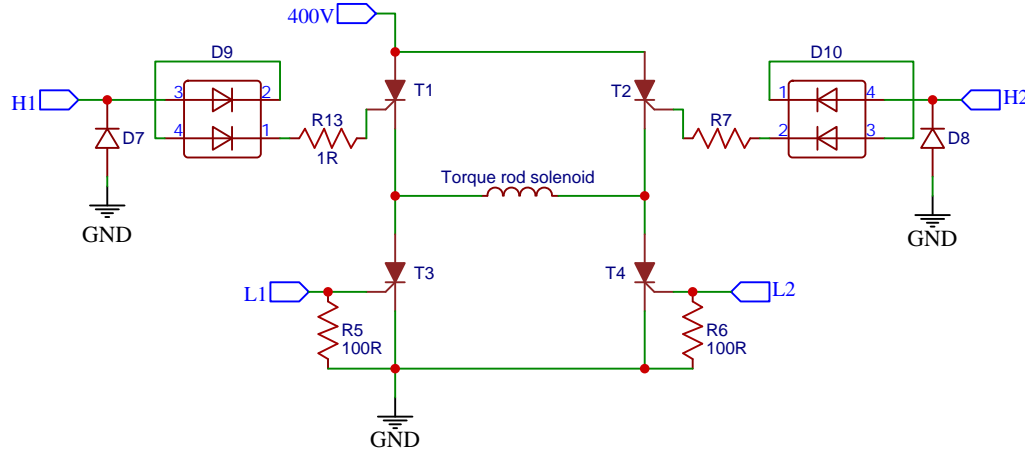


FIGURE 3.16. Schematic of one of the H-Bridge.

The H-bridge for one axis torque rod solenoid is shown in Fig. 3.16. The inductor symbol in the center of the H-Bridge represents the torque rod solenoid. The top half of the bridge is connected with the capacitor array, which makes the T1 and T2 high side gates. Since there is no isolation between the gate and the other electrodes, a diode array "BAW101,215" consists of two diodes with 300 V reverse block voltage each is used with two diodes connected in series to protect the microcontroller. The $1\ \Omega$ resistor restricts the inrush current once the gate pin goes high. For the low side, the gate pin is pulled down through a $100\ \Omega$ resistor to ensure the default close state of the gate.

3.2.2.5 Feedback control method

There is no doubt that the magnetorquer has to be under full control. Therefore all changing parameters have to be monitored and controlled. On the driving circuit, two key parameters determine the charging performance of the torque rod. The first parameter is the capacitor charging voltage, and the second is the torque rod magnetization status. The capacitor charging voltage can alter the pulse energy and change the i_{max} as described in section 3.2.2.2. The magnetization measurement can describe if the torque rod's magnetization reaches the desired value. In the previous sections, only the maximum discharge current is analyzed as it

determines the possible maximum magnetization. However, the change in the magnetization status is not instantaneous. If the duration of the externally applied field is too short, there may not be enough time for the magnet to be fully magnetized. Therefore multiple pulses are required in this case to ensure the torque rod reaches the desired magnetization, and the monitor of the magnetization provides a feedback signal.

The feedback of the capacitor charging voltage is not complex. A voltage divider consists of a 1 M Ω and a 10 k Ω resistor providing a 100 : 1 voltage reduction ratio is connected directly to the capacitor array to provide the analog voltage signal of the charging voltage and can be read by an analog to digital converter (ADC). Note that 2512 packaged 1 M Ω resistor is used to provide sufficient separation between electrodes to avoid arc discharge at low air pressure.

The magnetization measurement feedback, however, is not designed to measure the magnetization directly. As mentioned in the chapter 1, the direct measurement of a magnet's magnetization is hard and normally achieved using other indirect methods. Since the magnetization is directly related to the dipole moment according to the eq. (3.9), measuring dipole moment and calculating the average magnetization is usually used to obtain the magnetization of a magnet. There are several methods utilizing the measurement of the ambient field to measure the dipole moment. Bagus, R. introduced a method by measuring the magnet's magnetic field at arbitrary points and comparing the theoretical value at those points with an ideal solenoid. Once the measurement matches the theoretical one, the magnet can be treated as equivalent to the ideal solenoid, and the property can be calculated using solenoid formulas [111]. Hall, M. *et al.* suggested measuring the magnetic field strength at a distance greater than five times the separation of the dipole, and the dipole moment of that dipole can be calculated through these equations:

$$H_r = \frac{\mu_0}{4\pi} \frac{2m \cos \alpha}{x^3} \quad (3.20a)$$

$$H_\varphi = \frac{\mu_0}{4\pi} \frac{m \sin \alpha}{x^3} \quad (3.20b)$$

where the α is the angle between the direction of the moment and the line drawn from the center origin of the dipole to an arbitrary point P, and x is the distance from the origin to the point P. He claimed a $\pm 2.7\%$ uncertainty for a confidence level of 95% using this method [49].

However, these two methods require either a clean magnetic environment and accurate location of the arbitrary points or a measurement location far away from the magnet, which is not applicable for the EPM presented in this thesis. Instead of accurately measuring the dipole moment, a hall sensor placed and fixed directly on the surface of the magnet is used as a relative reference. Once the hall sensor's relative position to the magnet is fixed, it will output a voltage reading corresponding to the magnet's magnetization status. Mapping the hall sensor reading with the dipole moment measured through other dynamical methods will create a chart. After careful calibration, the dipole moment can be read out from this chart to calculate the magnetization. The hall sensor model "DRV5055A4" is used to measure the flux density of the magnet and is powered by 5 V. The TO-92-3 package is used for the X and Y axis torque rod, and the SOT-23-3 package is used for the Z axis.

3.2.3 Torque rod design and parametric study

After determining the driving circuit, the core of this magnetorquer, the torque rod, will be designed and analyzed in this section. Firstly the copper wire winding, which affects the inductance of the RLC circuit as mentioned in section 3.2.2.2, will be analyzed. Then the performance difference caused by the shape of the torque rod will be analyzed based on both simulation and experiment, followed by the final torque rod design description of the EPM.

3.2.3.1 Torque rod solenoid

As part of the RLC discharge circuit as analyzed in section 3.2.2.2, the inductance and serial resistance are mainly contributed by the torque rod solenoid. Therefore the equations (3.17) and (3.3) will be analyzed in this section together with the selected capacitors and capacitor initial voltages.

As analyzed before, the contribution to the i_{max} from the capacitance increase is less than the contribution from the increasing capacitor initial voltage. Due to the manufacturing limitations, the maximum voltage tolerance of the ceramic capacitor drops when the capacitance increases. Due to safety reasons, electrolytic capacitors, which usually feature high voltage and high capacitance, are not allowed to be launched into space. Therefore the 10 μF ceramic capacitors array with a maximum 450 V tolerance is selected as the main discharge capacitor.

Instead of finding capacitors with large capacitance, the series inductance and resistance, however, shall be kept minimal. As shown in Fig. 3.17 and Fig. 3.18, the Ψ shows a negative relationship with the inductance and resistance if the other two parameters remain unchanged.

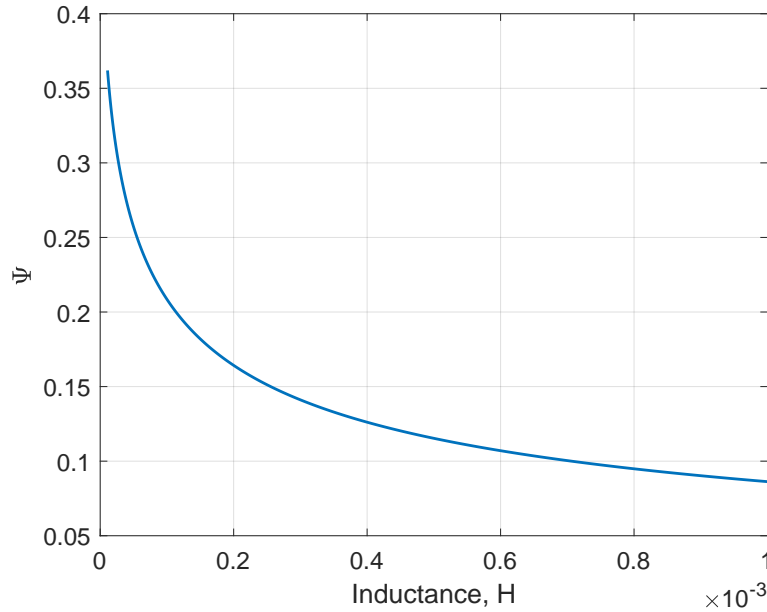


FIGURE 3.17. Coefficient Ψ as a function of inductance L with fixed capacitance and resistance.

However, the conclusion to the effect of the inductance and resistance cannot be made yet. The increase of the inductance and resistance corresponds to an increase in the number of turns of wire for the solenoid, where the induced magnetic field intensity, H , will change according to eq. (3.3). For a magnet core with a fixed length, the higher wire density n can be achieved by overlapping layers of wires. Therefore increasing the number of turns of the wire for a fixed-length magnet core will cause three major effects: (1) the length of the wire

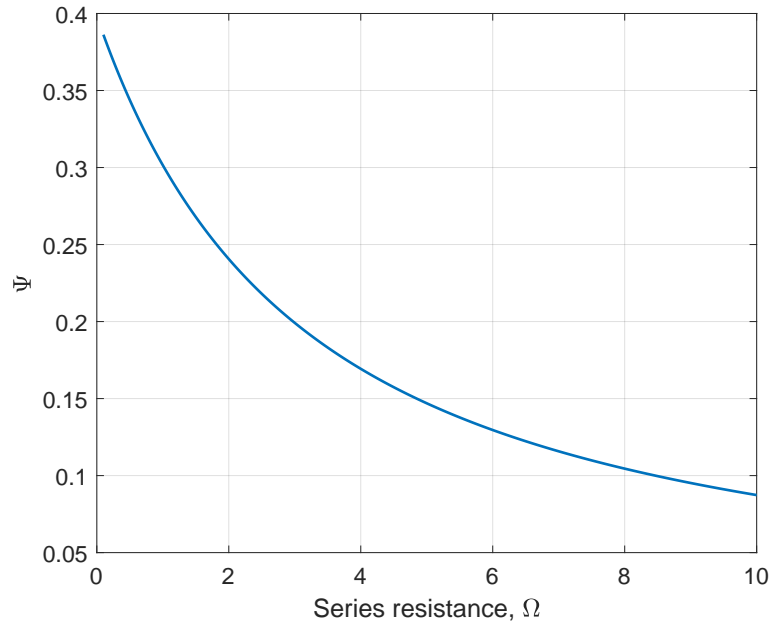


FIGURE 3.18. Coefficient Ψ as a function of resistance R with fixed capacitance and inductance.

will increase, which will increase the resistance, thus decreasing the i_{max} and field intensity H ; (2) the inductance will increase quadratically according to eq. (3.14), thus decrease the i_{max} and field intensity H ; (3) the wire density n in eq. (3.3) increases, which increases the field intensity H linearly. Since the turns of wire have both positive and negative effects on the i_{max} and field intensity H , there could be an optimal solution, which shall be solved analytically.

The eq. (3.3) can be rewritten as:

$$H_{max} = \frac{N \cdot i_{max}}{l} \quad (3.21)$$

where the N is the number of turns of wire of the solenoid, and l is the length of the solenoid. Replacing the i_{max} with equation (3.17), the upper equation can be written as:

$$\begin{aligned}
H_{max} &= \frac{N \cdot V_0 \cdot \Psi(R, L, C)}{l} \\
&= \frac{N \cdot V_0}{\omega_d l L} e^{-\alpha \frac{1}{\omega_d} \arctan \frac{\omega_d}{\alpha}} \sin \left(\arctan \frac{\omega_d}{\alpha} \right)
\end{aligned} \tag{3.22}$$

where α , ω_o , and ω_d are defined in eq. (3.10), (3.11), and (3.12). Substituting the equation (3.14), the previous equation can be written as:

$$H_{max} = \frac{N \cdot V_0}{\omega'_d \mu_r \mu_o N^2 A} e^{-\alpha' \frac{1}{\omega'_d} \arctan \frac{\omega'_d}{\alpha'}} \sin \left(\arctan \frac{\omega'_d}{\alpha'} \right) \tag{3.23}$$

where the single quote denotes the new parameter calculated with the substituted L . Let the turns of wire N be the variable, and d represent the wire diameter, the resistance R , which is not shown in the previous equation, is represented as:

$$R(N) = \begin{cases} R_0 + \rho N \pi D, & N \leq N_{max} \\ R_0 + \rho \pi D N_{max} + \rho \pi (N - N_{max})(D + 2d), & N_{max} \leq N \leq 2N_{max} \\ R_0 + \rho \pi N_{max} \left[\left(\lceil \frac{N}{N_{max}} \rceil - 1 \right) D + 2d \sum_{i=1}^{\lceil \frac{N}{N_{max}} \rceil - 2} \right] \\ + \rho \pi \left[N - \left(\lceil \frac{N}{N_{max}} \rceil - 1 \right) N_{max} \right] \left[D + 2d \left(\lceil \frac{N}{N_{max}} \rceil - 1 \right) \right], & N > 2N_{max} \end{cases} \tag{3.24}$$

where ρ is the resistivity of the copper wire, N_{max} is the maximum turns of wire per layer, calculated as $N_{max} = \lceil l/d \rceil$, and D is the diameter of the torque rod. Assuming a constant cross-sectional area and using the chosen capacitor array and initial voltage, the relationship between maximum field intensity H_{max} , maximum current i_{max} , time of maximum current t_{max} and turns of AWG 28 enameled copper wire is shown in Fig. 3.19 and 3.20, respectively.

From the Fig. 3.21 and 3.22, the maximum field $H_{max} = 376.1$ kA/m occurs with 1311 turns of AWG28 enameled copper wire wrapped on a 60 mm AlNiCo 5 torque rod. Although the maximum current is lower comparing with the estimation from section 3.2.2.2 (56.74 A), the

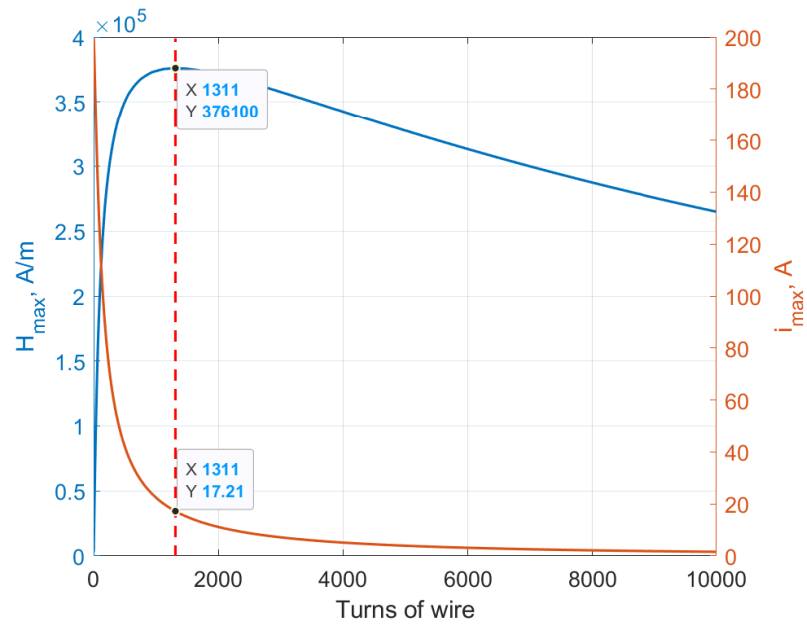


FIGURE 3.19. Maximum field intensity H_{max} and maximum discharge current i_{max} as a function of turns of wire with 60 mm torque rod and AWG 28 enameled copper wire.

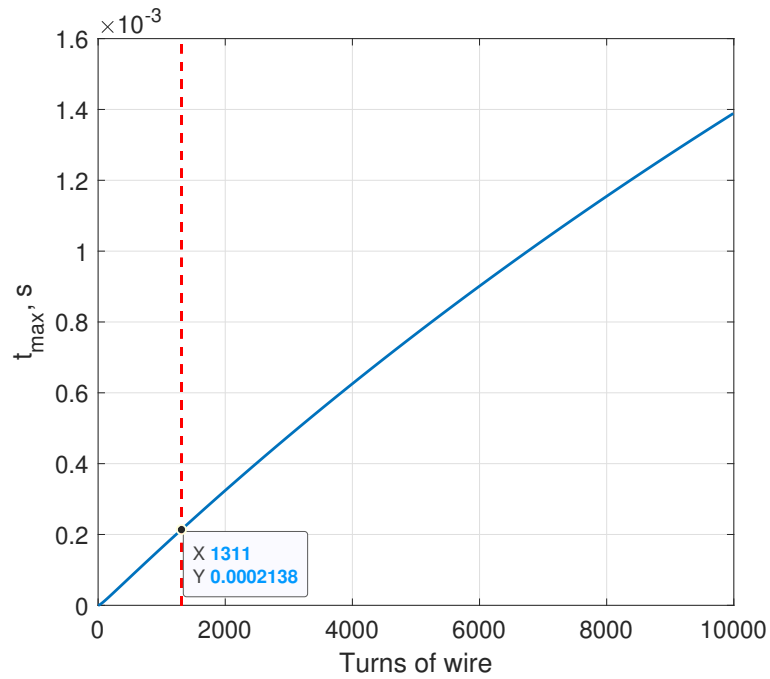


FIGURE 3.20. Time of maximum current t_{max} as a function of turns of wire with 60 mm torque rod and AWG 28 enameled copper wire.

maximum field intensity can be almost doubled (189.13 kA/m). The time when maximum current occurs t_{max} remains under 250 μ s when the turns of wire increases.

Although the maximum field intensity can be doubled by adding more turns of wire to the torque rod solenoid, the longer wire will cause introduce excessive weight, which shall be avoided in small satellites, especially CubeSats, where the weight budget is highly restricted. To further optimize the solenoid, copper wires of different AWGs are added to the analysis. Assuming the length of the magnet is unchanged, different wire gauges have different resistivity ρ and diameter d , which will also affect the N_{max} . In addition, the cross-sectional area A , which affects the inductance of the solenoid, cannot be assumed to be constant as the overlapping of thick wires will vastly increase the cross-section area. The accurate inductance of a solenoid with multiple layers of copper wires is hard to calculate. Therefore the mean radius of the solenoid will be used to calculate the area, and thus the inductance can be calculated as:

$$L' = \frac{\mu_r \mu_0}{4l} N^2 \pi (D + 2d[\frac{N}{N_{max}}])^2 \quad (3.25)$$

The effect of the turns and copper wire of different AWGs on the maximum magnetic field intensity H_{max} is shown in Fig. 3.21, followed by the corresponding t_{max} plot shown in Fig. 3.22.

From the figure, the maximum field intensity occurs at around $N = 300 - 1300$ for the copper wire of AWG 26 – 32. Note that when using high AWG wires, which is preferred for conventional magnetorquers, higher turns of wire will bring higher inductance and resistance, the maximum field intensity is significantly suppressed, and the discharge time is drastically extended. Considering the weight of the solenoid, the turns shall be kept minimal. Therefore one of the optimal torque rod solenoid configuration could be using AWG 28 enameled copper wire to wrap two layers for the 60mm long 6 mm diameter AlNiCo 5 torque rod. Due to the system weight, ease of manufacture, and PCB layout, the torque rod solenoid used for the EPM in this thesis has only one layer of winding with AWG 28 enameled copper wire, whose

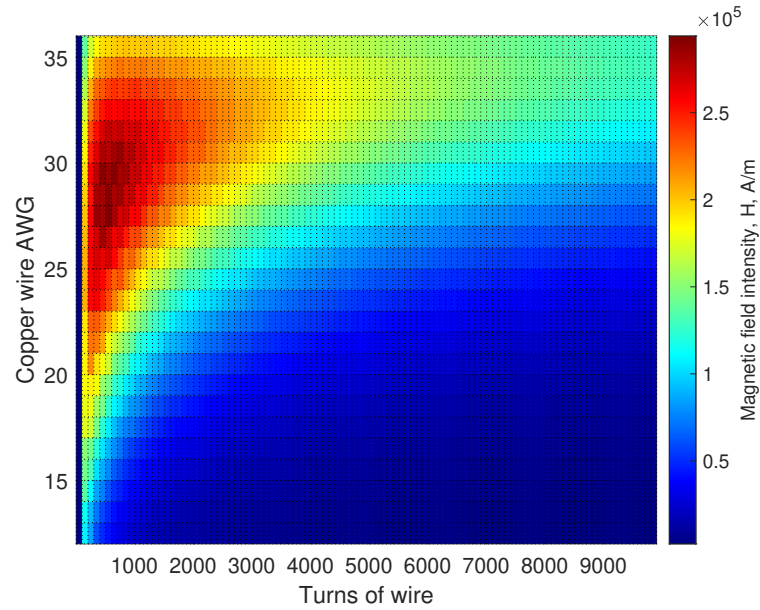


FIGURE 3.21. Maximum field intensity H_{max} as a function of turns of wire and wire with different AWG for 60 mm length torque rod.

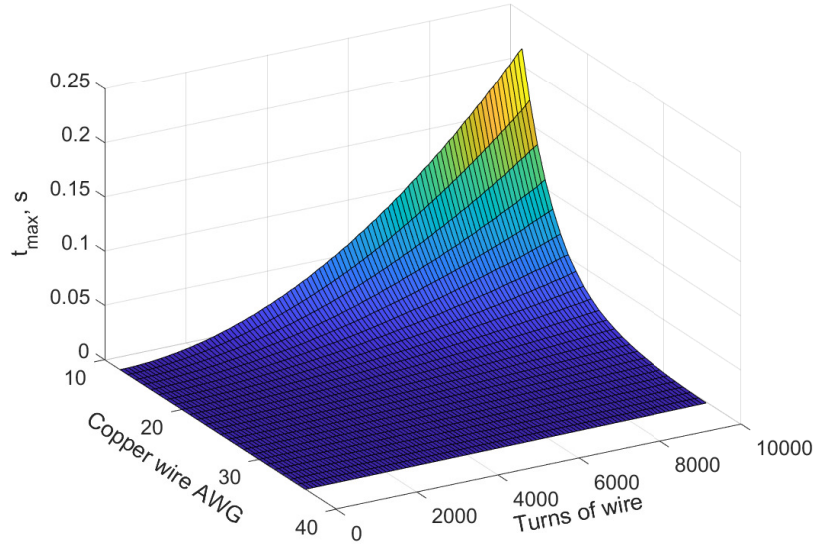


FIGURE 3.22. Time when maximum current occurs t_{max} as a function of turns of wire and wire with different AWG for 60 mm length torque rod.

performance is estimated at the end of section 3.2.2.2. Although the configuration is sub-optimal, it can still reach around 70 % of the maximum magnetization. Future versions will focus on using optimal configuration to reduce the power consumption further and increase

the magnetization. Note that this optimization is for the 10 μF capacitor array working at 400 V initial voltage and for a specific torque rod dimension. However, this optimization method could also be used for other electrical and torque rod dimension configurations.

3.2.3.2 Torque rod performance vs. shape parametric study

The shape of the torque rod is the last and the most important part of the EPM as it is the component that provides the torque. All the previously discussed aspects, including circuit design, components selection, and parameters optimization, aim to provide maximum magnetization of the rod with minimal energy in the shortest time. The effect of the shape of the torque rod on the magnetorquer performance shall be analyzed and determined as the final step of the design of the EPM. In this section, firstly, the magnetization of the torque rod in terms of rod diameter and length is investigated analytically. To verify the results, the dipole moment is then measured experimentally as an indirect method of measuring the magnetization, as mentioned before. Besides, since the dipole moment is the main parameter of interest of a magnetorquer, it can be used directly as a measure to compare the performance difference with different torque rod shape parameters.

The analytical model and the experiment setup shall be explained first. Firstly the torque rod solenoid configuration in the analytical model and experiments are kept the same. The magnet rods under test are wrapped with one layer of AWG 28 enameled copper wire from end to end. Although this configuration cannot guarantee the same applied field for magnets of different lengths and diameters, this study aims to investigate the performance of the magnet rods of different sizes for being used as torque rods for the EPM. To keep the applied field the same for all magnets is readily available by simply using one solenoid and the same discharge parameters for all the tests. However, this configuration is not applicable for the EPM, and wrapping the magnet rod from end to end is the most appropriate configuration for the EPM. Therefore the more accurate title for this section would be "The parametric study of the magnet rod for being the torque rod of the EPM." Fig. 3.23 shows the model configuration and parameters under control.

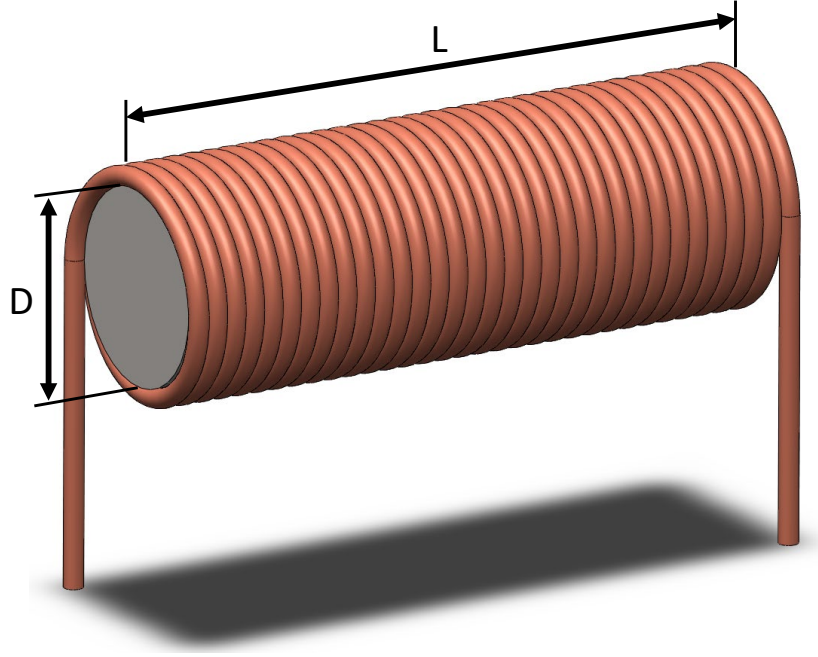


FIGURE 3.23. Indication of the torque rod configuration and parameters under control for the parametric performance study.

The magnetic field intensity H is assumed to be the same and uniform inside the solenoid and is described by equation (3.3). However, the field is not linear and uniform for a solenoid with finite length. The field in the axial and radial direction highly depends on the location of the measurement point and the geometry of the solenoid. Derby, N. summarized the general equations that describe the magnetic flux density in the radial and axial direction inside a cylinder of length $2b$ and radius a wrapped by a solenoid with a number of turns per unit length n carrying current I [33]:

$$B_\rho = B_o[\alpha_+ C(k_+, 1, 1, -1) - \alpha_- C(k_-, 1, 1, -1)] \quad (3.26)$$

$$B_z = \frac{B_o a}{a + \rho} [\beta_+ C(k_+, \gamma^2, 1, \gamma) - \beta_- C(k_-, \gamma^2, 1, \gamma)] \quad (3.27)$$

where

$$B_o = \frac{\mu_o}{\pi} n I,$$

$$\begin{aligned}
z_{\pm} &= z \pm b, \\
\alpha_{\pm} &= \frac{a}{\sqrt{z_{\pm}^2 + (\rho + a)^2}}, \\
\beta_{\pm} &= \frac{z_{\pm}}{\sqrt{z_{\pm}^2 + (\rho + a)^2}}, \\
\gamma &= \frac{a - \rho}{a + \rho}, \\
k_{\pm} &= \sqrt{\frac{z_{\pm}^2 + (a - \rho)^2}{z_{\pm}^2 + (a + \rho)^2}},
\end{aligned}$$

and function $C(k_c, p, c, s)$ is the generalized complete elliptic integral, can be expressed as:

$$C(k_c, p, c, s) = \int_0^{\pi/2} \frac{c \cos^2 \varphi + s \sin^2 \varphi}{(\cos^2 \varphi + p \sin^2 \varphi) \sqrt{\cos^2 \varphi + k_c^2 \sin^2 \varphi}} d\varphi \quad (3.28)$$

According to the equations, the magnetic field intensity inside a 60 mm long 6 mm diameter cylindrical solenoid carrying 100 A current is shown in Fig. 3.24.

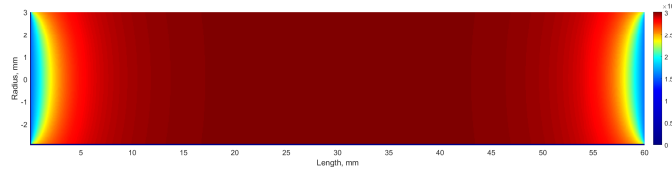
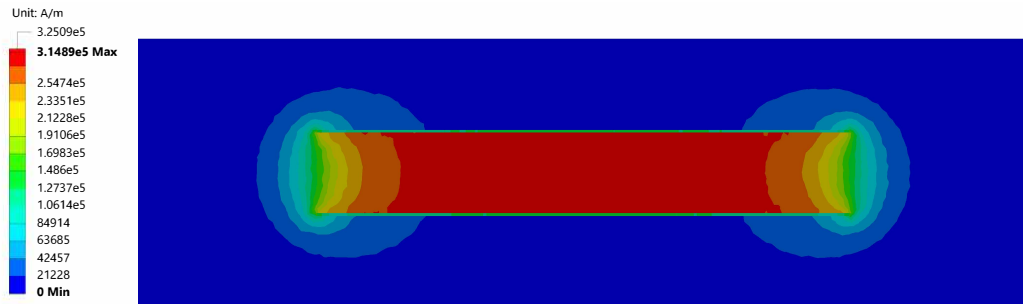


FIGURE 3.24. Magnetic field intensity inside a 60 mm long 6 mm diameter cylindrical solenoid carrying 100 A current.

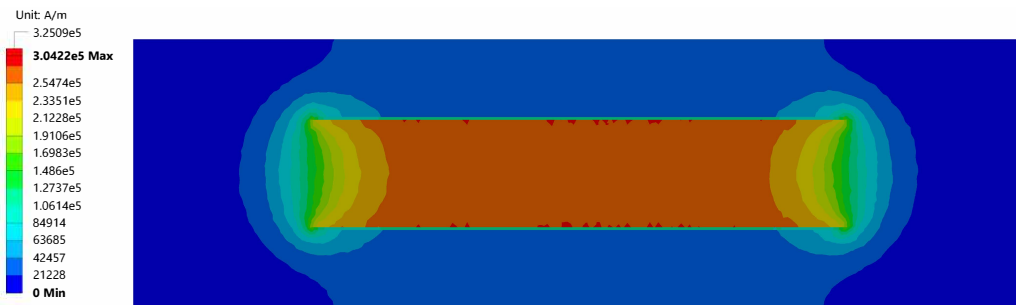
It can be seen that the field intensity is uniform in the middle of the solenoid. When approaching the end, however, the field strength decreases drastically. Eight simulations with the solenoid at a controlled diameter and length carrying 100 A current were performed in ANSYS to intuitively compare the effect of the radius to the magnetic field intensity. The first four simulations are performed for solenoid with 60 mm length and different diameter from 6 to 15 mm. The second four simulations kept the diameter unchanged at 6 mm and changes the length from 50 mm to 20 mm. The simulation results are shown in figs. 3.25 and 3.26. Note that colormap settings are the same for all plots.



(A) 6 mm diameter.



(B) 9 mm diameter

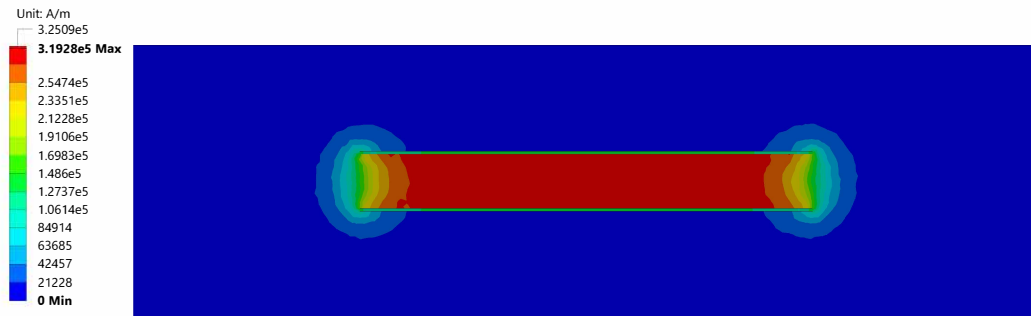


(C) 12 mm diameter

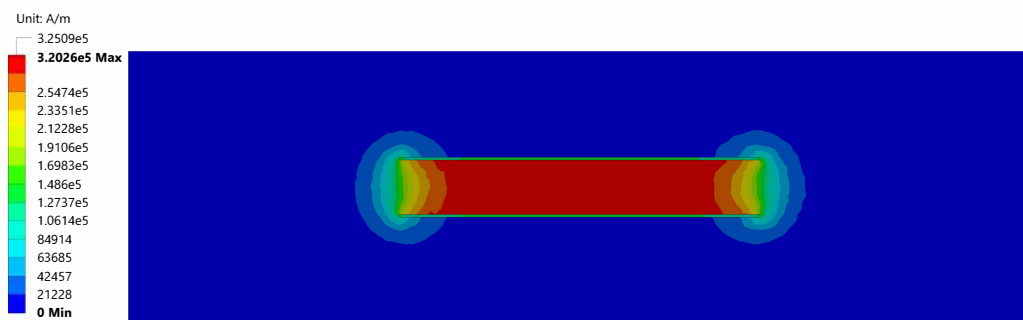


(D) 15 mm diameter

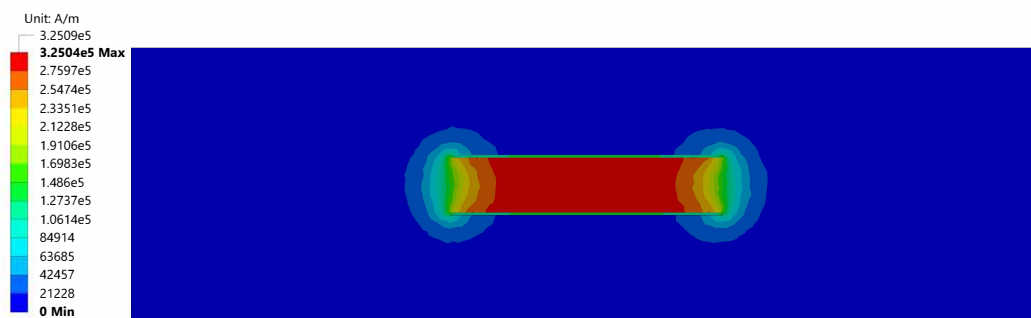
FIGURE 3.25. Magnetic field intensity inside a 60 mm long cylindrical solenoid carrying 100 A current with various diameter.



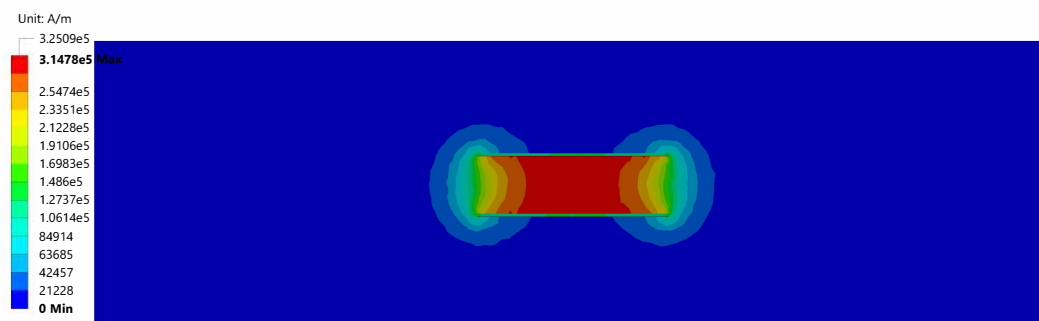
(A) 50 mm length.



(B) 40 mm length.



(C) 30 mm length



(D) 20 mm length

FIGURE 3.26. Magnetic field intensity inside a 6 mm diameter long cylindrical solenoid carrying 100 A current with various length.

From Fig. 3.25, the most uniform and high field intensity occur inside the solenoid with 6 mm diameter. Although the field gets weaker close to the end area, most of the inside area is strong and uniform. The field becomes weaker when the solenoid diameter increases and the non-uniform area start to enter the solenoid's center area. Besides, for the same driving current, the field intensity inside the solenoid decreases with the increase of the solenoid diameter. Therefore, a higher current is required for the thicker torque rod to achieve the same magnetization as a thinner rod. Although the dipole moment may increase due to the increase of the volume of the magnet, the low magnetization reduces the overall system efficiency, and the weight increase from the thick torque rod may reduce the overall performance. From the simulation with magnet bar with the same diameter and different length, as shown in Fig. 3.26, the magnetic field intensity inside the solenoid does not change significantly. However, the non-uniform field area at two ends of the magnet bar takes a larger volumetric percentage as the total magnet volume decrease, which would result in a slight decrease in overall magnetization when the magnet length decreases.

A test apparatus was designed and developed to test the magnet rod with different diameters and lengths to investigate the effect of the torque rod size experimentally. The major equipment is the Helmholtz cage, which consists of several squares or round solenoids with controlled size and position to generate a uniform, fully controllable magnetic field. The details of the Helmholtz cage will be introduced and described in section 3.3.1. The dipole moment is measured through the small angle oscillation method, which is achieved by hanging the magnet bar inside the test area of the Helmholtz cage and using a hall sensor to count the oscillation period to calculate the frequency. The details of this measurement method will be described in detail in section 3.3.3. Two groups of magnets bar are prepared to test the effect of the length and radius of the bar magnet. The first group consists of the magnet bars with the same length but changing radius, and the second group consist of the magnet bars with the same radius but changing length. Table 3.1 lists the length and diameter of the magnet rods for two groups under test. To ensure the magnet bars under test are experiencing the same excitation, the same demagnetization sequence and five magnetizing pulses with an initial capacitor voltage of 400 V are applied to all the magnet bars before the dipole moment test. The details of the demagnetizing sequence will be introduced in the later section.

TABLE 3.1. Two groups of magnet bars under test.

Material:		AlNiCo 5	
Group 1		Group 2	
Length (mm)	Diameter (mm)	Diameter (mm)	Length (mm)
20	4	6	10
	5		12
	6		15
	7		20
	8		25
	10		60
	14		-
	15		-

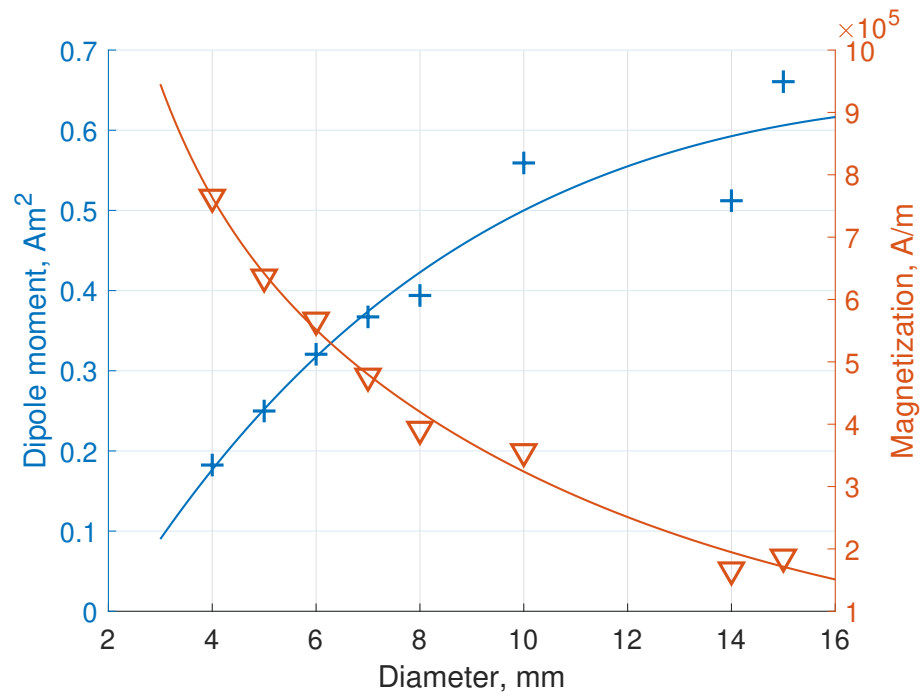
The measurement results of the dipole moment and magnetization for two groups of magnet bars are summarized in Table 3.2.

TABLE 3.2. Dipole moment and the magnetization measurement result of two groups of magnet bars.

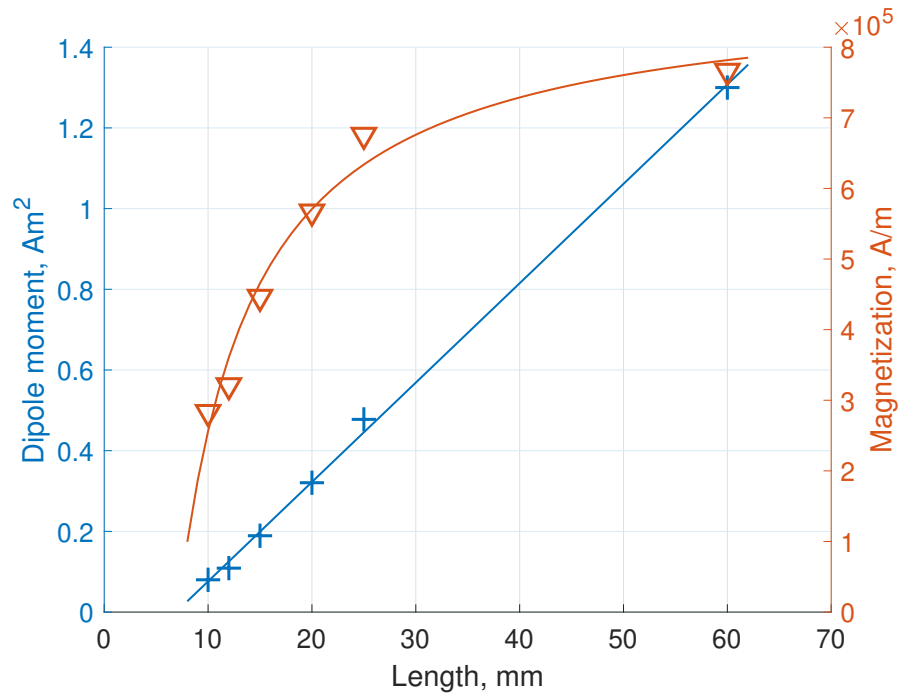
Group 1			Group 2		
Diameter (mm)	Dipole moment (Am^2)	Magnetization (A/m)	Length (mm)	Dipole moment (Am^2)	Magnetization (A/m)
4	0.1824	764038	10	0.08	283059
5	0.2498	636009	12	0.1089	320999
6	0.3206	566980	15	0.1892	446163
7	0.3672	477097	20	0.3206	566980
8	0.3939	391866	25	0.4776	675641
10	0.5592	355998	60	1.287	766302
14	0.5121	166332	-	-	-
15	0.6606	186911	-	-	-

To analyze the trend of the effect of magnet rod shape, the results in the previous table are visualized and shown in Fig. 3.27. The data points in table 3.2 are shown as markers, and the solid lines show the curve fitting of the data points.

From Fig. 3.27a, the overall dipole moment increases with the increasing magnet diameter, which confirms the results concluded from the simulation that using a thicker magnet bar



(A) Dipole moment and magnetization versus magnet diameter.



(B) Dipole moment and magnetization versus magnet length

FIGURE 3.27. Measured dipole moment and corresponding magnetization for magnet bars with different diameters and lengths.

could increase the dipole moment with the same discharge circuit, although the increase rate seems to become slower as the diameter rises. The magnetization, however, decreases with the increasing magnet diameter, which agrees with the trend shown in the simulation results. From Fig. 3.27b, the dipole moment seems to increase linearly with the increasing length of the magnet. This is caused by the volume difference of magnets according to the eq. (3.9). However, the magnetization of the magnets also increases with the length, and it seems to be saturated when the length further increases. Since the field intensity profile inside the solenoids with the same diameter and different lengths are similar, the different magnetization could be caused by the discharge time and discharge current profile due to the change of series resistance and inductance of the circuit. To reach higher magnetization, optimization must be performed to find the optimal wire AWG and the turns of the wire. However, even if the magnet reaches the maximum possible magnetization, a small volume will result in a small dipole moment. Therefore the selection of the size of the torque rod and the maximum dipole moment must be balanced and optimized for different target satellites and mission requirements.

Considering the maximum dipole moment, satellite mass budge, and system efficiency, the AlNiCo 5 magnet bar with 6 mm diameter and 60 mm length is selected as the main torque rod for the EPM in this thesis.

3.2.4 EPM test result

This section will test the prototype EPM regarding torque rod status under different charge and discharge conditions. The hall sensor reading will be used as feedback to monitor the torque rod status. Since the charging process is discrete, the magnet's residual induction will not follow the continuous hysteresis loop. Therefore the torque rod response under different pulse conditions is of interest and shall be determined as it is directly related to the energy consumption and overall performance.

3.2.4.1 Experimental setup

The driving circuit is described in great detail in the previous sections. The torque rod and torque rod solenoid are set up following the discussion result from the previous section. A 10×10 cm circuit board with all the integrated sub-systems has been manufactured and is shown in the figure. 3.28. The bottom side of the left figure is the capacitor charging circuit, and the top right corner is the breakout of the control pins. Two torque rod described in the previous section is installed on the 3D printed support structure with PLA material in the orthogonal position shown as the red structure in the left figure. The red block in the middle of the board is the torque rod for the Z axis. The ideal configuration for the Z-axis torque rod is the same as the X and Y axes. However, due to the size and weight limit, the shorter magnets are selected to be installed in the middle of the board and covered by a 3D printed case. The hall sensor is placed and fixed directly on one end of the torque rod. An Arduino Uno via wire connection controls the board. The Arduino built-in analog to digital converter (ADC) is used to read the hall sensor and capacitor voltage divider's analog signal. A customized 3-cell lithium-ion battery (not shown in the figure) is used to provide the main charging power to the board. On the back of the board, as shown in the right part of the figure 3.28, is used to place 12 of the thyristor and four main discharge capacitors as introduced in the previous sections. The board is configured that the top layer only contains low voltage, and the bottom layer is used for high voltage to avoid potential damage caused by the high voltage breakdown. The voltage reading from the Arduino built-in ADC of the capacitor voltage and hall sensor is monitored and plotted for the experiment.

3.2.4.2 Basic working principle

Firstly the general circuit working principle shall be introduced to demonstrate the basic operation process. Fig. 3.29 shows the capacitor voltage waveform and the hall sensor reading for four continuous pulses.

From the figure, the charging circuit started to operate at around -5 ms, and took around 10 ms to charge to around 230 V. The hall sensor's initial voltage is around 4 V, indicating that the magnet is now being magnetized in a certain direction. According to the manufacturer's

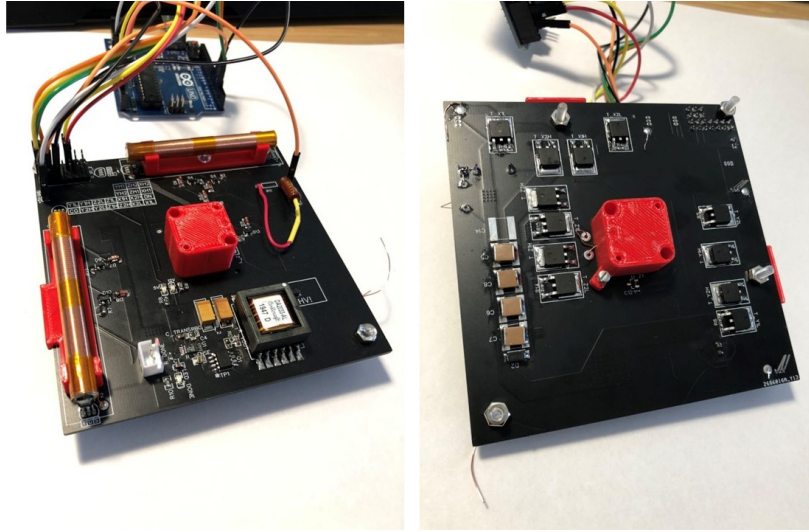


FIGURE 3.28. Prototype board of the EPM (left) top view, (right) bottom view.

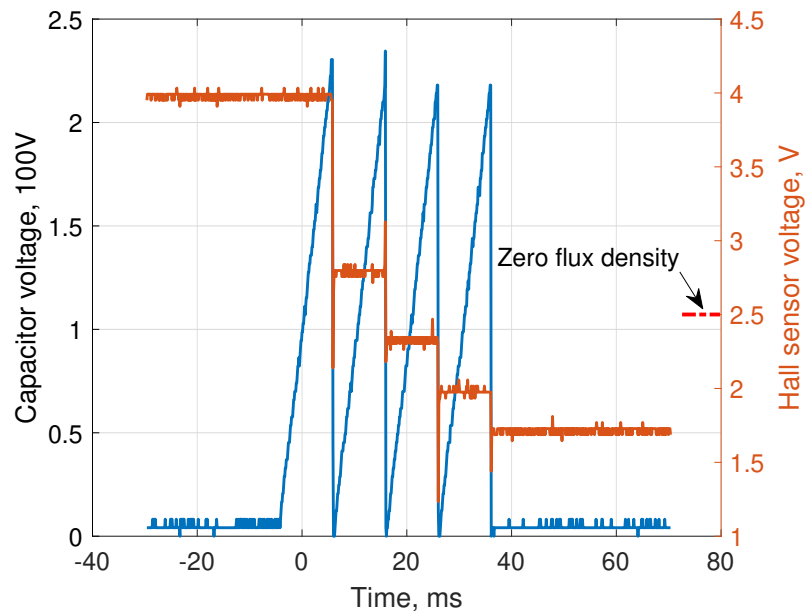


FIGURE 3.29. Waveform of capacitor voltage and corresponding hall sensor reading.

datasheet, the 2.5 V hall sensor voltage represents the zero magnetic flux density. Then the discharge command was sent to the H-bridge, and the energy inside the capacitor was discharged through the torque rod solenoid. This process is shown as the sudden drop of the capacitor voltage shown in the figure. Since the discharge process finished within the sample

rate of the Arduino, the detailed discharge profile cannot be seen in this figure. The field generated by the torque rod solenoid was against the original magnetization direction of the torque rod. Therefore, upon discharging, the hall sensor voltage dropped due to the change in the direction of the torque rod internal magnetization. However, due to the short pulse time and the limited i_{max} , the magnetization of the torque rod cannot be fully reversed after one pulse. However, a single pulse at around 230 V can almost bring the magnetization to almost zero. After the second pulse at the same voltage, the overall magnetization direction was reversed, which makes the hall sensor voltage drops below the 2.5 V zero thresholds. After the third and the fourth pulse, the hall sensor reading dropped to around 1.7 V. The hall sensor voltage will be converted to mT in the results below following the data sheet provided by the hall sensor manufacturer.

3.2.4.3 Measured flux density vs. capacitor voltage

The relationship between the torque rod magnetic flux density, the capacitor voltage, and the number of pulses is investigated at first. Fig. 3.30 shows the measured flux density of the torque rod with number of pulses at 100 V capacitor voltage. From the figure, the flux density reaches to around -80 mT after 20 pulses, and slowly approaching its final value, which is around -85 mT. After reaching the final value, further pulses cannot increase the magnetization, which agrees with the hysteresis loop that the residual induction of the magnet does not change if the applied field intensity is below a certain threshold. This phenomenon can be seen in the figure. 3.31a and 3.31b. The alternating and decreasing applied voltage is the demagnetization process, which will be introduced in the later section. After being demagnetized, the flux density reaches and remains at a certain value after 80 pulses of a certain capacitor voltage and then rises to a higher value when pulses with higher capacitor voltage are applied. Note that the capacitor voltage and flux density sign demonstrates the direction of the magnetization. The actual capacitor voltage is always positive, and only the discharge direction changes, which is controlled by H-bridge.

Fig. 3.31c shows the flux density measurement in response to step increase capacitor voltage but in the alternating direction. Firstly it can be seen that the saturated flux density profile

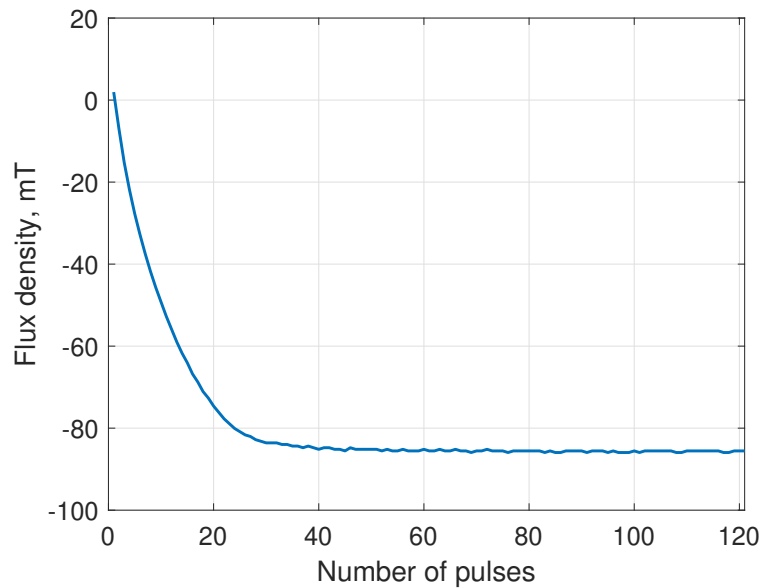
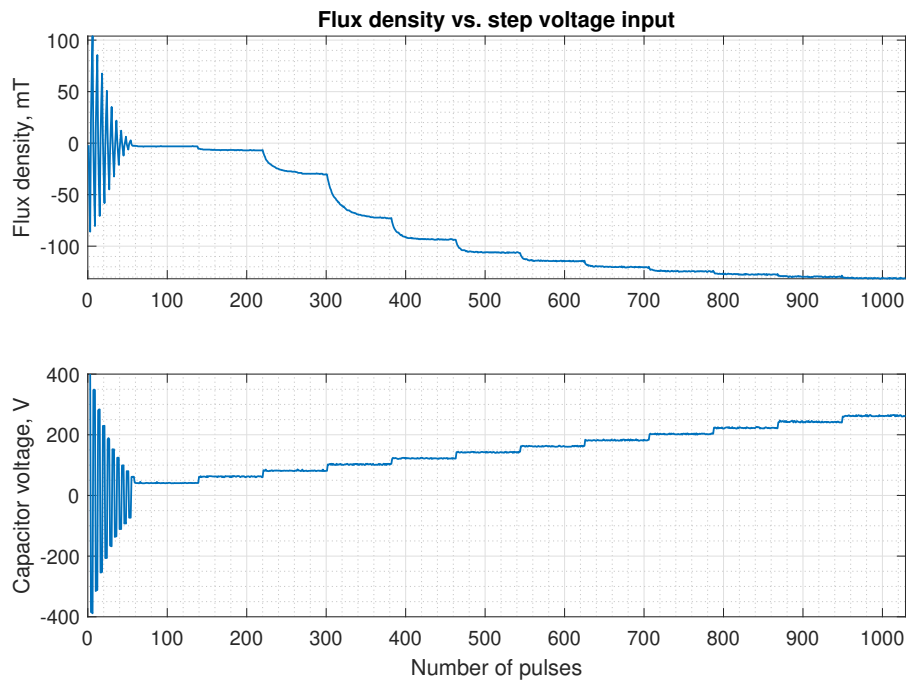


FIGURE 3.30. Torque rod magnetic flux density measurement for 120 charging pulses at 100 V.

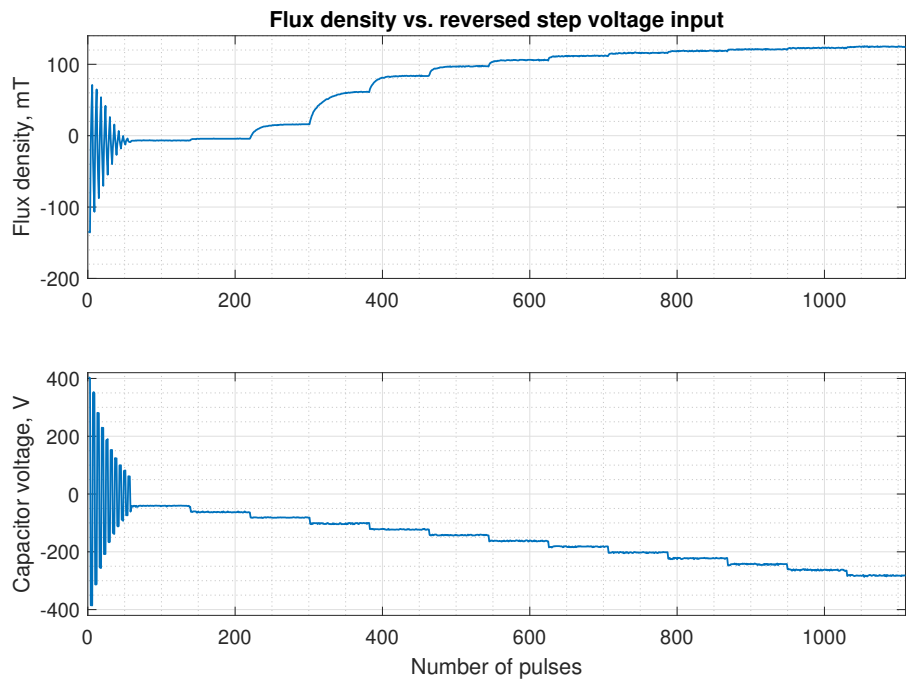
for different capacitor voltage is symmetrical about the zero density line for both directions. This shows great symmetry about the torque rod magnetization property, which is essential for being an actuator and a control input. The second thing to be observed from the figure is that it takes more pulses to reach the saturated flux density for lower input voltage. This phenomenon can be seen clearer in Fig. 3.32. 80 pulses are applied to the torque rod at different capacitor voltages. For the 100 V capacitor voltage, the magnet flux density does not reach its saturating value after 80 pulses. In contrast, for the 200 V capacitor voltage, the magnet flux density reaches saturation at the beginning of the discharge. For different capacitor voltages, the saturated flux density with different capacitor voltages is summarized in Fig. 3.33.

3.2.4.4 Demagnetize and residual B field

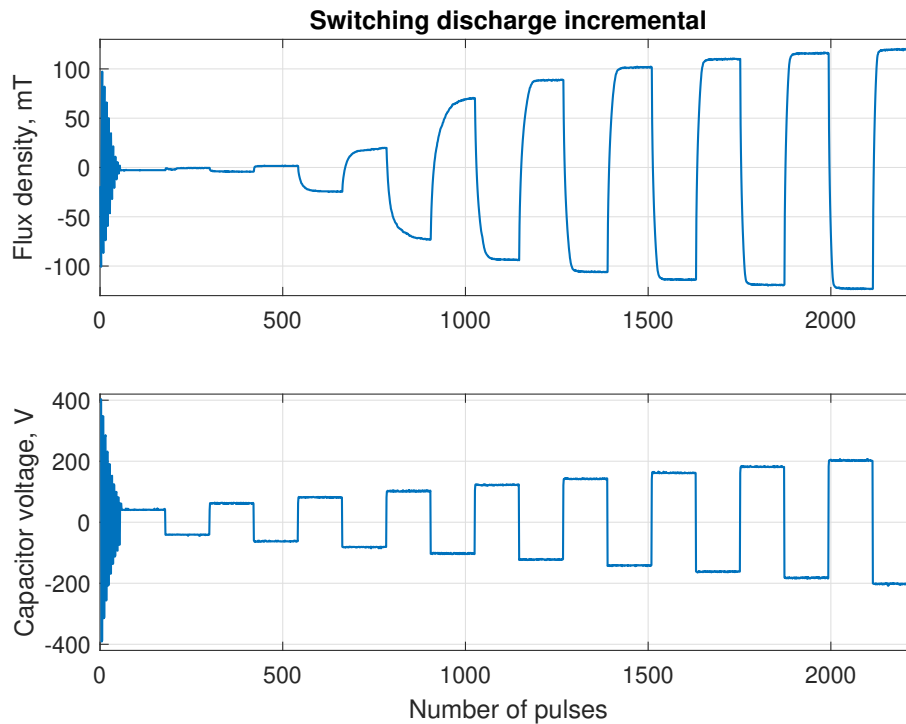
As the most important process, the demagnetization process determines if the EPM can be turned off and "how" the EPM can be turned off. As introduced in the section 2.1.2, the demagnetization of the ferromagnetic material requires the externally applied field to follow the pattern shown in Fig. 2.7. In the EPM, the required alternating field is achieved through



(A) Step increase of capacitor voltage in one direction.



(B) Step increase of capacitor voltage in reversed direction.

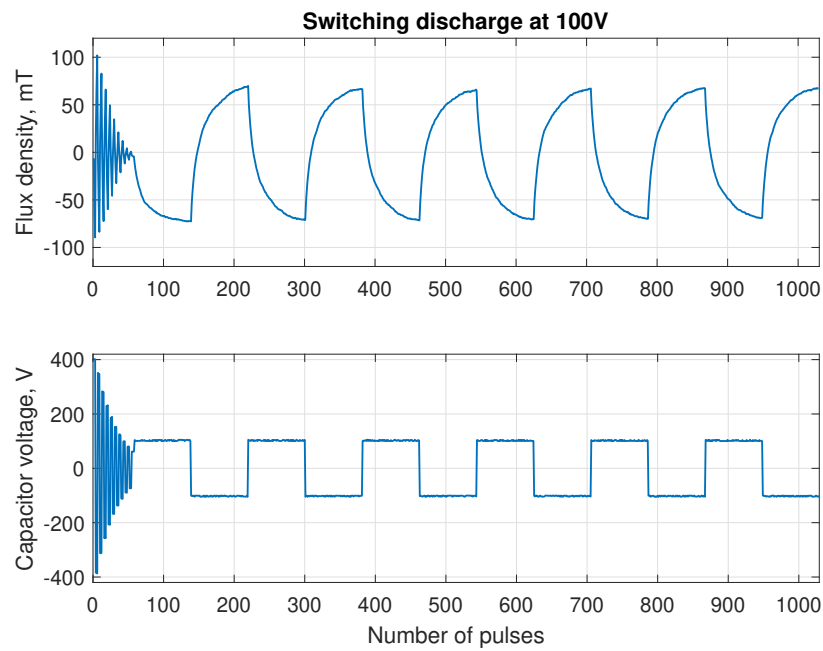


(C) Step increase of capacitor voltage in alternating direction.

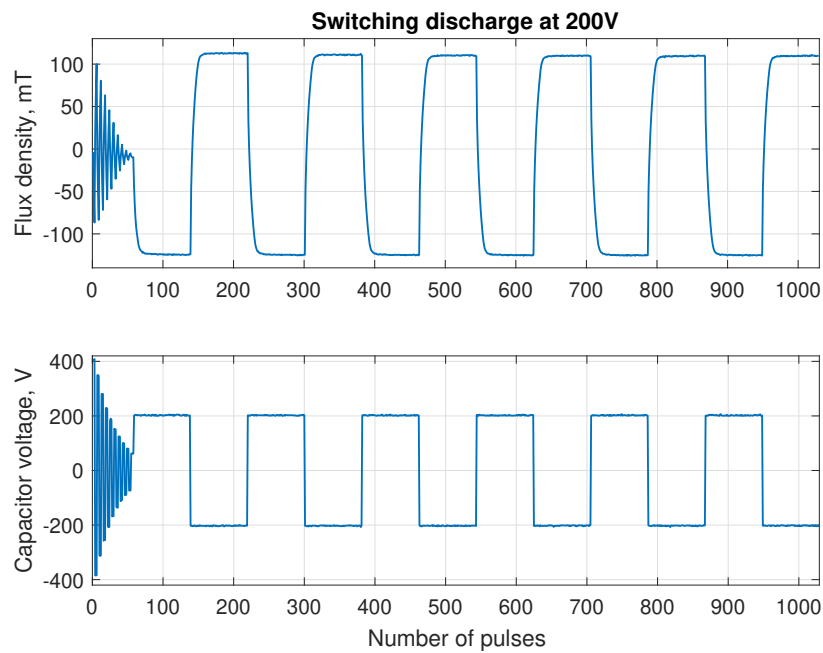
FIGURE 3.31. Torque rod flux density versus incremental and alternating capacitor voltage in two directions.

discharging the capacitor at descending voltage pattern in the alternating direction to the torque rod solenoid. Two capacitor voltage profiles are used to test the demagnetization performance. As shown in Fig. 3.34, profile 1 in the left part of the figure consists of linearly decreasing capacitor voltages, while profile 2 consists of exponentially decreasing capacitor voltage with three pulses at each voltage data point.

Both discharge profiles can reduce the magnet flux density reading to close to zero, as shown in Fig. 3.35. However, the charging response of the magnet shows asymmetry after different demagnetization profiles, and the flux density of the magnet during the demagnetization process shows different profiles. From Fig. 3.35a, both capacitor voltage and flux density show symmetry about the zero line, and the magnetic flux density measurement for the charging process in both directions look symmetrical. However, for the demagnetization profile 1, as shown in Fig. 3.35b, the flux density during the demagnetization process shifted to the bottom of the figure. The charging performance after the demagnetization is not



(A) Alternating discharge direction at 100 V capacitor voltage.



(B) Alternating discharge direction at 200 V capacitor voltage.

FIGURE 3.32. Magnet flux density in response to different capacitor discharge at the alternating direction.

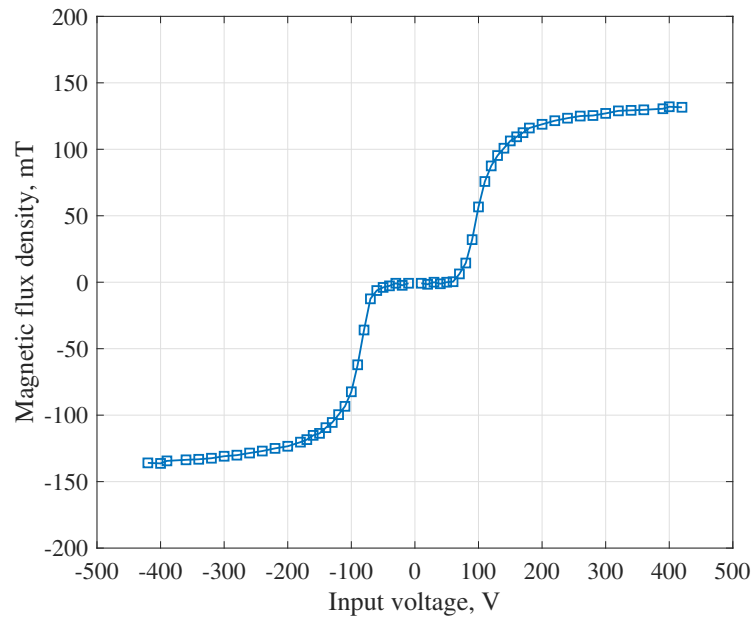


FIGURE 3.33. Saturated magnetic density versus the capacitor voltage.

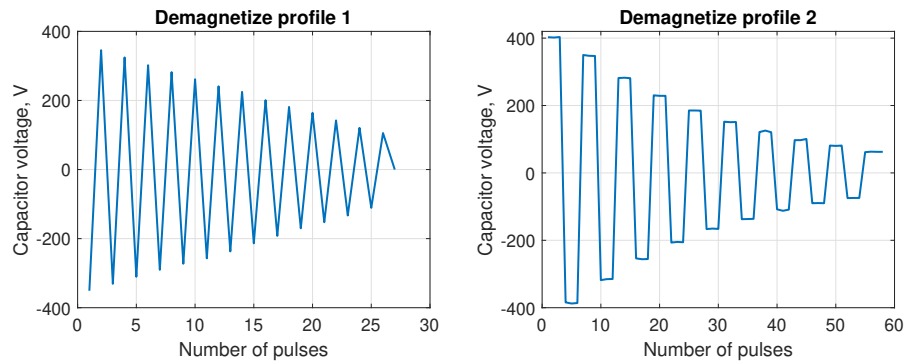


FIGURE 3.34. Two capacitor voltage profile for the demagnetization process.

symmetrical in two directions. The charging towards the bottom side seems to be faster and easier than that towards the plot's top side, which could be caused by the minor loop effect as introduced in section 2.1.2, and the charging would be easier towards the previously magnetized direction. Note that for the profile shown in Fig. 3.35b, three pulses at 400 V in both directions were applied to the torque rod to pre-eliminate the internal magnetization bias. However, the results show that this method has a negligible effect on the final magnetization results. The torque's final magnetization status does affect the flux density's leaning side, as

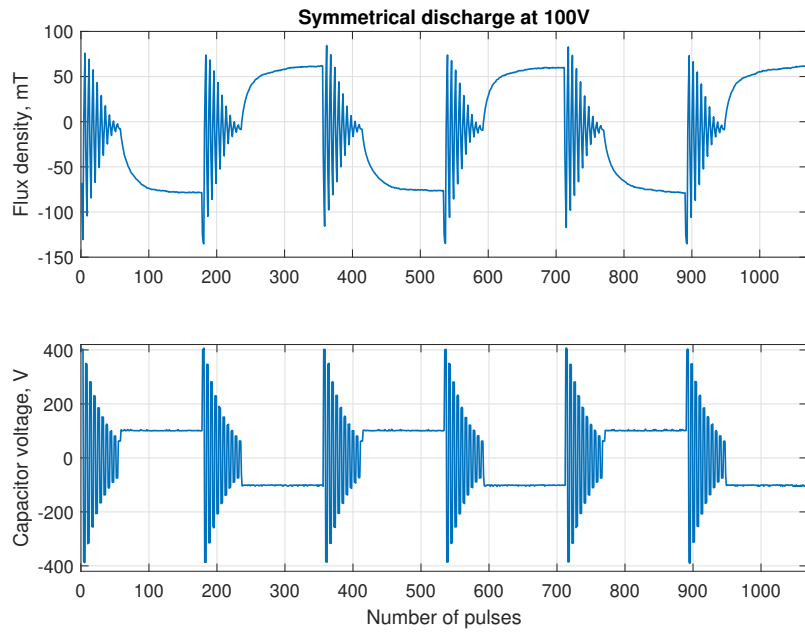
shown in Fig. 3.36. If the demagnetization starts when the magnet has positive measured flux density, the overall profile leans to the positive side, and vice versa.

Note that from Fig. 3.35a, the flux density after the demagnetization process does not fall on the zero line, which indicates a significant residual induction and will generate a residual dipole moment. This could be fixed by tuning the demagnetization voltage profile and shifting the voltage towards the positive direction. Fine tuning of the demagnetization voltage profile is crucial and will be carefully studied in future research.

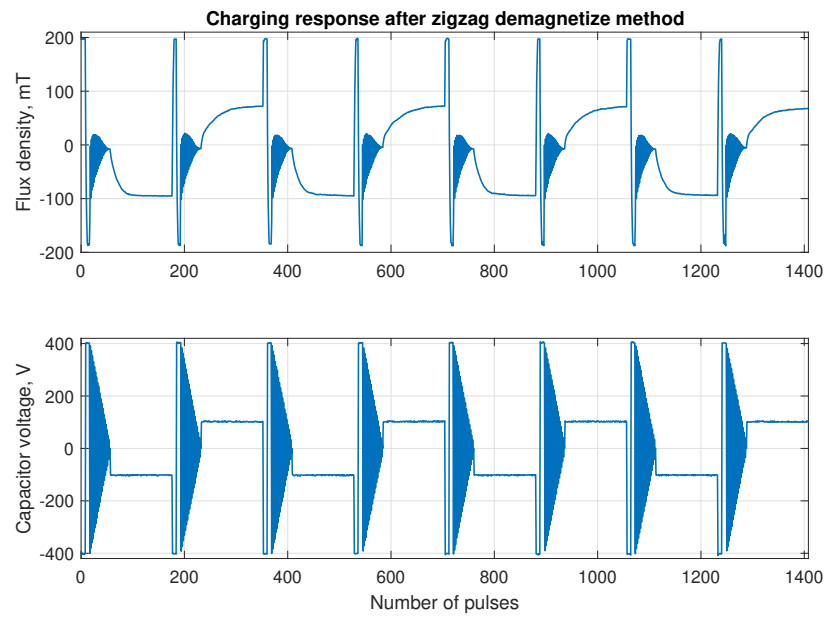
3.2.4.5 Discharge profile

The voltage and current trace details for each pulse are of interest and shall be investigated as part of validating the design parameters. Since the time for each pulse is within hundreds of microseconds, which is hard to be captured by the Arduino Uno due to the limited analog-to-digital (ADC) channel sampling frequency and system resources, and it is hard to visualize the response using a single microcontroller, the oscilloscope is used to capture and plot the details of the pulse. Direct measurement of the discharge current is tough, especially for this pulsed discharge circuit. Any inline resistance will affect the final current profile, and non-contact measurement devices are too big for such a small device. Therefore the capacitor voltage is measured instead, and the current profile is then recovered by curve fitting the captured voltage history to the relevant equation derived from the RLC circuit.

The current for the underdamped RLC circuit is described in equation (3.15) as discussed in section 3.2.2.2. According to the equation, to plot the current trace, the initial voltage V_0 , parameters $(\alpha \ \omega_o \ \omega_d)$ calculated from series resistance, inductance, and capacitance shall be determined. The capacitance can be measured directly using a multimeter. However, the inductance and resistance are hard to be measured directly as they are related to the opening characteristics of the H-bridges gate thyristors. To obtain these two parameters, the measured voltage trace is curve fitted to the equation (3.29) below using MATLAB Curve fitting function.



(A) Alternating discharge direction at 100 V capacitor voltage after exponentially decreasing capacitor voltage in demagnetization.



(B) Alternating discharge direction at 100 V capacitor voltage after linearly decreasing capacitor voltage demagnetization.

FIGURE 3.35. Charging response after different demagnetization profiles.

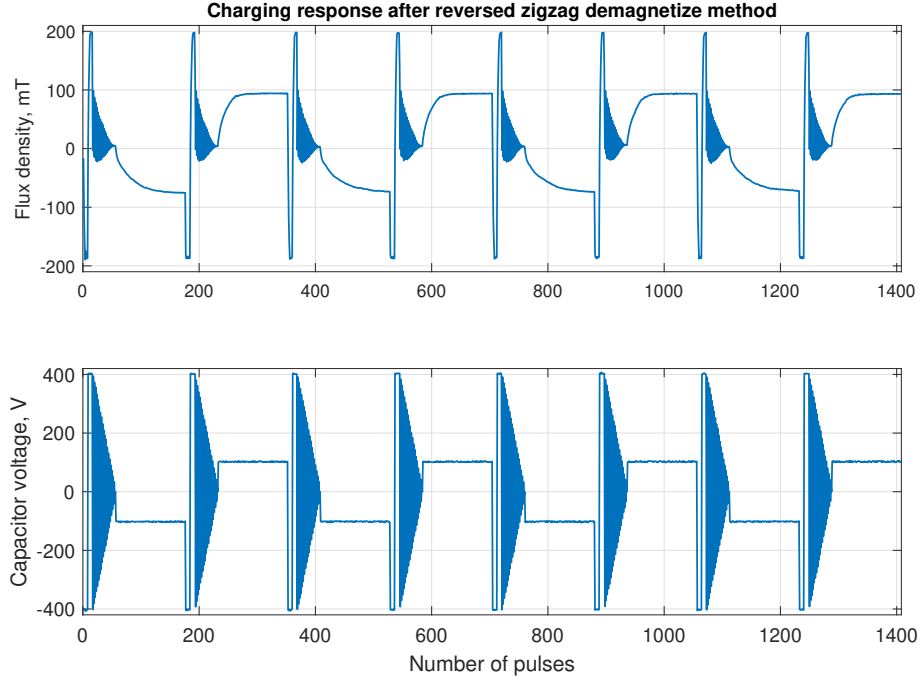


FIGURE 3.36. Alternating discharge direction at 100 V capacitor voltage after linearly decreasing capacitor voltage demagnetization with different pre-demagnetize torque rod status.

$$\begin{aligned}
 V_c &= \frac{1}{C} \int i dt \\
 &= -\frac{1}{C} \int \frac{V_0}{\omega_d L} e^{-\alpha t} \sin \omega_d t dt \\
 &= -\frac{V_0}{\omega_d L C} \cdot \frac{1}{1 + \alpha^2 \omega_d^2} \cdot [-\alpha e^{-\alpha t} \sin \omega_d t - \alpha^2 e^{-\alpha t} \omega_d \cos \omega_d t]
 \end{aligned} \tag{3.29}$$

After obtaining the inductance and resistance through curve fitting, the discharge current profile can be plotted by substituting all the parameters into the eq. (3.15). Fig. 3.37 shows a typical capacitor voltage trace and corresponding fitted current profile. The voltage spike at the beginning of the voltage trace could be caused by the noise generated by the pulse signal to the H-bridge.

The maximum discharge current can be found by substituting the fitted parameters into the equation (3.17). Voltage traces for a sequence of 10 pulses changing the magnetization

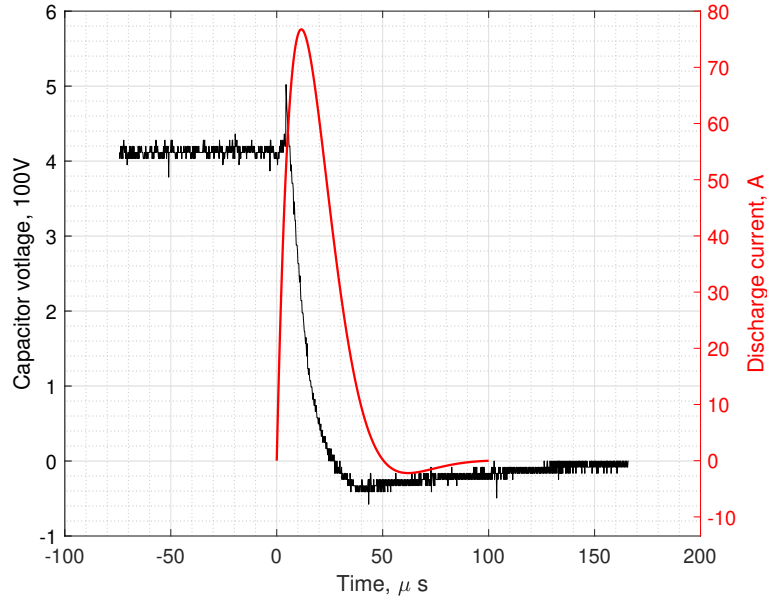


FIGURE 3.37. Measured discharge voltage trace and the fitted discharge current for a pulse at 400 V capacitor voltage.

direction of the torque rod is gathered. The peak current is calculated from the fitted parameters and is shown in Fig. 3.38.

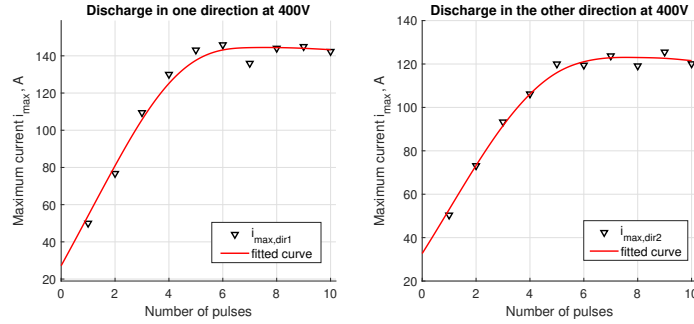


FIGURE 3.38. Maximum current i_{max} for continuous 10 pulses at 400 V capacitor voltage to charge the torque rod in one direction and the reversed direction.

From the figure, it can be observed that the peak current reaches a maximum value of around 140 A for charging in one direction and 120 A in the other direction from as low as around 50 A initial peak current for the first pulse. Although the initial peak current conforms to the estimation at the end of the section 3.2.2.2, the upcoming peak current increases with the increasing number of pulses. Since no obvious temperature change is

observed for each component, the capacitance and resistance of the discharge circuit cannot be changed. Therefore the only parameter that is changing is the inductance. Suppose the applied excitation field direction is opposite to the torque rod current magnetization direction. In that case, the torque rod solenoid has its maximum inductance, reducing the peak discharge current, according to Fig. 3.17. Once the magnetization direction of the torque rod is changed and complies with the external field direction, the equivalent inductance reduces, yielding a higher peak current. Once the torque rod reaches its maximum magnetization, the inductance remains unchanged. Therefore the peak current i_{max} will not change after several pulses. This phenomenon, in addition, can be used to determine if the torque rod reaches the maximum magnetization for a certain capacitor voltage. Let the microcontroller record the voltage signal at maximum speed and extract the peak current data from the recorded voltage signal. Suppose the calculated i_{max} remains unchanged after several pulses or reaches a certain pre-defined value. In that case, the magnet can be regarded as fully charged, and the charging program can be halted. This method provides a more accurate way to control the dipole moment of the torque rod, as the saturated magnetization for different capacitor voltage and the dipole moment corresponding to a different magnetization level can be accurately measured and calibrated in the laboratory. The only thing the onboard microcontroller should do is to ensure that the desired saturated magnetization is reached for different capacitor voltages. This method reduces the use of the hall sensor, which reduces the complexity of both hardware and software, as the hall sensor is a source of noise, and intensive filtering and calculation are required to remove the noise. In addition, as mentioned before, the hall sensor installation highly affects the reading of the magnetic flux density measurement. This method eliminates the dependency of the torque rod density measurement on the installation error, providing higher reliability for the whole system. However, the intensive and comprehensive calibration shall be carefully performed before using this control method, which is hard for a University-level laboratory.

3.2.5 Conclusion

In conclusion, the proposed EPM is designed and experimentally tested. The AlNiCo 5 is selected to be used as the torque rod material due to the high residual induction and low coercive force. The basic control logic is to charge the main energy storage capacitor and then discharge the energy into the torque rod solenoid to generate a short high current pulse to change the magnetization of the torque rod. The charging direction is controlled by the H-bridge, which consists of four thyristors, controlled directly by the microcontroller. The main capacitor is chosen to be a capacitor array consisting of four multi-layer ceramic capacitors (model: C5750X6S2W225K250KA) with a total capacitance of $8.8 \mu\text{F}$ that can withstand a maximum of 450 V. The "LT3750" capacitor charging IC made by Analog Devices with the required peripherals is selected as the capacitor charging module. The capacitor voltage and torque rod status are monitored using a voltage divider and hall sensor as the feedback signal to the controller. The optimal torque rod solenoid and torque rod shape are analyzed. Due to the ease of manufacture and overall weight consideration, the sub-optimal configuration is used for the current EPM built in this thesis. The optimal design will be tested in future development projects. The functionality of the EPM is tested, and the relationship between capacitor voltage, number of pulses, and torque rod magnetic flux density is investigated experimentally. It is found that the saturated flux density of the torque rod is related to the capacitor voltage, and the higher the capacitor voltage will result in a shorter time to reach saturation. The discharge voltage and current are measured and calculated. A new method of controlling the EPM is proposed using only the capacitor voltage measurement and a well-calibrated torque rod. This new method is not investigated deeply in this thesis and will be a good direction in future research. The proposed EPM can be magnetized in either direction with pulses of current from a charged capacitor bank, and it can be "turned off" by passing an alternating current with reducing magnitude into the magnet. Compared with conventional magnetorquer, the EPM proposed in this thesis can generate a significantly stronger dipole moment with a small amount of energy, and it can maintain the dipole moment without consuming energy. In addition, the time required to adjust the dipole moment is in milliseconds scale, which adds advantages to the controllability of the system.

3.3 Performance measurement

In this section, the performance of the EPM for satellite attitude control will be experimentally evaluated. Firstly the experiment equipment will be introduced and described in detail, including the Helmholtz cage, which is used to generate a controllable and uniform magnetic field, and the Air-Bearing Table (ABT), which is a test platform that can rotate freely in three axes within a certain boundary with minimal friction. Secondly, the EPM dipole moment measurement methodology, which is mentioned and used to measure the dipole moment of the bar magnets with different shape parameters in section 3.2.3.2, is introduced in detail. Then the detumbling performance of using the EPM and B-dot algorithm is introduced, followed by a simple controller design to demonstrate the controllability and pointing accuracy of the EPM. Finally, the overall performance of the EPM is summarized with future development and optimization direction pointed out.

3.3.1 Helmholtz cage

Helmholtz cage is a device that can generate a uniform artificial magnetic field in a small area. It is widely used in the space industry to test the satellite's attitude determination and control system (ADCS) in the desired magnetic field environment [55, 120, 22, 94]. It generally consists of three orthogonal pairs of coils in either square or round shape to generate a magnetic field in X, Y, and Z directions. General usage of the Helmholtz cage is generating the magnetic field counteracting with the Earth's magnetic field to generate a "zero field" area in the center of the cage and then adjusting the field strength in three axes to create the magnetic field with desired strength and direction in that small area. A small Helmholtz cage is designed and made in-house to test the performance of the EPM in terms of detumbling and pointing. The basic theory, design consideration, and calibration method will be introduced in this section.

3.3.1.1 Basic theory

The core of the Helmholtz cage is three pairs of magnetic coils placed in parallel, with each pair of the coil generating a magnetic field in one direction. The basic theory behind the coil is the Biot-Savart Law, which treats the magnetic field as a result of the electric current, and is represented below:

$$d\vec{B} = \frac{\mu_0 I d\vec{L} \times \vec{r}}{4\pi r^2} \quad (3.30)$$

where $d\vec{L}$ is the infinitesimal length of conductor carrying electric current I , and \vec{r} is the unit vector to specify the direction of the vector distance r from the current to the field point [19]. For a magnetic coil, the magnetic field at any point inside the coil can be found by integrating the length and current of the copper wire winding to that point. Consider two square-shaped parallel placed coils separated by h are placed along a center axis, and each coil has a side length of $2a$, as shown in Fig. 3.39, Alvarez, A.F.R *et al.* and Ghaly, S.M.A *et al.* calculated that the magnetic flux density at the point on the symmetric axis at a distance z from the center point O of the two coils could be expressed as [12, 43]:

$$B(z) = \frac{2\mu_0 N I a^2}{\pi} * \left[\frac{1}{\left(a^2 + \left(z + \frac{h}{2}\right)^2\right) \sqrt{2a^2 + \left(z + \frac{h}{2}\right)^2}} + \frac{1}{\left(a^2 + \left(z - \frac{h}{2}\right)^2\right) \sqrt{2a^2 + \left(z - \frac{h}{2}\right)^2}} \right] \quad (3.31)$$

According to [43], the square coil can provide a wider uniform area than the circular coil. Considering the difficulty of manufacturing, the Helmholtz cage is designed to use square shaped coil.

3.3.1.2 Cage design and development

The main objective of the Helmholtz cage is to cancel out the Earth's magnetic field and generate the desired magnetic field in the test region. Due to the small size of the EPM and

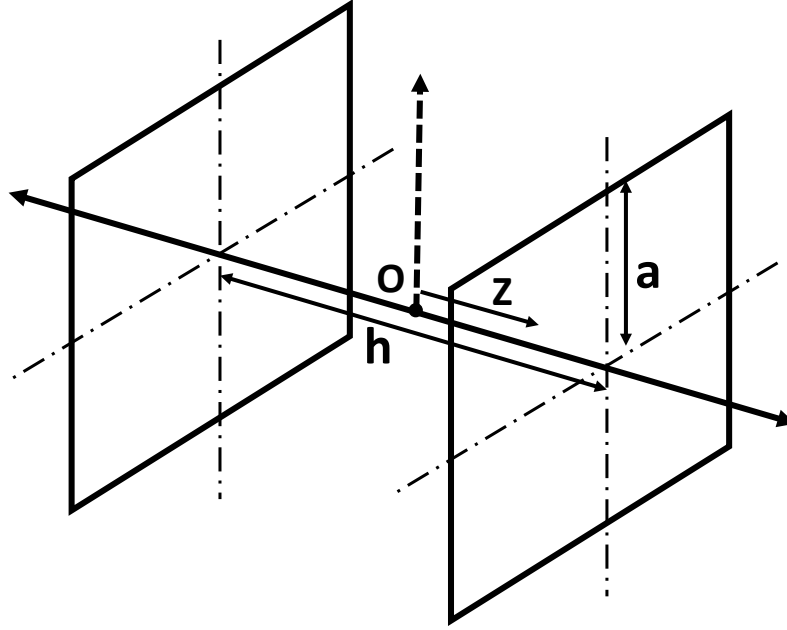


FIGURE 3.39. Square shaped Helmholtz coil configuration.

the Air-Bearing Table, the preliminary design parameter is estimated to build a cage with an cubic area with side length of 0.5m. It should be able to generate double the magnitude of the local Earth's magnetic field to ensure that the natural field can be reversed in the worst case. Therefore, the side length of each square coil is set to 0.5 m for calculation. The Earth magnetic field strength in Sydney is 57064.6 nT ($\sim 57.064 \mu\text{T}$) with a declination of $+12^\circ 45'$ and inclination of $64^\circ 24'$ [36]. To achieve the design requirements, based on the calculation from equation (3.31), each square coil shall have 20 turns of AWG 20 copper wires with maximum 2000 mA current to generate a center field of strength $\sim 130.304 \mu\text{T}$, which is slightly higher than the double of the Earth's magnetic field strength. Due to the overlapping of three orthogonal coil pairs, the actual side length of each coil has some offset, and the actual field strength will be measured and calibrated in the later section.

The side length and number of turns is determined to generate the desired magnetic field strength. However, the separation between the coils determines the uniformity of the magnetic field in the center area. To achieve a complete uniform magnetic field inside the center area, the equation (3.31) shall meet the requirement that:

$$\frac{\partial^2 B_z}{\partial z^2}(0) = 0 \quad (3.32)$$

Solving the above equation yields an equation relate the h to a :

$$\frac{h}{2} = 0.5445 * a \quad (3.33)$$

where the 0.5445 is the separation coefficient. For the Helmholtz coil pair configured following the design parameters described in the first paragraph, when the coil separation h and the side length $2a$ meet the above equation, assume a 1 A supplied current, the magnetic flux density along the center axis of the coil pair is shown in Fig 3.40.

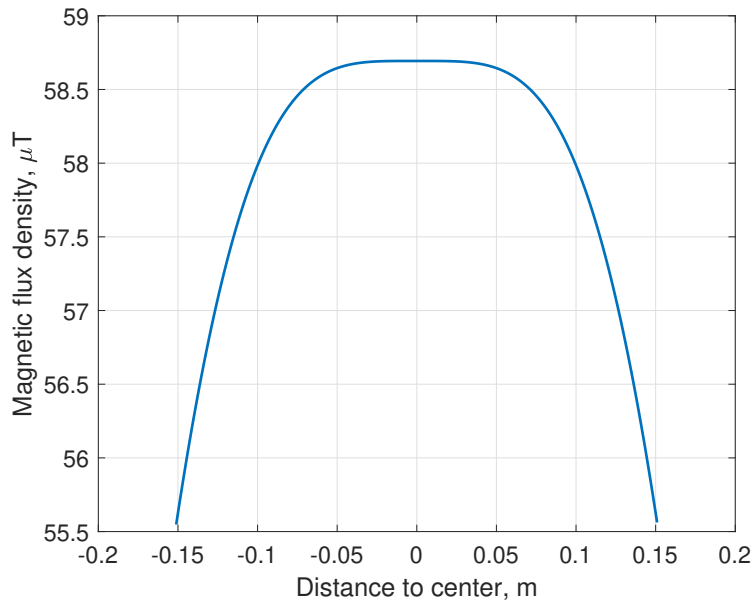


FIGURE 3.40. Magnetic flux density along the center axis of the two square Helmholtz coil.

The figure shows that the magnetic field strength is flat and uniform within around ± 0.05 m region at the center area. However, with this coil separation configuration, only around 10 cm diameter area has a uniform magnetic field. Beyond the region, the field deforms and decays fast. Making a larger cage can obviously solve this problem. However, the amount of copper and electric current increases with a larger coil, making it hard to manufacture. Another

solution is to increase the separation between the coil, which will destroy the magnetic field uniformity inside the center area, but only within a few percentages, which is acceptable for the practical experiment and will be measured to obtain the real value later. Therefore the separation coefficient in equation (3.33) is increased to 0.598, which results in an updated figure in Fig. 3.40, as shown in Fig. 3.41.

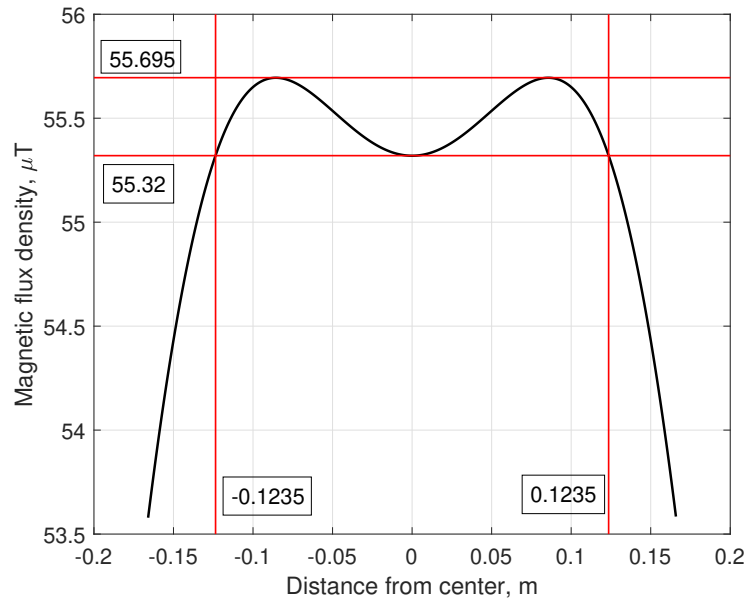


FIGURE 3.41. Magnetic flux density along the center axis of the two square Helmholtz coil with adjusted separation coefficient.

From the Fig. 3.41, the diameter of the area of interest increases to 24.7 cm, which is more than double the uniform configuration. Although the field becomes non-uniform, the field strength variation is only 0.34%, which is acceptable.

To manufacture the cage, the "C" section aluminum extrusion beam with a cross-sectional side length of 10×10 cm is selected as the main material to provide the structural stiffness and the base for the winding of the copper wire. Three coil pairs are installed concentrically, and each pair are offset toward the bigger size to ensure they are installed and tightly touching each other. For ease of connection, beams are connected through laser-cut acrylic sheets to form the corner of the coil. The overlapping joint between coils is fastened through 3D-printed brackets to ensure they are firmly attached and orthogonal. The whole cage is installed on a unique customized table and lifted through four PVC pipes. The nylon screws, bolts, and

nuts are used throughout the manufacturing of the cage, and the whole cage and table are made with non-ferromagnetic materials to avoid the distortion of the magnetic field. A spacer carefully controls the separation between the coil pairs with a length calculated from the actual side length of the coil. The completed outlook of the cage is shown in Fig. 3.42.

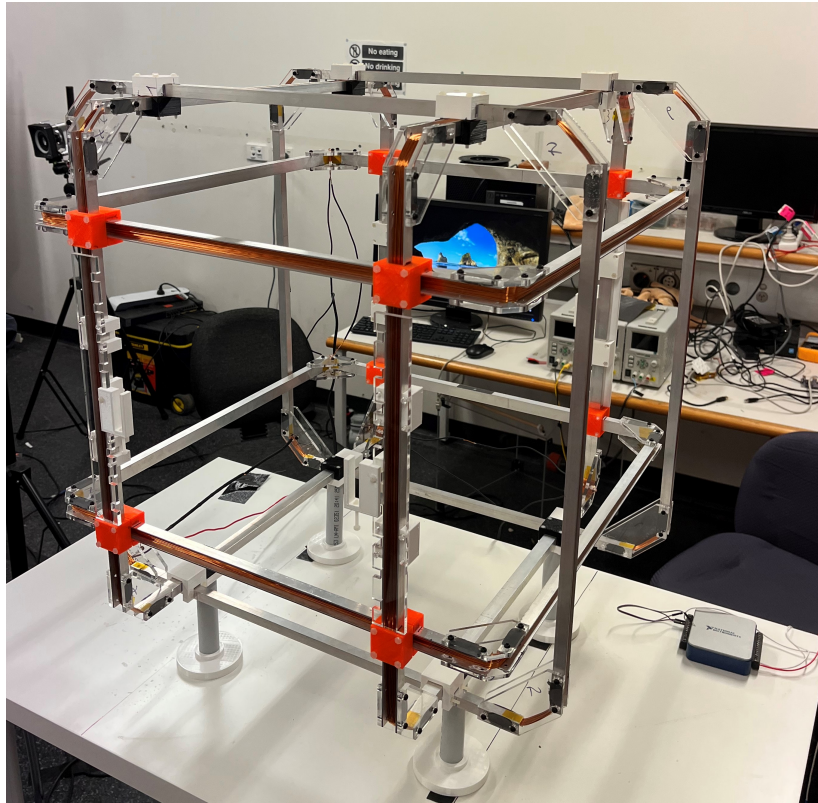


FIGURE 3.42. Photo of the completed Helmholtz cage.

The cage is powered by three individual benchtop power supplies made by Multicomp Pro (model MP710086) that can deliver a maximum of 30 V at 5 A. The power supply can be controlled by MATLAB through Standard Commands for Programmable Instruments (SCPI) commands to perform some orbit simulations. Each power supply controls a pair of coils for each axis through a customized H-bridge. Since the power supply can only generate a positive voltage bias, an H-bridge is required to switch the direction of the current, therefore switching the magnetic field direction. The H-bridge is made with three mechanical relay features a bi-stable coil, that a single pulse current can toggle the relay, and no power is required to hold the relay state until the next switch. The schematic of the Helmholtz H-bridge is shown in Fig. 3.43. This relay is controlled by another Arduino Uno, which is controlled

by MATLAB. Therefore the magnetic field strength and direction can be fully controlled by a single MATLAB code to simulate the orbital magnetic field environment and verify the ADCS system.

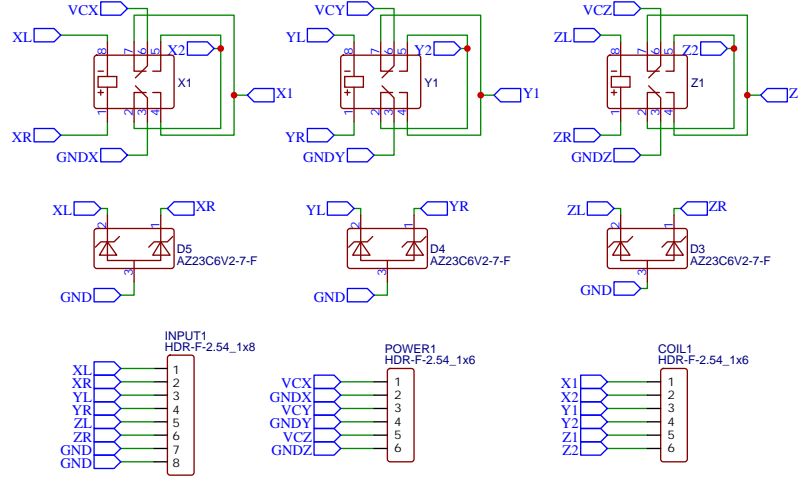


FIGURE 3.43. Schematic of the H-bridge used for Helmholtz Cage direction control.

3.3.1.3 Calibration and verification

As an in-house designed and manufactured device, the Helmholtz cage must be carefully calibrated before being used to test the EPM. Since only the center area is of interest, the calibration was performed only in the middle plane of the Helmholtz cage. An acrylic plate with mounting holes distributed as 9×9 matrix is made using a laser cutter and placed in the median plane of the Helmholtz cage. The mounting hole matrix is separated by 30 mm each and is used to position the magnetometer. The industry level 9 degree of freedom (DoF) inertia measurement unit (IMU) (Model: ADIS16405) made by Analog Devices is utilized to measure the three-axis magnetic field strength in the middle plane. The magnetometer is placed in multiple locations according to the mounting holes to measure the field strength at different locations. The measured three-axis magnetic field strength in the plane can be plotted to ensure the desired uniformity and symmetry are met. Note that the acrylic plate is placed on one coil pair with adjustable height capability. This ensures that the IMU is located within the plane where the EPM will be put in for measurements and experiments. The measurement configuration is shown in Fig. 3.44.

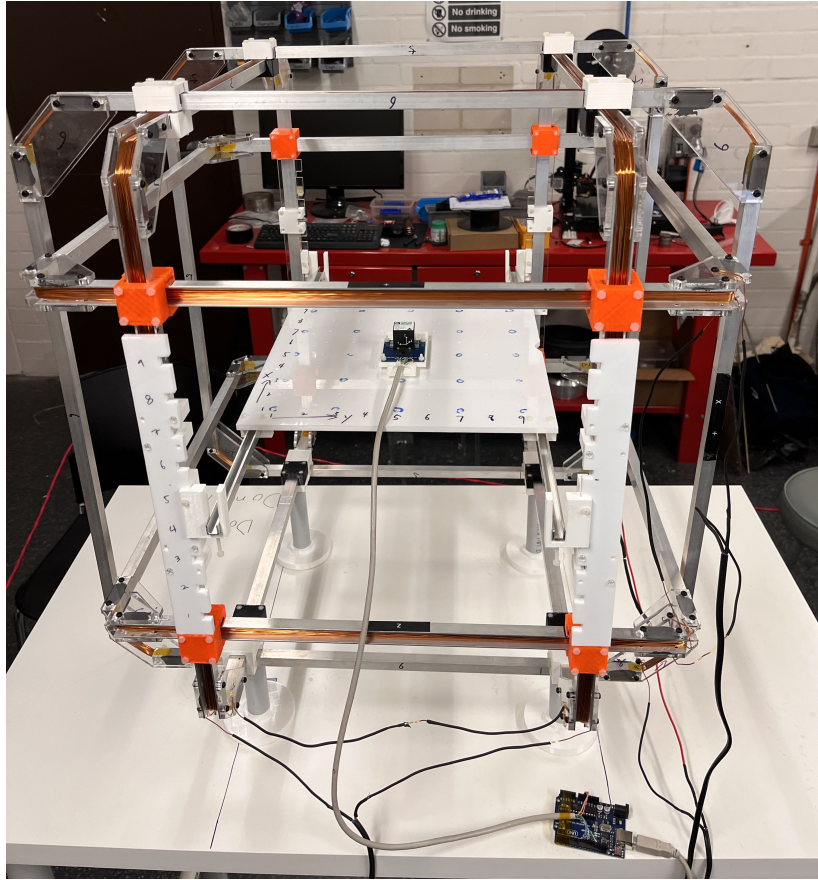


FIGURE 3.44. Configuration of calibration device for the Helmholtz cage.

Before calibration, the IMU, especially the magnetometer, shall be calibrated to eliminate soft and hard iron distortion. The magnetic field measurement result of a magnetometer on a 2-D plane without any distortion should produce the plot shown in Fig. 3.45a. However, the results will differ in the presence of hard iron and soft iron distortion. The hard iron distortion is generally caused by materials that can generate a constant and additive magnetic field so that the measured Earth's magnetic field on either axis equals the sum of true Earth's magnetic field plus the field produced by that material. This will result in a biased plot, as shown in Fig. 3.45b. Soft iron distortion is generally caused by the soft magnetic material, which can reinforce and concentrate the magnetic field in a certain direction, distorting the shape of the magnetic field. The effect of the soft iron distortion is shown in Fig. 3.45c.

For 3-D, the above circular measurement result turns into a spherical plot. The result without distortion will produce a sphere centered at zero. Similar to the 2-D case, the hard iron

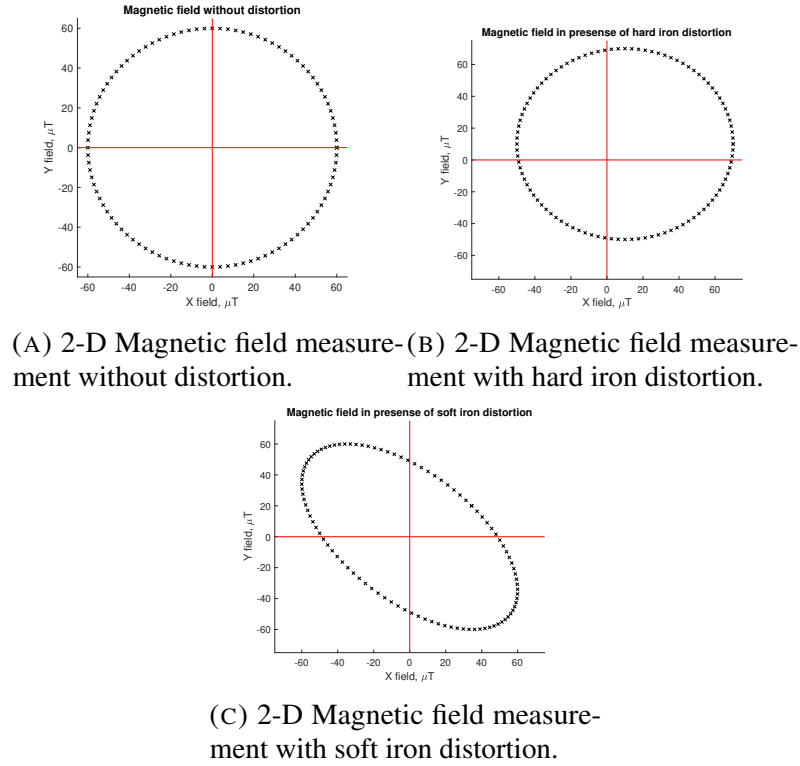


FIGURE 3.45. 2-D magnetic field measurement results under different types of distortion.

distortion will bias the center of the sphere, and soft iron will stretch the sphere into an ellipsoid. The magnetometer is calibrated using the built-in hard and soft iron calibration process and moved randomly inside the test area. The result is shown in Fig. 3.46. The figure shows that the magnetometer is greatly calibrated since the data points on all three orthogonal planes form three circles and the aforementioned distortion is not observed from the results, which indicates that neither soft nor hard iron distortion exists in the Helmholtz test area.

The magnetometer is placed at the center point of the mounting hole matrix, and the cage is tuned to zero the magnetometer's three-axis readings. Then the magnetometer is placed at each point of the matrix to record 1000 sets of the data. The average of this data will be used to represent the three-axis magnetic field reading at the corresponding measurement point. The magnitude of the magnetic field measured at each data point is then used to represent the total magnetic field strength at that point. The measurement of the natural magnetic field strength on the middle plane inside the Helmholtz cage is shown in Fig. 3.47 and the field

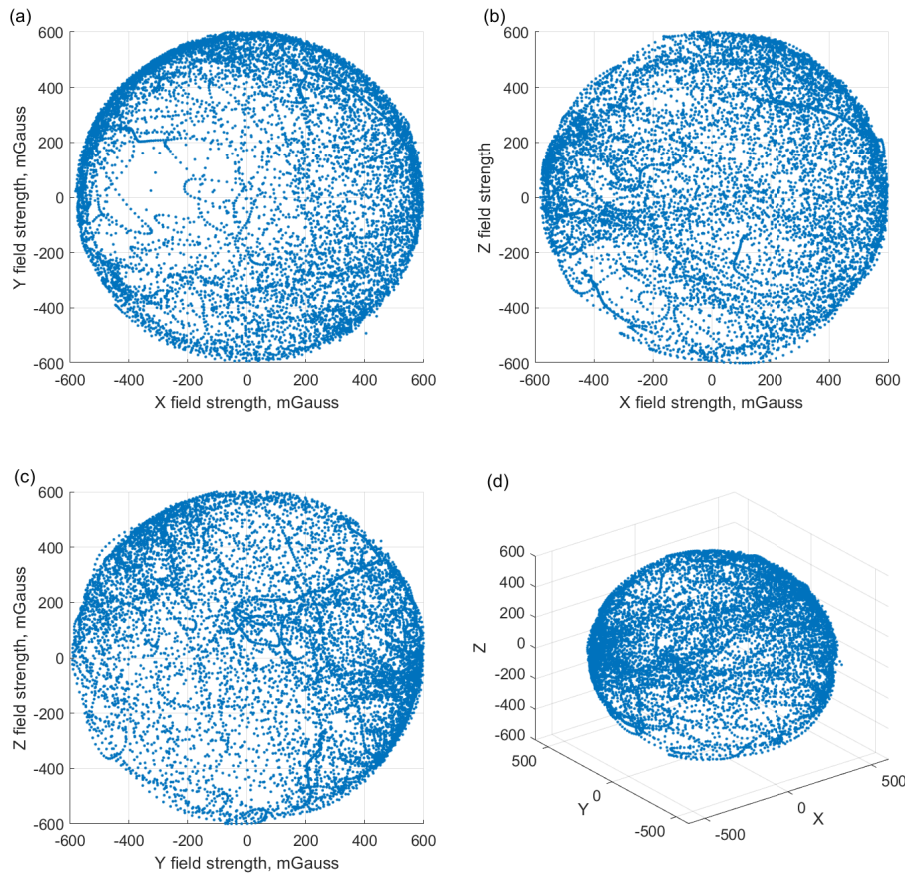


FIGURE 3.46. Calibration results for different planes and overall sphere plot.

strength at the same plane after the cancellation of the Earth's magnetic field is shown in Fig. 3.48.

From the figures, the Helmholtz cage can effectively neutralize the Earth's magnetic field, and the field inside the area of 100×100 mm at the center is exceptionally uniform. The overall field decay at the edge of the 240×240 mm area is only $6 \mu\text{T}$.

After the uniformity verification, the performance and characteristics of the Helmholtz cage shall be determined. According to equation (3.31), if the shape parameters are fixed, the field at the center of the coil pair is a function of current I , which can be simplified into the following equation:

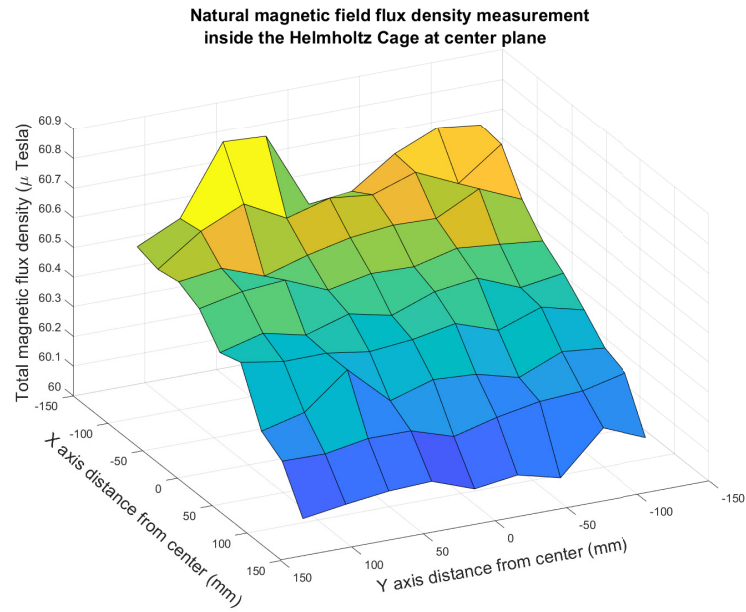


FIGURE 3.47. Natural magnetic field measurement in the middle plane of the Helmholtz cage.

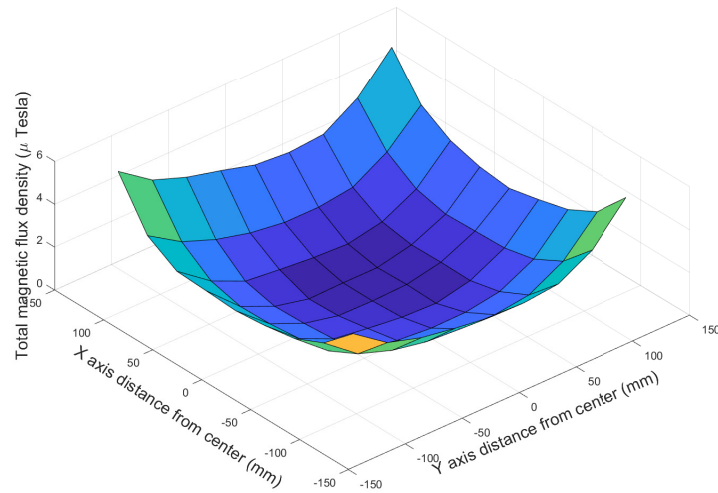


FIGURE 3.48. Magnetic field measurement in the middle plane after the cancellation of the Earth's magnetic field.

$$B(0) = \Phi I \quad (3.34)$$

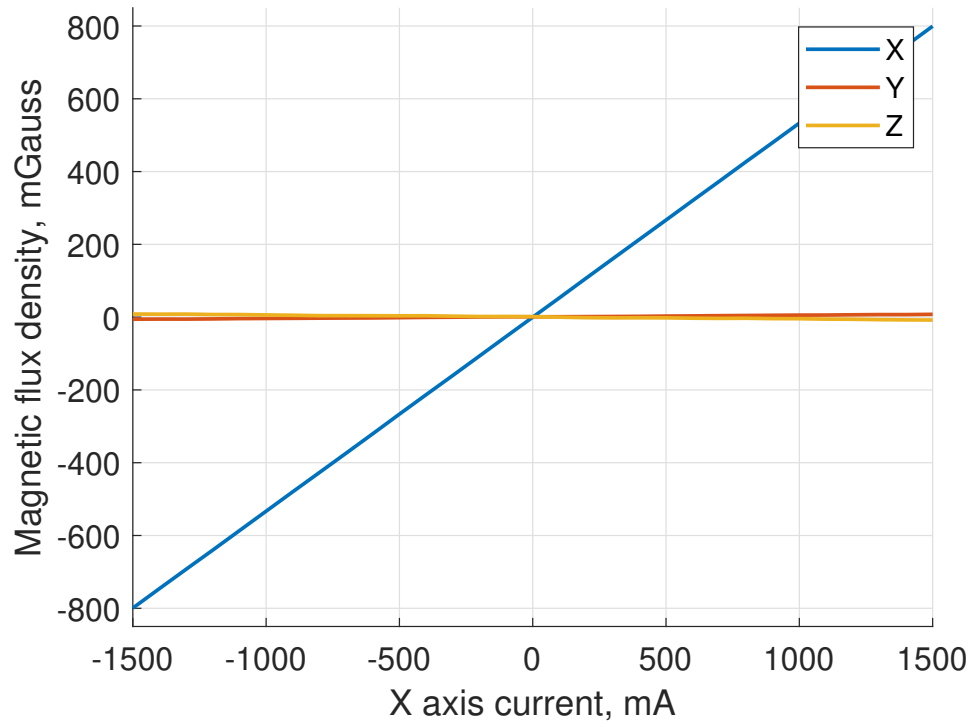
where Φ is the amplification coefficient determined by the size and separation between coils. To measure the Φ for each axis, the magnetometer is positioned in the center of the cage using the aforementioned acrylic measurement jig. Then the electric current for each axis is adjusted in both incremental and decremental directions. At each supplied current, the magnetic field strength measurement on three axes is recorded and plotted. Then the slope of the plotted line is the desired amplification coefficient. This method can also examine the orthogonality between the perpendicular coil pairs. If the two coils are not perpendicular, increasing one axis's current will induce a magnetic field in another axis. For the experiment, the current for each axis is increased from -1500 mA to 1500 mA with a 100 mA step increment. The result for each axis is plotted in Fig. 5.10.

From Fig. 3.49a, the Y axis magnetic field reading increases with the X axis current, indicating that the X and Y axis coils are not well perpendicular to each other. This can be confirmed from Fig. 3.49b that the X axis moves with Y axis current. However, Z-axis coils are well orthogonal to X and Y, which can be seen in the figure. 3.49c, that increasing Z axis current causes a negligible change in either X or Y axis magnetic field reading.

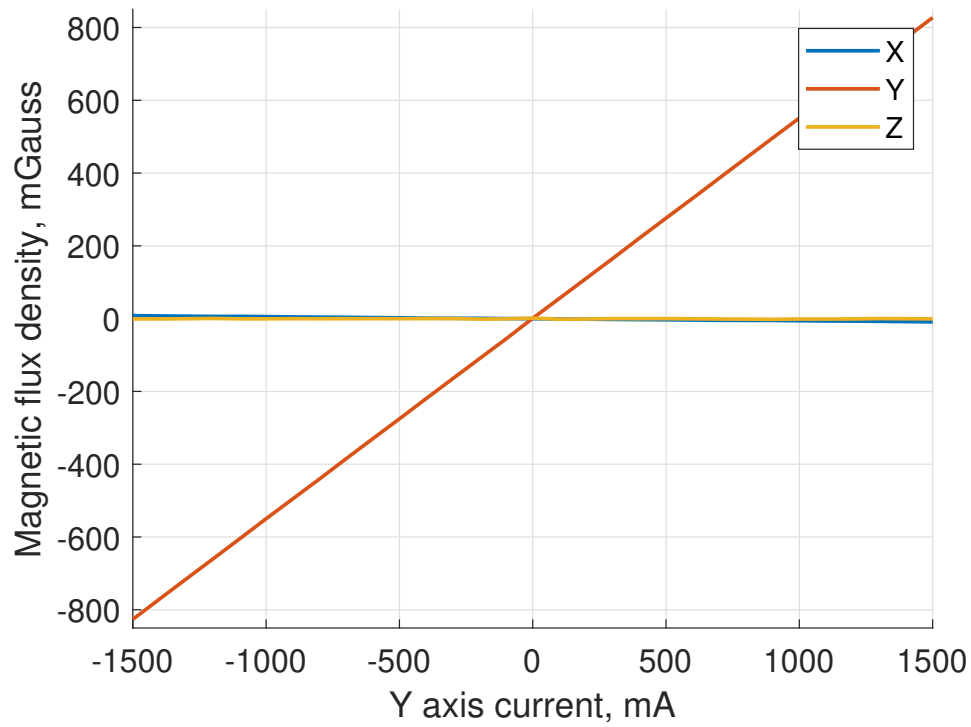
The slope of each axis is obtained from the curve fitting function, and the amplification coefficient Φ with R^2 for each axis is concluded in table 3.3. Note that the Φ is not equal for the three axes. Since the coefficient Φ is a function of coil side length and separation, coils for three axes differ in size to ensure the concentric installation. The Y coil pairs are the smallest ones and are installed in the innermost layer, which results in the highest Φ , and Z coil pairs are the largest in side length and are installed in the outer layer, which results in the smallest Φ .

TABLE 3.3. Curve fitting results and fitted amplification coefficient Φ for each axis.

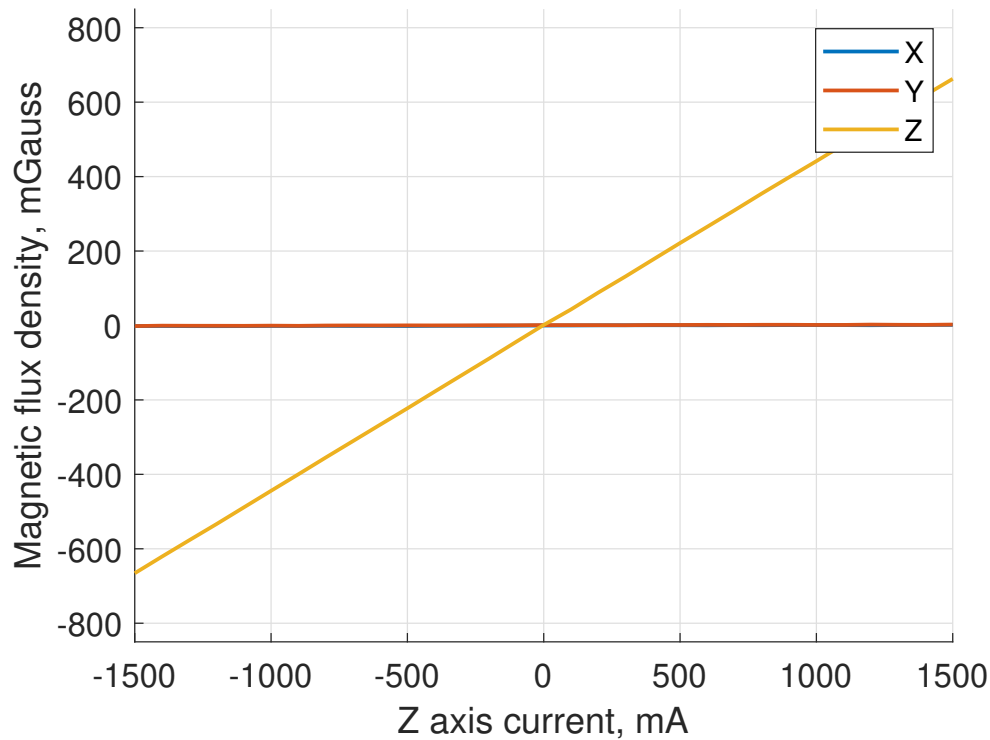
Fitted equation:	$f(x) = p1 * x + p2$			
Axis	p1	p2	R^2	Φ (Gauss/A)
X	0.5331	-0.01658	>0.9999	0.5331
Y	0.5509	0.471	>0.9999	0.5509
Z	0.443	-0.7702	>0.9999	0.443



(A) 3-Axis magnetic flux density measurement with increasing X axis current.



(B) 3-Axis magnetic flux density measurement with increasing Y axis current.



(C) 3-Axis magnetic flux density measurement with increasing Z axis current.

FIGURE 3.49. 3-Axis magnetic flux density measurement with an increasing current in different axis.

3.3.2 Air bearing table

When the satellite is in orbit, the total force acting on it reaches equilibrium, making it "floating" in space. In this state, a small force can change the satellite's attitude, following Newton's law of motion. However, due to the gravity, air drag, friction between materials, and various source of disturbance, it is hard to simulate the orbital dynamical condition. One common method is the aerodynamic bearing, also called air bearing. A customized air bearing table (ABT) with an innovative center of mass adjustment technique is made to test the performance of the EPM and to perform detumbling and pointing experiments. The details of the ABT will be introduced in this section.

3.3.2.1 Basic theory

The biggest problem of simulating the dynamic orbital environment is removing the friction and providing as much degree of freedom as possible to the satellite. However, any solid body requires support to stand on the floor to overcome gravity, which will introduce friction between two solid objects. One method to reduce this contact friction is to lift the object with air, similar to air hockey, to remove the direct contact between two solid objects. In this case, the major source of the friction will become the viscosity of the air and aerodynamic drag force, which is orders of magnitude smaller than the friction caused by the relative movement between solid objects. The basic working principle is illustrated in Fig. 3.50.

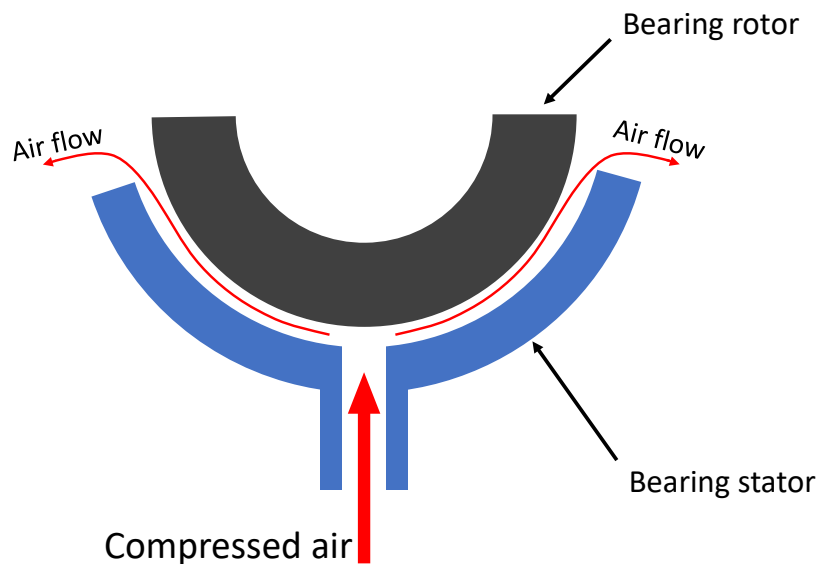


FIGURE 3.50. Working principle of the air bearing.

By using a carefully designed platform and mounting base, if the center of gravity is well below the center of rotation, the system will be stable and can rotate freely along the axis pointing in the same direction of gravity. If the center of mass is carefully adjusted to coincide with the center of rotation, then the platform will reach a critical balance state, that the platform can rotate freely on both axes. In this state, the system can simulate the orbital dynamics in three-axis rotation to test the attitude determination and control system.

3.3.2.2 Table design and development

Traditional ABTs are fixed and for testing ADCS only. Once the location is fixed and the weight of the mass is added to the point that the center of gravity is close to the center of rotation, the table is balanced and can rotate freely on three axes. This method is effective but less efficient, requiring intensive human power. When the center of the mass is close enough to the center of the rotation, the system is extremely sensitive, and a tiny mass movement will cause a huge change to the equilibrium state. To overcome the difficulty of balancing the ABT, a new mechanical structure is designed to make the balancing process easier and can be done automatically. Since the center of rotation is fixed, instead of adding extra mass to adjust the center of mass, a bi-directional linear stage is mounted on the air bearing, and the rest of the table structure is installed on the stage. Therefore when the payload and peripherals are installed, the linear stage can move the entire table to adjust the center of mass. The linear stage is driven through two NEMA 8-size stepper motor, which has 1.8° step size (200 steps/revolution). Using the stepper motor with an M5 lead screw can achieve $4\text{ }\mu\text{m}$ linear movement per step. Additional mass adjustment can be added if this stepping size is not enough to achieve the desired balance. The table can also move on the vertical axis to achieve 3-axis mass balance. The vertical axis is driven by a stepper motor and four lead screws synchronized by a timing belt. The compressed air is controlled by a small solenoid valve controlled by an Arduino Uno, which is then controlled by the computer. The SolidWorks model of the assembled ABT is shown in Fig. 3.51.

The auto-balancing process is achieved following these steps:

- (1) Install the payload and peripherals, including wireless communication module, battery pack, and other driver circuits; make sure that the center of gravity is within the moving range of the linear stage;
- (2) Fix the loose cables and connectors, ensure there is not any moving part that can affect the center of mass;
- (3) Lower the table vertically, adjust the linear stage to achieve horizontal balance;
- (4) Open and close the solenoid to quickly detumble the table from oscillation;

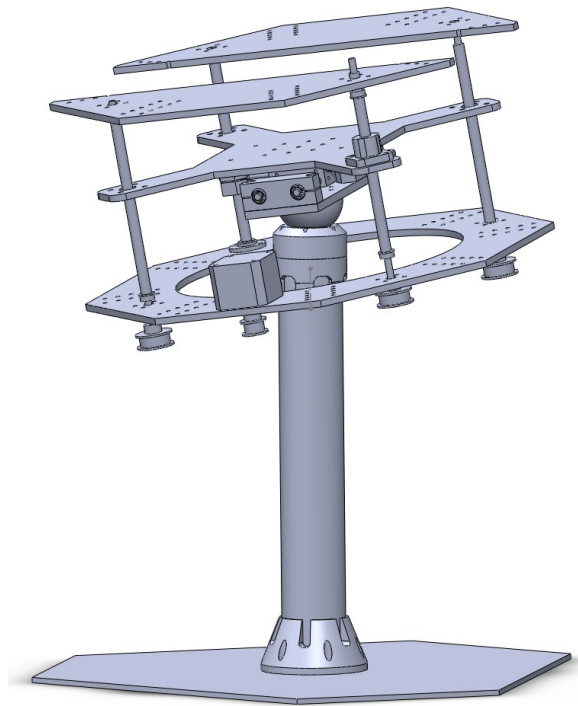


FIGURE 3.51. SolidWorks model of the designed ABT.

- (5) Lift the table vertically, adjust the linear stage to achieve horizontal balance using onboard IMU;
- (6) Repeat process (4) and (5) until the platform achieves the desired balance.

An inertia measurement device consists of three orthogonally installed EC 45 flat motors made by Maxon Motor with a known moment of inertia. After installing all the required modules and achieving the desired balance state, the 3-axis balance can be calculated using the conservation of angular momentum by turning on one motor at a time at a specified speed and monitoring the rotational speed of the whole system. The angular speed of the ABT is monitored using four motion tracking cameras made by OptiTrack. Only one horizontal axis magnetorquer is tested and utilized for the rest of the experiments, and the ABT is only balanced horizontally. 3-axis balance and control will be performed in the future project. The horizontal balance of the table is achieved through a bullseye bubble level installed parallel to the table surface. After installing all the required systems, the balance can be achieved by adjusting the position of the counterweight until the bubble stabilizes at the center of the

level. Although the level of balance cannot be quantified due to the lack of high accuracy digital level, the error is within several degrees, which is considered negligible. In addition, the parameter of interest in this thesis is the torque applied on the horizontal EPM, which is in the direction along with the vertical axis. A slightly tilted table will reduce the measured performance by the sine of the tilted angle. With small enough tilted angle, this performance reduction is considered negligible. Fig. 3.52 shows the complete setup of the ABT inside the Helmholtz cage with inertia measurement device, EPM, and reflect balls for OptiTrack installed. Note that the cage height is adjusted using PVC pipes to ensure that the EPM is positioned in the center of the cage, where the uniformity was measured and verified as described in the previous section.

3.3.3 Magnetic dipole moment measurement

The measurement methodology of the dipole moment, which is the most essential characteristic of the magnetorquer, will be introduced in this section.

Considering a mounted magnet that can rotate in a plane, the plane is filled with a uniform magnetic field. If the magnetic field direction is aligned with the plane, the magnet will try to align with the magnetic field according to its magnetization direction. Assuming the mounting mechanism is a thin string, then the dynamical model of the rotating magnet inside the uniform magnetic field can be expressed as:

$$I \cdot \ddot{\theta} = \tau_B + \tau_t \quad (3.35)$$

where the I is the moment of inertia of the magnet, θ is the angular displacement of the magnet, τ_B is the torque generated by the reaction between the magnet and magnetic field, and τ_t is the restoring torque from the string. The τ_t is neglected for the ABT as the disturbance from a balanced air bearing is too small compared with the torque generated by a magnet. For the measurement of the magnets with different sizes, as mentioned in section 3.2.3.2, the magnets are tied using a thin fish line, and the τ_t is represented as the restoring torque from the fish line. Considering the τ_t is orders of magnitude smaller than the τ_B ($\tau_t \ll \tau_B$), the τ_t

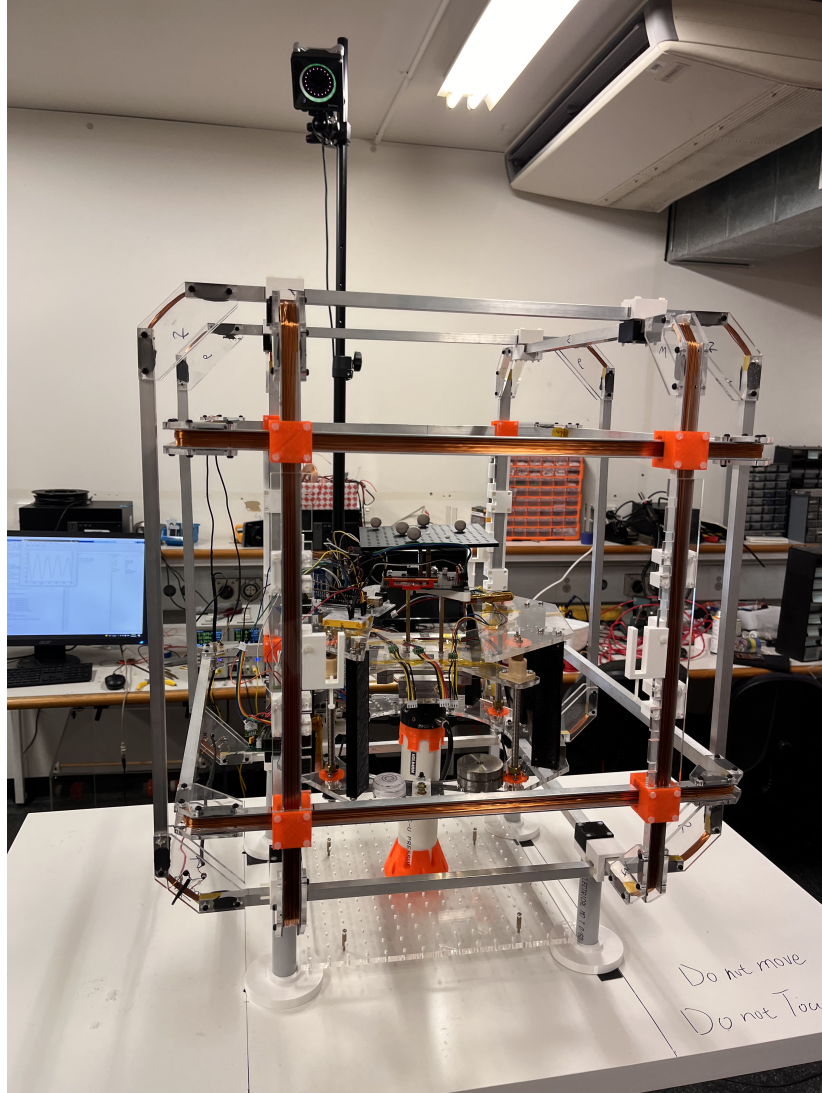


FIGURE 3.52. Complete setup of the ABT and EPM inside the Helmholtz Cage with OptiTrack camera.

is neglected as well. According to eq. (1.1), the τ_B can be represented by the production of dipole moment (m) and magnetic field flux density (B). For single axis rotation, the equation (3.35) can be written as:

$$I \cdot \ddot{\theta} = mB \sin \theta \quad (3.36)$$

Using small angle approximation, when $\theta < 15^\circ$, the $\sin \theta$ can be replaced by θ with around 1.1% error ($(\sin \pi/12 - \pi/12)/\sin \pi/12 \approx 1.1\%$). Then the above equation can be written as:

$$\ddot{\theta} = \frac{mB}{I}\theta \quad (3.37)$$

which is a simple harmonic oscillator with oscillation frequency f described by the following equation:

$$2\pi f = \sqrt{\frac{mB}{I}} \quad (3.38)$$

The magnetic flux density B in the above equation can be generated from the Helmholtz cage. Assuming the Y axis of the Helmholtz cage is used to generate the external magnetic field, then the B can be expressed as the equation mentioned in table 3.3. The above equation can then be expressed as:

$$f^2 = \frac{m}{4\pi^2 I} \cdot (0.5509i + 0.471) \quad (3.39)$$

where i is the Helmholtz cage Y axis driving current. Note that the equation (3.39) is a linear equation that describes the relationship between frequency square and the current. Therefore, by recording the oscillation frequency at different cage currents, the dipole moment can be calculated from the fitted slope of the data points.

The moment of inertia of the platform is also required to calculate the dipole moment. For the experiment configuration shown in Fig. 3.52, the inertia measurement device is used to measure the system inertia as mentioned in the previous section. The moment of inertia of the motor in the inertia measurement device is given in the manufacture data sheet: $I_{wheel} = 135 \text{ gcm}^2$. The motor-driver-embedded speed controller is used to set the spin speed accurately. After balancing the table and letting the table stabilize when the air bearing is turned on, turn on the motor and record the table's counter rotational speed using the OptiTrack. The table's

moment of inertia can then be calculated through the conservation of angular momentum. Only the horizontal EPM is tested using the ABT; therefore, only the angular momentum along the vertical axis is measured in this thesis. The momentum measurement of the table is summarized in table 3.4 below.

TABLE 3.4. Angular momentum measurement of the test platform along the vertical axis.

Item	Unit	Value
Inertia of the wheel	gcm^2	135
Speed of the wheel	rpm	2500
Speed of the wheel	$^\circ/\text{s}$	15000
Average speed of the table	$^\circ/\text{s}$	3.31
error (1σ)	$^\circ/\text{s}$	0.1086
Inertia of the table	kgm^2	0.061178248

For the dipole moment measurement of magnets with different radii and lengths mentioned in the section 3.2.3.2, the moment of inertia can be calculated using the equation:

$$I = \frac{1}{4}MR^2 + \frac{1}{12}ML^2 \quad (3.40)$$

where the R is the radius of the cylinder, M is the mass of the cylinder, and L is the length of the cylinder. The mass is measured using an analytical laboratory scale with a resolution of 100 μg . The mass and moment of inertia for the dipole moment measurement experiment mentioned in section 3.2.3.2 is listed in table 3.5.

The frequency measurement method is different for the EPM and magnet measurements, as mentioned in the section 3.2.3.2. For the measurement conducted on the ABT, the frequency data is obtained through the angle data from the OptiTrack. Firstly the steady state angle is obtained by turning on the EPM and air bearing and letting the system stabilize. Use the stabilized angle as the reference angle, and turn the table around 15° away from the reference angle to satisfy the small angle approximation. Once the table is detumbled, turn on the air bearing, then the table will oscillate around the reference angle. Due to the air drag force and

viscosity, the system forms a damped harmonic oscillator, and the system angle follows the below equation [32]:

$$\theta(t) = Ae^{-\eta\omega t} \sin \sqrt{1 - \eta^2\omega^2}t + \varphi \quad (3.41)$$

where the ω is the angular speed of the oscillation. Curve fitting the recorded angle history from the OptiTrack to the above equation, and then the oscillation frequency can be calculated from the fitted angular speed. The fitted frequency and dipole moment measurement using the table inertia calculated in table 3.4 is shown in table 3.6 below.

For the frequency measurement of different magnet bars, as mentioned in section 3.2.3.2, the bar magnet is hovered in the middle plane using a thin fish line. Since the OptiTrack system requires the installation of several reflective balls on the object under test, which affects the moment of inertia of the bar magnets, and it is not practical to install the balls on some bar magnets with relatively small diameter and lengths, the OptiTrack method does not work.

TABLE 3.5. Mass and moment of inertia of two groups of magnet bars.

	Diameter (mm)	Mass (kg)	error (1 σ)	Moment of iner- tia (kgm ²)
Group 1	4	0.0016689	2.91548E-07	5.1875E-08
	5	0.00294415	6.8374E-07	1.02739E-07
	6	0.004109475	8.29156E-08	1.46229E-07
	7	0.005732225	2.38485E-07	2.08629E-07
	8	0.007468675	1.08972E-07	2.78831E-07
	10	0.011417225	8.29156E-08	4.51932E-07
	14	0.0223933	1.67183E-06	1.02076E-06
	15	0.02573845	1.72844E-06	1.2199E-06
	Length (mm)	Mass (g)	error (1 σ)	Moment of iner- tia (kgm ²)
Group 2	10	0.0020544	3.24037E-07	2.17424E-08
	12	0.002438925	5.11737E-07	3.47547E-08
	15	0.003136225	8.1968E-07	6.58607E-08
	20	0.004109475	8.29156E-08	1.46229E-07
	25	0.00519945	2.06216E-06	2.82503E-07
	60	0.013275	4.58765E-07	4.01237E-06

TABLE 3.6. Fitted frequency for different magnetization directions, Helmholtz cage Y axis current, and the final calculated dipole moment.

	Current (A)	Frequency ² (Hz ²)
South	0.5	1.3953E-05
	1	2.84015E-05
	1.5	4.18666E-05
	2	5.45469E-05
	Current (A)	Frequency ² (Hz ²)
North	0.5	1.53788E-05
	1	3.02193E-05
	1.5	4.34361E-05
	2	5.78999E-05
Dipole moment	1.287	Am ²

The hall sensor is used instead to measure the oscillation frequency of the bar magnet. A hall sensor is placed near the pole of the bar magnet. Once the magnet is oscillating, the movement of the pole will cause a different induced hall voltage. Then the frequency can be obtained by measuring the frequency of the change of hall voltage. The hall voltage is powered and logged using the Compact DAQ (USB-6002) made by National Instruments, and the frequency is calculated using MATLAB.

3.3.4 EPM for satellite detumble

After the satellites are released from the rockets or the deployment pods, the attitude and dynamical status are not predictable. The satellite may spin fast in any direction due to the mechanical disturbance during the deployment, and this amount of unwanted momentum must be dissipated for a stable operation of the satellites. Since this initial angular momentum is obtained from another source and needs to be dissipated, the reaction/momentum wheels cannot be used as they can only store a limited amount of momentum. Thrusters could be used to detumble the satellites. However, due to the limited propellant capacity, thrusters are generally used for accurate attitude adjustment and orbital maneuvers. Therefore the detumbling of the satellites is usually achieved through magnetorquers as they do not have a momentum

budget and do not consume propellant. As a type of magnetorquer, the performance of the EPM in detumbling the satellite is examined in this section.

3.3.4.1 B-dot controller

The famous B-dot control algorithm is used to test the detumbling performance of the EPM. The B-dot algorithm was firstly proposed by Sticker, A.C., and Alfried, K.T. in 1974 as a simple but effective method to reduce the satellite's angular speed to zero [126]. The controller determines the control input by continuously measuring the Earth's magnetic field using the onboard magnetometer and calculating its time derivative, then multiplying by a control gain \vec{K} :

$$\mathbf{M} = -K\dot{\mathbf{B}} \quad (3.42)$$

This algorithm is analog to the "D" control, which determines the required torque based on the derivative of the satellite's attitude measured solely from the magnetometer and calculates the amount of dipole moment that the magnetorquer has to generate. The B-dot controller is widely used in numerous small satellite missions [76, 44], and the optimization, improvement, and other utilization have been well-studied [138, 60, 34]. There are two major types of B-dot controllers: proportional B-dot controller and Bang-Bang B-dot controller. From the name, the proportional B-dot controller determines the dipole moment of the magnetorquer base on the size of the B-dot, as shown in the equation (3.42), and the Bang-Bang B-dot controller simply generates the maximum dipole moment based on the sign of the B-dot:

$$\mathbf{M} = -\mathbf{M}_{\max} \cdot \text{sign}(\dot{\mathbf{B}}) \quad (3.43)$$

Since the Bang-Bang controller always uses the maximum dipole moment, it can effectively reduce the high angular speed in the shortest time compared with other B-dot variants. However, for conventional magnetorquers, generating maximum dipole moment will consume tremendous power and stress the thermal management system due to the continuous power

consumption. In addition, the Bang-Bang controller will induce an oscillation when the angular speed is approaching zero due to high control input, which is not optimal in terms of time and power. Therefore most of the effort to optimize the B-dot controller is contributed to finding the optimal gain K or calculating a more complex gain, including other factors. However, for the EPM developed in this thesis, the torque rod can hold the magnetization without consuming power, and the energy is consumed only when changing the state of the magnetorquer. When the torque rod is being magnetized, the system can be put into sleep mode, and the torque rod can continuously interact with Earth's magnetic field to generate torque force. Since there is no power consumption, the torque rod will not stress the thermal management system. When the direction or the strength of the magnetization shall be changed, the OBC could send a command to wake the EPM up and quickly run the pre-defined program, and the system can be put in sleep mode again. All these features make the Bang-Bang controller the most suitable for the EPM for detumbling the satellites, as the continuous change of the control input will make the EPM frequently consume power to change the dipole moment of the torque rod. Simply magnetizing the torque rod to its maximum depending on the sign of the B-dot can make the satellite detumble quickly and consume less power.

However, there are some issues with utilizing the Bang-Bang B-dot controller for the EPM. The first issue is the biased magnetic field measurement for the onboard magnetometer. For the conventional magnetorquer, the ambient magnetic field measurement can be performed after shutting off the magnetorquer. However, for the EPM, the torque rod will maintain the magnetization after being magnetized, and turning off the torque rod will consume power. Furthermore, the torque rod can be treated as a permanent magnet after being magnetized, generating magnetic field orders of magnitude higher than the Earth's magnetic field. This field will heavily affect the magnetometer's measurement and might cause the controller to generate incorrect control output. This problem could be solved by separating the EPM from the magnetometer to reduce the effect of the field generated by the torque rod. Another method is to treat the torque rod as a source of hard iron distortion, as introduced in section 3.3.1.3, and calibrate the magnetometer in the presence of the torque rod. After the installation of the satellite, the relative position between the torque rod and magnetometer is fixed, and

the bias caused by the torque rod can be easily measured and compensated. An example of the calibration of the magnetometer in the presence of the hard magnetic material has been done by Frey, J. in 2014 [41]. Another issue of using the Bang-Bang B-dot controller is the zero point oscillation problem, as pointed out in [44]. Since the control output has only three states, the satellite will oscillate when it approaches the final value, and it takes a long time to stabilize. To solve this problem, a dedicated controller shall be designed for the EPM considering its unique feature. The optimization of this controller could also be investigated in future research.

3.3.4.2 Setup

The detumbling experiment was conducted using the experimental setup shown in Fig. 3.52. The table is balanced in the horizontal direction to test one torque rod of the EPM in roll motion. The measured angle from the OptiTrack was used to determine the angular speed and the relative direction between the torque rod and the applied magnetic field. The Y-axis coil of the Helmholtz cage was used to provide the required external magnetic field. After neutralizing the magnetic field in the center area of the cage, 1000 mA current increment was supplied in Y axis, generating a magnetic field with magnetic flux density of 551.371 mGauss ($\approx 55.514 \mu\text{T}$), which is close to the Earth's magnetic field strength in Sydney ($\sim 57.064 \mu\text{T}$) as mentioned in section 3.3.1.2. The measured angle data from the OptiTrack was transmitted to the computer and handled by MATLAB. The computer was used as the main controller, and the command was made by MATLAB and sent to the EPM through Bluetooth. The EPM was controlled by an Arduino Uno, mounted on the ABT, and powered by a Li-ion battery pack. The EPM main charging power was supplied by another Li-ion battery pack consisting of three 1-cell Li-ion batteries, which provides 12.6 V when fully charged. For the detumbling test experiment, the EPM responded to three main commands: Magnetize the torque rod in direction one, magnetize the torque rod in direction two, and demagnetize the magnet. The magnetizing command consists of four pulses with capacitor voltage of 400 V, and the demagnetize profile two, as shown in Fig. 3.34 was used to demagnetize the torque rod. The MATLAB code used for the detumbling experiment is attached in Appendix A.

3.3.4.3 Result

The experiment was conducted through the following procedure. Firstly, the ABT was balanced in the horizontal plane and detumbled through rapidly turning on and off the compressed air control valve to the air bearing. Then the Helmholtz cage was tuned according to the description introduced in the previous section. Then the MATLAB code was executed to obtain the continuously measured angle data from the OptiTrack and decide if the EPM shall be turned on and which direction of magnetization the EPM needs to achieve. The angle history and other system status parameters were recorded upon the execution of the code. Then an initial angular velocity was applied to the ABT by manually pushing the ABT in a random direction. The ABT shall start to spin in response to the manual stimulation, and the EPM shall start to operate to stop the spin.

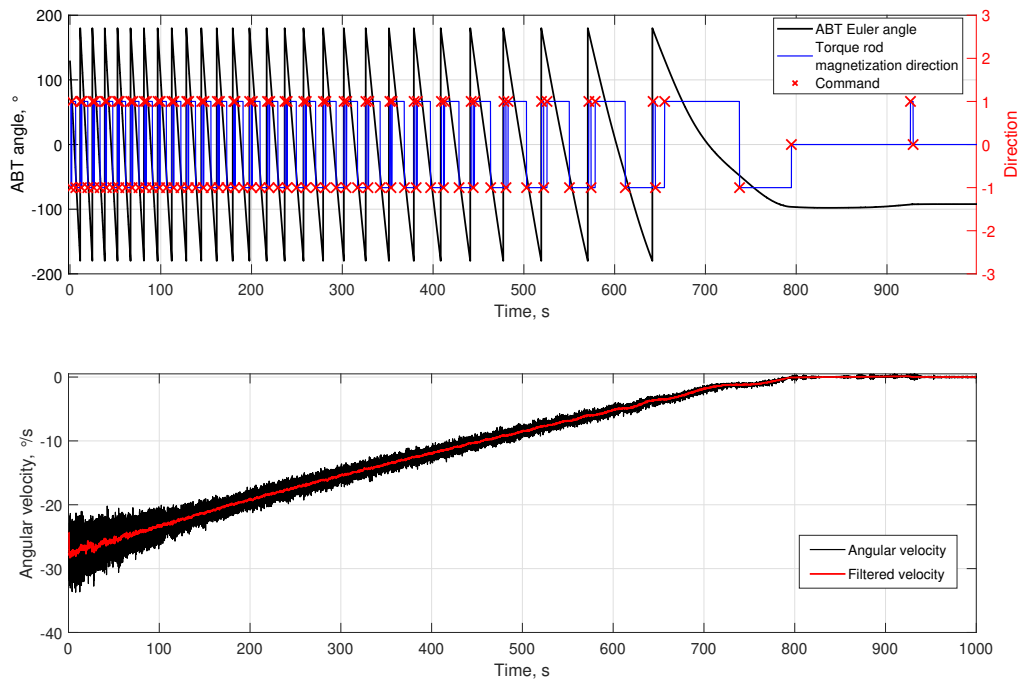


FIGURE 3.53. Detumble test result of the ABT with negative initial velocity.

Fig 3.53 shows one of the detumbling test results with a negative initial speed. The top part of the figure shows the ABT's Yaw angle and the corresponding EPM torque rod magnetization status. For easier interpretation, the direction of the magnetization is indicated using 1, -1,

and 0. ± 1 indicates the different direction of the magnetization, and 0 means the torque rod is demagnetized. The red cross indicates a command is sent to the EPM to change the magnetization. The bottom part of the figure shows the calculated angular speed and the filtered value. From the figure, the EPM can reduce the angular speed of the ABT from around $-30^\circ/\text{s}$ to almost stopped within around 800 s. The total amount of power dissipated can be calculated by counting the command sent to the EPM. Each charging command consists of four pulses at 400 V capacitor voltage. The capacitance of the capacitor array was measured to be $9.34 \mu\text{F}$. The energy consumption per command can be calculated as:

$$\begin{aligned}
 W &= \frac{1}{2}CV^2 \\
 &= 0.5 \times 9.34 \times 10^{-6} \times 400^2 \\
 &= 0.747\text{J}
 \end{aligned} \tag{3.44}$$

Neglecting the adjustment at the end of the detumbling process shown in Fig. 3.53, a total amount of 111 charging commands has been sent to the EPM, which result in around 82.92 J total power consumption. As a comparison, it took around 6000 s to detumble a 3U CubeSat (HuskySat-1) from initial angular speed of $11.5^\circ/\text{s}$ with a total of 1200 J energy consumed per torquer axis assuming a 200 mW power consumption per torquer [76]. Considering that the customized magnetorquer used for the HuskySat-1 can generate a dipole moment of 0.15 Am^2 with 0.2 W power, which is close to some of the COTS products, this data can be used as a benchmark for a general detumbling performance reference. If the initial angular speed for the HuskySat-1 increases to the same level as the experiment results shown in Fig. 3.53, the magnetorquer on the HuskySat-1 would consume more than doubled the energy to fully detumble the satellite.

The energy consumed for the detumble experiment is still not optimal. From the top part of Fig. 3.53, there are two more commands were sent to the EPM due to the wrong angular speed calculation when the angle jumps from -180° to 180° . If the program is well tuned to

calculate a correct angular speed at the transition point, the total amount of power could be further reduced by around a half.

3.3.5 EPM for single axis control

After the satellites have been detumbled, the attitude shall be adjusted to allow the payloads to operate appropriately and complete their missions. Conventional magnetorquers can perform the attitude adjustment, especially the pointing maneuver for a specific mission requirement. However, due to the weak torque force and short orbit time, conventional magnetorquers cannot be used solely for the pointing mission. Generally, it is used as a minor actuator to aid the main actuators, e.g., reaction wheel and thrusters, to achieve the desired pointing angle. For the EPM, however, since the torque force is significantly larger than the conventional magnetorquer and the time for changing the status of the torque rod is relatively short, the control performance for using only the EPM could be improved compared with conventional models. For some missions that do not require extremely high accuracy, the EPM could be used solely without needing propellant and reaction wheels to save power and propellant. Therefore a simple controller is designed for the EPM to briefly demonstrate the controllability and control accuracy of using the EPM solely as the control actuator.

3.3.5.1 Equation of motion

As a brief demonstration, only 2D planar rotation will be considered and examined in this thesis. Full 3D control experiments with advanced control algorithms will be performed in future works. The basic working principle of the magnetorquer can be simplified as a magnet inside a uniform ambient magnetic field with field flux density B , as shown in Fig. 3.54.

Suppose the magnet's magnetization direction is misaligned with the ambient field. In that case, a torque force will be generated, whose direction and magnitude relate to the angular displacement θ with respect to the ambient magnetic field direction. The system model can be simplified to:

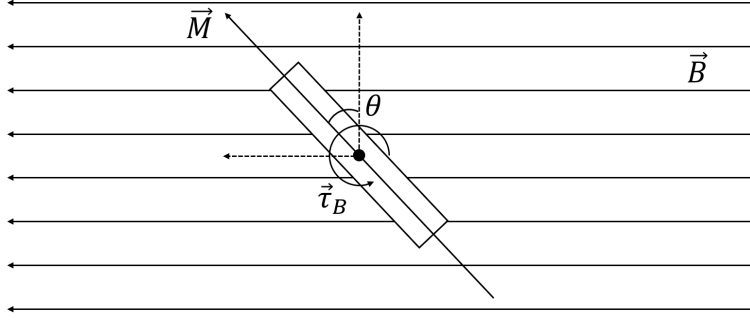


FIGURE 3.54. Torque generated by a magnet inside a uniform ambient magnetic field with flux density B .

$$J\ddot{\theta} = \tau + d \quad (3.45)$$

where J is the moment of inertia of the magnet, τ is the induced torque force, and d denotes the disturbance. The damping effect is neglected due to the minimal damping coefficient by using the air bearing. The torque force τ can then be expressed as the cross production of the magnet's dipole moment and ambient field strength B :

$$\tau = M \times B = MB \cos \theta \quad (3.46)$$

Note that the vector sign of the ambient field B is omitted since the system is limited to a 2D plane.

3.3.5.2 Controller design

A single axis sliding mode controller has been designed to perform the single axis control experiment. The detailed development and validation process of the controller are attached in Appendix B.

3.3.5.3 Experiment setup

The hardware configuration for the single-axis pointing experiment is the same as the single-axis detumbling experiment. The only difference is that for the detumbling test, the ABT was applied with an initial angular speed, and the program can perform the detumbling regardless of the angular position of the ABT. However, for the pointing experiment, since there is only one torque rod being used for the experiment, and the magnitude of the torque is related to the angular displacement with respect to the ambient magnetic field, which in the experiment is applied by the Helmholtz cage, there is a specific range where the ABT can be controlled. If the ABT is in an initial attitude where the torque rod's magnetization direction is aligned with the applied field direction, the torque rod cannot generate any torque force. Therefore the torque rod is set in an initial attitude where the torque rod's magnetization direction is perpendicular to the applied field direction, hence generating maximum torque force. The target angle is set to be within 60° of the initial angle for the controller to operate correctly. In the future study, the single axis single torque rod pointing control could be expanded to the entire three axes three torque rod control with a properly designed and optimized control algorithm. The MATLAB code for the control algorithm used in the single-axis single torque rod control can be found in Appendix C.

3.3.5.4 Result

With the control algorithm developed in the previous sections, the single axis pointing control experiments were conducted. The ABT angle was monitored by the OptiTrack same as the detumbling experiment. The ABT was stabilized at the initial angular position while the Helmholtz cage was turned on. Then the pointing control program was executed with a defined target angle. The angular position history for a 60° turning step input from around 40° to 100° is shown in Fig. 3.55 and the corresponding ABT angular speed, the command sent to EPM, and error are shown in Fig. 3.56.

From Fig. 3.55, the system angle in steady state is zoomed in as shown in the right part of the figure. After the system angle approaches the desired target angle, the system enters the

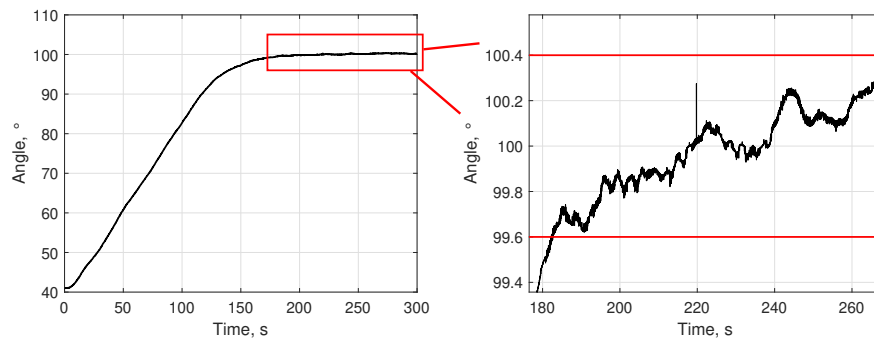


FIGURE 3.55. System angular position history for a 60° turning control input.

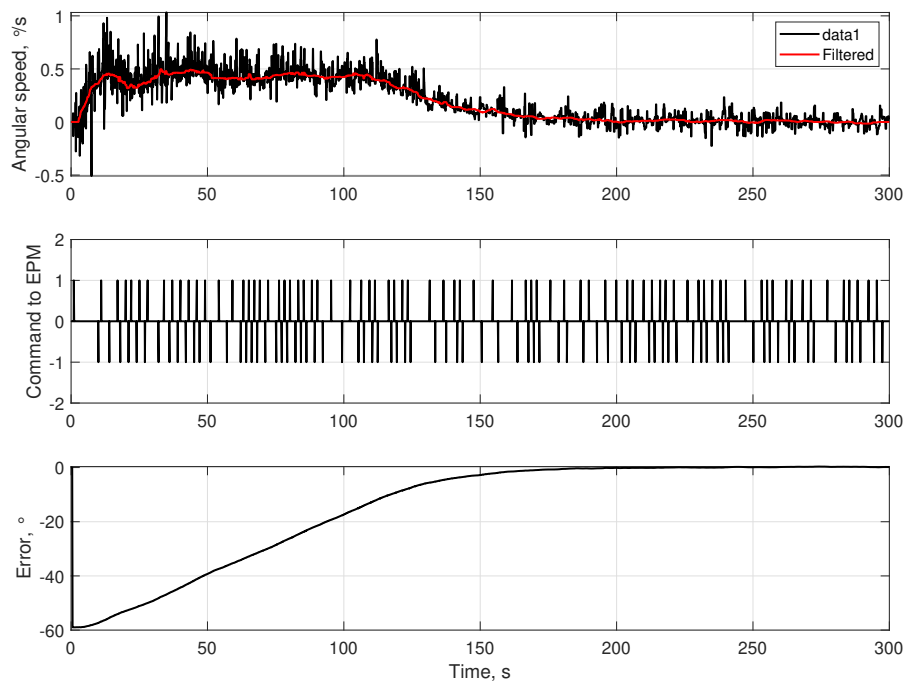


FIGURE 3.56. System angular speed (top figure), EPM command (middle figure), and control error (bottom figure) for the 60° turning control input.

steady state region, and the final angle can be within $\pm 0.4^\circ$ of the desired target angle. The angle history for multi-target control input is shown in Fig. 3.57.

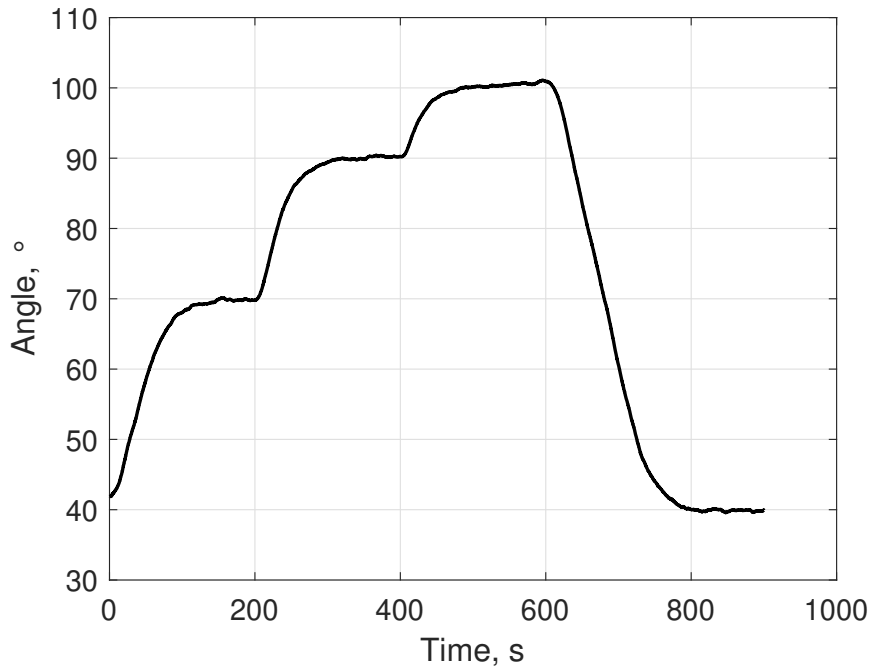


FIGURE 3.57. System angular position history for multi-target turning control input.

3.3.5.5 Discussion

A single-axis single torque rod pointing control experiment was performed using a sliding control algorithm. The controller can achieve the target angle and maintain a $\pm 0.4^\circ$ error discrepancy within a specific initial and target angle region. However, from Fig. 3.56, the controller is not optimal in system efficiency. It can be seen that after the first EPM command, the ABT starts to accelerate due to the torque force generated from the torque rod. After reaching a certain angular speed, the \dot{e} reaches the designated sliding manifold, and the controller sends multiple commands to change the magnetization state of the EPM to maintain the \dot{e} and e following the sliding manifold. Although the system operated well following the designed controller, the overall efficiency is not optimal. Due to the nature of the EPM, the system consumes energy only when the magnetization of the torque rod needs to be changed and does not consume energy when maintaining the previous magnetization state. Hence, for the controller used for the pointing control, considerable energy was spent on maintaining the speed following the sliding manifold, which delays the settling time and makes the overall

control efficiency low. The same actions occurred when the error was approaching zero, and multiple control commands were sent to EPM to ensure the \dot{e} and e followed the sliding manifold, which wasted numerous of energy and reduced the overall efficiency. For the final pointing accuracy, the $\pm 0.4^\circ$ error discrepancy is significantly better than the conventional magnetorquers ($\sim 5^\circ$). However, a new control algorithm could be developed to further decrease the error discrepancy. Note that the EPM worked in Bang-Bang mode for the pointing experiment, which means the torque rod was always charged to its maximum to generate torque force. Although this method can provide maximum possible control input, the consumed energy is significantly higher than those using lower capacitor voltage. In addition, the large torque input will make the system hard to achieve high pointing accuracy in a steady state. Therefore a dedicated control algorithm for optimizing the magnetization of the torque rod could also be developed and examined in the future study.

Despite the sub-optimal control performance and low energy efficiency of the pointing control algorithm, the experiment successfully demonstrated that the EPM could be used for pointing control. Further study could focus on optimizing the control algorithm to reduce the amount of command sent to EPM to achieve higher energy efficiency. Another controller could also be developed to control the magnetization of the torque rod depending on the required control input to further save energy. Three-dimensional control algorithms and experiments shall also be performed in future studies to demonstrate the capability of fully controlling the satellite.

3.3.6 Conclusion

In this section, the performance of the EPM in terms of satellite detumbling and single-axis single torque rod pointing control is experimentally investigated. The experiments were conducted using an in-house designed and manufactured Helmholtz cage and a self-designed air-bearing table with an innovative center of mass adjustment technique for fast and automated table balancing. The Helmholtz cage was designed following the well-known cage equations, and the cage-generated magnetic field uniformity and orthogonality are experimentally validated and calibrated using an industrial magnetometer. The technique to measure the torque rod's dipole moment has been introduced utilizing small angle oscillation

with an external artificial magnetic field generated by the Helmholtz cage. A single-axis detumbling experiment was conducted using the well-known B-dot control law, and the detumbling performance was examined experimentally. With only one torque rod, the EPM can reduce the angular speed of the ABT that has a moment of inertia of $\sim 0.06118 \text{ kg m}^2$ along the rotational angle from around $27^\circ/\text{s}$ to nearly zero within 800 s with a total of 82.92 J energy consumption. A comparison was made with the HuskySat-1 developed by the University of Washington, who requires around 1200 J to detumble the satellite from around $11.5^\circ/\text{s}$ to zero in around 6000 s [76]. A single axis sliding-mode control algorithm has been developed with proven control stability to perform the pointing control using only one torque rod. The experimental results show a $\pm 0.4^\circ$ pointing error discrepancy within a defined angular position range. Although the control accuracy and efficiency are sub-optimal, it proved that the EPM could be used for satellite attitude control with higher pointing accuracy than conventional magnetorquer. Future study directions were advised to focus on optimizing the power efficiency and developing the controller to control the magnetization of the torque rod to achieve higher pointing accuracy.

CHAPTER 4

Micro Air-fed Magnetoplasmadynamic Thruster

This chapter will introduce the details of the micro air-fed magnetoplasmadynamic thruster. Firstly the design of the thruster nozzle will be described. Then the methods to calculate the performance parameters are introduced, including determining mass bit, pulse energy, and impulse measurement. Since the thruster stand is in-house designed and made, the calibration procedure of the thruster stand shall be introduced and explained thirdly. Then experiment environment and the required equipment will be described. The results of the calibration and thruster test will be demonstrated, followed by the discussion of the experimental results, including performance parameters and efficiency calculation, performance comparison, and analysis of other findings during the experiment. Lastly, the critical performance data of the μ AF-MPDT will be concluded, with the possible future study direction pointed out.

4.1 Methodologies

4.1.1 Thruster design

As shown in Fig. 2.18, general MPDT has an arc discharge chamber where the propellant is fed through the rear insulator wall. The μ AF-MPDT, as shown in Fig. 4.1, has a similar structure to the conventional MPDT except for a reduced overall size and shallower arc chamber and converging anode nozzle. Since the propellant flow rate is also reduced after miniaturization, the chamber has to be shrunk to maintain the propellant density. The cathode tip and anode nozzle edge are sharpened to constrain the plasma and generate a higher plasma current density, which increases the thrust and efficiency. This structure also prevents the

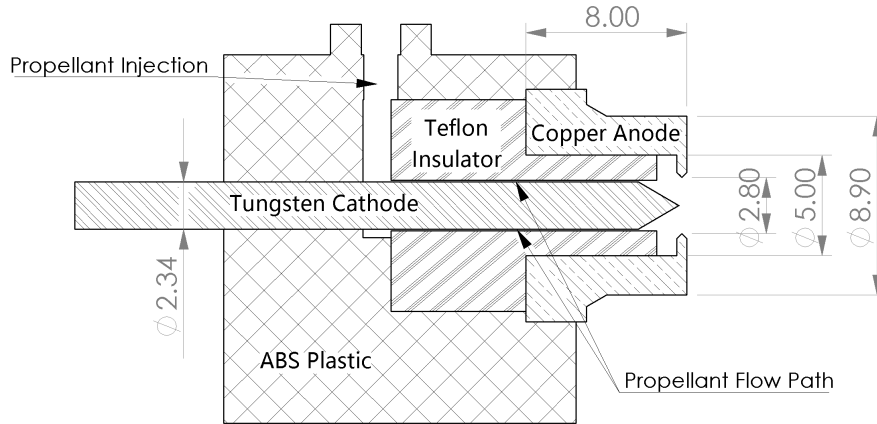


FIGURE 4.1. Cross-sectional view of the proposed μ AF-MPDT.

insulator from directly contacting the hot plasma, which could erode the brittle insulator and sometimes crack it due to thermal expansion [101].

Copper is selected as the anode material due to its low electrical resistance, and tungsten is selected as the cathode material due to its high melting temperature. This could prevent the cathode erosion at the arcing spot, in this design the cathode tip from the thermal load at high discharge current. The anode outer diameter is 8.9 mm and the cathode is 2.34 mm. Teflon is selected as the insulator material based on its flexibility and good electrical properties, which can hold the cathode and anode in place and eliminate electric breakdown between electrodes under high voltages. There are grooves on the inner wall of the insulator for the propellant to flow. This structure prevents the propellant from contacting the two electrodes before entering the discharge chamber, which could result in unwanted arc discharge. The photo of thruster built and used in this paper is shown in Fig. 4.2.

4.1.2 Performance calculation

The pulse-mode thrusters are generally described by 3 major characteristics: specific impulse (I_{sp}), thrust to power ratio (T/P) and overall efficiency (η) [143]. The specific impulse is a general performance character for thrusters to describe how efficiently the thruster uses propellant. For classical thrusters, this parameter is calculated by dividing the average thrust

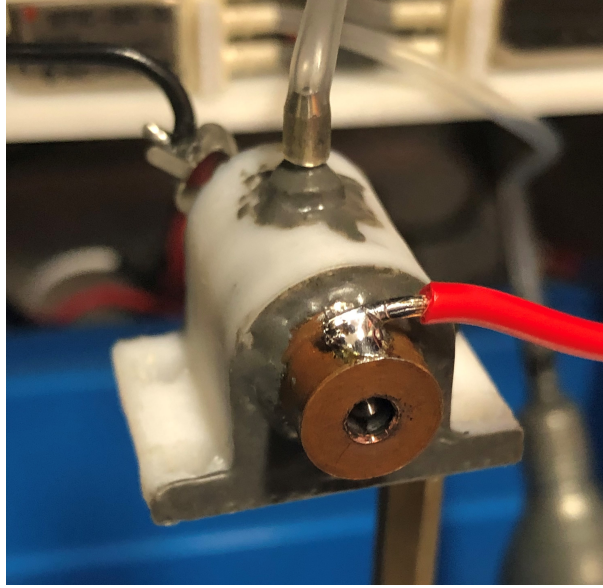


FIGURE 4.2. Photo of μ AF-MPDT with power cable and propellant feed pipe connected.

force F by the production of propellant mass flow rate \dot{m} and standard gravity g . For pulse-mode thrusters, however, it is calculated as the ratio between impulse bit and the weight of the propellant usage for one pulse on earth:

$$I_{sp} = \frac{F}{\dot{m}g} = \frac{I_{bit}}{m_{bit}g} \quad (4.1)$$

where g is the standard gravity, the impulse bit I_{bit} is the total impulse generated in one pulse which will be described in section 2.2.3 and mass bit m_{bit} is the mass of propellant used in one pulse, which will be described in the next section.

The thrust to power ratio for pulsed thrusters is calculated similar to normal thrusters by replacing the thrust (T) and power (P) by impulse bit (I_{bit}) and energy used per pulse (E):

$$\frac{T}{P} = \frac{I_{bit}}{E} = \frac{I_{bit}}{\frac{1}{2}CV^2} \quad (4.2)$$

where the energy per pulse E is calculated as the energy stored in capacitor and C is capacitance of the capacitor and V is the initial voltage applied on the capacitor.

The efficiency of the pulse-mode thruster is defined here as the ratio of kinetic energy output ($E_{kinetic}$) to the total input energy ($E_{electric}$):

$$\eta = \frac{E_{kinetic}}{E_{electric}} = \frac{\frac{1}{2}m_{bit}\bar{v}_e^2}{\frac{1}{2}CV^2} = \frac{I_{bit}^2}{m_{bit}CV^2} \quad (4.3)$$

where the \bar{v}_e is the average plasma exhaust velocity defined as $\bar{v}_e = I_{bit}/m_{bit}$. Therefore there are 4 parameters that are required to be measured to determine all performance characteristics for μ AF-MPDT: "impulse bit, mass bit and energy". Detailed methods and techniques of obtaining these parameters will be discussed in the following sections. All data presented in this thesis is the average value of at least 10 measurements under the same condition. The schematic of the experiment layout is shown in Fig. 4.3.

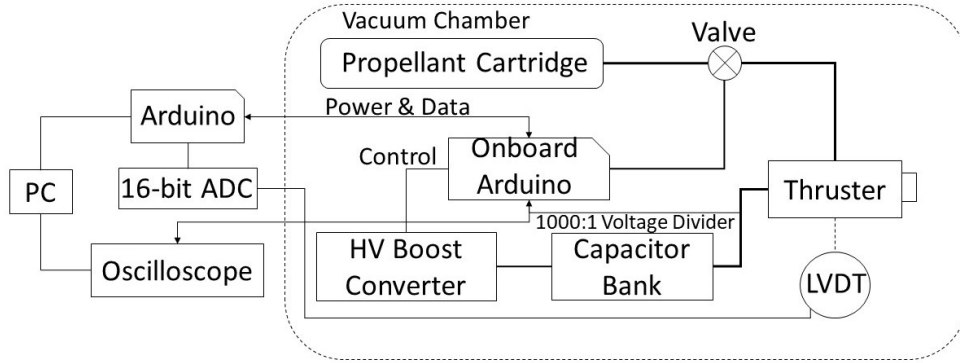


FIGURE 4.3. Layout of the experimental devices.

4.1.2.1 Mass bit determination

The propellant used for this thruster experiment is chosen to be air, which is stored in a commercially available 16g CO_2 cartridge at 1 atmospheric pressure. The cartridge is connected to a solenoid valve (model: SMC S070C-6AG-32) controlled by an onboard mini-Arduino Leonardo and a transistor, and the valve is connected to the thruster head through a 5 cm silicon tube. The mass bit is controlled by changing time interval between power on and off signals from the Arduino controller. According to the data sheet provided by the manufacturer of the valve, the response time for this valve to be fully opened after power on is 5 ms and 3 ms to be fully closed after power off, which indicates an 8 ms on-off cycle time.

However, during experiment, it is found that there is too much propellant be released if the time interval is set to 8 ms, making a tremendous waste of propellant. Moreover, during the experiment, it is found that the shortest time interval setup for a successful hot pulse is tested to be 5 ms. Any time interval setup shorter than 5 ms results in null response from LVDT in Cold Gas test and unsuccessful ignition in Hot Pulse test. Therefore the interval is set to 5 ms to let the valve partially open and close to reduce the waste and hence increase the propellant utilization efficiency. The actual time interval is measured to be ranging from 4.8 to 6.2 ms using the oscilloscope due to the Arduino internal timing error. Nonetheless, the mass bit tested is excessively higher than normal PPT's working range, making an enormous waste of propellant and thus results in a tremendously low propellant utilization efficiency.

As emphasized and experimentally proven by Lim J.W.M. *et al.*, a small deviation in propellant mass flow rate will lead to large errors when conduct micro-thruster performance characteristics tests [83]. Thus to precisely evaluate the mass bit, the propellant flow path between the Teflon insulator and tungsten cathode shown in Fig. 4.1 is treated as an orifice plate. Since the air flow rate through an orifice is proportional to the pressure difference between the upstream and downstream of the orifice, the mass flow rate can then be calculated with known parameters. The propellant flow path consists of four individual grooves carved on the inner surface of the Teflon insulator with total cross-sectional area of 0.188 mm^2 . Since the propellant cartridge is recharged to room pressure before each test, it is safe to assume the maximum possible pressure upstream the flow path is 1 atmospheric pressure (14.7 psi) once the flow reaches steady state. Therefore the maximum allowable mass flow rate is calculated to be 37.76 mg/s, which is reasonable comparing with 9.78 mg/s under 46.67 kPa pressure difference through an orifice with 0.102 mm^2 area in [143].

Since the pulse is ignited by the contact between propellant and electrode, it is safe to assume that the discharge is initiated once the propellant reaches the discharge chamber. The details of ignition process will be discussed in the next section. Therefore the maximum allowable mass bit can be calculated as the total mass flow during the discharge time based on the assumption that the propellant fed during this time interval is fully ionized and accelerated.

Since the average discharge time is measured to be $40.2 \mu s$, the actual mass bit is calculated to be:

$$m_{bit} < m_{max} = 37.76 \text{ mg/s} \times 40.2 \mu s = 1.518 \mu g \quad (4.4)$$

The average discharge time will be discussed in the next section.

4.1.2.2 Pulse energy determination

The pulse energy is stored in a capacitor bank which consists of two high-voltage power AC film capacitors connected in parallel and a high-voltage boost converter that can boost 5-V DC voltage to over 2000-V DC voltage is used to charge the capacitor bank. The capacitor bank is measured by the multimeter before and after each pulse experiment to ensure the capacitance remains constant. The boost converter is powered by the National Instrument Virtual Bench, which has two tunable DC power supply channels at $+6V/3A$ and $\pm 25V/1A$.

The anode and cathode are connected directly to the capacitor bank and charged to desired voltage prior to each pulse. Taking advantage of low breakdown voltage of gaseous propellant, ignition is triggered by directly feeding propellant into discharge chamber. Ionization happens once the propellant reaches the electrodes, and then discharge begins. This ignition technique eliminates the use of spark plugs which is essential in solid state PPTs, and consequently simplifying the structure of the system.

The pulse energy can be calculated by measuring the charged voltage and capacitance of the capacitor bank and the average input power can be determined by monitoring the power input to the boost converter. The charging voltage is monitored by an onboard 1000:1 voltage divider. The voltage signal is fed back to the onboard Arduino and is precisely controlled at the same level for each pulse. The discharge current is measured through a shunt resistor connected in series with the discharge circuit using the oscilloscope function in Virtual Bench. Discharge is considered to start when the current signal starts to rise and considered as the end when the current reading returns steady zero. Average discharge time is hence measured

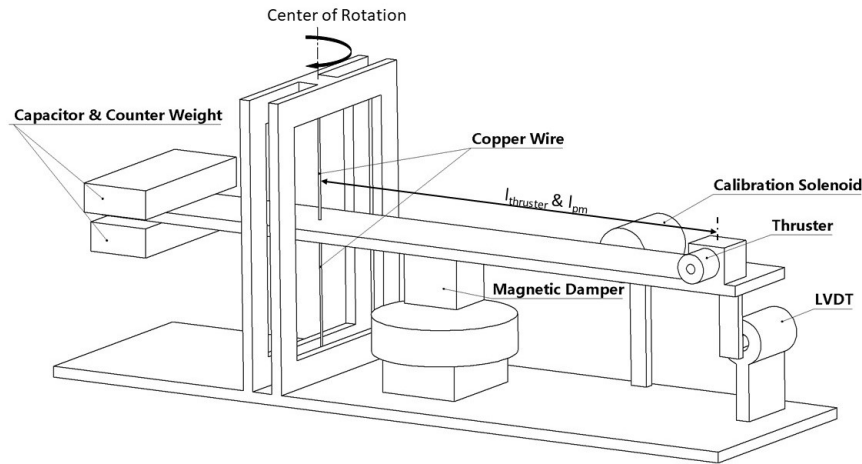


FIGURE 4.4. Schematic of the thruster stand.

through the time interval between start and stop of the current pulse. Results of the average discharge time measurement is show in section 3.2.

4.1.2.3 Impulse measurement

The impulse bit is measured by monitoring the position of the thruster mounted on a house-made torsional-pendulum-type thruster stand, which can rotate along the Z-axis pointing upwards through the torsional bearing. Figure 4.4 shows the schematic of the thruster stand. Copper wire is selected to serve as torsional bearing as the angular displacement for copper is purely elastic with a known shear modulus within a small angular deformation, which is suitable for this design. The elasticity of the copper wire in this experiment is periodically checked.

From the figure, the pendulum arm is suspended by two 1.12-mm diameter copper wires under tension to eliminate small balance weight errors. As the arm and copper wire form a harmonic oscillator and takes hours to become static after excitation in vacuum due to the significantly reduced atmospheric resistance, an eddy current magnetic passive damper is used to shorten the settling time. The Omega LDI-619-6.4-A010S linear variable displacement transducer (LVDT) is mounted on the long side of the arm at the same position of the thruster to translate its position signal into electric signal, which is then recorded by the computer through an ADS1115 16-bit analog-to-digital (ADC) converter placed outside the chamber.

The position history of the thruster allows the impulse bit to be calculated from the dynamics of the calibrated torsional-pendulum.

The dynamic model for this type of torsional pendulum thruster stand has been widely discussed [66, 28, 116, 74, 48, 139]. The general dynamic equation describing the force produced by the thruster $f(t)$, the distance of the thruster from the rotational axis $l_{thruster}$, and the pendulum arm deflection angle θ is:

$$\ddot{\theta} + 2\zeta\omega_n\dot{\theta} + \omega_n^2\theta = \frac{f(t)l_{thruster}}{I_\theta} \quad (4.5)$$

where I_θ is the moment of inertia of the pendulum arm to the rotational axis, ζ is the damping coefficient, and ω_n is the natural frequency of the pendulum arm.

Ziemer [144] concluded that by assuming ω , ζ , and I_θ are constant, the impulse bit I_{bit} can be calculated when the initial angular velocity is known using the equation:

$$I_{bit} = \frac{\dot{\theta}(0)I_\theta}{l_{thruster}} \quad (4.6)$$

The thrust force T can be calculated when the final angular deformation $\theta(\infty)$ and torsional spring constant k_θ are known using the equation:

$$T = \frac{\theta(\infty)k_\theta}{l_{thruster}} \quad (4.7)$$

where $\dot{\theta}(0)$ and the final angle $\theta(\infty)$ can be replaced by $\dot{x}(0)$ and x_{final} , which are the initial linear speed and the final position of a point on the pendulum arm, respectively. In this experiment, the LVDT has a distance of l_{pm} to the rotational axis for small angular deformations. Then, I_{bit} and T become:

$$I_{bit} = \frac{\dot{x}(0)I_\theta}{l_{thruster}l_{pm}} \quad (4.8)$$

and

$$T = \frac{x_{final} k_{\theta}}{l_{thruster} l_{pm}} \quad (4.9)$$

It is known that for a torsional pendulum, the relationship between the natural frequency, the spring constant, and the moment of inertia is:

$$\omega_n = \sqrt{\frac{k_{\theta}}{I_{\theta}}} \quad (4.10)$$

In the experiment, the LVDT is placed at the same position as the thruster ($l_{pm} = l_{thruster}$), by defining the effective mass m_{eff} as

$$m_{eff} = \frac{I_{\theta}}{l_{thruster}^2} \quad (4.11)$$

Equations (5) and (6) can be written as:

$$I_{bit} = \dot{x}(0) m_{eff} \quad (4.12)$$

and

$$T = x_{final} m_{eff} \omega_n^2 \quad (4.13)$$

Therefore, the impulse bit is the product of the initial linear speed of the thruster after one pulse and the effective mass. The initial linear speed can be obtained by numerically taking derivative of the position history of the thruster and the effective mass should be determined during the calibration procedure.

4.1.3 Calibration

4.1.3.1 Thruster stand calibration

From the previous section, the effective mass should be determined and calibrated to calculate the impulse bit. From Eq. 4.13, the effective mass m_{eff} can be calculated by applying a known constant force T to the pendulum arm and measuring the final distance of the thruster using LVDT. Natural frequency ω_n can be obtained from the sinusoidal wave of the LVDT when excited. Furthermore, since the electromagnetic force is not applied at the same position of the thruster, it should be converted to the equivalent force applied at the thruster using the conservation of momentum.

As described by Ziemer [144], the thruster measurement accuracy is strongly dependent on the position measurement along the arm axis. The most accurate way to measure the impulse bit of the thruster is to deliver a known impulse to the point at the same position as the thruster and use the response to calculate the thruster impulse bit. As there is a lack of equipment to generate a known impulse, the accuracy of this approach is dominated by the accuracy from the m_{eff} calculation, which is highly dependent on the position measurement. The pendulum arm is made using a laser cutter, and the actual distance is measured with a digital vernier caliper at an accuracy of 0.01 mm.

4.1.3.2 Solenoid calibration

As mentioned before, the calibration requires a known constant force T . A solenoid-magnet pair is chosen to generate the constant force. The force generated by the solenoid to the coaxial-placed permanent magnet is difficult to calculate. Thus it is easier, more reliable, and more direct to calibrate the solenoid using a high precision scale.

The calibration procedure is listed below:

- (1) Place the rounded permanent magnet on the weighing pan of the aforementioned high-precision analytical balance scale;

- (2) Place the solenoid above the magnet coaxially using 3D-printed structure with adjustable height;
- (3) Control the gap between the solenoid and permanent magnet using spacers with known thicknesses (1 to 5 mm);
- (4) Set the solenoid 1 mm above the magnet and set the driving current to 10 mA;
- (5) Turn power on and record the scale reading when stabilized;
- (6) Repeat step 5 for 10 times to reduce error;
- (7) Increase the driving current to 20 mA and repeat the step 5 and 6 until driving current reaches 100 mA;
- (8) Set the solenoid 1.5 mm above the magnet and set the driving current to 10 mA;
- (9) Repeat step 5 to 8 until the gap size reaches 5 mm.

After calibration, the relationship between the force, current and gap size can be obtained by curve fitting the recorded data. Therefore by supplying a known current to the solenoid, the applied force T can be obtained by measuring the gap size using LVDT. Note that since the initial gap size cannot be zero, it should be measured before the calibration.

4.1.4 Experiment environment

During the experiment, the stainless steel vacuum chamber that has the inner volume of 0.12175 m^3 is evacuated to $2.4 \times 10^{-2} \text{ Pa}$ using a PFEIFFER HiCube 300 Classic vacuum pump. Although this pressure can only represent the pressure at around 70 – 90 km altitude and is orders of magnitude higher than those in higher altitudes, the effect on the thruster measurement results from the insufficient pressure is considered negligible. The mean free path of the air molecules at the target pressure is around 28 cm, where the atmospheric drag force acting on the pendulum is considered as orders of magnitude smaller than other sources of friction and can be neglected. Due to the small size of the chamber, each pulse results in a $1 - 3 \times 10^{-2} \text{ Pa}$ pressure increase. Thus a small period of time delay is applied to allow the chamber pressure to reduce back to $2.4 \times 10^{-2} \text{ Pa}$. Since the pressure is kept below $5.4 \times 10^{-2} \text{ Pa}$ during the whole measurement procedure, the influence to the measurement results due to the pressure rise is considered negligible.

The power and data wires connecting the on-arm Arduino are selected to have a 0.1-mm diameter to reduce the interference from the cable stiffness. The wires are also mounted as close to the center of rotation of the arm as possible and connected using a "waterfall" structure to further reduce the interference.

The integrated device, including the thruster, thruster stand and all related components, is shown in Fig. 4.5

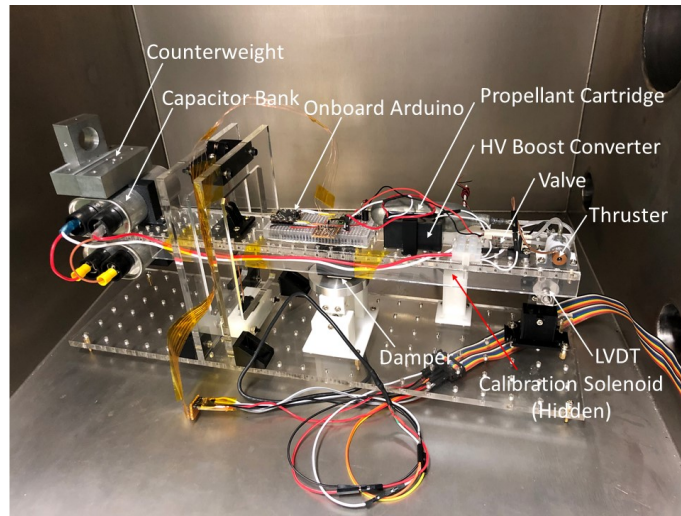


FIGURE 4.5. Thruster testing device in a vacuum chamber.

4.2 Results

4.2.1 Calibration results

Figure 4.6 summarizes the calibrated relationship between the current and force and between the measured gap size and force. It is noted that the standard deviation for each data point is on the order of 10^{-5} , which is too small to plot and demonstrates the small repeatable error. From the figure, it is seen that the electromagnetic force increases linearly with current at a fixed gap size and decrease with increasing gap size following the inverse-square law.

The mathematical model describing the force and gap size is obtained using the quadratic curve fitting method:

$$Y = AX^2 + BX + C \quad (4.14)$$

where Y is the force in mN and X is the gap size in mm, which is then used to calculate the electromagnet force. Noted that R^2 for linear regression models as estimated from Fig. 4.6a is checked with $R^2 > 0.99999$, which demonstrates the accuracy of the estimated model. Table 4.1 summarizes the coefficients of the quadratic curve fitting function for different current values.

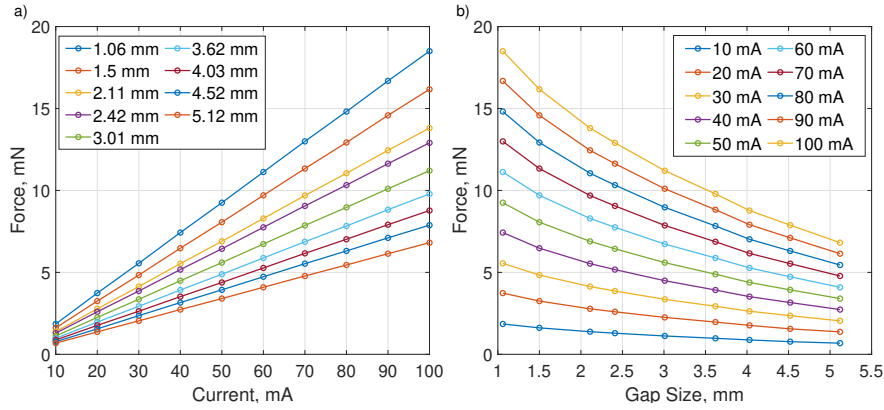


FIGURE 4.6. Relationship between force, current and gap size (error bar too short for plot). (a) Force with increasing current. (b) Force with increasing gap size

TABLE 4.1. Mathematical model for the quadratic curve fitting

Current (mA)	A	B	C
10	0.038677625	-0.518682985	2.330585372
20	0.078791500	-1.050526477	4.701607742
30	0.117052859	-1.556966111	6.984840583
40	0.156558905	-2.082948304	9.346566682
50	0.194591133	-2.591518684	11.63707965
60	0.233493589	-3.113512180	13.99211448

After calibrating the solenoid, it is mounted on the measurement arm at a distance of 185 mm to the center of rotation of the arm. It is noted that the permanent magnet is mounted on the arm and the solenoid is fixed on the base plate with an initial gap size measured at 4.08 mm.

The averaged position measurement values as described in section 2.2.3 are summarized in Table 4.2. Table 4.3 summarizes the calibrated parameters described in section 2.3.1 and 2.3.2 that will be used to calculate the impulse bit.

TABLE 4.2. Position measurement results

Item	Position (mm)	Designed Position (mm)	Error
LVDT	250.06	250	0.024%
Solenoid	184.70	185	0.16%
Thruster	250.06	250	0.024%

Table 4.4 summarizes the pulse energy and mass bit calculation results mentioned in section 2.2.1 and 2.2.2.

Fig. 4.7 shows the pendulum arm reaction to the current sweep from 10 to 60 mA, which indicates a small repeatability error and the copper wire does not exceed the elasticity range under a 60 mA driving current, which shows that the torsional spring assumption is satisfied.

4.2.2 Thruster test results

The experiments were conducted using two configurations: thruster fired with an average of 5.5 ms pulse interval without high voltage, which can be treated as "Cold Gas" thrust test and the one with same pulse time interval with high voltage applied, which will be named "Hot Pulse" in the rest part of this paper. Figure 4.8 demonstrates the thruster and plasma plume

TABLE 4.3. Torsional pendulum calibration results

Item	Value	Error
Initial Gap Size (mm)	4.080	0.4%
Natural Frequency (rad/s)	4.243	1.48%
m_{eff} (kg)	0.183	2.36%

TABLE 4.4. Electrical parameters measurement results

Item	Value	Error
Total Capacitance (μF)	2.085	3%
Charge Voltage (V)	2002	0.12%
Average Input Power (W)	1.857	3.66%
Mass bit (μg)	< 1.518	-

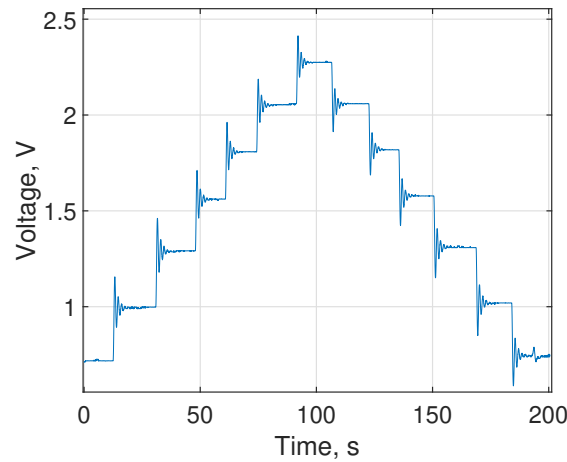


FIGURE 4.7. Thrust stand reaction to the current sweep from 10 to 60 mA.

during one pulse. Figure 4.9a shows the comparison of thruster position history for one pulse under different configurations and Fig. 4.9b shows the typical discharge current trace for one pulse in hot test. The gray wire shows the raw measurement data and the solid black wire shows the filtered data obtained by simply averaging the raw data. The average discharge time measured from several current traces is $40.2 \mu\text{s}$. Note that the Y-axis unit "Voltage" in Figure 4.9a is the voltage change in relative to the neutral position of the LVDT output. Thus it can be directly translated into position change of the thruster.

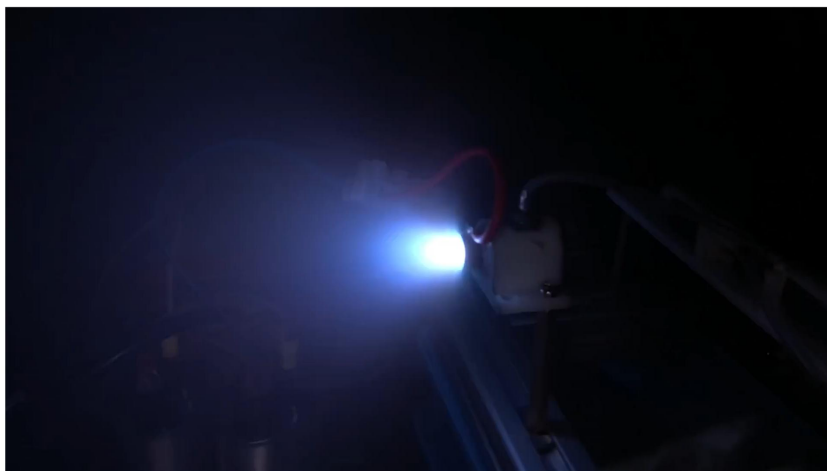


FIGURE 4.8. Plasma plume during one pulse.

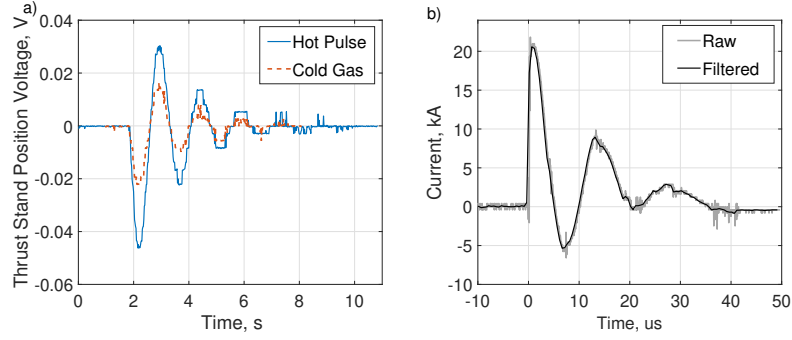


FIGURE 4.9. Typical waveform for one pulse (a) Comparison of position history for one pulse for Cold Gas and Hot Pulse configuration. (b) Raw and filtered current trace for one pulse.

TABLE 4.5. Thruster test results

Method	Mass Pulse Time (ms)	$\dot{x}(0)$ (mm/s)	σ (mm/s)	I_{bit} (μ Ns)
Cold Gas	5	5.713×10^{-2}	1.58×10^{-2}	10.471
Hot Pulse	5	1.884×10^{-2}	5.76×10^{-2}	34.534

The initial velocity $\dot{x}(0)$ is found from curve fitting the raw data of each pulse from Figs. 4.9a to calculate the impulse bit I_{bit} . Each experiment was repeated several times and the results are summarized in Table 4.5.

4.3 Discussion

From Table 4.5, it is readily found that the μ AF-MPDT increases the impulse bit by

$$\frac{34.534 - 10.471}{10.471} = 229.806\% \quad (4.15)$$

Compared with the cold gas thruster, Eq. 15 indicates an successful thruster design. From table 5, the maximum available pulse energy can be calculated by:

$$E_{bit} = \frac{1}{2}CV^2 = 4.178J \quad (4.16)$$

Note that this value indicates the maximum energy available for each pulse. Since energy will be dissipated in form of plasma heating, electromagnetic wave, electric circuit loss, etc. and the actual energy stored in capacitor may be smaller than calculated value due to decrease of capacitance when fully charged, actual energy that been converted into kinetic energy is hard to find. Thus the maximum available energy is used as total input energy for the rest of the calculation to calculate the performance.

Substitute E_{bit} with the data from Table 4.4, 4.5 into Eq. 4.1, 4.2 and 4.3, the "Hot Pulse" performance parameters can be calculated as:

$$I_{sp,min} = \frac{I_{bit}}{m_{max}g} = 2,319 \text{ s} \quad (4.17)$$

$$\frac{T}{P} = \frac{I_{bit}}{E_{bit}} = 8.266 \mu\text{N/W} \quad (4.18)$$

$$\eta_{min} = \frac{I_{bit}^2}{m_{max}CV^2} = 9.402\% \quad (4.19)$$

where the subscript "min" represents the minimum value indicating the lower limit of the calculated parameters. As mentioned in section 2.2.1, the pulse energy and mass bit used in the calculations are the maximum available energy and the maximum allowable mass, respectively. Therefore the actual pulse energy and mass bit could be smaller, resulting in higher specific impulse and efficiency than the calculated value. Consequently, the calculated value represents the lower limit of the range where parameters lie in.

The calculated performance data show an improvement comparing with the solid-state and liquid-fed PPTs that have similar pulse energy and mass bit as listed in table 4.6.

It may be possible to further optimize the performance using an external magnetic coil similar to the "Applied-Field Magnetoplasma Dynamic Thrusters". This technique has been widely used in micro propulsion systems, for instance, micro vacuum arc thrusters to enhance the performance and extend the lifetime [68]. Zolotukhin *et al* successfully increased the thrust

TABLE 4.6. Comparison between the μ AF-MPDT and other PPTs/VATs

Propellant	E_{bit} (J)	m_{bit} (μ g)	I_{bit} (μ Ns)	Isp (s)	η (%)	T/P (μ N/W)	Ref.
Argon	4.0 \pm 0.1	1.5	18.7	1270	2.76	4.68	[142]
Teflon	5.23 \pm 0.26	11.8	56.1 \pm 9.9	483 \pm 85	2.60	8.74	[108]
Aluminum	0.266	0.28	4.31	1571	12.5	16.3	[81]
Water	10	6	80	1550	6	8	[67]
Air	4.178	1.518	34.534	2319	9.402	8.266	This paper

force as well as the impulse bit by a factor of around 4 - 5 with an external magnetic field coil driven with 17.2 A direct current for the μ CAT thruster [145]. Based on this performance increase, the specific impulse could exceed 10,000s with external magnetic coil, making μ AF-MPDT a powerful competitor with conventional solid state PPTs.

The propellant flow is controlled by altering the valve opening time in this experiment, which is affected by the tank pressure, control signal accuracy and valve response time. This could be improved in the future design by adding another valve and a temporary gas reservoir. A specified amount of propellant can be charged into the reservoir from the first valve and then fed into the nozzle through the second valve. Then the mass bit can be controlled by changing the volume of the reservoir according to the propellant property. This could also be controlled via a well designed and manufactured sonic orifice as mentioned in section 2.2.1. However, this control method requires higher power input to generate several pulses during the discharge time period to maximize the propellant utilization, which is not suitable for small satellites.

The average discharge time as measured from the oscilloscope was $\tau=40.2 \mu s$ for each pulse. Therefore, by dividing the discharge energy by the discharge time, the average power for each pulse was calculated as:

$$P_{avg} = \frac{4.178}{40.2 \mu s} = 103.93 kW \quad (4.20)$$

This value lies in the normal MPD thruster working power range, which makes it reasonable to believe that the μ AF-MPDT is operating properly while pulsing. The average input power is measured to be 1.857 W, which is affordable by general 3-U CubeSats.

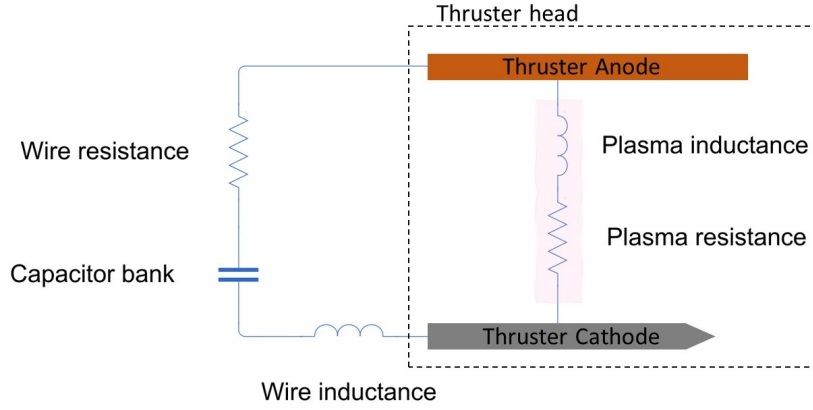


FIGURE 4.10. Simplified circuit diagram for μ AF-MPDT system.

From Fig. 4.9b, the current across the thruster oscillates after discharge happened. This indicates that after the breakdown, the current oscillates through the conductive plasma before it has been ejected out from the nozzle. Assuming the thruster circuit as a simple RLC circuit as shown in Fig. 4.10, the specific impulse for a co-axial PPT can be calculated using equation [141],

$$I_{bit} = \frac{\mu_0}{4\pi} \ln \frac{r_{out}}{r_{in}} \int J^2 dt \quad (4.21)$$

From the equation, the I_{sp} has a linear relationship with the integral of the square of the current. Since the current passes through zero several times during oscillation, the specific impulse is reduced and thus decrease the performance. This could be improved by redesigning the circuit to let the current critically damped after discharge. To achieve this, the half period time should be kept longer than the time required for the plasma to be completely ejected from the nozzle, which can be translated into reducing the frequency of the circuit. Comparing with increasing the resistance and inductance which could reduce the performance of the thruster, the simplest method is to increase the capacitance.

The propellant used in this thruster design is air, which makes it possible to be a candidate of the air-breathing electric propulsion methods. There has already been several air-breathing thrusters design based on the conventional electric propulsion systems (i.e. ion thruster, hall thruster, inductive plasma thruster and PPT) to compensate the drag force at VLEO. [35, 13, 112, 15]. Also, Schönherr *et al* [118] pointed out that PPT could be used for drag compensation for small satellites. Although these propulsion methods demonstrated the possibility of using air in upper atmosphere as propellant to generate thrust force, they are huge in size compared to the small satellites and consume too much power. However, Jackson and Marshall [56] analyzed that it is possible for CubeSats to counteract drag force in LEO, and Li *et al* [82] has successfully demonstrated that it is possible to compress gas collected in 150–240 km to an atmospheric pressure at a flow rate of 0–50 sccm. Considering the fact that the current design of μ AF-MPDT requires air at 1 atmospheric pressure to operate, it is possible to be used for small satellites to maintain the orbit at VLEO using air collected from the upper atmosphere with a well designed inlet and compressor.

4.4 Conclusions

A micro air-fed magnetoplasmadynamic thruster (μ AF-MPDT) that operates in a pulse mode was built and tested on a house-made thruster stand. The thrust stand was calibrated and shows good accuracy with a small repeatable error. The thruster generated a $34.534 \mu N s$ impulse bit with a specific impulse of 2319 s using air as propellant with an average of 5.5 ms pulse time and 4.178 J pulse energy under 1.857 W average input power. The thrust to power ratio and efficiency is calculated to be 8.226 $\mu N/W$ and 9.402%, respectively. Although the performance calculations demonstrate an improvement comparing with other PPTs/VATs using various propellants, the excessive propellant waste caused by long response time of the solenoid valve need to be further optimized. Solutions to the excessive mass waste are proposed including using two solenoid in series with a controllable temporary gas reservoir and using a well designed and manufactured sonic orifice. Further improvement in specific impulse and thrust performance can be achieved by adding an external magnetic coil. The discharge waveform is discussed and thruster performance can be further improved

by increasing the capacitance of the energy storage capacitor. The possibility of using the μ AF-MPDT to compensate atmospheric drag force in VLEO was discussed, which leading to a conclusion that it is possible to use the proposed thruster design for CubeSats to counteract the atmospheric drag force to maintain the orbit, and therefore extending the satellites' lifetime and mission time.

EPM for CUAVA-2 Payload Design

The Electro-permanent magnetorquer, an attitude control system designed for small satellites, has been designed with basic functionality proved by simulations and experiments in the lab environment. However, as a satellite payload, the best way to prove the functionality, suitability, and performance is to launch it with a satellite and monitor the actual in-orbit performance. The Australian Research Council Centre for CubeSats, UAVs, and Their Applications (CUAVA) develop the technology and commercial products to grow a world-class Australian industry in CubeSats, UAVs, and related areas. As part of the project, a 3U CubeSat "CUAVA-1" was successfully launched on Aug 29th, 2021, through Falcon 9 and deployed from International Space Station on 12nd October 2021 into the Low Earth Orbit (LEO, 405 km) [29, 30]. Another CubeSat mission which aims to develop and launch a 6U Cubesat, named "CUAVA-2", is under development and construction when the thesis is being compiled. The EPM will be integrated as a payload and tested in orbit. To meet the design requirements and electronic specifications of the CUAVA-2 CubeSat, a new EPM payload is developed based on the EPM prototype with some modifications and considerations. The details of the EPM payload design for the CUAVA-2 CubeSat mission will be introduced in this chapter.

5.1 Electronic design

As an actual satellite, there are some size, weight, and power constraints to ensure the safety and functionality of the whole satellite system. The prototype board, shown in Fig. 3.28 cannot be used directly for the CUAVA-2. Firstly the control of the EPM prototype was

achieved through an external Arduino Uno. To make it suitable for being used as a payload, the microcontroller must be integrated into the board to allow the EPM to operate by sending a command following a specific protocol. Secondly, the EPM was powered by a 3-cell Li-ion battery through a standard JST XH2.54 2P onboard connector. Since the power system on the CubeSat has to feed the whole satellite, the direct connection from the power supply to the EPM is not allowed for safety reasons. Therefore the power system must be modified to suit the capability of the satellite's power system. Thirdly the EPM must be able to provide detailed payload status information to the payload computer, e.g., current consumption and magnetization status. Then the EPM shall be able to connect to the satellite via a supported interface. The interface shall meet the desired communication specifications and power rating and be easily accessible for debugging. Lastly, the square-shaped board cannot be installed in a proper CubeSat frame. The overall board size must be shrunk and follow specific design requirements to fit the structure. The board layout must be re-designed with all the aforementioned design considerations and requirements to fit all the sub-systems properly. With all the considerations and design requirements, the details of the electronic design of the payload for the CUAVA-2 mission will be introduced in this section.

5.1.1 Main controller

The magnetorquer board cannot be controlled directly from the payload computer and requires a built-in micro controller dedicated for the communication with the payload computer and control of the EPM sub-system. For ease of integration, programming, and environmental requirement, the Atmega32U4-AU microcontroller made by Atmel is selected as the central controller for the EPM payload board. The chip has a pre-loaded Arduino bootloader that can be recognized as a COM port when connected to the payload computer through the built-in USB pins, making it easy to debug and update the program after integration. Besides, the chip works on 5 V, which can be powered directly from the 5 V bus the satellite's power system.

The chip features six individual ADC channels with 12 bits resolution and 17 GPIOs. Three of the ADC pins are assigned to hall sensors for each axis as a measure of the torque rod magnetization, one is assigned to measure the capacitor charging voltage, and the rest two are

used to monitor the system current, which will be introduced in the later section. Since there are three axes of the torque rods, and each axis requires an H-bridge to operate, 12 GPIOs are assigned to each thyristor to control the bridge directly. Two GPIOs are assigned to control the capacitor charger, and another two are dedicated for I²C communication. The last GPIO is assigned to control the main power to the capacitor charger for safety reasons, which will be introduced in the next section.

The chip is turned on and off by controlling the power to the EPM payload board. The microcontroller will start to run the pre-compiled initialization code after being supplied with power. When the system is initialized, it stays in standby mode and waits for the command from the payload computer. At the end of the payload mission, the power system only need to cut the power to the EPM to turn the whole EPM system off.

5.1.2 Power system

The power system is the major system that needs to be adjusted to suit the CUAVA-2's power system. For the prototype EPM, the logic power is supplied by the Arduino Uno onboard 5 V regulator and the capacitor charging power is provided by a separate 3-cell Li-ion battery. However, as introduced at the beginning of this section, the battery cannot be connected to the EPM directly for safety reasons, and the maximum available voltage is 5 V. Furthermore, only one power channel can be used by EPM, and the maximum available current for each channel is 2 A, resulting in a 10 W maximum available power. Since the LT3750 capacitor charger requires at least 12 V to operate, and the peak power required for the chip is beyond the capability of the channel, a new capacitor charger is required to charge the capacitor to the required voltage (400 V) while maintaining the overall power consumption below 5 W. To meet both the high voltage and low power requirements, the high voltage DC-DC power module AH05P-5 made by XP Power is selected to charge the capacitor array. Each of the AH05P-5 module can output maximum 500 V with 5 V 1.5 W power input. The module can work directly with the 5 V bus voltage without any voltage conversion and regulation, and the power consumption is well below the channel power capability. However, if a 400 V capacitor voltage is required, a total of 0.747 J energy shall be stored in the capacitor. For the

selected power module, assuming it operates at 1.5 W with 100% conversion efficiency, it still requires $0.747/1.5 = 0.498$ s to charge the capacitor. For a charging command consists of four continuous pulses, it will take $0.498 \times 4 = 1.992$ s to complete, which is not optimal. To fully use the bus power capability, four of the AH05P-5 module is installed on the EPM payload board to charge the capacitor array in parallel, as shown in the block diagram of the power system (Fig. 5.1). As mentioned in the previous section, two modules form a group and are controlled by a GPIO pin. Therefore if the system power is limited, only one group of powers module can be activated when charging the capacitor array. If fast charging is required, all four modules can operate simultaneously.

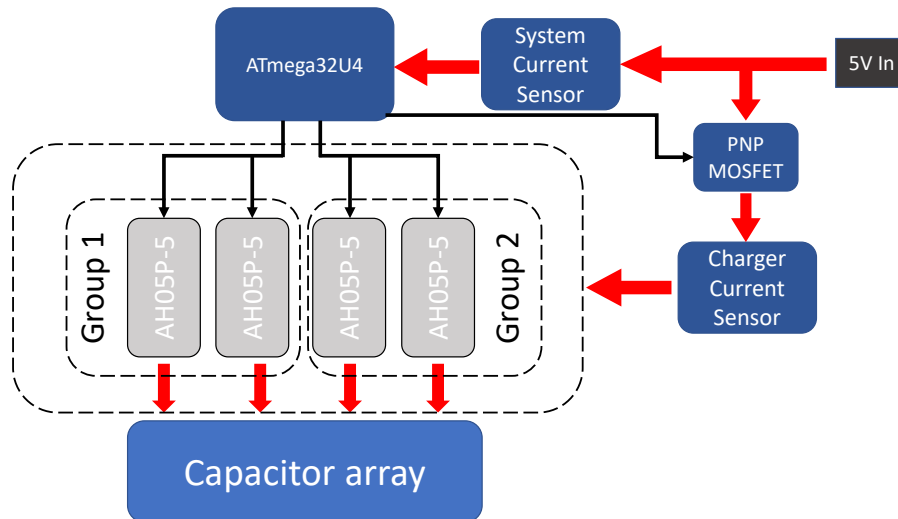


FIGURE 5.1. Block diagram of the power system with current monitoring.

To ensure safety, the input power is separated into two branches. The first branch connects directly to the microcontroller and all the sensor peripherals. This feature ensures that once the power is supplied to the EPM, the microcontroller can be powered on at the first instance to initialize the board and make the EPM ready to operate. The second branch connects to the charging module through a PNP MOS-FET. The MOS-FET works as an ON-OFF switch to control the power to the charging module. The gate pin of the MOS-FET is pulled high in default, which keeps the MOS-FET in the OFF state in case the charger is turned on by mistake, and the microcontroller can only turn on the MOS-FET under command. The current flow in the two branches is monitored by MAX44284 current sensor IC made by Analog

Devices, which measures the current flow by measuring the voltage drop across a resistor when the current pass through. Since the estimated current flow into two branches is different, different voltage sensing resistors and sensors with different gains are selected to ensure the current is within the measurement range of the Arduino embedded ADC.

5.1.3 System status monitoring

It is essential to inform the payload computer of the system status of the EPM while it is being powered. If any abnormal occurs, the payload computer can directly cut the power to the EPM to avoid further damage to the satellite system. The critical status data to monitor is the current flow, as any faulty components and system malfunction translate directly to the power consumption, which can be directly reflected in the current flow. Two current sensors ICs, as introduced in the previous section, are used to monitor the current flow into the system and charging modules.

Another parameter to monitor is the torque rod magnetization status. A torque rod with unknown magnetization status risks the satellite's attitude. Suppose the demagnetization procedure is not performed on the EPM's torque rod. In that case, it remains the magnetization and continuously generates torque to the satellite, which may cause the loss of control of the reaction wheel and thrusters. DRV5055 linear hall sensor made by Texas Instruments is used as the torque rod status monitor, as mentioned in the previous sections. The TO-92 package is glued to the further end of the X and Y torque rod to measure the flux density generated by each torque rod. The installation position is to avoid the cross-influence by the adjacent torque rod. For the Z axis, the same sensor in the SOT-23 SMD package is soldered on the bottom side of the circuit board to sense the flux density generated by the Z axis torque rod. The capacitor voltage and charging modules' status will be monitored and reported to the payload computer simultaneously.

5.1.4 Interface

The connection between the EPM and the satellite must be established using connectors supported by the satellite system and meet the specific requirements. The electrical connection is usually achieved through PC104 connectors for a normal CubeSat. However, as advised by the CUAVA-2 engineer, besides the standard PC104 connector, additional connection interfaces shall be designed on the PCB on the opposite side of the PC104 connector. As widely used in the CubeSat, the PicoBlade wire-to-board connection system provides an additional connection interface to the satellite system. For the functionality and connectivity consideration, the ATmega32U4 built-in USB connector is assigned to one of the 4-pin PicoBlade connectors to enable debugging using the native COM port with the Arduino bootloader installed. The ATmega32U4 In-Circuit Serial Programming (ICSP) is assigned to another 4-pin PicoBlade connector to provide direct access to the chip in case the bootloader or the program is corrupted. Another 6-pin PicoBlade is installed to provide the I²C communication and power connection. Since each pin of the PicoBlade connector supports a maximum 1 A current, a total of 4-pins are used to provide the power to the EPM, with 2-pins serving as a positive connection and 2-pins as a ground current return. The other 2-pins are used as SDA and SCL pins for I²C communication.

The power and I²C communication can also be accessed from the PC104 connectors. Three "NON-POP" zero ohm resistors are assigned to three pins of PC104 for manual adjustment of the source of 5 V power. Besides all the aforementioned interfaces, there are not any other connectors provided. The three LEDs between the 4-pin and 6-pin PicoBlade connectors are for debugging use only. The LEDs can be disabled by desoldering a common cathode zero ohm resistor.

5.1.5 PCB layout

The square-shaped prototype PCB cannot be fitted into the CUAVA-2 structure directly. The PCB outline shall follow special requirements, e.g., hole locations, edge cutout, and clearance, to be embedded into the satellite structure. In detail, the PCB specifications of the PUMPKIN

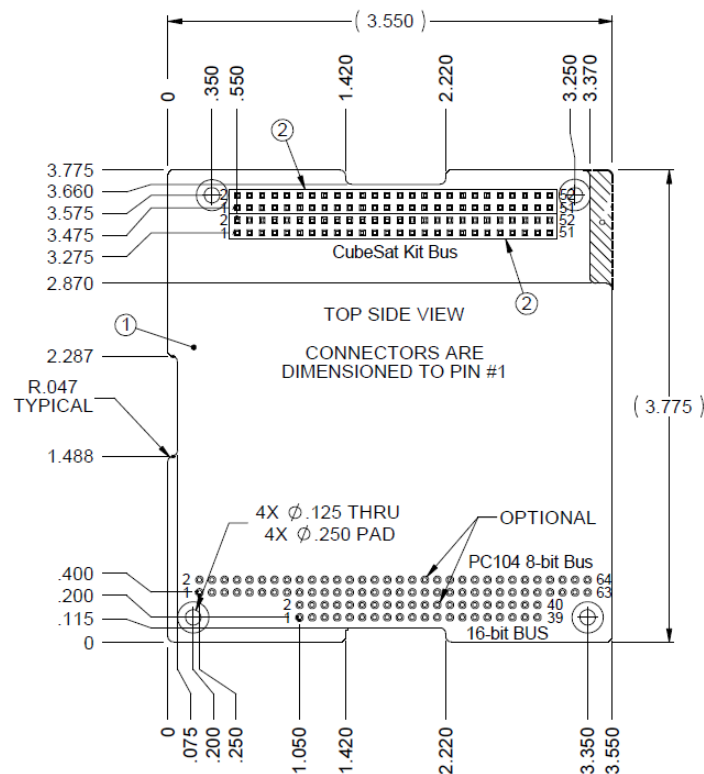


FIGURE 5.2. PCB Specifications of Pumpkin CubeSat [100]

CubeSat kit, as shown in Fig. 5.2 shall be referred to as the PCB outline of the EPM payload. In addition, the PCB is designed to be inserted in an aluminum shell to protect the EPM and other payloads, which will be introduced in the later section. Therefore, an additional 1.5 mm offset shall be left for the wall thickness of the shell, which will be introduced in the later section. Since the prototype board, as a core function unit, is already crowded, further shrinking the size with numerous additional parts is challenging.

Firstly, there should not be any components in the area where the PC104 socket is installed. Secondly, there should be clearance near the four mounting holes in the corner of the board. Thirdly, the edge cutout for the routing of the wire must be designed and not interfere with any components. Then the PicoBlade connectors must be opposite to the PC104 connector, which overlaps with the main torque rod and protection components. Lastly, the high voltage side shall be physically separated from the low voltage side to avoid any potential breakdown due to the low atmospheric pressure.

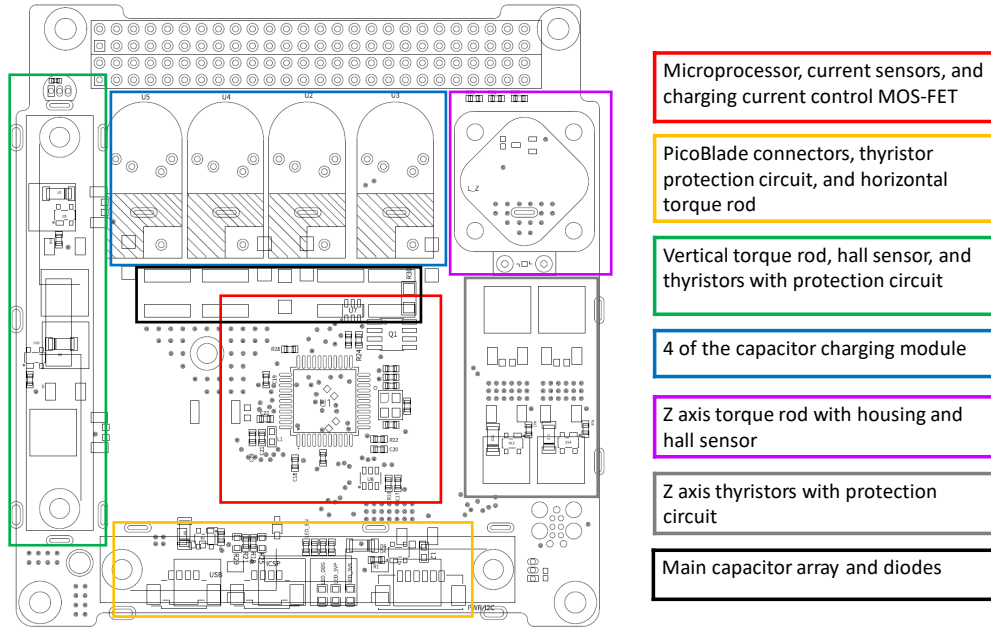


FIGURE 5.3. PCB layout of EPM payload.

With all the design requirements and considerations, the final PCB layout is shown in Fig. 5.3 with each functional area pointed out in different color. The heavy components are placed on the outer side of the board and distributed according to the mass to achieve overall mass balance. Besides the four corner mounting holes, another hole for the reinforcement standoff is placed in the center of the board to enhance the overall rigidity to pass the vibration test. Four 6 mm diameter 12 mm length AlNiCo 5 magnet bars are selected as the Z axis torque rod due to the height restrictions. The four magnets are wrapped with AWG 28 copper wire in the same direction and are put into a shell made with brass, which is then infused with 3M DP2216-Gray epoxy adhesive to enhance the rigidity and durability. The photo of the complete EPM payload board is shown in Fig. 5.4.

5.2 Hardware design

Besides the modifications of the electronics components and layout, the EPM payload board's hardware must be modified to meet the design requirements. Although there is no interference observed during all the tests on the prototype board, the pulse working principle of the EPM makes it has the potential to generate an electromagnetic pulse (EMP), which could

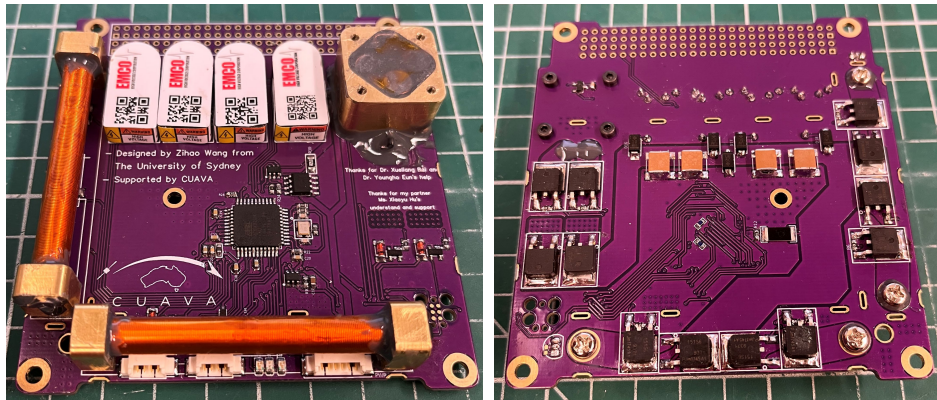


FIGURE 5.4. Photo of the top and bottom of the final EPM payload board.

damage or interfere with other electronic devices on the satellite. Therefore the shielding shall be designed to isolate the sensitive components from the outer environment and provide structural stiffness. The torque rod stand must be re-designed to provide structural rigidity to the torque rod while maintaining a good electrical connection to the circuit board. The hardware considerations and modifications of the EPM payload will be introduced in this section.

5.2.1 Shielding shell

Since the EPM works in pulse mode, the instantaneous pulse current may generate Electro-Magnetic Pulse (EMP), which has the potential to damage other electronic devices. To avoid the potential risk of the EMP, and to suppress the electromagnetic interference with other components during the discharge, proper shielding of the high voltage and high current is required. Since the location of the EPM payload was not confirmed by the systems engineer at the time this thesis was written, there are two shielding designs based on different sizes and thickness considerations: An aluminum box and a copper sheet shield.

The first shielding method is to put the whole EPM inside an aluminum box, which serves as a Faraday cage and also provides the stiffness and rigidity to the overall structure. The outline of the aluminium box shall follow the specifications shown in Fig. 5.2. The box has a average wall thickness of 1.5 mm, and a 1.5 mm thick aluminium plate is used as the top cover of

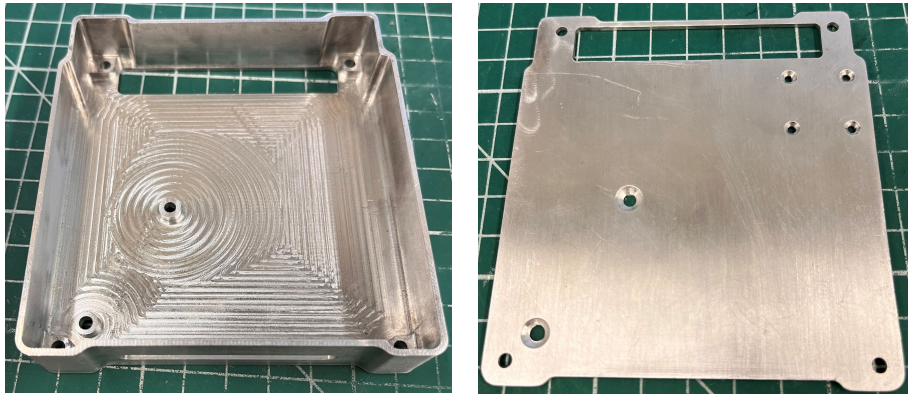


FIGURE 5.5. Photo of the top and bottom of the aluminium box.

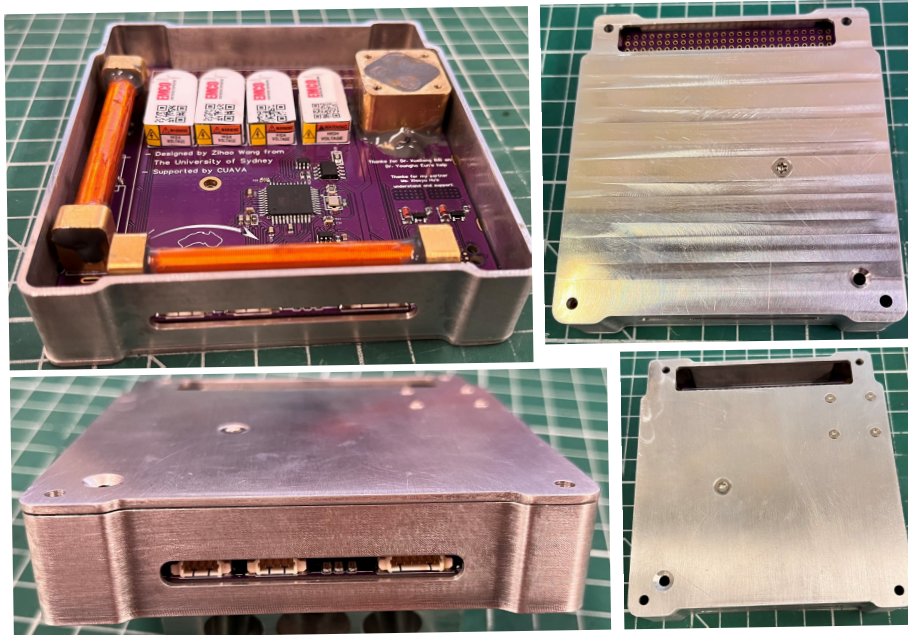


FIGURE 5.6. Photos of the assembly of the aluminium box with EPM board.

the aluminium box. Note that the Z-axis torque rod is sandwiched by the aluminum box and PCB for maximum structural strength and rigidity. The finished aluminum shell is shown in Fig. 5.5, and the aluminium box with the EPM board assembled is shown in Fig. 5.6. The designed thickness of the assembly shall achieve 20.4 mm, and the measured thickness of the assembly is 20.7 mm, which shall be checked with the assembly engineer.

Another version of the shielding is designed using only copper sheets. Similar to the aluminum shielding in some of the sensitive circuit board, especially in some of the board that contains

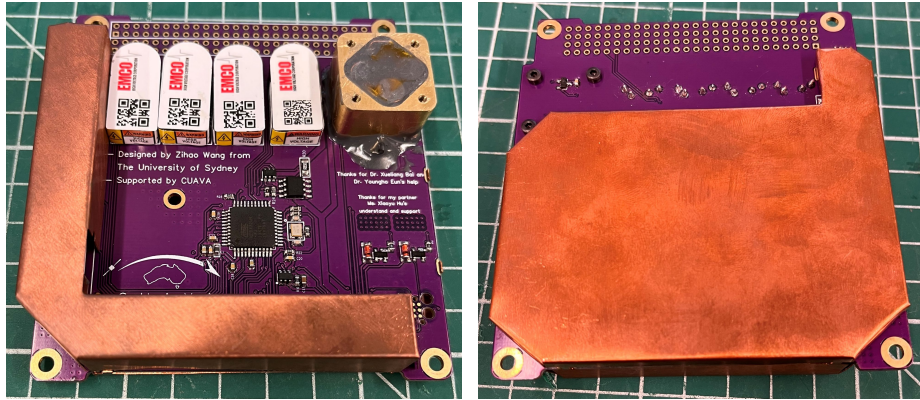


FIGURE 5.7. Assembly of the EPM payload board with copper shielding.

high-frequency radio communication components, a customized copper shielding is designed to provide similar shielding to the high voltage and current part of the EPM board. The shielding is manufactured by cutting a 0.3 mm thickness copper plate following the designed 2D sketch using the laser cutter, which is then folded back into the 3D box following the designed pattern. The shielding is soldered to the PCB in the designated soldering pads. All exposed metal is grounded for safety reason. The EPM board with top and bottom copper shielding installed is shown in Fig. 5.7. With the copper sheet shielding, the overall thickness of the EPM module can be brought down to 18.0 mm, which makes it take less space compared with the aluminum box.

5.2.2 Torque rod stand

For the EPM payload board for CUAVA-2, a proper torque rod stand shall be designed to provide adequate structural stiffness while reducing the electrical impedance at the connection joint.

As the main torque rod for the EPM, the X and Y axis torque rod shall provide as high structural stiffness as possible as the connection joint will experience the most repetitive force during the vibration. Due to the limited on-board room, the conventional bolt-clamp structure cannot be used here. Therefore a single-piece torque rod stand made with brass is designed, as shown in Fig. 5.8.



FIGURE 5.8. X and Y axis torque rod stand.

The torque rod is inserted into the larger hole of the torque rod stand, and the solenoid wire can be fed through the small hole on the blind end, which will then be soldered on the stand. The torque rod stand is bolted on the board using an M3 screw for the maximum structural stiffness and the stand is directly soldered on the board to increase the contact area and volume and reduce the joint electrical impedance. The contact area between the torque rod and the stand will be filled with DP2216-Gray epoxy adhesive to prevent wiggling movement.

The Z-axis torque rod highly depends on the satellite's height budget for the magnetorquer. If a strong Z axis dipole moment is required, a torque rod with the same dimension as the X and Y axis torque rod can be used, and even a longer torque rod could be installed to provide stronger actuation in the Z axis. For the EPM payload for CUAVA-2, the thickness of the component above the circuit board is restricted to be less than 13 mm. Therefore four of the 12 mm 6 mm diameter torque rods are selected to provide around $0.1089 \times 4 = 0.4356$ A m² vertical dipole moment based on the experimental data obtained in section 3.2.3.2. The enclosure is designed to be "cap-less" to further reduce the thickness, as shown in Fig. 5.9.

The M2 bolts are selected to fasten the enclosure due to the limited size, and brass is selected to manufacture the enclosure due to their higher material hardness compared with aluminum

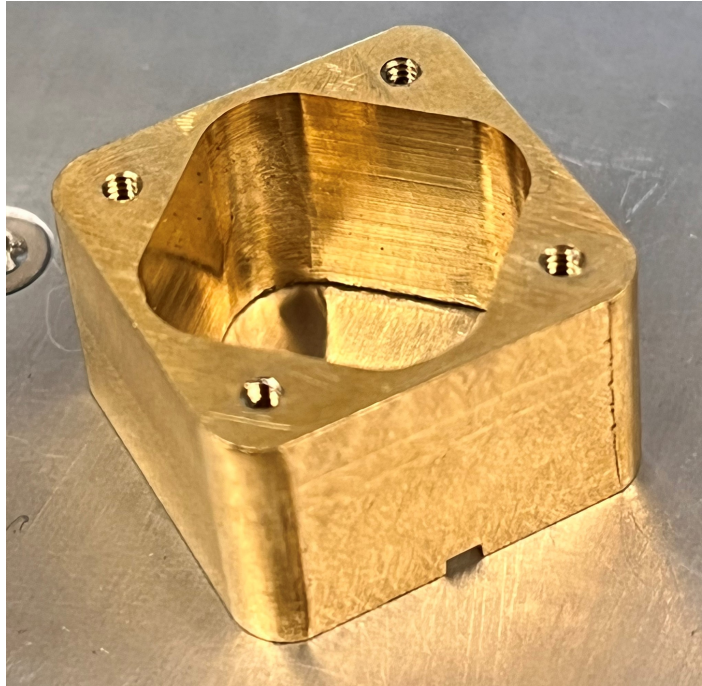


FIGURE 5.9. Z axis torque rod stand.

to provide enough binding strength when small threaded bolts are used. After the installation of the torque rods, the gap with the enclosure is filled with DP2216-Gray epoxy adhesive to make the whole Z-axis torque rod a rigid body for maximum structural stiffness. The solenoid copper wire is routed out of the enclosure and soldered on the board directly to provide an electrical connection. The same epoxy adhesive is applied to the exposed wire to provide protection. The finished Z-axis torque rod with a stand mounted on the board is shown in Fig. 5.4, 5.6, and 5.7.

5.2.3 Integration and vibration test results

The EPM payload has been integrated with other CUAVA-2 payloads and sent for vibration test. The photo of the test assembly with other payloads is shown in Fig. 5.10, and the test results are attached in the Appendix D.

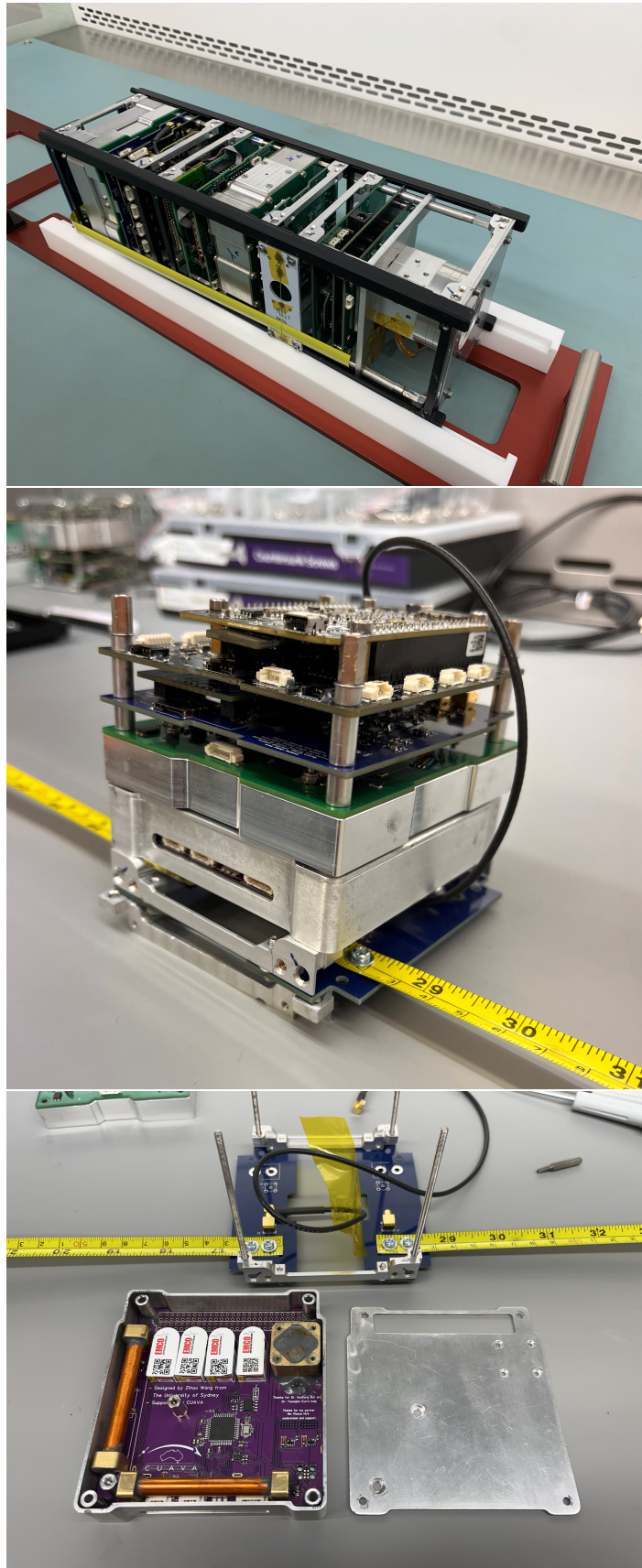


FIGURE 5.10. Assembled CUAVA-2 payloads for vibration test.

5.3 Conclusion

The EPM payload board for CUAVA-2 has been designed and introduced in detail in this section. The significant changes are the board outline and the capacitor charging circuit. To make it able to be embedded into the CUAVA-2, the board outline has been trimmed according to the design reference, and an extra 1.5 mm offset has been applied to the board outline for the aluminum shielding case. With the shrunken board size, the components layout and torque rod stand have been re-designed to ensure that all components can be squeezed into the tiny space without interfering with each other while maintaining a balanced mass distribution. The vertical axis torque rod has been shortened due to the height restriction of the available room for the EPM, and a proper torque rod stand has been made for the vertical torque rod. Four of the AH05P-5 DC-DC power converter modules made by XP power are selected as the main capacitor charger module due to the power constraint of the CUAVA-2 power system. The four power modules are divided into two groups, with two modules forming a group for programmable power and charging speed requirements. Both the standard PC104 connectors and the PicoBlade connectors are enabled to support multiple connection interfaces to the satellite payload computer and power module.

The program for the microcontroller ATmega32U4 on the EPM payload board was not ready when this thesis was being composed, and the communication to the payload computer has not been tested. Due to the delay in the process of CUAVA-2, the function and communication test will be postponed. The details of the EPM payload board test results will be conducted in the future study.

Three axis control algorithm for Smart Attitude Control System

The smart ACS consists of two actuators, EPM and μ AF-MPDT. As described in previous chapters, both can provide attitude control and actuation capability. The EPM can provide momentum adjustment without consuming propellant, and the μ AF-MPDT can provide ultra-accurate attitude adjustment for small satellites, especially CubeSats taking advantage of the ultra-small and compact form factor. It is proven that the EPM is capable of satellite's angular momentum dissipation for detumbling and fine attitude control, e.g., pointing, with a pointing error discrepancy of $\pm 0.4^\circ$. Combining these two actuators, taking advantage of high torque force, fast response time, low energy consumption, and zero propellant consumption of the EPM, and the high accuracy and compact size of the μ AF-MPDT, a complete ACS that can perform ultra-high precision attitude control with low power consumption can be achieved with a proper controller that properly controls both actuators. Therefore in this chapter, a three-axis control algorithm is designed for the smart ACS to perform high accuracy three-axis pointing maneuver. Simulation results using the experimentally obtained performance characteristics of the EPM and μ AF-MPDT will be shown to illustrate the performance of the smart ACS.

6.1 Controller design

In this section, a three-dimensional pointing control algorithm is developed using sliding mode control algorithm.

The kinematics of the controller can be described as:

$$\begin{cases} \dot{q}_{ev} &= \frac{1}{2}(q_{ev}^X + q_{e4}I_3)\omega_e \\ \dot{q}_{e4} &= -\frac{1}{2}q_{ev}^T\omega_e \end{cases} \quad (6.1)$$

where q_e is the quaternion error satisfying following equation:

$$q_e = [q_{ev}^T, q_{e4}]^T = q \otimes q_d = \begin{bmatrix} q_{d4}q_v - q_4q_{dv} + q_v^X q_{dv} \\ q_{d4}q_4 + q_{d4}^T q_v \end{bmatrix}$$

$q = [q_1, q_2, q_3, q_4]^T$ is the spacecraft attitude, and $q_v = [q_1, q_2, q_3]$

$q_d = [q_{d1}, q_{d2}, q_{d3}, q_{d4}]^T$ is the desired attitude, and $q_{dv} = [q_{d1}, q_{d2}, q_{d3}]$

and the notation $\mathbf{a}^X \in \mathbb{R}^{3 \times 3}$ for any arbitrary vector $\mathbf{a} = [a_1, a_2, a_3]^T \in \mathbb{R}^3$ is utilized to denote a skew-symmetric matrix

$$\mathbf{a}^X = \begin{bmatrix} 0 & -a_3 & a_2 \\ a_3 & 0 & -a_1 \\ -a_2 & a_1 & 0 \end{bmatrix}$$

The tracking error dynamics can be described as follows:

$$J\dot{\omega}_e = -\omega^X J\omega + J(\omega_e^X C\omega_d - C\dot{\omega}_d) + u + d \quad (6.2)$$

where d is disturbance, u is control input, J is the inertia matrix of spacecraft, ω is the rotation speed of spacecraft, ω_e is the error rotation speed, ω_d is the desired rotation speed. ω_e and ω_e satisfy the following equation.

$$\begin{cases} \omega_e &= \omega - C\omega_d, C = (q_{e4}^2 - q_{ev}^T q_{ev})I_3 + 2q_{ev}q_{ev}^T - 2q_{e4}q_{ev}^X \\ \omega_d &\text{satisfies: } \dot{q}_{dv} = \frac{1}{2}(q_{dv}^X + q_{d4}I_3)\omega_d, \text{ and } \dot{q}_{d4} = -\frac{1}{2}q_{dv}^T\omega_d \end{cases}$$

With two assumptions:

- (1) step tracking that q_d is constant quaternions and $\omega_d = 0$;
- (2) There is no disturbance to the system ($d = 0$);

the following sliding manifold can be designed:

$$s = \omega_e - \alpha \quad (6.3)$$

where:

$$\alpha = [\alpha_1, \alpha_2, \alpha_3]^T$$

$$\alpha_i = \begin{cases} -sgn(q_{e4})\Sigma_{vi} \cdot \sin\left(\frac{\pi}{2} \cdot \frac{q_{evi}}{\Sigma_{\omega i}}\right), & |q_{evi}| \leq \Sigma_{\omega i} \\ -sgn(q_{e4})\Sigma_{vi} \cdot sgn(q_{evi}), & \text{else} \end{cases}, i = 1, 2, 3$$

Where Σ_{vi} and $\Sigma_{\omega i}$ are 2 positive parameters determined by users.

Theorem 1

For the previously developed system (6.2), if the system's initial state, magnetic torque M , and parameters $\Sigma_{\omega i}$, $\Sigma_{V i}$ ($i=1,2,3$) satisfy (6.4), the controller $u = -M \cdot sgn(s)$ can achieve the asymptotic stability such that $\lim_{t \rightarrow \infty} q_e(t) = [0, 0, 0, 1]^T$:

$$M \geq 2\left(\frac{2V_2(0)}{\lambda_{min}(J)} + \|\Sigma_V\|^2\right)\lambda_{max}(J) + \sqrt{V_2(0)} + \lambda_{max}(J) \cdot \frac{\pi}{2} \cdot \|\bar{A}\| \cdot \left(\sqrt{\frac{2V_2(0)}{\lambda_{min}(J)}} + \|\Sigma_V\|\right) \quad (6.4)$$

where:

$$\Sigma_V = [\Sigma_{V1}, \Sigma_{V2}, \Sigma_{V3}]^T$$

$$\bar{A} = \text{diag}\left\{\left[\frac{\Sigma_{V1}}{\Sigma_{W1}}, \frac{\Sigma_{V2}}{\Sigma_{W2}}, \frac{\Sigma_{V3}}{\Sigma_{W3}}\right]\right\}$$

$$\text{sgn}(s) = [s_1, s_2, s_3]^T$$

Proof

Set the Lyapunov candidate:

$$\begin{aligned} V_1 &= q_{ev}^T q_{ev} + (1 - |q_{e4}|)^2 \\ V_2 &= V_1 + \frac{1}{2} S^T J S \end{aligned} \tag{6.5}$$

(6.5) can be further written as (6.6)

$$V_2 = 2 - 2|q_{e4}| + \frac{1}{2} S^T J S \tag{6.6}$$

Taking the derivative of (6.6), (6.7) can be obtained.

$$\begin{aligned} \dot{V}_2 &= \text{sgn}(q_{e4}) q_{ev}^T \omega_e + S^T (J \dot{\omega}_e - J \dot{\alpha}) \\ &= \text{sgn}(q_{e4}) q_{ev}^T \alpha + S^T [u - \omega^X J \omega - J \dot{\alpha} \\ &\quad + \text{sgn}(q_{e4}) q_{ev} + J(\omega_e^X C \omega_d - C \dot{\omega}_d) + d] \end{aligned} \tag{6.7}$$

where $J(\omega_e^X C \omega_d - C \dot{\omega}_d) = 0$ due to assumption 1 and $d = 0$ due to assumption 2.

$$\dot{V}_2 = \text{sgn}(q_{e4}) q_{ev}^T \alpha + S^T u - S^T \omega^X J \omega - S^T J \dot{\alpha} + S^T \text{sgn}(q_{e4}) q_{ev} \tag{6.8}$$

where:

$$\begin{aligned}
-S^T \omega^X J \omega &\leq \|S\| \cdot \|\omega\|^2 \cdot \lambda_{max}(J) \\
&= \|S\| \cdot \|S + \alpha\|^2 \cdot \lambda_{max}(J) \\
&\leq \|S\| \cdot (\|S\|^2 + \|\Sigma_V\|^2 + \|S\|^2 + \|\Sigma_V\|^2) \lambda_{max}(J) \\
&\leq \|S\| \cdot 2\left(\frac{2\Psi_2}{\lambda_{min}(J)} + \|\Sigma_V\|^2\right) \cdot \lambda_{max}(J) \\
-S^T J \dot{\alpha} &\leq \|S\| \cdot \lambda_{max}(J) \cdot \left\| \left[\frac{\pi}{2} \cdot \frac{\Sigma_{Vi}}{\Sigma_{Wi}} \cos\left(\frac{\pi}{2} \cdot \frac{q_{evi}}{\Sigma_{\omega i}}\right) \dot{q}_{evi} \right] \right\| \\
&\leq \|S\| \cdot \lambda_{max}(J) \cdot \frac{\pi}{2} \cdot \|\bar{A}\| \cdot \frac{1}{2} \|1 + 1\| \cdot \|\omega_e\| \\
&\leq \|S\| \cdot \lambda_{max}(J) \cdot \frac{\pi}{2} \cdot \|\bar{A}\| \cdot \left(\sqrt{\frac{2\Psi_2}{\lambda_{min}(J)}} + \|\Sigma_V\| \right) \\
S^T \text{sgn}(q_{e4}) q_{ev} &\leq \|S\| \cdot \|q_{ev}\| \leq \|S\| \sqrt{\Psi_2}
\end{aligned}$$

By inserting the equation of controller $u = -M \cdot \text{sgn}(s)$ into (6.8), (6.9) can be derived

$$\begin{aligned}
\dot{\Psi}_2 &\leq - \sum_{j=1}^L \Sigma_{vj} |q_{evj}| - \sum_{k=1}^{3-L} \Sigma_{vk} q_{evk} \sin\left(\frac{\pi}{2} \cdot \frac{q_{evk}}{\Sigma_{wk}}\right) - S^T M \text{sgn}(s) \\
&\quad + \|S\| \left[2\left(\frac{2\Psi_2}{\lambda_{min}(J)} + \|\Sigma_v\|^2\right) \lambda_{max}(J) + \sqrt{\Psi_2} \right. \\
&\quad \left. + \lambda_{max}(J) \frac{\pi}{2} \cdot \|\bar{A}\| \cdot \left(\sqrt{\frac{2\Psi_2}{\lambda_{min}(J)}} + \|\Sigma_v\| \right) \right] \quad (6.9)
\end{aligned}$$

where L is a non-negative integer no greater than 3.

$$\begin{aligned}
S^T M \text{sgn}(s) &= -M \sum_{i=1}^3 |S_i| = -M \sum_{i=1}^3 \sqrt{S_i^2} \leq -M \sqrt{\sum_{i=1}^3 S_i^2} \\
&= -M \|S\|
\end{aligned}$$

(6.9) can be further written as (6.10)

$$\begin{aligned}
\dot{V}_2 \leq & - \sum_{j=1}^L \Sigma_{vj} |q_{evj}| - \sum_{k=1}^{3-L} \Sigma_{vk} q_{evk} \sin\left(\frac{\pi}{2} \cdot \frac{q_{evk}}{\Sigma_{wk}}\right) \\
& + ||S|| \left[-M + 2\left(\frac{2V_2}{\lambda_{\min}(J)} + ||\Sigma_v||^2\right) \lambda_{\max}(J) + \sqrt{V_2} \right. \\
& \left. + \lambda_{\max}(J) \frac{\pi}{2} \cdot ||\bar{A}|| \cdot \left(\sqrt{\frac{2V_2}{\lambda_{\min}(J)}} + ||\Sigma_v||\right) \right] \quad (6.10)
\end{aligned}$$

Apparently, the function $f(V_2)$ defined in (6.11) is monotonically increasing among $V_2 \in [0, +\infty]$. Therefore, if $-M > f(V_2)$ is valid when $t = 0$, then $\dot{V}_2(0) \leq 0$ makes $V_2(0 + dt) \leq V_2(0)$, which makes $f(V_2(0 + dt)) \leq f(V_2(0))$. Then, it is easy to conclude $-M + f(V_2(t)) \leq 0$ when $t > 0$.

$$f(V_2) = 2\left(\frac{2V_2}{\lambda_{\max}(J)} + ||\Sigma_v||^2\right) \lambda_{\max}(J) + \sqrt{V_2} + \lambda_{\max}(J) \frac{\pi}{2} ||\bar{A}|| \cdot \left(\sqrt{\frac{2V_2}{\lambda_{\min}(J)}} + ||\Sigma_v||\right) \quad (6.11)$$

Therefore, (6.10) can be written as (6.12).

$$\dot{V}_2 \leq - \sum_{j=1}^L \Sigma_{vj} |q_{evj}| - \sum_{k=1}^{3-L} \Sigma_{vk} q_{evk} \sin\left(\frac{\pi}{2} \cdot \frac{q_{evk}}{\Sigma_{wk}}\right) \quad (6.12)$$

Based on (6.10), it is apparent that $\dot{V} < 0$ as long as $||q_{ev}|| \neq 0$. Therefore, q_e is asymptotic stable such that $\lim_{t \rightarrow \infty} q_e(t) = [0, 0, 0, 1]$.

Proof end.

6.2 Simulation

The controller developed in the previous section has been verified using MATLAB-based simulation using experimentally obtained actuator performance data. The first simulation was conducted using only EPM activated as the actuator. The Bang-off-Bang control algorithm

was used to perform attitude control with a maximum torque force of $50 \mu\text{N m}$, which occurs when the torque rod is orthogonal to the ambient field. The system's moment of inertia matrix I is assumed to be (unit: kgm^2):

$$I = \begin{bmatrix} 0.0614 & 0 & 0 \\ 0 & 0.0614 & 0 \\ 0 & 0 & 0.0614 \end{bmatrix}$$

and the system has an initial attitude represented by roll, pitch, and yaw angle $\theta_{init} = [40.85, 35.18, 20.82]$ in degrees. The ambient magnetic field is assumed to be constant. With a control target of bringing the roll, pitch, and yaw angle to zero, the simulated system attitude history is shown in Fig. 6.1, with three-axis torque rod magnetization history shown in Fig. 6.2. Another simulation was performed with both actuators activated in a sequence. When the error to the target angle is large, only EPM is activated to bring the satellite attitude close to the target angle. After the attitude angle reaches within 0.05° to the target angle, the EPM will be turned off, and the thrusters will take over the satellite's control to provide accurate attitude adjustment. The system attitude history for the simulation with both actuators enabled is shown in Fig. 6.3, with the thrusters actions record shown in Fig. 6.4. The simulation for the thrusters runs on the assumption that the thrusters are configured in pairs to generate torque force in each of the rotational axes. The thrusters work in pulse mode with an interval of 0.1 s between pulses and $40 \mu\text{s}$ pulse time, which is obtained from the experimental results. An average thrust force of $\sim 860 \text{ mN}$ is generated for each thruster during the active pulse time, and two thruster in a pair are separated by 0.1 m , which result in a 0.086 N m torque force during the pulse time.

6.3 Analysis

For the control simulation using only EPM as the actuator, the steady state system attitude is zoomed in, as shown in the right part of Fig. 6.1, where the system can achieve $\pm 0.04^\circ$ pointing accuracy on three axes under the given system parameters and initial conditions.

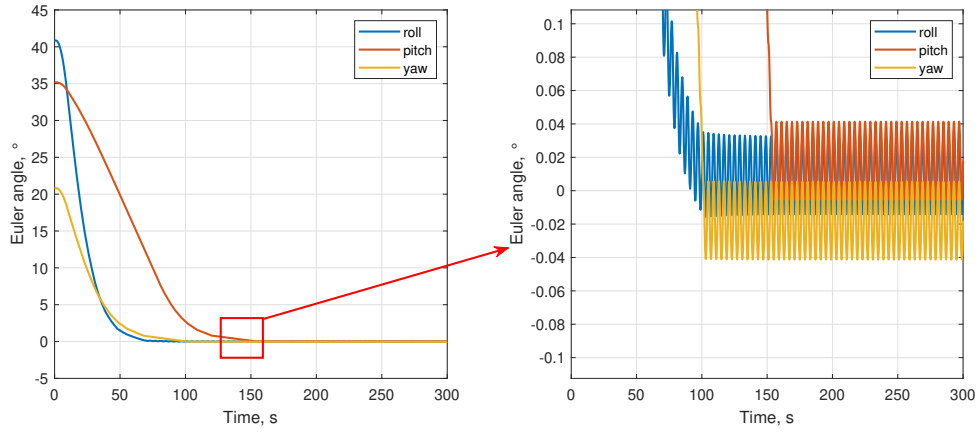


FIGURE 6.1. The system attitude history for the simulation using only EPM as the actuator. System angles are represented in roll, pitch, and yaw angle in degree.

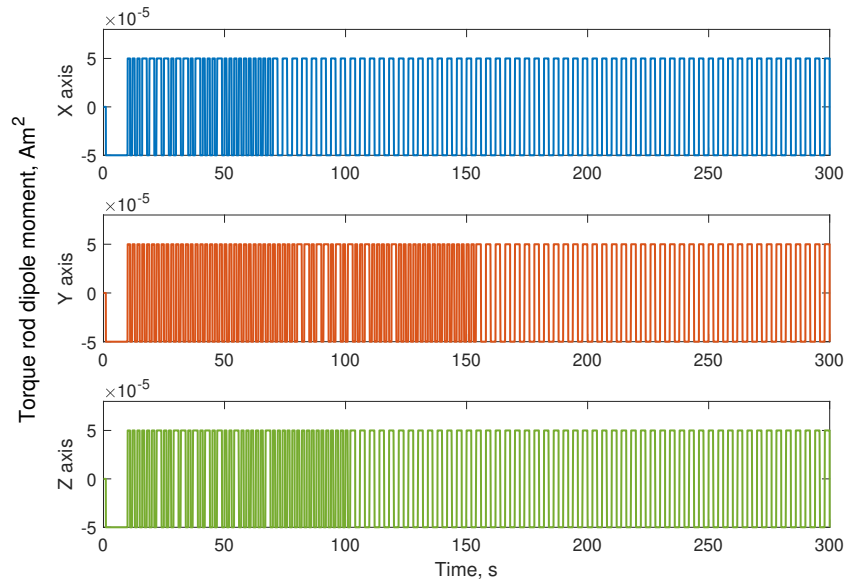


FIGURE 6.2. The total amount of dipole moment generated by each axis torque rod of the simulation using only EPM as the actuator.

Since the EPM is assumed to work only in "Bang-Bang" mode, when approaching the target angles, the controller sends the command to the EPM to change the magnetization direction back and forth due to the too strong torque input, which makes the system oscillates around the target angle. After adding the thrusters, this oscillation around the target angle due to the EPM can be well suppressed, and the pointing error discrepancy can be decreased by a factor

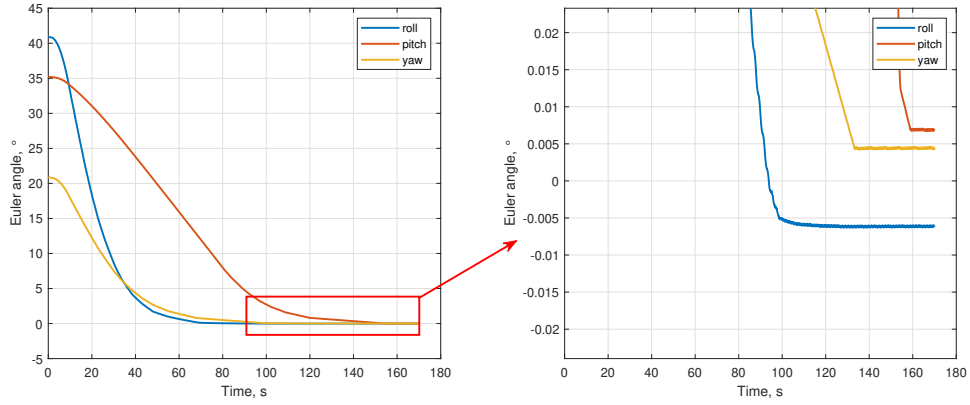


FIGURE 6.3. The system attitude history for the simulation using both EPM and μ AF-MPDT as the actuator. System angles are represented in roll, pitch, and yaw angle in degree.

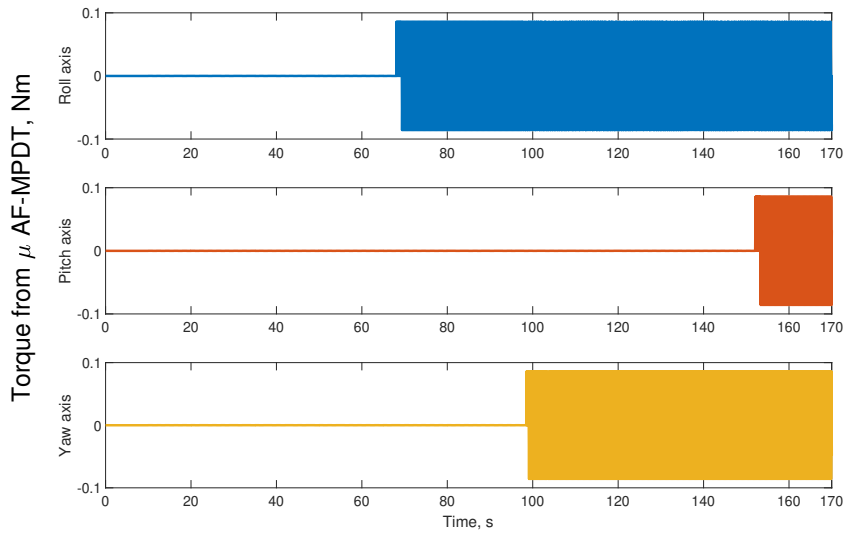


FIGURE 6.4. The three axis torque force generated by the thrusters of the simulation using both EPM and μ AF-MPDT as the actuator.

of around 10, reaching around $\pm 0.005^\circ$. Although the oscillation still exists due to the pulse mode operation, its magnitude is smaller than that generated by the EPM, which increases the control accuracy. Future studies could focus on developing another control algorithm for the magnetization of the torque rod to achieve a smoother and continuous control input to increase the control accuracy further and reduce the oscillation.

Although the control algorithm is proven to be capable of providing the attitude control with pointing error discrepancy of around $\pm 0.005^\circ$ with both actuators activated, the control law is not optimized in terms of power and propellant efficiency. Similar to the single torque rod single axis controller developed in section 3.3.5, numerous control commands were sent to the EPM to maintain the system on the designed sliding manifold, which is unnecessary and a waste of energy. Like the thrusters, a considerable amount of propellant and energy were wasted following the sliding manifold. Therefore another controller can be designed and implemented, focusing on energy and propellant optimization while maintaining and even improving the control accuracy and settling time.

6.4 Conclusion

A three-axis controller has been developed in this section and proven to meet the control target through mathematical calculation and MATLAB-based simulation. Simulations were performed with experimentally obtained system parameters from the previous sections with some assumed initial state and geometrical parameters. Two simulations were conducted, the first using only EPM as the actuator and the second using both EPM and μ AF-MPDT as the control input. The results show that a pointing error discrepancy of $\pm 0.05^\circ$ can be achieved using only EPM as the actuator, and the attitude angle oscillates around the target angle due to the use of the "Bang-off-Bang" operation method for the EPM. This oscillation problem can be well suppressed by replacing the EPM with μ AF-MPDT when the control error is smaller than around 0.05° for each axis, which reduces the oscillation amplitude and decreases the pointing error discrepancy to around 0.005° . Due to the pulse mode operation of the μ AF-MPDT and the "Bang-Bang" operation mode of the EPM, the steady state oscillation problem cannot be removed at this stage. Future studies could focus on a smoother control input for the EPM to remove the steady state oscillation and further increase control accuracy.

Conclusion and future work

A smart satellite attitude control system has been designed and developed in this thesis. The control system consists of a novel electro-permanent magnetorquer (EPM) that can generate magnetic dipole moment with controllable direction and strength and an ultra-compact micro air-fed magnetoplasmadynamic thruster (μ AF-MPDT), which utilizes normal air as the propellant to generate thrust force. Conventional magnetorquers utilize either air or soft magnetic material as the core material. Unlike conventional magnetorquers, the EPM utilized hard magnetic material as the core material, which is normally used as permanent magnet as it can hold the magnetization after the external magnetic field is removed. Since the EPM needs to change the magnetization direction and strength of the torque rod frequently, and the remaining magnetization strength shall be as high as possible to achieve a high dipole moment, the material shall have high residual induction and low coercive force. Therefore after comparing the properties of common hard magnetic material, the AlNiCo 5 has been selected to be the torque rod of the EPM. Since a relatively high external magnetic field is required to change the magnetization of the torque rod, a driving circuit based on the famous "RLC" circuit has been designed. The capacitance of the capacitor array and turns the copper wire winding to the torque rod, which will affect the series resistance and induced inductance, were analyzed mathematically. The optimal configurations in terms of magnetization and power efficiency have been analyzed. Although the EPM prototype configuration is not optimal in magnetization efficiency, it is at the boundary of the optimal region. The current configuration is selected due to the ease of in-house manufacture. Future studies could focus on experimentally validating the theoretical calculation of the optimal configuration in magnetization and power efficiency. The effect of the size of the torque rod on the dipole moment and magnetization has been investigated using both simulation and experiment. It has

been found that for one layer of copper wire fully covering the outer surface of a cylindrical torque rod, for a fixed torque rod length, increasing the diameter will increase the overall dipole moment and decrease the magnetization. For a torque rod with a fixed diameter, increasing the length of the torque rod will increase the dipole moment linearly. However, the magnetization of the torque rod increases with the increasing rod length and seems to be saturated when further increases the length. Final main torque rod are selected to be 6 mm in diameter and 60 mm in length. The EPM functionality has been tested experimentally. It has been found that the measured flux density of the torque rod is strongly related to the capacitor's initial charging voltage, which indicates that the dipole moment of the EPM could be adjusted by changing the capacitor charging voltage. The repeatability and demagnetization of the EPM have also been examined experimentally. The performance of the EPM has been experimentally measured using an in-house designed and manufactured Helmholtz cage and air bearing table (ABT). The Helmholtz cage has been calibrated, and the measured dipole moment for the X and Y torque rod is 1.287 A m^2 for the designed maximum capacitor initial charging voltage of 400 V. The single axis single torque rod detumbling experiment has been conducted on the ABT inside the Helmholtz cage. Using the famous "B-dot" control algorithm, one torque rod can detumble the ABT that has a moment of inertia of $\sim 0.0612 \text{ kg m}^2$ from around $27^\circ/\text{s}$ to almost static in around 800 s, with a total energy of $\sim 82.92 \text{ J}$ consumed. A simple single axis single torque rod sliding mode control algorithm for accurate attitude adjustment has been developed and tested on the same ABT inside the Helmholtz cage. The experiment shows that a single torque rod can achieve the target angle and maintain the error discrepancy within ± 0.4 degree boundary under a specific system configuration.

The EPM has been accepted to be embedded into CUAVA-2 6U CubeSat to perform an in-orbit test. An EPM payload board has been designed based on the EPM prototype board with several adjustments to meet the CUAVA-2 specifications. The board outline and layout have been adjusted following the specifications of the Pumpkin CubeSat circuit board. The main capacitor charging circuit has been replaced with the AH05-P DC-DC power module due to the voltage and power limit of the CUAVA-2. Interfaces have been changed to meet the connectivity requirements of the CUAVA-2 payload computer. The program, connectivity,

and communication of the EPM payload board has yet been tested when this thesis was being composed, and the payload board is pending thermal and vibration test.

As part of the smart attitude control system, a micro air-fed magnetoplasmadynamic thruster (μ AF-MPDT) has been developed using air as the propellant and operates in pulse mode. The thruster can generate $34.534 \mu\text{N s}$ impulse bit with a specific impulse of 2319 s . The average pulse time is 5.5 ms under the 1.857 W average input power, consuming 4.178 J pulse energy. The thrust to power ratio and overall efficiency is calculated to be $8.226 \mu\text{N/W}$ and 9.402% , respectively. The μ AF-MPDT utilizes air as propellant, making it a great actuator for small satellites with air-collecting devices for air-breathing-related missions. The thruster head features ultra-small form factor, which has only 8.9 mm in diameter and 8 mm in length. The thruster head can be directly embedded into the satellite frame and structure to reduce system size and complexity further.

A simple control algorithm has been developed for the smart attitude control system to achieve ultra-high pointing accuracy using both EPM and μ AF-MPDT. The simulations were made with experimentally obtained system performance parameters, some assumed platform parameters, and initial conditions. The simulation results show that when utilizing only the EPM in "Bang-off-Bang" mode, the final angle will oscillate within $\pm 0.04^\circ$ error boundary. The system oscillates around the target angle due to the strong control input and discrete operation mode. With the thrusters enabled, the oscillation can be well suppressed with the amplitude of 0.005° .

Due to some constraints and limitations, the work conducted in this thesis may not cover all aspects, and some design parameters used in the prototype are sub-optimal. There are some recommended directions for future study to cover aspects not covered in this thesis and further improve the current design. Firstly the optimized torque rod configurations in terms of magnetization and power efficiency could be experimentally validated. To achieve this, an improved manufacturing process shall be implemented to make multi-layer copper wire windings. Secondly, the method of monitoring the magnetization status of the torque rod could be improved by measuring the capacitor voltage during the pulse. Currently, the hall sensors are used to measure the flux density of the torque rod to determine if the desired magnetization

level has been reached, which increases the chance of being faulty due to extra components. A non-direct measurement method could reduce the use of extra components, increasing the success rate and reducing the system complexity. Thirdly, the three-axis experiments shall be conducted in future studies with a well-balanced ABT to test the system's complete performance. In addition, an improved control algorithm focusing on reducing the power consumption and settling time could be developed in future studies. To achieve that, another controller could be developed to control the magnetization of the torque rod in future studies to replace the current inefficient "Bang-Bang" control algorithm.

Bibliography

- [1] URL: <https://gomspace.com/UserFiles/Subsystems/datasheet/gs-ds-nanopower-p110-210.pdf> (visited on 09/07/2022).
- [2] URL: <http://hyperphysics.phy-astr.gsu.edu/hbase/Tables/magprop.html#c2> (visited on 12/07/2022).
- [3] URL: <https://www.kjmagnetics.com/blog.asp?p=magnet-grade#BH> (visited on 14/07/2022).
- [4] URL: <http://what-when-how.com/electric-motors/hard-magnetic-materials-permanent-magnets-electric-motors/> (visited on 14/07/2022).
- [5] URL: <https://magnetsim.com/grades/LNG40> (visited on 16/07/2022).
- [6] URL: https://ucpcdn.thyssenkrupp.com/_binary/UCPthyssenkruppBAMXSchulten/products/permanent-magnets/link-thyssenkruppMagnettechnik-Factsheet-AINiCo-magnets.pdf (visited on 17/07/2022).
- [7] KS Ahmed et al. 'Optimized Design and Analysis of Printed Magnetorquer for a 3-U Nano-Satellite'. In: *Journal of Aerospace Engineering* 35.1 (2022), p. 04021103.
- [8] A Ali et al. 'Embedded magnetorquer for the more demanding multi-cube small satellites'. In: *The Aeronautical Journal* (2022), pp. 1–13.
- [9] A Ali et al. 'Embedded magnetorquer for the more demanding multi-cube small satellites'. In: *The Aeronautical Journal* (2022), pp. 1–13.
- [10] H Ali et al. 'Design and analysis of a rectangular PCB printed magnetorquer for nanosatellites'. In: *IEEE Journal on Miniaturization for Air and Space Systems* 2.3 (2020), pp. 105–111.
- [11] L Alminde et al. 'Educational value and lessons learned from the AAU-CubeSat project'. In: *International Conference on Recent Advances in Space Technologies, 2003. RAST'03. Proceedings of. IEEE*. 2003, pp. 57–62.

- [12] AFR Alvarez, Edinson Franco-Mejia and Carlos R Pinedo-Jaramillo. ‘Study and analysis of magnetic field homogeneity of square and circular Helmholtz coil pairs: A Taylor series approximation’. In: *2012 VI Andean Region International Conference*. IEEE. 2012, pp. 77–80.
- [13] T Andreussi et al. ‘Development Status and Way Forward of SITAEL’s Air-breathing Electric Propulsion Engine’. In: *AIAA Propulsion and Energy 2019 Forum*. 2019, p. 3995.
- [14] H Ashida et al. ‘Design of Tokyo Tech nano-satellite Cute-1.7+ APD II and its operation’. In: *Acta Astronautica* 66.9-10 (2010), pp. 1412–1424.
- [15] M Azuara Rosales, Robert M Winglee and Corwin A Hansen. ‘Theoretical and Experimental Analysis for an Air-Breathing Pulsed Plasma Thruster’. In: *AIAA Propulsion and Energy 2019 Forum*. 2019, p. 3888.
- [16] X Bai et al. ‘The CUAVA-1 CubeSat—a pathfinder satellite for remote sensing and Earth observation’. In: *Proceedings of the AIAA/USU Conference on Small Satellites 2021*. University of Utah. 2021, SSC21–WKII.
- [17] OV Batishchev. ‘Minihelicon Plasma Thruster’. In: *IEEE Transactions on Plasma Science* 37.8 (2009), pp. 1563–1571. DOI: [10.1109/TPS.2009.2023990](https://doi.org/10.1109/TPS.2009.2023990).
- [18] N Bellini. ‘Magnetic actuators for nanosatellite attitude control’. 2014.
- [19] *Biot-Savart Law*. URL: <http://hyperphysics.phy-astr.gsu.edu/hbase/magnetic/Biosav.html#c1> (visited on 26/07/2022).
- [20] A Blanchet et al. ‘Plasma Jet Pack Technology for Nano-Microsatellites’. In: *36th International Electric Propulsion Conference, IEPC-2019-271*. 2019.
- [21] M van den Bos. ‘Design and Testing of Magnetic Torquers for Pico Satellite Attitude Control’. 2019.
- [22] MR Brewer. *CubeSat attitude determination and helmholtz cage design*. Tech. rep. AIR FORCE INST OF TECH WRIGHT-PATTERSON AFB OH GRADUATE SCHOOL OF ..., 2012.
- [23] *BT151S Data-sheet*. URL: <https://www.ween-semi.com/sites/default/files/2018-10/bt151s-6501.pdf> (visited on 20/07/2022).

- [24] MM Burlacu and Pascal Lorenz. ‘A survey of small satellites domain: challenges, applications and communications key issues’. In: *ICaST, Institute for Computer Sciences, Social-Informatics and Telecommunications Engineering (ICST)* (2010), pp. 1–11.
- [25] RJ Cassady et al. ‘A Micro Pulsed Plasma Thruster (PPT) for the ‘Dawgstar’ Spacecraft’. In: *2000 IEEE Aerospace Conference. Proceedings (Cat. No. 00TH8484)*. Vol. 4. IEEE, Mar. 2000, pp. 7–14. DOI: [10.1109/AERO.2000.878359](https://doi.org/10.1109/AERO.2000.878359).
- [26] FF Chen. ‘Ion Ejection from a Permanent-Magnet Mini-Helicon Thruster’. In: *Physics of Plasmas* 21.9 (2014), p. 093511. DOI: [10.1063/1.4896238](https://doi.org/10.1063/1.4896238).
- [27] J Chen, Jian Li and Ronghai Qu. ‘Maximum-torque-per-ampere and magnetization-state control of a variable-flux permanent magnet machine’. In: *IEEE Transactions on Industrial Electronics* 65.2 (2017), pp. 1158–1169.
- [28] EY Choueiri and JK Ziemer. ‘Quasi-Steady Magnetoplasmadynamic Thruster Performance Database’. In: *Journal of Propulsion and Power* 17.5 (2001), pp. 967–976. DOI: [10.2514/2.5857](https://doi.org/10.2514/2.5857).
- [29] CUAVA-1. URL: <https://www.cuava.com.au/projects/cuava-1/> (visited on 01/08/2022).
- [30] CUAVA-1 Details. URL: <https://www.nanosats.eu/sat/cuava-1> (visited on 01/08/2022).
- [31] Cubetorquer. URL: <https://www.cubespace.co.za/products/adcs-components/cubetorquer/#cubetorquer-specifications> (visited on 07/07/2022).
- [32] *Damped and Driven Oscillations*. URL: [https://phys.libretexts.org/Bookshelves/University_Physics/Book%3C%3A_Physics_\(Boundless\)/15%5C%3A_Waves_and_Vibrations/15.4%5C%3A_Damped_and_Driven_Oscillations](https://phys.libretexts.org/Bookshelves/University_Physics/Book%3C%3A_Physics_(Boundless)/15%5C%3A_Waves_and_Vibrations/15.4%5C%3A_Damped_and_Driven_Oscillations) (visited on 29/07/2022).
- [33] N Derby and Stanislaw Olbert. ‘Cylindrical magnets and ideal solenoids’. In: *American Journal of Physics* 78.3 (2010), pp. 229–235.
- [34] MAA Desouky and Ossama Abdelkhalik. ‘A new variant of the B-dot control for spacecraft magnetic detumbling’. In: *Acta Astronautica* 171 (2020), pp. 14–22.

- [35] G Dressler. ‘Spacecraft propulsive device using ambient upper atmospheric constituents for reaction mass’. In: *42nd AIAA/ASME/SAE/ASEE Joint Propulsion Conference & Exhibit*. 2006, p. 4650.
- [36] *Earth magnetic field*. URL: <https://www.magnetic-declination.com/Australia/Sydney/124736.html> (visited on 27/07/2022).
- [37] Y Eun, Wang Zihao and Wu Xiaofeng. ‘Parametric Study on the Magnetic Properties of the Electropermanent Magnetorquer’. In: *The Proceedings of the 2021 Asia-Pacific International Symposium on Aerospace Technology (APISAT 2021)*. Springer. 2021.
- [38] *Exa MT01 Compact Magnetorquer*. Dec. 2021. URL: <https://www.cubesatshop.com/product/mt01-compact-magnetorquer/> (visited on 06/07/2022).
- [39] RE Fischell. ‘Spin control for earth satellites’. In: *Peaceful Uses of Automation in Outer Space*. Springer, 1966, pp. 211–218.
- [40] J Frey. ‘Hardware and software implementation of a low power attitude control and determination system for cubesats’. University of Alaska Fairbanks, 2014.
- [41] J Frey, Joseph Hawkins and Denise Thorsen. ‘Magnetometer calibration in the presence of hard magnetic torquers’. In: *2014 IEEE Aerospace Conference*. IEEE. 2014, pp. 1–6.
- [42] M Getzlaff. ‘Introduction’. In: *Fundamentals of Magnetism*. Berlin, Heidelberg: Springer Berlin Heidelberg, 2008, pp. 1–6. ISBN: 978-3-540-31152-2. DOI: [10.1007/978-3-540-31152-2_1](https://doi.org/10.1007/978-3-540-31152-2_1). URL: https://doi.org/10.1007/978-3-540-31152-2_1.
- [43] SMA Ghaly and Mohammad Obaidullah Khan. ‘Design, simulation, modeling, and implementation of a square helmholtz coil in contrast with a circular coil for MRI applications’. In: *Engineering, Technology & Applied Science Research* 9.6 (2019), pp. 4990–4995.
- [44] J Gilliam. ‘Attitude Determination and Control of ARKSAT-1’. 2020.
- [45] MS Glascock, Joshua L Rovey and Kurt A Polzin. ‘Specific Impulse of Electric Solid Propellant in an Electrothermal Ablation-fed Pulsed Plasma Thruster’. In: *36th International Electric Propulsion Conference, IEPC-2019-421*. 2019.

- [46] H Gong and Shengping Gong. ‘Design of foldable PCBSat enabling three-axis attitude control’. In: *Acta Astronautica* 192 (2022), pp. 291–300.
- [47] A Gurciullo et al. ‘Experimental performance and plume characterisation of a miniaturised 50W Hall thruster’. In: *36th International Electric Propulsion Conference, IEPC-2019-142*. 2019.
- [48] TW Haag. ‘Thrust Stand for Pulsed Plasma Thrusters’. In: *Review of Scientific Instruments* 68.5 (1997), pp. 2060–2067. DOI: [10.1063/1.1148097](https://doi.org/10.1063/1.1148097).
- [49] M Hall, JG Bartholomew and LCA Henderson. ‘Measurement of the magnetic dipole moment of ferromagnetic material specimens.’ In: (2001).
- [50] MA Hopkins and Lyon B King. ‘Performance Comparison Between a Magnesium-and Xenon-Fueled 2 Kilowatt Hall Thruster’. In: *Journal of Propulsion and Power* 32.4 (Apr. 2016), pp. 1015–1021. DOI: [10.2514/1.B35731](https://doi.org/10.2514/1.B35731).
- [51] *How to Select the Appropriate Permanent Magnet Material*. URL: https://www.arnoldmagnetics.com/wp-content/uploads/2017/10/TN_0205_rev_150716-1.pdf (visited on 15/07/2022).
- [52] TK Imken, Terry H Stevenson and E Glenn Lightsey. ‘Design and Testing of a Cold Gas Thruster for an Interplanetary CubeSat Mission’. In: *Journal of Small Satellites* 4.2 (2015), pp. 371–386. URL: <https://pdfs.semanticscholar.org/c310/ba2bda5fb1770eb0821aac343f4756cfa592.pdf>.
- [53] *IMTQ Magnetorquer Board*. June 2022. URL: <https://www.isispace.nl/product/isis-magnetorquer-board/> (visited on 06/07/2022).
- [54] Inc. ITHACO. *Development and Fabrication of a Chargeable Magnet System for Spacecraft Control*. NASA-CR-130077. NASA, 27th July 1972. URL: <https://ntrs.nasa.gov/citations/19720026222> (visited on 14/07/2022).
- [55] DS Ivanov et al. ‘Testing of attitude control algorithms for microsatellite “Chibis-M” at laboratory facility’. In: *Journal of Computer and Systems Sciences International* 51.1 (2012), pp. 106–125.
- [56] SW Jackson and Robert Marshall. ‘Conceptual design of an air-breathing electric thruster for CubeSat applications’. In: *Journal of Spacecraft and Rockets* 55.3 (2018), pp. 632–639. DOI: [10.2514/1.A33993](https://doi.org/10.2514/1.A33993).

- [57] J Jarrige et al. 'Thrust Measurements of the Gaia Mission Flight-Model Cold Gas Thrusters'. In: *Journal of Propulsion and Power* 30.4 (2014), pp. 934–943. DOI: [10.2514/1.B35091](https://doi.org/10.2514/1.B35091).
- [58] M Jesenik, Marjan Mernik and Mladen Trlep. 'Determination of a hysteresis model parameters with the use of different evolutionary methods for an innovative hysteresis model'. In: *Mathematics* 8.2 (2020), p. 201.
- [59] N Jovanovic et al. 'Design of Magnetorquer-Based Attitude Control Subsystem for FORESAIL-1 Satellite'. In: *IEEE Journal on Miniaturization for Air and Space Systems* 2.4 (2021), pp. 220–235.
- [60] G Juchnikowski, T Barcinski and J Lisowski. 'Optimal control gain for satellite detumbling using B-dot algorithm'. In: *2nd CEAS Specialist Conference on Guidance, Navigation and Control*. 2013, pp. 1158–1168.
- [61] LJ Kamm. 'Magnetorquer-a satellite orientation device'. In: *ARS Journal* 31.6 (1961), pp. 813–815.
- [62] B Karaoglu. 'Magnetic Field'. In: *Classical Physics: A Two-Semester Coursebook*. Cham: Springer International Publishing, 2020, pp. 319–330. ISBN: 978-3-030-38456-2. DOI: [10.1007/978-3-030-38456-2_19](https://doi.org/10.1007/978-3-030-38456-2_19). URL: https://doi.org/10.1007/978-3-030-38456-2_19.
- [63] B Karaoglu. 'Sources of Magnetic Field'. In: *Classical Physics: A Two-Semester Coursebook*. Cham: Springer International Publishing, 2020, pp. 331–349. ISBN: 978-3-030-38456-2. DOI: [10.1007/978-3-030-38456-2_20](https://doi.org/10.1007/978-3-030-38456-2_20). URL: https://doi.org/10.1007/978-3-030-38456-2_20.
- [64] SA Khan et al. 'Reconfigurable asymmetric embedded magnetorquers for attitude control of nanosatellites'. In: *IEEE Journal on Miniaturization for Air and Space Systems* 2.4 (2021), pp. 236–243.
- [65] J Köhler et al. 'A Hybrid Cold Gas Microthruster System for Spacecraft'. In: *Sensors and Actuators A: Physical* 97 (2002), pp. 587–598. DOI: [10.1016/S0924-4247\(01\)00805-6](https://doi.org/10.1016/S0924-4247(01)00805-6).

- [66] H Koizumi, Kimiya Komurasaki and Yoshihiro Arakawa. ‘Development of Thrust Stand for Low Impulse Measurement from Microthrusters’. In: *Review of Scientific Instruments* 75.10 (2004), pp. 3185–3190. DOI: [10.1063/1.1790568](https://doi.org/10.1063/1.1790568).
- [67] H Koizumi et al. ‘Performance improvement of a liquid propellant pulsed plasma thruster’. In: *Proceedings of 29th International Electric Propulsion Conference, Princeton, NJ*. 2005-69. 2005.
- [68] J Kolbeck et al. ‘Micro-propulsion based on vacuum arcs’. In: *Journal of Applied Physics* 125.22 (2019), p. 220902. DOI: [10.1063/1.5081096](https://doi.org/10.1063/1.5081096).
- [69] JR Kopacz, Roman Herschitz and Jason Roney. ‘Small satellites an overview and assessment’. In: *Acta Astronautica* 170 (2020), pp. 93–105.
- [70] HJ Kramer and Arthur P Cracknell. ‘An overview of small satellites in remote sensing’. In: *International journal of remote Sensing* 29.15 (2008), pp. 4285–4337.
- [71] M Kuehn et al. ‘Solid fuel vacuum arc thrusters-new concepts for space propulsion’. In: *35th International Electric Propulsion Conference, IEPC-2017-35, Atlanta, GA*. 2017.
- [72] W Kun-Long et al. ‘Design and Experimental Study of a Miniature Ion Thruster’. In: *36th International Electric Propulsion Conference, IEPC-2019-175*. 2019.
- [73] D Kuwahara, Shunjiro Shinohara and Kazuki Yano. ‘Thrust Characteristics of High-Density Helicon Plasma using Argon and Xenon Gases’. In: *Journal of Propulsion and Power* 33.2 (2017), pp. 420–424. DOI: [10.2514/1.B36199](https://doi.org/10.2514/1.B36199).
- [74] JP Lake et al. *Resonant Operation of a Micro-Newton Thrust Stand*. Tech. rep. Edwards AFB, CA: U.S. Air Force Research Lab., Space and Missile Propulsion Division, TR AFRL-PR-ED-TP-2002-308, Jan. 2003.
- [75] V Lappas and Vassilis Kostopoulos. ‘A Survey on Small Satellite Technologies and Space Missions for Geodetic Applications’. In: *Satellites Missions and Technologies for Geosciences*. IntechOpen, 2020. DOI: [10.5772/intechopen.92625](https://doi.org/10.5772/intechopen.92625).
- [76] U Lee et al. ‘Development of Attitude Determination and Control Subsystem for 3U CubeSat with Electric Propulsion’. In: *AIAA SPACE and Astronautics Forum and Exposition*. 2017, p. 5320.

- [77] K Lemmer. ‘Propulsion for Cubesats’. In: *Acta Astronautica* 134 (2017), pp. 231–243. DOI: [10.1016/j.actaastro.2017.01.048](https://doi.org/10.1016/j.actaastro.2017.01.048).
- [78] I Levchenko et al. ‘Explore space using swarms of tiny satellites’. In: *Nature* 562 (2018), pp. 185–187. DOI: [10.1038/d41586-018-06957-2](https://doi.org/10.1038/d41586-018-06957-2).
- [79] I Levchenko et al. ‘Hopes and concerns for astronomy of satellite constellations’. In: *Nature Astronomy* 4.11 (2020), pp. 1012–1014. DOI: [10.1038/s41550-020-1141-0](https://doi.org/10.1038/s41550-020-1141-0).
- [80] I Levchenko et al. ‘Perspectives, frontiers, and new horizons for plasma-based space electric propulsion’. In: *Physics of Plasmas* 27.2 (2020), p. 020601. DOI: [10.1063/1.5109141](https://doi.org/10.1063/1.5109141).
- [81] Y Li, Jun-You Pan and Georg Herdrich. ‘Design and demonstration of micro-scale vacuum cathode arc thruster with inductive energy storage circuit’. In: *Acta Astronautica* (2020). DOI: [10.1016/j.actaastro.2020.03.012](https://doi.org/10.1016/j.actaastro.2020.03.012).
- [82] Y Li et al. ‘Design and analysis of vacuum air-intake device used in air-breathing electric propulsion’. In: *Vacuum* 120 (2015), pp. 89–95. DOI: [10.1016/j.vacuum.2015.06.011](https://doi.org/10.1016/j.vacuum.2015.06.011).
- [83] JWM Lim et al. ‘Precise calibration of propellant flow and forces in specialized electric propulsion test system’. In: *IEEE Transactions on Plasma Science* 46.2 (2017), pp. 338–344. DOI: [10.1109/TPS.2017.2783954](https://doi.org/10.1109/TPS.2017.2783954).
- [84] M Long et al. ‘A cubesat derived design for a unique academic research mission in earthquake signature detection’. In: *Proc. AIAA Small Satellite Conference*. 2002.
- [85] *Low Earth orbit*. URL: [https://www.esa.int/ESA_Multimedia/Images/2020/03/Low_Earth_orbit#:~:text=A%5C%20low%5C%20Earth%5C%20orbit%5C%20\(LEO,very%5C%20far%5C%20above%5C%20Earth's%5C%20surface](https://www.esa.int/ESA_Multimedia/Images/2020/03/Low_Earth_orbit#:~:text=A%5C%20low%5C%20Earth%5C%20orbit%5C%20(LEO,very%5C%20far%5C%20above%5C%20Earth's%5C%20surface). (visited on 30/06/2022).
- [86] *LT3750 Data-sheet*. URL: <https://www.analog.com/media/en/technical-documentation/data-sheets/3750fa.pdf> (visited on 19/07/2022).
- [87] Willy M. *RLC natural response - variations*. June 2022. URL: <https://spinningnumbers.org/a/rlc-natural-response-variations.html> (visited on 26/06/2022).

- [88] *Magnetorquers MTQ3X*. URL: <https://satsearch.co/products/nanoavionics-magnetorquers-mtq3x> (visited on 07/07/2022).
- [89] AC Malliaris et al. 'Performance of Quasi-Steady MPD Thrusters at High Powers'. In: *AIAA journal* 10.2 (1972), pp. 121–122. DOI: [10.2514/3.50074](https://doi.org/10.2514/3.50074).
- [90] S Mazouffre. 'Electric Propulsion for Satellites and Spacecraft: established technologies and novel approaches'. In: *Plasma Sources Science and Technology* 25.3 (2016). DOI: [10.1088/0963-0252/25/3/033002](https://doi.org/10.1088/0963-0252/25/3/033002).
- [91] DB Mentch. 'CubeSat attitude control utilizing low-power magnetic torquers & a magnetometer'. University of Alaska Fairbanks, 2011.
- [92] RM Millan et al. 'Small satellites for space science: A COSPAR scientific roadmap'. In: *Advances in space research* 64.8 (2019), pp. 1466–1517. DOI: [10.1016/j.asr.2019.07.035](https://doi.org/10.1016/j.asr.2019.07.035).
- [93] Y Mimasu et al. 'Attitude determination and control system for QSAT'. In: *17th Workshop on Astrodynamics and Flight Mechanics, ISAS/JAXA, 23rd-24th*. 2007.
- [94] D Modenini et al. 'A dynamic testbed for nanosatellites attitude verification'. In: *Aerospace* 7.3 (2020), p. 31.
- [95] J Mueller, Richard Hofer and John Ziemer. *Survey of propulsion technologies applicable to cubesats*. Tech. rep. Jet Propulsion Laboratory, 2010. URL: <http://hdl.handle.net/2014/41627>.
- [96] MR Mughal et al. 'Optimized design and thermal analysis of printed magnetorquer for attitude control of reconfigurable nanosatellites'. In: *IEEE Transactions on Aerospace and Electronic Systems* 56.1 (2019), pp. 736–747.
- [97] *NCTR-M002 magnetorquer rod*. Dec. 2021. URL: <https://www.cubesatshop.com/product/nctr-m002-magnetorquer-rod/> (visited on 07/07/2022).
- [98] M Palmroth et al. 'FORESAIL-1 CubeSat Mission to measure radiation belt losses and demonstrate deorbiting'. In: *Journal of Geophysical Research: Space Physics* 124.7 (2019), pp. 5783–5799.
- [99] KI Parker. 'State-of-the-Art for Small Satellite Propulsion Systems'. In: *4th 2016 biennial Aerospace Systems Conference of the National Society of Black Engineers (NSBE), NASA GSFC-E-DAA-TN33641*. Arlington, VA, Aug. 2016.

- [100] *PCB specifications for Pumpkin CubeSat kit*. URL: http://www.cubesatkit.com/docs/CSK_PCB_Spec-A5.pdf (visited on 03/08/2022).
- [101] M Pietzka. ‘Development and Characterization of a Propulsion System for CubeSats based on Vacuum Arc Thrusters’. PhD thesis. Neubiberg, Germany: Universitätsbibliothek der Universität der Bundeswehr München, 2016.
- [102] M Polites, C Quarles and D Kaderbek. ‘Pulse width modulating low power magnetic torquers for precise spacecraft attitude stabilization’. In: *Proceedings of the Institution of Mechanical Engineers, Part G: Journal of Aerospace Engineering* 219.6 (2005), pp. 471–482.
- [103] M Polites et al. ‘A spacecraft attitude stabilization system with low-power magnetic torquers’. In: *Proceedings of the Institution of Mechanical Engineers, Part G: Journal of Aerospace Engineering* 218.2 (2004), pp. 99–109.
- [104] ME Polites and Charles A Gibson. ‘A low-power magnetic torquer for satellite attitude control’. In: *The Space Congress@ Proceedings*. Vol. 1. 1971, pp. 7-21 7–30.
- [105] S Pottinger et al. ‘Performance Characterization of a Helicon Double Layer Thruster using Direct Thrust Measurements’. In: *Journal of Physics D: Applied Physics* 44.23 (2011), p. 235201. DOI: [10.1088/0022-3727/44/23/235201](https://doi.org/10.1088/0022-3727/44/23/235201).
- [106] SJ Pottinger and CA Scharlemann. ‘Micro Pulsed Plasma Thruster Development’. In: *30th International Electric Propulsion Conference, IEPC-2007-125*. 2007.
- [107] S Rawashdeh and James Lumpp. ‘Nano-satellite passive attitude stabilization systems design by orbital environment modeling and simulation’. In: *AIAA Infotech@ Aerospace 2010*. 2010, p. 3413.
- [108] C Rayburn et al. ‘Development of a micro pulsed plasma thruster for the Dawgstar nanosatellite’. In: *36th AIAA/ASME/SAE/ASEE Joint Propulsion Conference and Exhibit*. 2000, p. 3256.
- [109] CD Rayburn, Mark E Campbell and A Thomas Mattick. ‘Pulsed Plasma Thruster System for Microsatellites’. In: *Journal of Spacecraft and Rockets* 42.1 (2005), pp. 161–170. DOI: [10.2514/1.15422](https://doi.org/10.2514/1.15422).

- [110] A Rezaeiha and Tony Schönherr. ‘Review of worldwide activities in liquid-fed pulsed plasma thruster’. In: *Journal of Propulsion and Power* 30.2 (2014), pp. 253–264. DOI: [10.2514/1.B34807](https://doi.org/10.2514/1.B34807).
- [111] B Riwanto. ‘Cubesat attitude system calibration and testing’. 2015.
- [112] F Romano et al. ‘System analysis and test-bed for an atmosphere-breathing electric propulsion system using an inductive plasma thruster’. In: *Acta Astronautica* 147 (2018), pp. 114–126. DOI: [10.1016/j.actaastro.2018.03.031](https://doi.org/10.1016/j.actaastro.2018.03.031).
- [113] P Saevets et al. ‘Development of a long-life low-power Hall thruster’. In: *The 35th International Electric Propulsion Conference, IEPC-2017-38, Atlanta, GA*. 2017.
- [114] SA Samples and Richard E Wirz. ‘Development Status of the Miniature Xenon Ion Thruster’. In: *36th International Electric Propulsion Conference, IEPC-2019-143*. 2019.
- [115] R Sandau, Klaus Brieß and Marco D’Errico. ‘Small satellites for global coverage: Potential and limits’. In: *ISPRS Journal of photogrammetry and Remote Sensing* 65.6 (2010), pp. 492–504.
- [116] A Sasoh and Yoshihiro Arakawa. ‘A High-Resolution Thrust Stand for Ground Tests of Low-Thrust Space Propulsion Devices’. In: *Review of Scientific Instruments* 64.3 (1993), pp. 719–723. DOI: [10.1063/1.1144204](https://doi.org/10.1063/1.1144204).
- [117] A Scholz et al. ‘Flight results of the COMPASS-1 picosatellite mission’. In: *Acta Astronautica* 67.9-10 (2010), pp. 1289–1298.
- [118] T Schönherr et al. ‘Analysis of atmosphere-breathing electric propulsion’. In: *IEEE Transactions on Plasma Science* 43.1 (2014), pp. 287–294. DOI: [10.1109/TPS.2014.2364053](https://doi.org/10.1109/TPS.2014.2364053).
- [119] S Shinohara et al. ‘Development of Electrodeless Plasma Thrusters with High-Density Helicon Plasma Sources’. In: *IEEE Transactions on Plasma Science* 42.5 (2014), pp. 1245–1254. DOI: [10.1109/TPS.2014.2313633](https://doi.org/10.1109/TPS.2014.2313633).
- [120] RC da Silva et al. ‘Helmholtz cage design and validation for nanosatellites HWIL testing’. In: *IEEE Transactions on Aerospace and Electronic Systems* 55.6 (2019), pp. 3050–3061.

- [121] JJE Slotine, Weiping Li et al. *Applied nonlinear control*. Vol. 199. 1. Prentice hall Englewood Cliffs, NJ, 1991.
- [122] A Solbes, Keith Thomassen and Robert J Vondra. ‘Analysis of Solid Teflon Pulsed Plasma Thruster’. In: *Journal of Spacecraft and Rockets* 7.12 (1970), pp. 1402–1406. DOI: [10.2514/3.30181](https://doi.org/10.2514/3.30181).
- [123] P Song et al. ‘Micro-Newton Electrospray Thrusters for China’s Space-Borne Gravitational Wave Detection Mission (TianQin)’. In: *36th International Electric Propulsion Conference, IEPC-2019- A-284*. 2019.
- [124] NJ Sorensen. ‘Efficiency-optimized design of PCB-integrated magnetorquers for CubeSats’. In: *IEEE Transactions on Aerospace and Electronic Systems* 57.6 (2021), pp. 3623–3632.
- [125] JS Sovey and Maris A Mantenicks. ‘Performance and Lifetime Assessment of Magnetoplasma-dynamic Arc Thruster Technology’. In: *Journal of Propulsion and Power* 7.1 (1991), pp. 71–83. DOI: [10.2514/3.23296](https://doi.org/10.2514/3.23296).
- [126] AC Stickler and KT Alfrend. ‘Elementary magnetic attitude control system’. In: *Journal of spacecraft and rockets* 13.5 (1976), pp. 282–287.
- [127] LN Stras et al. ‘The design and operation of the Canadian advanced nanospace eXperiment (CanX-1)’. In: *Proc. AMSAT-NA 21st Space Symposium, Toronto, Canada*. Citeseer. 2003, pp. 150–160.
- [128] M Sweeting. ‘Modern small satellites-changing the economics of space’. In: *Proceedings of the IEEE* 106.3 (2018), pp. 343–361.
- [129] J Szabo, Mike Robin and Vlad Hruby. ‘Bismuth Vapor Hall Effect Thruster Performance and Plume Experiments’. In: *the 35th International Electric Propulsion Conference, Atlanta, Georgia, USA, IEPC-2017-25*. 2017, pp. 2017–25.
- [130] J Szabo et al. ‘Measurements of a krypton fed 1.5 kW Hall effect thruster with a centrally located cathode’. In: *the 35th International Electric Propulsion Conference, Atlanta, Georgia, USA, IEPC-2017-26*. 2017.
- [131] J Szabo et al. ‘Performance Evaluation of an Iodine-Vapor Hall Thruster’. In: *Journal of Propulsion and Power* 28.4 (2012), pp. 848–857. DOI: [10.2514/1.B34291](https://doi.org/10.2514/1.B34291).

- [132] S Tumanski. 'Handbook of magnetic measurements'. In: CRC press, 2016, p. 145. ISBN: 9780429103902. DOI: [10.1201/b10979](https://doi.org/10.1201/b10979).
- [133] DM Velez, Elizabeth I Dawson and Nell Elizabeth Nassiff. 'Attitude Determination and Control Subsystem Design for a CubeSat'. In: *Worcester Polytechnic Institute, Worcester* (2012).
- [134] Z Wang, Youngho Eun and Xiaofeng Wu. 'Design and demonstration of a micro air-fed magnetoplasmadynamic thruster for small satellites'. In: *Acta Astronautica* 181 (2021), pp. 482–491.
- [135] H Watanabe et al. 'Performance Evaluation of a Two-Kilowatt Magnetically Shielded Hall Thruster'. In: *Journal of Propulsion and Power* 36.1 (Nov. 2019), pp. 1–11. DOI: [10.2514/1.B37550](https://doi.org/10.2514/1.B37550).
- [136] Peter Wilson. 'Chapter 3 - Passive Components'. In: *The Circuit Designer's Companion (Fourth Edition)*. Ed. by Peter W. Fourth Edition. Newnes, 2017, p. 139. ISBN: 978-0-08-101764-7. DOI: <https://doi.org/10.1016/B978-0-08-101764-7.00003-7>. URL: <https://www.sciencedirect.com/science/article/pii/B9780081017647000037>.
- [137] X Xia et al. 'Nanosats/cubesats adcs survey'. In: *2017 29th Chinese Control And Decision Conference (CCDC)*. IEEE. 2017, pp. 5151–5158.
- [138] X Xia et al. 'Revisit to B-dot Rate Damping Algorithm'. In: *2021 40th Chinese Control Conference (CCC)*. IEEE. 2021, pp. 7903–7908.
- [139] Y Yang et al. 'A Torsion Balance for Impulse and Thrust Measurements of Micro-Newton Thrusters'. In: *Review of Scientific Instruments* 83.1 (2012). DOI: [10.1063/1.3675576](https://doi.org/10.1063/1.3675576).
- [140] T Yoshinori et al. 'Development of Ionic Liquid Electrospray Thrusters with a Massive Emitter Array for Higher Thrust Density'. In: *36th International Electric Propulsion Conference, IEPC-2019-149*. 2019.
- [141] J Ziemer and E Choueiri. 'Dimensionless performance model for gas-fed pulsed plasma thrusters'. In: *34th AIAA/ASME/SAE/ASEE Joint Propulsion Conference and Exhibit*. 1998, p. 3661.

- [142] J Ziemer, Edgar Choueiri and Daniel Birx. ‘Is the gas-fed PPT an electromagnetic accelerator? An investigation using measured performance’. In: *35th Joint Propulsion Conference and Exhibit*. 1999, p. 2289.
- [143] J Ziemer et al. ‘Performance characterization of a high efficiency gas-fed pulsed plasma thruster’. In: *33rd Joint Propulsion Conference and Exhibit*. 1997, p. 2925.
- [144] JK Ziemer. *Performance Measurements Using a Sub-Micronewton Resolution Thrust Stand*. Tech. rep. 27th International Electric Propulsion Conference, Paper IEPC-01-238, Pasadena, CA, Oct. 2001.
- [145] DB Zolotukhin et al. ‘Magnetoplasmadynamic two-stage micro-cathode arc thruster for CubeSats’. In: *Plasma Sources Science and Technology* 28.10 (2019), p. 105001. DOI: [10.1088/1361-6595/ab4170](https://doi.org/10.1088/1361-6595/ab4170).

1 Appendix A: MATLAB Code for detumbling experiment

```
clearvars -except s

if (exist('s') == 0)
    s = serialport("COM13",115200);
else
    flush(s) ;
end

x=1;
if (x==1)
    addpath(genpath(pwd))

    fprintf('NatNet Polling Sample Start\n')
    % create an instance of the natnet client class
    fprintf('Creating natnet class object\n')
    natnetclient = natnet;
```

```
natnetclient.HostIP = '169.254.104.249';
natnetclient.ClientIP = '169.254.104.249';
natnetclient.ConnectionType = 'Multicast';

fprintf( 'Connecting to the server\n' )
natnetclient.connect;
if ( natnetclient.IsConnected == 0 )
fprintf( 'Client failed to connect\n' )
fprintf( '\tMake sure the host is connected to ...
        the network\n' )
fprintf( '\tand that the host and client IP addresses ...
        are correct\n\n' )
return
end
figure
fig = plot(0,0);
data = zeros(1e4,7) ;
t = [];
t_old = 0;
euler = [];
angle_tmp = zeros(100,1);
angle_mean= 0;
angle_old = 0;
angle = 0;
coolDown = 0;
err = 0;
polar = 0;
polar_old = 0;
stop = 0;
direction = 1;
```

```

tic
i = 1;
j = 1;
fileID = fopen('Detumble_X1000_6.txt','w');
fprintf(fileID,'%s\n',"Time,theta,polar");
motor = 0 ;
while(toc < 1000)
    packet = natnetclient.getFrame;
    t(i) = toc ;
    data(i,1) = packet.RigidBody(1).x;
    data(i,2) = packet.RigidBody(1).y;
    data(i,3) = packet.RigidBody(1).z;
    data(i,4) = packet.RigidBody(1).qx;
    data(i,5) = packet.RigidBody(1).qy;
    data(i,6) = packet.RigidBody(1).qz;
    data(i,7) = packet.RigidBody(1).qw;
    euler(i,:) = quat2eul(data(i,4:7),'ZYX') ;
    set(fig,'XData',t) ;
    set(fig,'YData',euler(:,3)*180/pi) ;
    angle = euler(i,3)*180/pi;
    drawnow ;
    if ( ...
        ( ...
            (angle<=-48 && angle>=-180)|| (angle<=180...
                && angle>131) ...
            )&& (coolDown == 0 && stop ~= 1))
        if(direction ==1 && polar ~=1)
            write(s,"S","Char");
            coolDown = 1;
            polar = 1;

```

```

else
    if(direction ==2 && polar ~=2)
        write(s,"N","Char");
        coolDown = 1;
        polar = 2;
    end
end
end
if ( ...
    (angle<=131 && angle>-48) ...
    && (coolDown ==0 && stop ~=1))
    if(direction ==2 && polar ~=1)
        write(s,"S","Char");
        coolDown = 1;
        polar = 1;
    else
        if(direction ==1 && polar ~=2)
            write(s,"N","Char");
            coolDown = 1;
            polar = 2;
        end
    end
end
polar_old = polar;
angle_tmp(j) = angle;
fprintf(fileID,'% .3f,% .3f,%u\n',t(i),...
    euler(i,3)*180/pi,polar);
j = j+1;
if (j>100)
    angle_mean = mean(angle_tmp);

```

```
err = angle_mean - angle_old;
if (err <=0.2 && err >= -0.2 && coolDown == 0 ...
    && polar ~=0)
    write(s,"C","char");
    coolDown =1;
    stop = 1;
    polar = 0;
end
if(err >0.2)
    stop = 0;
    direction = 2;
end
if (err <-0.2)
    stop = 0;
    direction = 1;
end
angle_old = angle_mean;
j=1;
end
if(t(i)-t_old>1)
    coolDown = 0;
    t_old = t(i);
end
i = i+1 ;
end
fclose(fileID);
end
```

2 Appendix B: Design and validation of the sliding mode controller for single axis attitude control using EPM

As the objective of this controller is to guarantee stability while performing the pointing maneuver, the following error dynamic is defined to establish the control law [121].

$$e = \theta - \theta_d \quad (.1)$$

where θ_d is the constant desired pointing angle and $\dot{\theta}_d = 0$. We will use the following sliding manifold to obtain the tracking performance within Σ_w and Σ_v , which represents the desired boundary of e and \dot{e} , respectively, as illustrated in Fig. .1.

$$s = \begin{cases} \dot{e} + \Sigma_v \sin \frac{\pi}{2} \frac{e}{\Sigma_w}, & |e| \leq \Sigma_w \\ \dot{e} + \Sigma_v \text{sign}(e), & |e| > \Sigma_w \end{cases} \quad (.2)$$

The time derivative is

$$\dot{s} = \begin{cases} \ddot{e} + \frac{\pi}{2} \frac{\Sigma_v}{\Sigma_w} \cos \frac{\pi}{2} \frac{e}{\Sigma_w} \dot{e}, & |e| \leq \Sigma_w \\ \ddot{e}, & |e| > \Sigma_w \end{cases} \quad (.3)$$

Set the Lyapunov function as

$$V = \frac{1}{2}e^2 + \frac{1}{2}Js^2 \quad (.4)$$

and its time derivative is

$$\dot{V} = e\dot{e} + Js\dot{s} \quad (.5)$$

We can further analyze the system's stability based on the current state, which can be divided into two cases. Note that the disturbance in Eq. ((3.45)) is neglected afterward for the sake of simplicity.

Case 1 - ($|e| \leq \Sigma_w$)

To reflect the working mechanism of the novel magnetorquer (bang-off-bang), we choose the following control law

$$M = -m\text{sign}(s) \quad (.6)$$

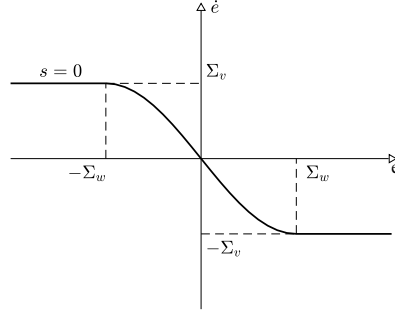


FIGURE .1. Sliding manifold illustrated on the phase plane.

where m is the magnitude of the magnetic dipole moment of the magnetorquer. By substituting the first derivatives obtained from Eq. (.2) and (.3), we can rewrite Eq. (.5) as

$$\dot{V} = e[s - \Sigma_v \sin \frac{\pi}{2} \frac{e}{\Sigma_w}] + Js[\ddot{e} + \frac{\pi}{2} \frac{\Sigma_v}{\Sigma_w} \cos \frac{\pi}{2} \frac{e}{\Sigma_w} \dot{e}] \quad (.7)$$

and to keep the derivation simple, we define the following variables

$$\begin{aligned} \Phi_1 &= \Sigma_v \sin \frac{\pi}{2} \frac{e}{\Sigma_w} \\ \Phi_2 &= J \frac{\pi}{2} \frac{\Sigma_v}{\Sigma_w} \cos \frac{\pi}{2} \frac{e}{\Sigma_w} \end{aligned} \quad (.8)$$

and by substituting Eq. ((3.45)), ((.2)), and (.8) into Eq. ((.7)) yields

$$\begin{aligned} \dot{V} &= e(s - \Phi_1) + s(\tau + \Phi_2 \dot{e}) \\ &= -e\Phi_1 + s[\tau + e + \Phi_2(s - \Phi_1)] \end{aligned} \quad (.9)$$

and substituting the torque with Eq. ((3.46)) and replace the control input with Eq. ((.6)) and defining

$$\Phi_3 = mB \cos \theta \quad (.10)$$

yields to

$$\begin{aligned} \dot{V} &= -e\Phi_1 + s[-\Phi_3 \text{sign}(s) + e + \Phi_2(s - \Phi_1)] \\ &= -e\Phi_1 - \Phi_3|s| + s[e + \Phi_2(s - \Phi_1)] \end{aligned} \quad (.11)$$

where

$$\Phi_{12} = \Phi_1 \Phi_2 = J \frac{\pi \Sigma_v^2}{4 \Sigma_w} \sin \frac{\pi e}{\Sigma_w} \quad (.12)$$

if we assume $|\theta| \leq \theta_{max} < 90^\circ$,

$$\dot{V} \leq -(\Phi_3 - |e| - \Phi_2 |s| + \Phi_{12}) |s| \quad (.13)$$

and implying

$$|e| \leq \sqrt{2V}, \quad |s| \leq \sqrt{\frac{2V}{J}} \quad (.14)$$

the above condition becomes

$$\dot{V} \leq -(\Phi_3 - \sqrt{2V} - \Phi_2 \frac{\sqrt{2V}}{J} + \Phi_{12}) |s| \quad (.15)$$

therefore by choosing Σ_w and Σ_v , which satisfies

$$m \geq (\sqrt{2V_0} + \Phi_{2_{max}} \frac{\sqrt{2V_0}}{J} + \Phi_{12_{max}}) / B \cos \theta_{max} \quad (.16)$$

Where V_0 is the initial value of the Lyapunov function and the subscript *max* denotes the maximum possible value. Thus, the system becomes stable and bounded.

Case 2 - ($|e| > \Sigma_w$)

Similar with Case 1, starting from Eq. (.5),

$$\begin{aligned} \dot{V} &= e [s - \Sigma_v \text{sign}(e)] + Js\ddot{e} \\ &= e [s - \Sigma_v \text{sign}(e)] + s\tau \\ &= -\Sigma_v |e| + s(\tau + e) \\ &= -\Sigma_v |e| + s(-\Phi_3 \text{sign}(s) + e) \\ &= -\Sigma_v |e| - \Phi_3 |s| + es \end{aligned} \quad (.17)$$

which then implies

$$\dot{V} \leq -(\Phi_3 - |e|) |s| \quad (.18)$$

to be satisfied. With the condition above in Eq. (.14),

$$\dot{V} \leq -(\Phi_3 - \sqrt{2V})|s| \quad (.19)$$

therefore as long as the condition below holds, we can assure the stable system will be attracted to the sliding manifold.

$$m \geq \frac{\sqrt{2V_0}}{B \cos \theta_{max}} \quad (.20)$$

3 Appendix C: MATLAB Code for the single torque single axis pointing experiment

```
qr=60*pi/180;
J=0.0614;
umax=50e-6;
q_max=80*pi/180;
u=0;
sig_w=20*pi/180;
sig_v=sqrt(sig_w*(4/pi)*(cos(q_max)/J)*umax);

clearvars -except s

if (exist('s')== 0)
    s = serialport("COM13",115200); %% arduino uno
else
    flush(s) ;
end
x = 1;
if (x==1)
    addpath(genpath(pwd))
```

```

fprintf( 'NatNet Polling Sample Start\n' )
% create an instance of the natnet client class
fprintf( 'Creating natnet class object\n' )
natnetclient = natnet;
natnetclient.HostIP = '169.254.104.249';
natnetclient.ClientIP = '169.254.104.249';
natnetclient.ConnectionType = 'Multicast';

fprintf( 'Connecting to the server\n' )
natnetclient.connect;
if ( natnetclient.IsConnected == 0 )
fprintf( 'Client failed to connect\n' )
fprintf( '\tMake sure the host is connected to the network\n' )
fprintf( '\tand that the host and client IP addresses ...
are correct\n\n' )
return
end

figure
fig = plot(0,0) ;

data = zeros(1e4,7) ;
t = [];
t_old = 0;
euler = [];
tic
i = 1;
polar = 0;

q_tmp = zeros(10,2);

```

```

q = 0;

fileID = fopen('Dipole_New_S2000_8.txt','w');
fprintf(fileID,'%s\n',"Time,w");
j = 1;

while(toc < 600)
    packet = natnetclient.getFrame;
    t(i) = toc ;
    data(i,1) = packet.RigidBody(1).x;
    data(i,2) = packet.RigidBody(1).y;
    data(i,3) = packet.RigidBody(1).z;
    data(i,4) = packet.RigidBody(1).qx;
    data(i,5) = packet.RigidBody(1).qy;
    data(i,6) = packet.RigidBody(1).qz;
    data(i,7) = packet.RigidBody(1).qw;
    euler(i,:) = quat2eul(data(i,4:7),'ZYX') ;

    set(fig,'XData',t) ;
    set(fig,'YData',euler(:,3)*180/pi) ;
    drawnow ;
    %control part
    q_tmp(j,1) = euler(i,3);
    q_tmp(j,2) = t(i);
    if (j>10)
        q = mean(q_tmp);
        qd = (q_tmp(10,1)-q_tmp(1,1))/(q_tmp(10,2)-...
            q_tmp(1,2));
        e=q-qd;
        if abs(e)<=sig_w

```

```

        s=qd+sig_v*sin((pi/2)*(e/sig_w));
    else
        s=qd+sig_v*sign(e);
    end
    j=1;
end
if (t(i)-t_old>1)
    if(sign(s)>=0 && polar ~=1)
        write(s,"S","Char");
        polar = 1;
    end
    if(sign(s)<0 && polar ~=2)
        write(s,"N","Char");
        polar = 2;
    end
    t_old = t(i);
end
fprintf(fileID,'% .3f,% .3f,% .3f,%u,% .3f,% .3f,\n',t(i),...
    euler(i,3)*180/pi,qd*180/pi,polar,e*180/pi,s);
i = i+1 ;
j = j+1;
end
fclose(fileID);
end
end

```

4 Appendix D: EPM for CUAVA-2 vibration test results

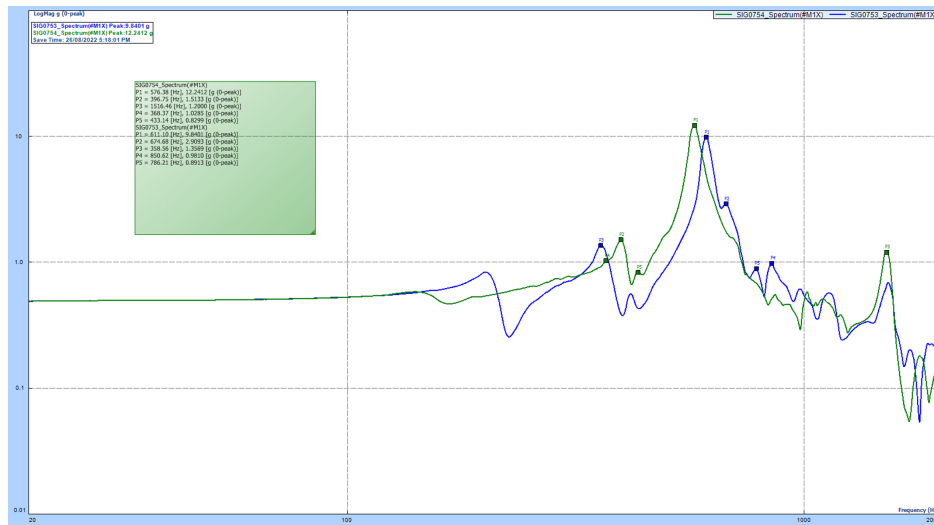


FIGURE .2. Load response to vibration in X axis from 20 to 2000Hz before and after 14.501 g RMV.

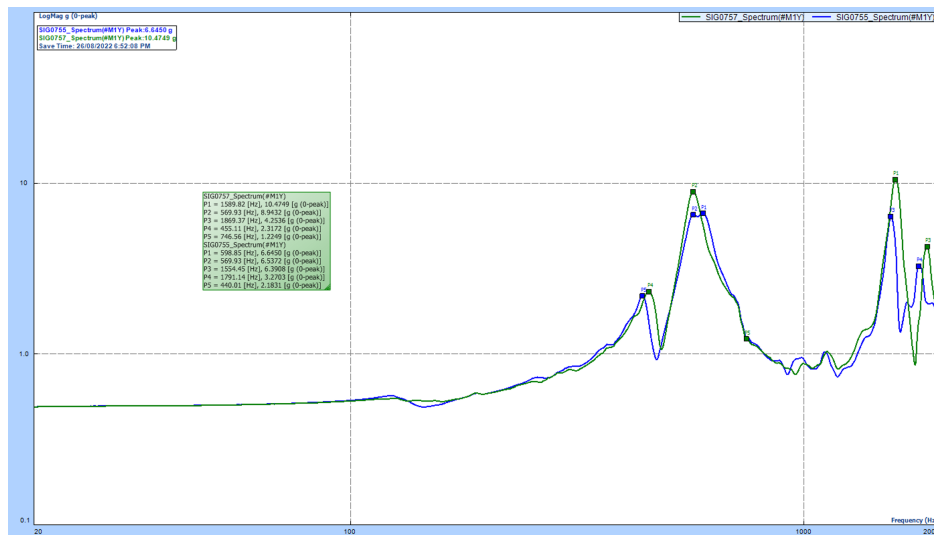


FIGURE .3. Load response to vibration in Y axis from 20 to 2000Hz before and after 14.501 g RMV.

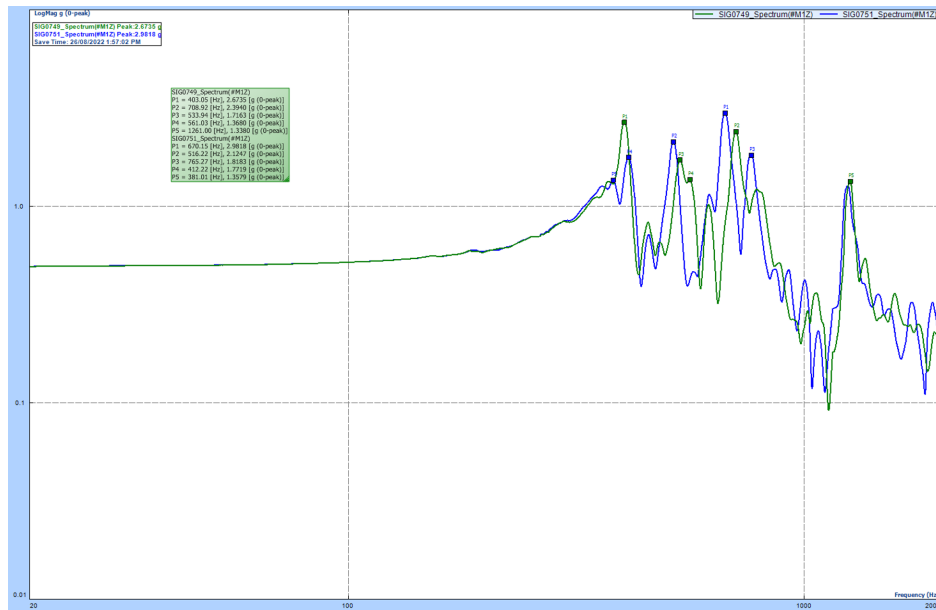


FIGURE .4. Load response to vibration in Z axis from 20 to 2000Hz before and after 14.501 g RMV